

**Investigating the DNA-Binding Interactions of Small Organic Molecules Utilizing
Ultrafast Nonlinear Spectroscopy**

By

Phi Doan

A dissertation submitted in partial fulfillment
of the requirements for the degree of
Doctor of Philosophy
(Chemistry)
in the University of Michigan
2016

Doctoral Committee:

Professor Theodore Goodson III, Chair
Professor Zhan Chen
Associate Professor Kenichi Kuroda
Professor Richard Robertson

© Phi Doan 2016

Dedication

I dedicate my dissertation to my family who have always supported and believed in me,
especially my mother and sister.

I dedicate this to both of my grandpas and my grandmas.

I also dedicate this to my friend, SMF 2005.

Acknowledgements

There are several individuals whom I would like to acknowledge. These are people who have encouraged and helped me throughout my life. First, I would like to thank Prof. Theodore Goodson III for the opportunity. He is one of the few people who has stood up and fought for me. Without him, this would have not been possible. He has provided me the guidance, support, and resources to be successful as a scientist. I will be forever thankful for Prof. Goodson. He will be a lifetime mentor and friend. I would like to thank Prof. Valerie Pierre who has always supported me as well as being a great mentor. My work with her as an undergraduate student has built the foundation for me to succeed as a scientist. I would like to thank Dr. Carl Fung Kee Fung for being the catalyst for my passion towards chemistry. Without her, I would have never pursued a career in chemistry. I would like to thank Dr. Yifan Zhang for giving me the opportunity to work in industry. He was one of the few people willing to take a chance on me. I would like to thank the Goodson Group members for their help and support. I consider the Goodson group to be family. I would also like to thank my collaborators (Prof. Wilson, Prof. Imperiali, Prof. Laine) and dissertation committee members (Prof. Chen, Prof. Kuroda, Prof. Robertson). Finally, I would like to thank Ms. Hanson. She was one of the few people who contacted me directly and told me to not waste it when things were not going so well. In the end, I would have never made it where I am today without these people. I

am thankful for the opportunity and support that has been provided by each of these individuals. Well, I guess it all worked out in the end nonetheless.

Table of Contents

Dedication	ii
Acknowledgments	iii
List of Figures	ix
List of Schemes	xv
List of Tables	xvi
Abstract	xvii
Chapter 1: Introduction and Background of the DNA-Binding Interactions of Small Organic Molecules	1
1.1 Dissertation Outline	1
1.2 Introduction and the Impact of Cancer	5
1.3 An Overview on the Functions and Importance of DNA in Cellular and Biological Processes	10
1.4 The Binding Interactions of Small Organic Molecules with DNA: Intercalation and Groove Binding	15
1.5 Methodologies to Characterize the DNA-Binding Interactions of Small Organic Molecules	19
1.6 Utilization of Two-Photon and Time-Resolved Spectroscopies to Examine Biological-Based Systems	25
Chapter 2: Experimental Instrumentation and Techniques	34
2.1 An Overview and Introduction of Ultraviolet–Visible Spectroscopy and Single-Photon Excited Fluorescence	35

2.2 An Overview of Circular Dichroism Spectroscopy to Investigate the DNA-Binding Interactions of Small Organic Molecules	37
2.3 An Introduction and Overview of Two-Photon Absorption Spectroscopy	39
2.4 An Introduction and Overview of Time-Resolved Fluorescence Upconversion	43
2.5 An Introduction and Overview of Time-Correlating Single-Photon Counting	46
2.6 An Introduction and Overview of Confocal Microscopy to Image Live Cells	49
2.7 Summary and Standard Operating Procedures to Culture Mammalian Cells	56
Chapter 3: Two-Photon Spectroscopy as a New Sensitive Method for Determining the DNA Binding Mode of Fluorescent Nuclear Dyes	71
3.1 Original Publication Information	71
3.2 Abstract	71
3.3 Introduction	72
3.4 Experimental	76
3.5 Results and Discussion	80
3.6 Conclusion	92
Chapter 4: A New Design Strategy to Tailor the DNA-Binding Mechanism of Small Organic Molecules and Drugs	98
4.1 Original Publication Information	98
4.2 Abstract	98
4.3 Introduction	99
4.4 Experimental	102
4.5 Results	107
4.6 Discussion	137

4.7 Conclusion	147
Chapter 5: Photophysical Investigation and Imaging of Sox-Based Fluorescence Chemosensor Peptide for Kinase Activity with Continuous Real-Time Analysis in Live Cells	155
5.1 Explanation	155
5.2 Introduction	156
5.3 Results and Discussion	163
5.4 Conclusion	176
Chapter 6: Microporous Inorganic/Organic Hybrids via Oxysilylation of a Cubic Symmetry Nanobuilding Block [(HMe₂SiOSiO_{1.5})₈] with R_xSi(OEt)_{4-x}	179
6.1 Original Publication Information	179
6.2 Abstract	179
6.3 Introduction	180
6.4 Experimental	182
6.5 Results and Discussion	184
6.6 Conclusion	191
Chapter 7: Avoiding Carbothermal Reduction: Distillation of Alkoxysilanes from Biogenic, Green, and Sustainable Sources	198
7.1 Original Publication Information	198
7.2 Abstract	198
7.3 Introduction	199
7.4 Experimental	206
7.4 Results and Discussion	209
7.5 Conclusion	222

Chapter 8: Overview: Summary, Importance, and Future Work of Dissertation	227
8.1 Explanation	227
8.2 The Drug Development Process	228
8.3 Investigating the DNA-Binding Interactions of Small Organic Molecules (Chapters 3 and 4)	230
8.3.1 TPA as a New Sensitive Methodology to Diagnose the DNA-Binding Interactions of Small Organic Molecules	230
8.3.2 A New Design Strategy to Tailor the DNA-Binding Mechanism of Small Organic Molecules and Drugs	232
8.3.3 RNA as a Target for Therapeutics Aimed at Diseases and Disorders	235
8.4 Examining Kinase Activity by Implementing a Chemosensor Peptide with Continuous Real-Time Analysis in Live Cells (Chapter 5)	237
8.5 Synthesis and Characterization of Silsesquioxane-Based Microporous Materials (Chapter 6)	241
8.6 Avoiding Carbothermal Reduction: Distillation of Alkoxysilanes From Biogenic, Green, and Sustainable Sources (Chapter 7)	244

List of Figures

Figure 1.1. Acquired functional capabilities of cancer.	6
Figure 1.2. Classes of DNA-targeted drugs and their interactions with DNA.	9
Figure 1.3. Structure of DNA.	11
Figure 1.4. Summary of DNA replication.	13
Figure 1.5. Summary of transcription.	14
Figure 1.6. Importance of DNA for protein synthesis and gene expression.	14
Figure 1.7. Cartoon representation of intercalation and groove binding.	17
Figure 1.8. Minor versus major groove of DNA.	18
Figure 1.9. General procedure for fluorescent displacement dye assay.	21
Figure 1.10. Information on the DNA-binding mode by absorption, LD, and CD spectroscopy.	24
Figure 2.1. Jabolonski diagram representing one-photon absorption (OPA), two-photon absorption (TPA), and the emission process.	40
Figure 2.2. TPA set-up in our laboratory.	41
Figure 2.3. Fluorescence upconversion set-up in our laboratory.	45
Figure 2.4. TCSPC setup in our laboratory.	48
Figure 2.5. Representation of wide-field vs point scanning of a specimen.	50
Figure 2.6. Diagram representation of confocal microscopy.	51
Figure 2.7. Principle of FLIM based on TCSPC.	52
Figure 2.8. Inverted confocal microscope located in the MIL Core at the University of Michigan.	56

Figure 2.9. (A) Laminar flow hood and (B) CO ₂ incubation oven in our laboratory.	57
Figure 2.10. Standard operating procedure to stain cells with fluorescent nuclear dyes.	60
Figure 2.11. (A) Simplified directions to use BioPORTER peptide delivery kit. (B) Summary of how the BioPORTER reagent works.	61
Figure 3.1. (A) Intercalative and (B) groove binding modes. Orientation of the S ₀ → S ₁ transition dipole is shown in green. The DNA electric field is shown in red.	73
Figure 3.2. Chemical structures of 4,6-bis(4-(4-methylpiperazin-1-yl)phenyl) pyrimidine (1), 4,6-bis(4-(4-methylpiperazin-1-yl)phenyl) pyrimidin-2-ol (2), acridine orange (3), Hoechst 33258 (4), thioflavin t (5), and topotecan (6).	74
Figure 3.3. ¹ H-NMR of 1 .	79
Figure 3.4. ¹³ C-NMR of 1 .	80
Figure 3.5. (A) Absorption and (B) emission spectra of 3 . Measurements were conducted at different DNA (base pairs) concentrations with units of μM.	82
Figure 3.6. (A) TPA cross-section of 3 (5 μM) plotted as a function of DNA (base pairs) concentration. Inset graph: Enlargement at low DNA concentration. Results are the mean with ± SD (<i>n</i> = 3). (B) TPA cross-section plotted in the presence of [poly(dG-dC)] ₂ . The red line is to guide the eye.	82
Figure 3.7. (A) Absorption and (B) emission spectra of 4 . Measurements were conducted at different DNA (base pairs) concentrations with units of μM.	83
Figure 3.8. (A) TPA cross-section of 4 (5 μM) plotted as a function of DNA (base pairs) concentration. Inset graph: Enlargement at low DNA concentration. Results are the mean with ± SD (<i>n</i> = 3). (B) TPA cross-section plotted in the presence of [poly(dA-dT)] ₂ . The red line is to guide the eye.	84
Figure 3.9. CD spectra of (A) 3 and (B) 4 at different DNA concentrations. Measurements were conducted at different DNA (base pairs) concentrations with units of μM.	85
Figure 3.10. (A) TPA cross-section of 5 (5 μM) plotted as a function of DNA (base pairs) concentration. Inset graph: Enlargement at low DNA concentration. Results are the mean with ± SD (<i>n</i> = 3). The red line is to guide the eye. (B) CD spectra of 5 at different DNA concentrations. Measurements were conducted at different DNA (base pairs) concentrations with units of μM.	86

Figure 3.11. (A) Absorption and (B) emission spectra of 5 at different DNA concentrations. Measurements were conducted at different DNA (base pairs) concentrations with units of μM .	86
Figure 3.12. (A) Absorption and (B) emission spectra of 6 . Measurements were conducted at different DNA (base pairs) concentrations with units of μM .	88
Figure 3.13. (A) TPA cross-section of 6 ($5 \mu\text{M}$) plotted as a function of DNA (base pairs) concentration. Inset graph: Enlargement at low DNA concentration. Results are the mean with \pm SD ($n = 3$). The red line is to guide the eye. (B) CD spectra of 6 at different DNA concentrations. Measurements were conducted at different DNA (base pairs) concentrations with units of μM .	88
Figure 3.14. (A) Absorption and (B) emission spectra of 1 . Measurements were conducted at different DNA (base pairs) concentrations with units of μM .	89
Figure 3.15. (A) TPA cross-section of 1 ($5 \mu\text{M}$) plotted as a function of DNA (base pairs) concentration. Inset graph: Enlargement at low DNA concentration. Results are the mean with \pm SD ($n = 3$). The red line is to guide the eye. (B) CD spectra at different DNA concentrations.	90
Figure 3.16. (A) Absorption and (B) emission spectra of 2 . Measurements were conducted at different DNA (base pairs) concentrations with units of μM .	91
Figure 3.17. (A) TPA cross-section of 2 ($5 \mu\text{M}$) plotted as a function of DNA (base pairs) concentration. Inset graph: Enlargement at low DNA concentration. Results are the mean with \pm SD ($n = 3$). The red line is to guide the eye. (B) CD spectra at different DNA concentrations.	91
Figure 4.1. Chemical structures of the fluorescent nuclear dyes. The fluorophores adopt a donor-acceptor-donor motif with varying conjugation length between the electron donor arms and electron acceptor core.	108
Figure 4.2. Steady-state spectra of the fluorophores. Normalized absorption spectra of the fluorescent nuclear dyes in the (a) absence and (b) presence of DNA. Normalized emission spectra of the fluorescent nuclear dyes in the (c) absence and (d) presence of DNA.	111
Figure 4.3. CD spectra. Evidence of DNA-binding interactions for (a) 1 , (b) 2 , (c) 3 , (d) 4 , (e) 5 , (f) 6 , (g) 7 . (h) An ICD signal was not detected for 8 , which indicates that the molecule is neither intercalating nor groove binding with DNA. Measurements were conducted at [fluorophore] = $5 \mu\text{M}$ and [DNA] = $100 \mu\text{M}$.	116

Figure 4.4. TPA cross-section (δ) plotted as a function of DNA concentration. The TPA cross-section was measured for (a) 1 , (b) 4 , (c) 5 , (d) 6 with [fluorophore] = 5 μ M at increasing DNA concentrations to determine the DNA-binding mode. The red line is to guide the eye.	118
Figure 4.5. Fluorescence lifetime dynamics. Fluorescence upconversion of (a) 1 , (b) 2 , (c) 3 , (d) 4 , (e) 5 , (f) 6 , (g) 7 , (h) 8 in the absence of DNA.	121
Figure 4.6. Fluorescence lifetime dynamics of fluorescent nuclear dyes in the presence of DNA.	123
Figure 4.7. Fluorescence anisotropy in the absence of DNA for (a) 1 , (b) 2 , (c) 3 , (d) 4 , (e) 5 , (f) 6 , (g) 7 , (h) 8 .	125
Figure 4.8. Fluorescence anisotropy in the presence of DNA for (a) 1 , (b) 2 , (c) 3 , (d) 4 , (e) 5 , (f) 6 , (g) 7 , (h) 8 .	127
Figure 4.9. Single-photon excited fluorescence confocal microscopy images of (a) 1 , (b) 2 , (c) 3 , (d) 4 , (e) 5 , (f) 6 , (g) 7 , (h) 8 . The cells were incubated at 2 μ M of fluorophore for 1 h. Bar: 20 μ m.	136
Figure 4.10. Two-photon excited fluorescence confocal microscopy images of (a) 1 , (b) 2 , (c) 3 , (d) 4 , (e) 5 , (f) 6 , (g) 7 , (h) 8 . The cells were incubated at 2 μ M of fluorophore for 1 h. λ_{ex} = 800 nm. Bar: 20 μ m.	136
Figure 4.11. Two-photon excited fluorescence confocal microscopy images of a single HeLa cell. (a) One-photon and (b) two-photon excited fluorescence confocal microscopy images of cells stained with 1 . Bar: 5 μ m.	137
Figure 5.1. Signaling pathways of a cell.	156
Figure 5.2. Cartoon representation of kinase enzymes.	158
Figure 5.3. DFG motif location on kinase enzyme. These residues are responsible for preparing ATP for phosphorylation.	159
Figure 5.4. (Top) Catalytic cycle of kinase phosphorylation of peptide/protein substrate and (bottom) simplified schematic diagram of protein kinase mechanism.	160
Figure 5.5. Schematic representation of Sox-labeled peptide for probing kinase activity.	162
Figure 5.6. (A) Absorption and (B) emission spectra of JNKP19 in the absence (- -) and presence (-) of 10 mM MgCl ₂ .	164

Figure 5.7. (A) Fluorescence quenched in the absence of a divalent metal due to the PET effect. (B) Fluorescence enhancement in the presence of a divalent metal due to the CHEF effect.	165
Figure 5.8. (A) Absorption and (B) emission spectra of JNKS19 (red) and JNKP19 (black) in the presence of 10 mM MgCl ₂ .	166
Figure 5.9. The fluorescence of JNKS19 was monitored as a function of time in the presence of JNK2, ATP, and MgCl ₂ .	166
Figure 5.10. Confocal microscopy image of cells (A) before and (B) after transfection of fluorescein labeled goat antibody. $\lambda_{\text{ex}} = 490 \text{ nm}$.	168
Figure 5.11. Confocal microscopy image of cells (A) before and (B) after transfection of JNKP19. $\lambda_{\text{ex}} = 780 \text{ nm}$.	169
Figure 5.12. Fluorescence of JNKP19 at varied concentrations of MgCl ₂ .	169
Figure 5.13. Fluorescence decay of JNKP19 at various concentrations of MgCl ₂ .	171
Figure 5.14. FLIM images of cells incubated with ionophore A23187 in the (A) absence and (B) presence of JNKP19. The cumulative histogram of fluorescence lifetime values is shown below the images.	173
Figure 5.15. Fluorescence dynamics of JNKP19 at varying peptide concentrations. Experiments were carried out at pH = 7.4 and 1 mM MgCl ₂ .	174
Figure 5.16. FLIM of HeLa cells transfected (A) without and (B) with 16.6 μM JNKP19.	174
Figure 5.17. Cumulative histogram of fluorescence lifetime values of cells transfected with various concentrations of JNKP19.	175
Figure 6.1. 1:1 OHS:TEOS (A) gel immediately after reaction and (B) after drying for 3 weeks.	186
Figure 6.2. FTIR spectrum of (A) OHS and (B) 1:1 OHS:TEOS.	187
Figure 6.3. XRD pattern of (A) OHS and (B) 1:1 OHS:TEOS gel.	189
Figure 7.1. EI-MS of II .	211
Figure 7.2. ¹ H-NMR of II .	212
Figure 7.3. ¹³ C-NMR of II .	212

Figure 7.4. ^{29}Si -NMR of II .	213
Figure 7.5. FTIR spectrum of II .	213
Figure 7.6. TGA of II .	214
Figure 7.7. ^1H -NMR of spirosiloxane synthesized from 1,4-butanediol.	214
Figure 7.8. ^{13}C -NMR of spirosiloxane synthesized from 1,4-butanediol.	215
Figure 7.9. ^{29}Si -NMR of spirosiloxane synthesized from 1,4-butanediol.	215
Figure 7.10. EI-MS of spirosiloxane III .	216
Figure 7.11. ^1H -NMR of III .	216
Figure 7.12. ^{13}C -NMR of III .	217
Figure 7.13. ^{29}Si -NMR of III .	217
Figure 7.14. FTIR spectra of exchange reaction with MeOH and 1,4-butanediol spirosiloxane is shown in red. $\text{Si}(\text{OMe})_4$ is shown in blue.	218
Figure 7.15. ^1H -NMR exchange reaction with MeOH and of spirosiloxane synthesized from 1,4-butanediol.	218
Figure 7.16. ^{29}Si -NMR exchange reaction with MeOH and of spirosiloxane synthesized from 1,4-butanediol.	219
Figure 7.17. XRD pattern of RHA.	219
Figure 7.18. (A) Colloidal silica at pH 1 is transparent without scattering light. (B) A gel forms scattering light on neutralizing with Na_2CO_3 (pH 7, 30 min).	222
Figure 8.1. Chemical structures of kinase inhibitors.	242
Figure 8.2. Potential applications of spirosiloxane synthesized from RHA.	248

List of Schemes

Scheme 3.1. Synthesis of 1 .	75
Scheme 6.1. (A) Oxysilylation reaction with a catalytic amount of $(\text{C}_6\text{F}_5)_3\text{B}$. (B) Proposed mechanism of oxysilylation reaction.	181
Scheme 6.2. General oxysilylation reaction of OHS with $\text{RSi}(\text{OEt})_3$ with a catalytic amount of $(\text{C}_6\text{F}_5)_3\text{B}$.	182
Scheme 8.1. Synthesis of Alexa 488 amino acid derivative. This fluorophore can be integrated into the Sox-peptide substrate via SPPS, which can undergo FRET with the Sox-fluorophore. This will allow the fluorescence to be monitored at a lower energy wavelength to minimize autofluorescence from the cells.	240
Scheme 8.2. Synthesis of $\text{Si}(\text{OEt})_3$ -cysteine.	244

List of Tables

Table 3.1. Fluorescence quantum yield of dyes at various DNA concentrations.	81
Table 4.1. Summary of steady-state properties of the fluorophores in the absence of DNA.	113
Table 4.2. Summary of steady-state properties of the fluorophores in the presence of DNA.	113
Table 4.3. TPA cross-section (δ) of fluorescent nuclear dyes in the absence of DNA.	117
Table 4.4. Summary of fluorescence lifetime data in the absence of DNA.	122
Table 4.5. Summary of fluorescence lifetime data in the presence of DNA.	123
Table 4.6. Rotational anisotropy decay.	127
Table 4.7. Molecular orbitals diagrams.	131
Table 4.8. Experimental TPA cross-sections (δ) and electronic properties of the unbound fluorophore.	133
Table 5.1. Summarized fluorescent lifetime of JNKP19 at various concentrations of MgCl_2 .	171
Table 6.1. Specific conditions explored for the synthesis of the gels.	185
Table 6.2. Selected properties for various gels, 1:1 OHS:RSi(OEt) ₃ (Si-H/Si-OEt).	188
Table 6.3. Selected properties for various gels, 1:1 OHS:R[Si(OEt) ₃] ₂ (Si-H/Si-OEt).	188
Table 7.1. Percent SiO ₂ depolymerization and characterization data given.	209

Abstract

Cancer is one the leading causes of death in the United States. Researchers have focused on designing and developing therapeutics aimed at DNA in order to treat cancer and other disorders. In this dissertation, the DNA-binding interactions of small organic molecules were investigated. We developed a highly sensitive methodology to determine the DNA-binding mode of small molecules unambiguously unlike other conventional techniques. Furthermore, we established structure-property relationships for a set of newly synthesized small molecules that allows tailoring of the DNA-binding mode by modifying the electron acceptor properties of the heterocyclic core of the binding molecule. By understanding how small organic molecules bind and interact with DNA, this work could have a profound impact on the design and development of small organic molecules, such as therapeutics, aimed at DNA.

The DNA-binding mechanism of small organic molecules, such as DNA-targeted drugs and fluorescent nuclear dyes, is key to their performance. Therefore, understanding the DNA-binding mechanism is critical for the design and development of molecules targeted at DNA. The purpose of this present research is to investigate the DNA-binding interactions of small organic molecules by employing ultrafast nonlinear spectroscopy. While basic design principles are proposed, the DNA-binding modes of many small organic molecules cannot be unambiguously assigned based either on their structure, or through the use of many well-established spectroscopic techniques. A new methodology

utilizing two-photon spectroscopy was developed to determine the DNA-binding modes of small organic molecules definitively, contrarily to other well-established spectroscopic techniques. The impact of this work is imbedded with the ultrafast nonlinear spectroscopic studies of the DNA-binding interactions of small organic molecules. The newly developed methodology demonstrated superior sensitivity at both low drug and DNA concentrations by more than order of magnitude in comparison to circular dichroism (CD). This indicates that our approach can be used to probe DNA-drug interactions at biologically relevant conditions, which is critical in drug research and development.

The impact of this work also investigated the DNA-binding interactions of newly synthesized fluorescent nuclear dyes. This study has led to the emergence of structure-property relationships of DNA-binding molecules that adopt a crescent or V-shaped scaffold. The findings reveal that the structure of these fluorophores can be designed to either intercalate or groove bind with DNA by structurally modifying the electron acceptor properties of the central heterocyclic core. This is important because it allows the performance, specificity, and localization of a DNA-binding molecule to be controlled. The localization and cellular uptake of these small molecules were evaluated by conducting a series of bio-imaging studies in live HeLa cells. This work is significant because the design strategy can be applied towards the development of small molecules aimed at DNA.

In addition to examining the DNA-binding interactions of small organic molecules, the research presented in this dissertation focused on the synthesis and characterization of silicon hybrid materials and polymers. A new class of cross-linked microporous

silsesquioxane-based materials was synthesized by the Piers-Rubinsztajn (oxysilylation) reaction. These materials offer high specific areas ($> 700 \text{ m}^2/\text{g}$) and high thermal stability ($> 300 \text{ }^\circ\text{C}$) with pore sizes of 0.6 – 2.0 nm. Moreover, these materials are attractive because multiple functionalities can be introduced to the system, which opens further applications. Because of this, the microstructure, chemical composition, surface properties, and porosity can be tailored. Another portion of the dissertation concentrated on synthesizing silicon compounds from biogenic silica sources, such as rice hull ash. We developed a new route for the synthesis of alkoxysilanes by a base-catalyzed depolymerization of silica. This is the first example that has demonstrated a direct synthesis of alkoxysilanes from silica, which has been examined for over 80 years without success. Our process is an alternative to the carbothermal reduction of silica, which offers several advantages as it is not a high energy/temperature process, does not produce toxic byproducts, and does not leave a large carbon footprint. Since these alkoxysilanes can be distilled, they can be easily purified meaning that this process can be employed for applications that require high purity silicon. This is significant because this process has the potential to reduce the cost of many silicon containing products.

Chapter 1

Introduction and Background of the DNA-Binding Interactions of Small Organic Molecules

1.1 Dissertation Outline

In Chapter 1, the introduction is presented. The objective of the introduction is to provide the reader a background with regards to the research. The introduction discusses the motive behind the present work. It is important to connect the research to the big picture as it is directly to cancer. Cancer is major concern in today's society. As a result, DNA has been a major target to treat cancer. Unlike chemotherapy which requires the use of radiation, DNA-targeted drugs do not expose cells to radiation and are more selective towards cancerous cells. The work presented will focus on the DNA-binding interactions of small organic molecules. It is important to understand such interactions because the performance and selectivity of DNA-targeted drugs and fluorescent nuclear dyes are dependent on the DNA-binding mechanism. However, there remain limitations with the convention techniques used to understand the DNA-binding interactions of small organic molecules as these techniques offer ambiguous interpretations and low sensitivity. An overview of the background and methodologies used to investigate the DNA-binding interactions of small organic molecules will be presented.

The instruments and techniques employed in this dissertation are discussed in Chapter 2. Explanations of steady-state spectroscopy, two-photon spectroscopy, time-resolved spectroscopy (fluorescence upconversion, time-correlated single-photon counting), circular dichroism, and fluorescence confocal microscopy are included. Additionally, the culture of mammalian cells is discussed. Standard operating procedures for the confocal microscope and the culture of mammalian cells are presented. This section is used to inform the reader about the fundamental details of the experiments.

In Chapter 3, a new methodology was developed utilizing two-photon spectroscopy to determine the DNA-binding mode (groove binding vs intercalation). This work was published in the *Journal of the American Chemical Society*. The objective of this work was to demonstrate a new approach to evaluate the DNA-binding interactions of DNA-targeted drugs and fluorescent nuclear dyes. The key results indicate that the changes in the TPA cross-sections are able to differentiate between the DNA-binding modes. Furthermore, our approach demonstrated higher sensitivity at both low DNA and drug concentrations by more than an order of magnitude as compared to CD, indicating that the methodology can be used at biologically relevant conditions. The importance of this work is that the methodology can be employed to understand how small organic molecules interact with DNA, which is important for drug research and development.

In Chapter 4, we investigated a series of newly synthesized fluorescent dyes that possess a crescent shaped donor-acceptor-donor motif. This study has led to the emergence of structure-property relationships in regards to the DNA-binding mechanism. The findings reveal that the structure of these fluorophores can be designed to either intercalate or groove bind with DNA by structurally modifying the electron accepting

properties of the central heterocyclic core. Our new approach utilizing TPA was employed to diagnose the DNA-binding mode. These fluorophores offer several advantages over commercially available dyes as they exhibit low cytotoxicity and high photostability as well as require low energy excitation wavelengths. The steady state properties and the fluorescence dynamics were investigated. The dyes were found to possess high turn on/off sensitivity upon binding with DNA. The results indicate that the optical properties of the dyes can be finely tuned by varying the conjugation length and electron accepting properties of the heterocyclic core. A series of bio-imaging experiments were conducted in live HeLa cells to evaluate the performance of the dyes. This work has been submitted to *Nature Chemistry*. The work in Chapters 3 and 4 was done in collaboration with Prof. James Wilson at the University of Miami.

The work presented in Chapter 5 examined kinase activity by implementing a custom fluorescent-based chemosensor peptide. The Sox-labeled peptide offers several advantages over traditional kinase assays as it is highly sensitive and allows for continuous real-time analysis as well as high-throughput applications. In collaboration with Prof. Barbara Imperiali at MIT, the kinase activity was examined by TPA and time-correlated single-photon counting (TCSPC). In addition, bio-imaging studies were carried out in live HeLa cells to study the kinase activity at physiological conditions. This is the first example that has employed a kinase assay in live cells with continuous real-time analysis. Fluorescence lifetime imaging microscopy (FLIM) was utilized to examine the kinase activity. Kinase activity is important for cellular communication and signaling. As a result, many disorders, such as cancer, are associated with abnormal kinase activity.

Therapeutics aimed at targeting kinase activity are of considerable interest. This project is still ongoing and will be resumed by new graduate student,

Chapter 6 presents a series of silsesquioxane-based network microporous polymers that were synthesized by a new route via the Piers-Rubinsztajn reaction. The reactions were carried out in mild conditions in hydrocarbon solvents in the presence of a Lewis acid catalyst. The materials were characterized by Fourier-transform infrared spectroscopy (FTIR), thermal gravimetric analysis (TGA), and X-ray diffraction (XRD). Porosity and surface area analyses were done by Brunauer–Emmett–Teller (BET) method. These materials were found to possess high surface areas ($>700 \text{ m}^2/\text{g}$), high thermal stability ($>300 \text{ }^\circ\text{C}$), and amorphous structures. The materials have the potential to be tailored so that multiple functionalities can be introduced into the system. Some potential applications of these materials include gas storage and sieving as well as absorbent materials. This work was published in the *Journal of the Ceramic Society of Japan*.

In Chapter 7, the “Grand Challenge” of silicon chemistry was explored. The dissolution of silica has been reported in past decades. However, this is the first report of direct, base catalyzed depolymerization of silica by the reaction with hindered diols to yield spirocyclic alkoxy silanes or spiro siloxanes that can be distilled with high purity. We developed a renewable process to produce spiro siloxanes from biogenic silica sources, such as rice hull ash. This process offers several advantages over conventional methods used in industry. For example, the process is not energy intensive, does not produce a toxic, polluting byproduct, and does not require expensive capital equipment. These spiro siloxanes can be used as a precursor for many silicon-based materials, such as

fumed silica or sol-gel processing. The impact of this work is that this new process may significantly reduce the cost of many silicon containing products. This work was published in *Angewandte Chemie*. The work completed in Chapters 6 and 7 was done in collaboration with Prof. Richard Laine in the Materials Science and Engineering Department located at the University of Michigan.

In Chapter 8, the impact of the work presented in the dissertation will be discussed. This chapter is significant as it summarizes the work to the general audience. The main focus of this chapter is to relate the research to the “big picture”. Although the work only addresses a small portion of the big picture, the research has contributed to each field in some aspect. Perhaps, the research can be applied to future research, which may lead to significant contributions to the big picture. Future work with regards to each project will be discussed in significant detail. The work here paves the way for future research. The work will be carried out by future students and/or researchers. This chapter is important because it provides the foundation and background for others to continue future research.

1.2 Introduction and the Impact of Cancer

Cancer also known malignant neoplasm or malignant tumor is a disease that involves abnormal cell growth that can spread to other regions within the body, which results in death if the spread is not controlled. Cancer is the second most cause of death after heart disease, accounting for 23% of deaths in the US.¹ It has been reported that 90 – 95% of cancer is due to external factors and 5 – 10 % is due to internal factors.² It is estimated that over 1.6 million new cases and approximately 600,000 deaths were a result of cancer in 2015² as well as over 14.5 million people are currently living with cancer as of 2014.³

Furthermore, it has been reported that over 100 different known cancers exist today.⁴ Cancer cells cause defects in cellular and biological regulatory processes that govern cell homeostasis and proliferation. The complexity of cancer provokes a number a questions that requires further investigation. In general, most cancers acquire the same set of functional capabilities as shown in Figure 1.1.⁵ As a consequence, chemotherapeutic and cytotoxic drugs are widely used for the treatment of cancer although their effectiveness is compromised by several disadvantages.⁶ Hence, new methodologies and technologies have been of considerable interest to better understand the complexity of cancer.

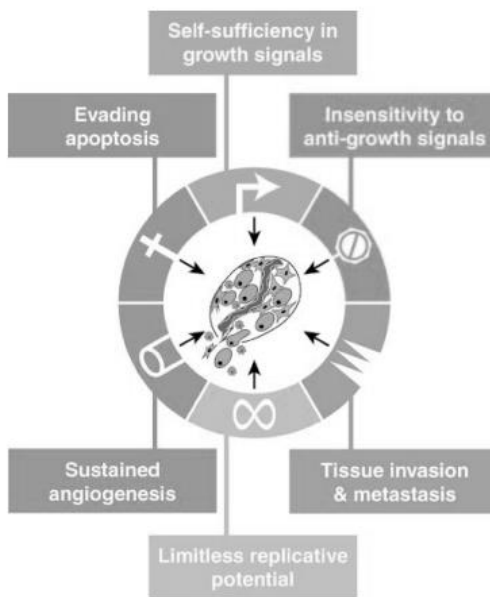


Figure 1.1. Acquired functional capabilities of cancer.

In general, cancer therapy involves exposing cells to anti-cancer agents that can increase cancer cell apoptosis more efficiently than healthy cells. These therapies are designed to target specific molecular and cellular processes directly related to cancer. It

has been reported that cancerous cells proliferate more rapidly than normal cells.^{5,6} Thus, many therapies have been targeted at cell proliferation. Therapeutics targeted directly at deoxyribonucleic acid (DNA) are of considerable interest because DNA is essential for cell proliferation. More specifically, DNA-targeted drugs have been investigated as therapeutics aimed at cancer. These drugs work by inhibiting or preventing the growth and spread of cancer by interfering with processes directly related to DNA.⁷ Unlike chemotherapy which requires the use of radiation, DNA-targeted drugs do not require elaborate instruments and does not expose cells to radiation. Remarkably, anti-cancer agents that target DNA are some of the most effective agents for cancer treatment.⁷ However, some are considered to be very toxic.⁸ The efficacy of small organic molecules targeted at DNA is more dependent on their effect on the DNA structure rather than the sequence selectivity.⁷ The binding mechanism of DNA-targeted drugs correlate to the biological activity or effectiveness of the drug, which is an important parameter in the screening process.⁹ The simplest form of designing DNA-targeted drugs is by blocking access of proteins and/or enzymes to DNA.¹⁰ This results in the inhibition of DNA-related processes leading to cell apoptosis. Consequently, there have been efforts in understanding on how drugs interact with DNA as well as design strategies to control the DNA-binding mechanism, which is necessary for the development of more selective and less toxic DNA-targeted therapies.

There have been significant advances in the development of DNA-targeted drugs over the last century. The modern era of cancer therapy was a consequence of chemical warfare from World War I and II.¹¹ Research during World War II led to further discoveries of alkylating agents for cancer therapy.¹² Nitrogen mustards were the first

alkylating agents used for cancer therapy, which work by covalently binding or cross-linking with DNA to prevent DNA replication. However, these agents are extremely toxic and carcinogenic. Later, antibiotics were revolutionized in the 20th century. Antibiotics are generally used to treat bacterial infections. Interestingly, it was discovered that antibiotics can also be utilized to treat cancer.¹² Antitumor antibiotics, such as doxorubicin, were found to have to high selectivity for cancerous cells.¹³ These drugs act by interfering with enzyme access to DNA. This was important as it encouraged researchers to consider processes relevant to DNA, including transcription and replication.⁷ This has led to the development of code-reading drugs that target specific DNA sequences. These drugs act by targeting the minor or major groove of DNA,¹⁴ which inhibits or activates enzyme interactions with DNA. Another class of drugs acts by intercalating with DNA, which are known as enzyme inactivators. Topoisomerase I and II are the most widely targeted enzymes since they are required for DNA transcription and replication. By hindering or inactivating these processes, the formation and spread of cancerous cells can be inhibited.

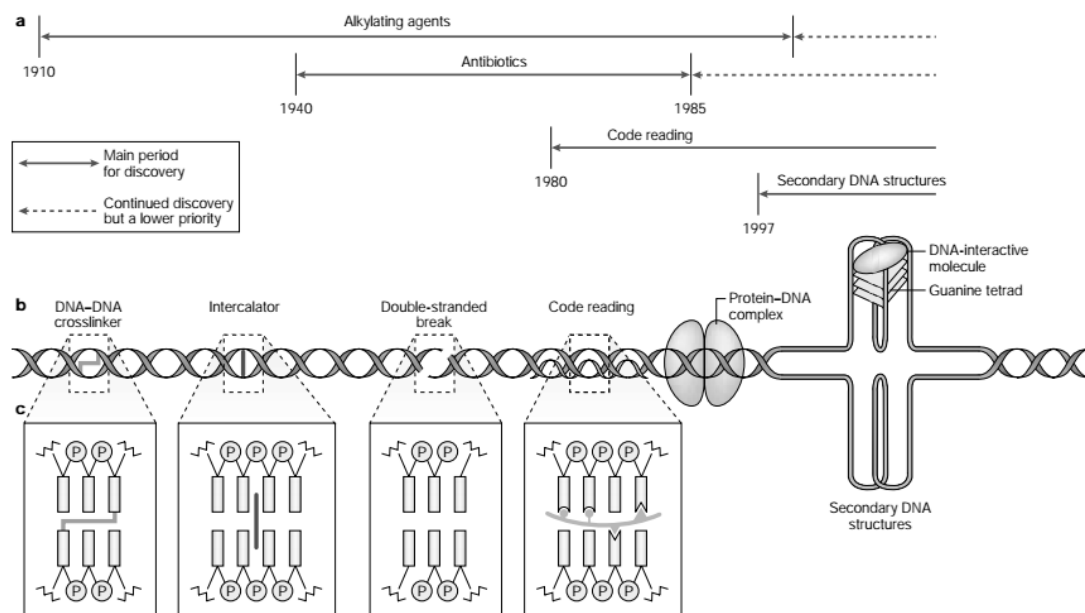


Figure 1.2. Timeline and classes of DNA-targeted drugs and the types of interactions with DNA.

Several FDA clinically approved DNA-targeted drugs have been used to treat cancer, such as topotecan¹⁵ and actinomycin D.¹⁶ Although DNA-targeted drugs exhibit toxicity towards healthy cells, these drugs can be aimed more selectively towards cancerous cells. As a result, DNA-related pathways can be directly targeted. Hence, understanding the interactions of small organic molecules with DNA is critical for developing DNA-targeted drugs that exhibit high specificity and low cytotoxicity. In order to examine DNA-binding interactions at biologically relevant conditions, sensitive methodologies and design strategies are of considerable interest.

1.3 An Overview on the Functions and Importance of DNA in Cellular and Biological Processes

DNA plays an important role in several biological and cellular processes, which is vital to cell survival and proliferation. DNA is essentially the blueprint of biological life. DNA can interact reversibly with a wide range of complexes including water, proteins, small organic molecules, and ions.¹⁷ Its discovery has revolutionized science and modern medicine in addition to its impact on society ranging from criminal justice to inheritance information. DNA is made up of chemical building blocks called nucleotides that are composed of a phosphate group, sugar group, and nitrogen containing nucleobase. There are four types of nitrogen bases, which include adenine (A), thymine (T), guanine (G), and cytosine (C) as detailed in Figure 1.3. The nucleobases are covalently bonded between the sugars of one nucleotide to the phosphate group of another nucleotide to form a DNA sequence. According to the base pair rules, the bases of DNA interact with other bases through hydrogen-bonding interactions to form double stranded DNA (dsDNA). The sequence for nucleotide interaction is important as adenine interacts with thymine and guanine interacts with cytosine. The backbone of DNA is composed of negatively charged phosphodiester bonds, which is resistant to cleavage.¹⁸ The order of the nucleobase sequence is critical for instructions towards cellular and biological expression. DNA serves a biological storage center for genetic information, which is considered one of its main functions.¹⁹

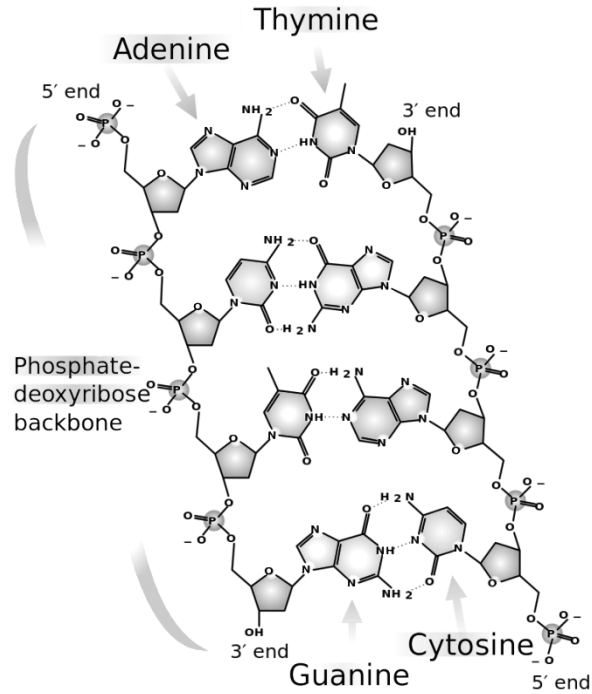


Figure 1.3. Structure of DNA.

DNA has two main functions, which includes replication and transcription. These processes begin when a signal is received. This generally occurs when a regulatory protein binds to a specific region of DNA.²¹ DNA replication is the process where two identical DNA strands are produced from a strand of DNA. DNA replication plays an important step in cell growth, division, and proliferation.²² This occurs in all living organisms and is essential for biological inheritance. In order to achieve DNA replication, DNA polymerases are required. These enzymes are responsible for carrying out the DNA replication process.,²³ which occurs at specific regions of DNA or origins of replications. Topoisomerase enzymes act by unwinding DNA, preparing the DNA strand for replication. DNA helicases separate the annealed DNA strand to produce the replication fork, which is the structure of DNA that forms for replication. Single-stranded binding

proteins stabilize the unwound DNA. A short strand of RNA called a primer is produced from the primase. This primer acts as a starting point for DNA synthesis on the leading strand. DNA polymerase continuously synthesizes the new strand of DNA in the 5'→3' direction, which is known as the leading strand. It is important to note that DNA is always synthesized in the 5'→3' direction.²⁴ It should be emphasized that DNA synthesis of the leading strand is a continuous process. On the lagging strand, DNA synthesis occurs in the opposite direction of the leading strand. RNA primers are produced by primase enzymes and bind at various locations on the lagging strand. Due to the complexity of DNA synthesis on the lagging strand, DNA is synthesized in short, separated complementary fragments called Okazaki fragments.²⁵ Contrarily to the leading strand, DNA synthesis on the lagging strand is discontinuous. Once the base pairs are matched up with complementary base pairs, nuclease enzymes remove the primase enzymes. DNA ligases join the Okazaki fragments to form the other strand of DNA. Additionally, ligases seal up the DNA sequence forming two strands of DNA. As a result of DNA synthesis, two new DNA molecules consisting of one old strand and one new strand are produced. This process is described as semi-conservative.²⁶ The DNA replication process is detailed in Figure 1.4.

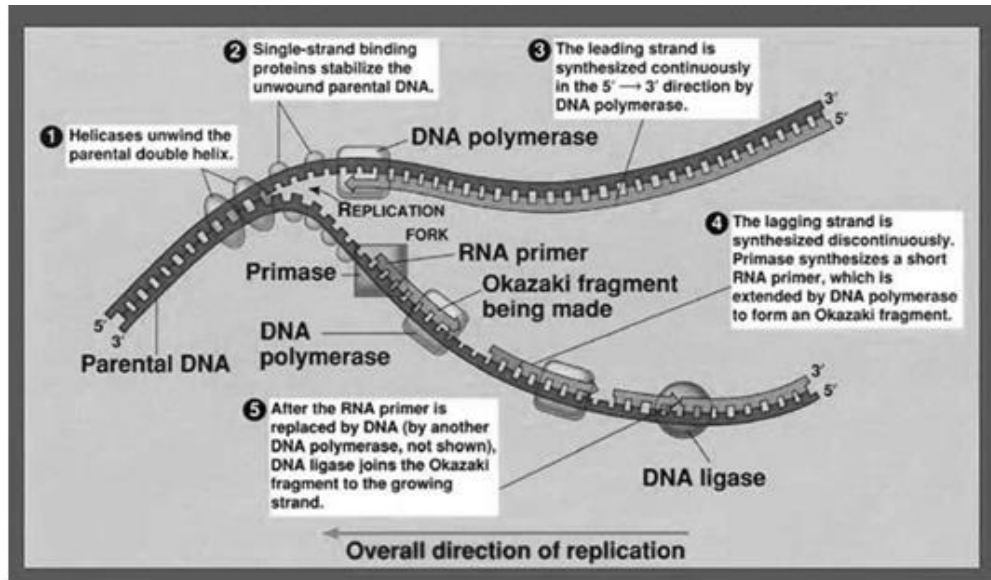


Figure 1.4. Summary of DNA replication.

DNA plays a critical role in transcription, which is required for gene expression and protein synthesis. A summary of transcription is shown in Figure 1.5. In eukaryotic cells, DNA does not leave the nucleus so the information must be copied. Thus, transcription occurs in the cell nucleus. Transcription is initiated when RNA polymerase binds with DNA, separating the two strands of DNA. This is achieved by breaking the hydrogen-bonding interactions between the complementary nucleobases. It is important to note that transcription factors mediate the binding of RNA polymerase. Elongation occurs when the RNA polymerase begins synthesizing the RNA nucleobases with the complimentary DNA base pairs. In addition, the phosphate backbone is formed from RNA polymerase, producing an RNA strand. It should be emphasized that adenosine is replaced with uracil for RNA synthesis. Once the synthesis of the RNA strand is complete, transcription is terminated when the termination sequence of bases (stop codon) is encountered. This is completed by recognition of a termination sequence to give mRNA.²⁷ The sequences of

mRNA nucleotides are arranged in codons consisting of three base pairs. These codons are responsible for specific amino acids that are required for protein synthesis.²⁹ mRNA then undergoes translation where the codons are correlated to a specific amino acids to form proteins for gene expression. From Figure 1.6, it is clear that DNA plays an important role in protein synthesis, which is required for cell proliferation.

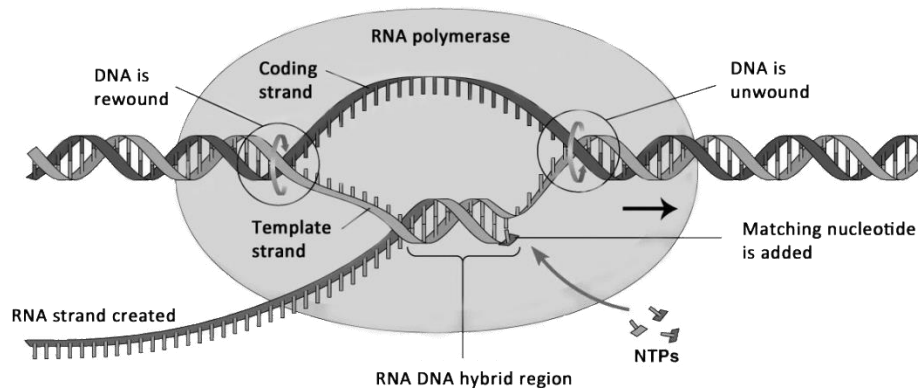


Figure 1.5. Summary of transcription.

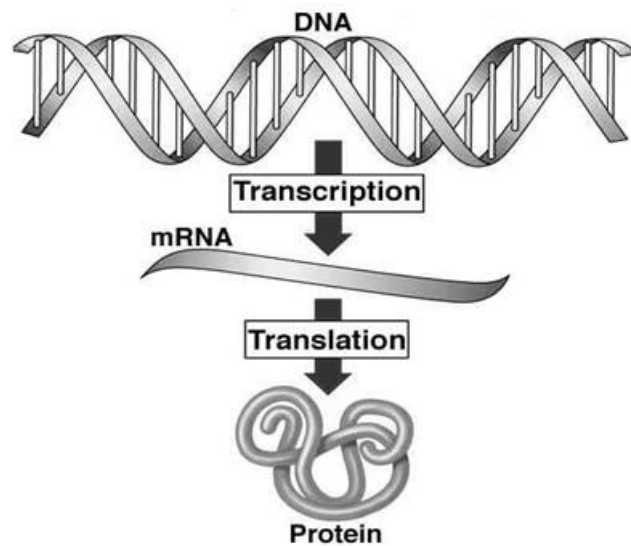


Figure 1.6. Importance of DNA for protein synthesis and gene expression.

Small organic molecules can resemble the binding strength and specificity of signaling regulatory proteins. These molecules can activate DNA replication and/or transcription, which leads to a larger production of proteins and/or induce DNA replication. In contrast, small organic molecules can also inhibit DNA-related processes, restricting DNA replication and protein synthesis that result in cell apoptosis. In most cases, DNA-targeted drugs are designed to inhibit DNA-related processes, which leads to cell apoptosis for antibiotic and antitumor applications.³⁰ Small organic molecules can interact with DNA through groove binding, intercalation, and/or cross-linking (covalent bonding).³¹ A complex formation occurs when small organic molecules bind or interact with DNA, which results in a change in the functional properties and thermal stability of DNA.³² The binding interactions of small organic molecules with DNA often change the DNA properties, which has an important impact on physiological functions.³³ Therefore, it is critical to understand the DNA-binding mechanism to elucidate the functional properties of DNA-binding molecules, which has application for drug research and development.

1.4 The Binding Interactions of Small Organic Molecules with DNA: Intercalation and Groove Binding

In this work, we have focused on understanding how small organic molecules intercalate or groove bind with DNA non-covalently as shown in Figure 1.7. Both intercalators and groove binders can be viewed as “lock-and-key” or “induced-fit” models similar to enzyme-substrate binding.³⁴ Contrarily to DNA cross-linking agents, these non-covalent binding interactions are reversible. DNA-targeted drugs that interact

with DNA non-covalently are preferred over molecules that bind covalently with DNA because they are considered less toxic and dangerous. Intercalation was first recognized by Leonard Lerman where he studied aminoacridines binding with DNA.³⁵ Lerman noted a physical distortion in the helical axis of DNA, which has become the hallmark of intercalation. Intercalating molecules generally have planar aromatic rings incorporated into the structure that bind with the DNA by inserting between the DNA nucleobases to form a binding pocket or intercalation cavity. Lengthening, unwinding, and distortion of the DNA helical axis are most prominent upon intercalation.³⁶ In order for intercalation to occur, three essential steps are required. First, DNA must undergo a conformation change to form the intercalation site where the base-pairs separate. As a consequence, the DNA strand is unwound and the spacing of the phosphate groups is increased.³⁷ This results in the reduction of the local charge density.³⁸ Once the intercalation pocket is formed, there is a transfer from the intercalator in solution to the binding site, which can be thought as a hydrophobic transfer process since the binding molecule will be buried in the DNA structure. As a result, further counter ions are released.³⁹ Finally, intercalation requires important driving factors, such as π -stacking and stabilizing electrostatic interactions, where the binding molecule seeks optimal overlap with the DNA nucleobases.⁴⁰ Each of these steps required for intercalation contributes to the overall free energy. It is important to note that the hydrophobic transfer of the binding molecule from a hydrophilic microenvironment is one of the most critical driving forces for intercalation.³³ Most intercalators prefer to bind at GC regions of DNA or do not have a defined preference, meaning that they bind at both AT and GC regions of DNA.³³

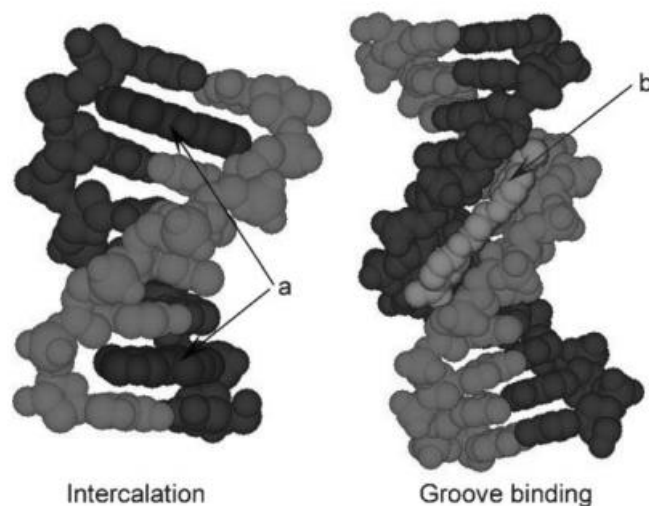


Figure 1.7. Cartoon representation of intercalation and groove binding.

Small organic molecules can groove bind with DNA at either the minor or major groove of DNA as illustrated in Figure 1.8. The minor and major grooves are a result of the DNA helical structure. In regards to the glycosidic bonds, they are in the same location within the base pairs such that they are not parallel or perpendicular relative to one another. In other words, the major groove is located where the backbone of DNA is far apart whereas the minor groove occurs when the backbone is close together. Groove binding is characterized by little to no perturbation in the DNA structure. In general, groove binding molecules contain unfused-aromatic structures with terminal basic functions.⁴² Additionally, groove binding molecules are, in most cases, crescent or V-shaped that give conformational flexibility, which allows the molecule to fit into the DNA groove as well as functional groups that interact with the nucleobases through hydrogen bonding and/or van der Waals interactions with minimal steric hinderance.³³ Groove depth, groove width, electrostatic potential, and floor functionality are structural features found to be critical for groove binding recognition.⁴³ In general, groove binding

is a two-step process contrarily to intercalation. The first step takes place when the binding molecule undergoes a hydrophobic transfer from solution to the groove of DNA. Next, the binding molecule forms non-covalent interactions with DNA nucleobases. As noted, groove binding does not require the DNA helical axis to unwind for binding. Typically, groove binders prefer to bind at AT sequences because GC sequences contain a $-NH_2$ group that sterically inhibits the binding.⁴⁴ Additionally, binding at AT-rich sequences provides better van der Waals interactions between the binding agent and groove walls since the AT regions are narrower than GC regions.⁴⁵ However, this is not always the case as some small organic molecules bind at GC-rich sequences, such as topotecan.^{46,47} Fluorescence quenching is generally observed when a fluorescent nuclear dye groove binds at GC-rich regions due to the photoinduced electron transfer (PET) between the dye and nucleobase.⁴⁸ It is important to note that the binding constants of an intercalator and groove binder are on the order of $10^4 - 10^6$ and $10^5 - 10^9$ M^{-1} , respectively.³³

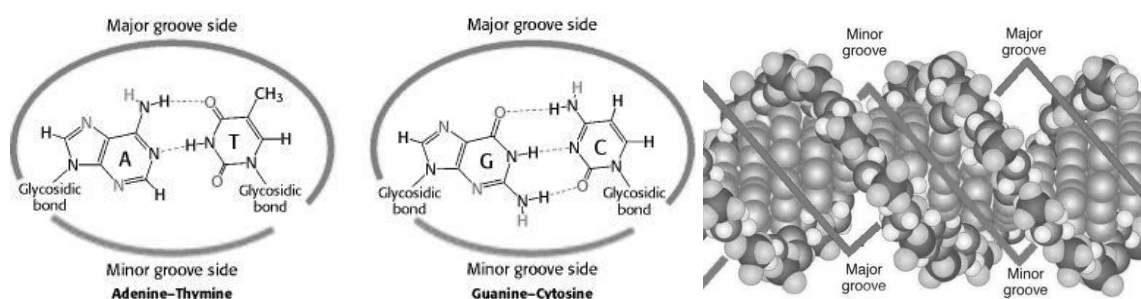


Figure 1.8. Minor versus major groove of DNA.

It has been reported that groove binding is mainly entropically driven whereas intercalation is primarily enthalpically driven.⁵¹ Groove binders have a higher affinity for

DNA as compared intercalators. Intercalation is coupled to the unstacking of the nucleobases to form the binding site. As a consequence, intercalation results in distortion of the helical axis upon binding, which requires energy. The cost of energy for disrupting the nucleobase stacks is $0.5 - 2.0 \text{ kcal mol}^{-1}$, which is the difference in the average binding free energy between an intercalator and groove binder.⁵² In regards to intercalation, favorable enthalpy arises from the intermolecular interactions required for binding, such as hydrogen-bonding interactions, between the binding molecule and DNA base-pairs. On the other hand, there is usually an entropic penalty when a bimolecular complex is formed due to the loss of rotational and translational degrees of freedom.^{53,54} There are entropic contributions when a binding molecule electrostatically interacts with DNA regardless of the binding mode.⁵⁵ The work done by Chaires *et al.* noted that groove binders are entropically driven while intercalation is primarily enthalpically driven.⁵¹ However, the origin of this phenomenon remains unclear.

1.5 Methodologies to Characterize the DNA-Binding Interactions of Small Organic Molecules

Several techniques have been employed to investigate the DNA-binding interactions of small organic molecules. However, many of these techniques used to evaluate the DNA-binding interactions do not provide sufficient information and offer limitations. For example, NMR can provide detailed localized information about the binding molecule. However, a major issue with NMR is that it requires large quantities of materials for screening. In addition, screening requires isotopic enrichment of the sample as well as long acquisition time.⁵⁶ Another method that has been used to examine the DNA-binding

interactions of external molecules is mass spectrometry, such as chemical ionization,⁵⁷ electrospray ionization (EI-MS),⁵⁸ and matrix assisted laser desorption ionization (MALDI-TOF).⁵⁹ A major concern with mass spectrometry is the inability to distinguish between specific and non-specific binding. Mass spectrometry does not provide information about the binding site of the binding agent and DNA complex structure.⁶⁰ Optical techniques can provide indirect information about the DNA-binding mode. Fluorescence and absorption spectra changes can be used to monitor these interactions; however, they do not provide sufficient information about the binding mechanism. Such methods can provide information about the binding constant.

Fluorescence displacements assays have been used to examine the DNA-binding mechanism of small organic molecules as illustrated in Figure 1.9. Additionally, these assays have been employed to examine DNA binding affinity, sequence selectivity, and binding stoichiometry.⁶¹ The advantages of this technique is that it is non-destructive, non-demanding, and can be applied for high-throughput screening. However, there are also several issues with this methodology. For instance, displacements assays are generally used for only intercalating molecules. Thus, this method is not practical when investigating groove binding molecules. In addition, the results may be deceptive if the binding molecule exhibits multiple binding modes. Another issue with this technique is that it is commonly used with hairpin or single-stranded DNA. Because of this, high quality DNA is required in which the concentration must be known. The issue is that the concentration of single stranded DNA can be underestimated by up to 25% by using the standard coefficient of DNA.⁶¹ A final problem with this approach occurs when investigating the DNA-binding interactions of a molecule, which has a similar emission

spectrum as the displacement dye. This makes it difficult to monitor the change in fluorescence since there is overlap between the fluorescent binding molecule and displacement dye.

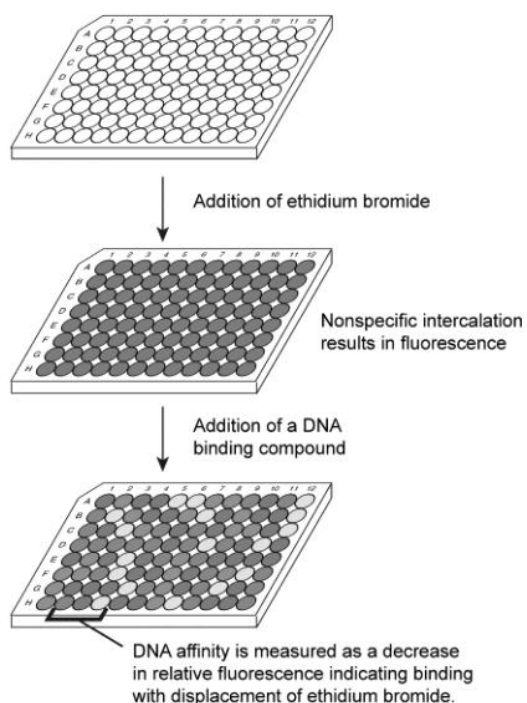


Figure 1.9. General procedure for fluorescent displacement dye assay.

Circular dichroism (CD) spectroscopy has been extensively used to study the functions and interactions of DNA complexes.^{62,63} CD is a differential absorption technique that measures the difference in the left- and right-handed circularly polarized light. In general, small organic molecules are achiral, meaning that they do not display CD signal. Optical activity arises when there are parallel molecular magnetic and electronic transition dipole moments that can couple with the electric field of a circularly polarized light source.⁶⁴ An induced circular dichroism (ICD) signal is observed when an

achiral molecule binds to chiral DNA due to a nondegenerate coupling of the chromophore with the DNA-base transitions.⁶⁴ The magnitude and direction of the ICD signal is dependent on DNA sequence, binding mechanism, and orientation of the transition dipole of the binding molecule.⁶⁵ Therefore, interpretation of the CD spectra is complicated as there are several factors that must be considered. In general, a strong positive ICD signal is observed when the dipole is polarized perpendicular to the long axis of the pocket, which is a characteristic feature of a groove binding molecule. The strong ICD signal for a groove binder is likely due to the molecule interacting with the DNA base pairs (on average 4 – 6 base pairs) while undergoing a conformation change to follow or fit the groove of DNA.⁶⁵ Contrarily, an intercalator has a weak negative ICD signal when the transition dipole of the binding molecule is polarized along the long axis of the binding pocket or parallel to the nucleobases.⁶⁶ Intercalators will often display weak ICD signals because the binding molecule does not come in contact with as many base pairs and does not twist as compared to groove binders.⁶⁵ A major drawback of CD is that there remains ambiguity when evaluating the DNA-binding mode. In particular, the direction of the transition dipole must be known to provide sufficient information regarding the orientation of the binding molecule.⁶⁷ Another issue is that the signal indicative of an intercalating binding mode may not be observed because a stronger, more intense signal due to other interactions, such as aggregation, can overwhelm the intercalating signal.

Linear dichroism (LD) is another common technique that has been utilized to examine the DNA-binding interactions of small organic molecules. LD is a differential absorption technique that measures the difference in the parallel or perpendicular

polarized light with respect to the macroscopic orientation axis. A representation of the common absorption methods used to investigate the DNA-binding interactions is presented in Figure 1.10. In order to conduct LD, the DNA strands must be oriented properly in a flow cell. Thus, the binding molecule will also be oriented in the same direction, which will exhibit a LD signal. The direction or sign of the LD signal is directly related to the orientation of the transition dipole of the binding molecule relative to the direction of the flow. The transition dipole of a groove binder will align approximately parallel with the flow. On the other hand, the transition dipole of an intercalator will be oriented perpendicular with the flow.⁶⁶ As a result, LD signals in the opposite direction will arise. Groove binders will exhibit a positive signal whereas intercalators will display a negative signal. However, there are several drawbacks with LD. First, a specialized flow cell is required to perform the experiment since standard cuvettes cannot be used. Another issue is that only long DNA strands can be employed. This is problematic when investigating the binding interactions of short and well-defined DNA sequences. As a consequence, detailed information about the binding interactions cannot be elucidated with short DNA sequences. Similar to CD, the direction of the transition dipole moment of the binding molecule must be known in order to determine the DNA-binding mode by LD.

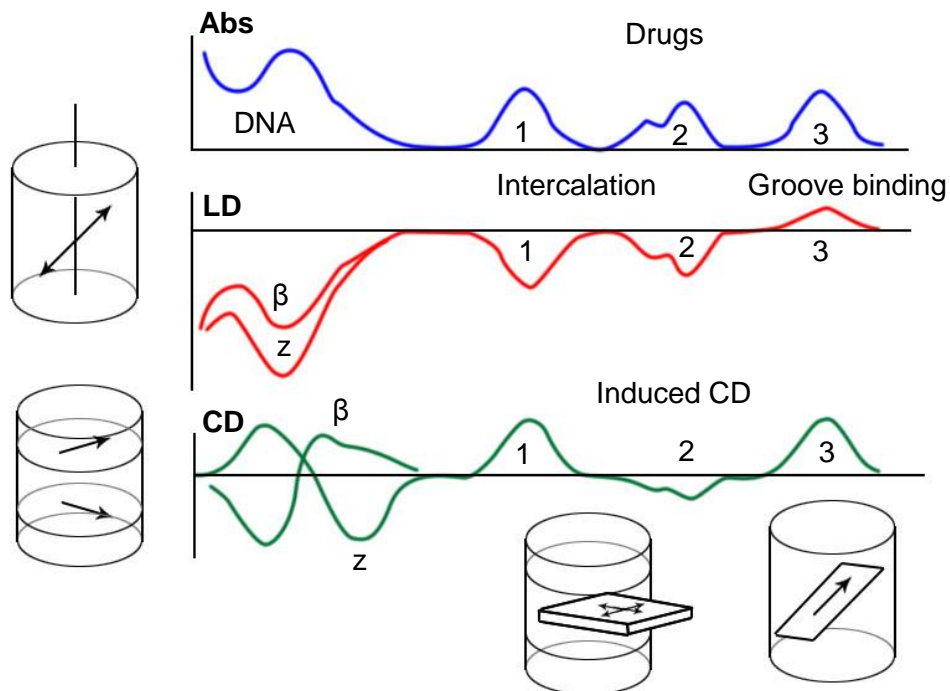


Figure 1.10. Information about the DNA-binding modes of small organic molecules by absorption, LD, and CD spectroscopy.

It has been reported that only a combination of select methods provides sufficient information about the binding mode.^{68,69} The only method that provides detailed information about the DNA-binding mode is X-ray diffraction analysis of crystalline structures.³³ However, the growth of single crystals is difficult to achieve. As noted above, there are several limitations with the current techniques used to investigate the DNA-binding mode. Designing and developing drugs that target and bind to DNA with high specificity and selectivity remains a challenge. Therefore, highly sensitive methodologies that provide sufficient information about the DNA-binding interactions are of considerable interest.

1.6 Utilization of Two-Photon and Time-Resolved Spectroscopies to Examine Biological-Based Systems

Two-photon spectroscopy has been previously employed to investigate biological-based systems, which can provide information inaccessible with other conventional techniques. The two photon absorption (TPA) process is a third-order process with a quadratic dependence on the intensity of the incident radiation. TPA occurs when two photons are simultaneously absorbed to promote the electron from the ground state to the excited state. The TPA process will be discussed in Chapter 2. Two-photon excited fluorescence (TPEF) has been widely used to examine the fundamentals of the excited state as well as correlating structure-function relationships in organic molecules.⁷⁰ Two-photon spectroscopy has been increasingly used as a tool for investigating environmental changes, charge transfer character, and application towards fluorescence imaging.⁷¹ TPA materials have been utilized for several applications including microscopy,⁷² photodynamic therapy,⁷³ and optical limiting.⁷⁴ Therefore, materials that possess TPA properties are invaluable tools to investigate biological systems.

In our group, we have previously investigated several biological systems by employing our ultrafast nonlinear spectroscopic techniques. Peptide aggregation has been reported to be associated with neurodegenerative diseases, such as Alzheimers and Parkinson's disease. Yang *et al.* investigated the conformational changes associated with the aggregation of amyloid-beta peptides by employing nonlinear ultrafast spectroscopy. This was achieved by examining the aggregation process of TAMRA-labeled A β 1-42 peptide.⁷⁵ Furthermore, Clark *et al.* investigated the photophysical properties of a series of newly synthesized green fluorescent proteins (GFP).⁷⁶ The GFP was then covalently

bonded to form a GFP-labeled A β 1-42 peptide in which the aggregation process was monitored by TPA. TPA demonstrated superior sensitivity at low peptide concentration compared to CD. As a result, TPA can provide detailed information about the aggregation process at biologically relevant conditions, which is critical for developing therapeutics. Mclean *et al.* investigated the binding of calmodulin with calcium.⁷⁷ Calmodulin is a signaling protein that is responsive to calcium ion fluxes. Hence, calmodulin regulates many cellular processes and is critical in nearly all biological processes.^{78,79} TPA provides detailed information regarding the conformation change of the calmodulin protein upon binding with calcium and the local environment of the fluorophore. Evidently, understanding these processes is critical for drug research and development. Our research group has demonstrated that TPA and ultrafast time-resolved spectroscopy can provide valuable information about biological-based systems with high sensitivity. Therefore, we are interested in applying ultrafast nonlinear spectroscopy to probe other biological systems, such as the DNA-binding interactions of small organic molecules. The work done may provide information that can be applied towards the design and development of therapeutics.

The dissertation work follows the outline of employing a combined approach of steady-state spectroscopy along with ultrafast nonlinear spectroscopy to investigate biological-based systems. The DNA-binding interactions of DNA-targeted drugs and fluorescent nuclear dyes were examined. A new methodology was developed to diagnose the DNA-binding mode of small organic molecules. Additionally, a series of newly synthesized fluorescent nuclear dyes were studied. By understanding the structure-property relationships, the results indicate that these fluorophores possess promising

properties as biological markers, which is important in monitoring DNA-related processes. Additionally, this study has led to the emergence of structure-property relationships of DNA-binding molecules that adopt a crescent or V-shaped donor-acceptor-donor motif. These fluorophores can be designed to either intercalate or groove bind with DNA by structurally modifying the electron accepting properties of the central heterocyclic core.

In addition to understanding DNA-binding interactions, it has been reported that abnormal kinase activity is associated with several diseases, such as cancer.⁸⁰ Kinase activity was investigated by implementing a custom fluorophore labeled peptide. These findings are the first example to monitor kinase activity in live cells with continuous real-time analysis. The potential impact of this work lies in the ability to further understand these systems. This will provide detailed information about the biological processes, which is critical in designing and developing therapeutics. Additionally, this will allow drugs and therapeutics to be screen in live cells with continuous real-time analysis. In fact, several anti-cancer therapies have been aimed at either inhibiting or activating these processes. A major advantage of employing nonlinear ultrafast spectroscopy is the high sensitivity at low concentrations, suggesting it can be utilized at biologically relevant conditions. Additionally, TPA can provide both qualitative and quantitative information about the system, which is important for bio-imaging applications.

References

1. Jemal, A.; Siegel, R.; Ward, E.; Murray, T.; Xu, J.; Thun, M. J. *Cancer J. Clin.* **2007**, *57*, 43.
2. Anand, P.; Kunnumakkara, A. B.; Kunnumakara, A. B.; Sundaram, C.; Harikumar, K. B.; Tharakan, S. T.; Lai, O. S.; Sung, B.; Aggarwal, B. B. *Pharmaceutical Research* **2008**, *25*, 2097.
3. www.cancer.org/acs/groups/content/@editorial/documents/document/acspc-044552.pdf
4. www.seer.cancer.gov/statfacts/html/all.html
5. Hanahan, D.; Weinberg, R. A. *Cell*, **2000**, *100*, 57.
6. Helleday, T.; Petermann, E.; Lundin, C.; Hodgson, B.; Sharma, R. A. *Nature Reviews Cancer* **2008**, *8*, 193.
7. Hurley, L. H. *Nature Reviews Cancer* **2002**, *2*, 188.
8. Slapak, C. A. & Kufe, D. W. in Harrison's Principles of Internal Medicine 14th edn (eds Isselbacher, K. J. et al.) 523–537 (McGraw–Hill, Inc. (Health Professions Div., New York, 1998.
9. Antonini, I.; Polucci, P.; Jenkins, T. C.; Kelland, L. R.; Menta, E.; Pescalli, N.; Stefanska, B.; Mazerski, J.; *J. Med. Chem.* **1997**, *40*, 3749.
10. Broggini, M.; D'Incalci, M. *Anti-Cancer Drug Des.* **1994**, *9*, 373.
11. Kohn, K. *Cancer Res.* **1996**, *56*, 5533.
12. Ward, K. *J. Am. Chem. Soc.* **1935**, *57*, 914
13. Giovannangeli, C.; Hélène, C. *Curr. Opin. Mol. Ther.* **2000**, *2*, 288.
14. Thuong, N.; Hélène, C. *Angew. Chem. Int. Ed. Engl.* **1993**, *32*, 666.

15. Streltsov, S.; Sukhanova, A.; Mikheikin, A.; Grokhovsky, A.; Zhuze, A.; Kudelina, I.; Mochalov, L.; Oleinikov, V.; Jardillier, J.-C.; Nabiev, I. *J. Phys. Chem. B* **2001**, *105*, 9643.
16. Chen, A. Y.; Liu, L. F. *Annual Review of Pharmacology and Toxicology* **1994**, *34*, 191.
17. Brana, M. F.; Cacho, M.; Gradillas, A.; Pascual-Teresa, B. D.; Ramos, A. *Current Pharmaceutical Design*, **2001**, *7*, 1745.
18. De Mesmaeker, A.; Altmann, K. H.; Waldner, A.; Wendeborn, S. *Current Opinion in Structural Biology* **1995**, *5*, 343.
19. Champoux, J. J. *Annual Review of Biochemistry* **2001**, *70*, 369.
20. Micklos, D. A.; Freyer, G. A.; Crotty, D. A. *DNA Science*
21. Moritz, C. *Molecular Ecology* **1994**, *3*, 401.
22. Brana, M. F.; Cacho, M.; Gradillas, A.; Pascual-Teresa, B. D.; Ramos, A. *Current Pharmaceutical Design*, **2001**, *7*, 1745.
23. Berg, J. M.; Tymoczko, J. L.; Stryer L.; Clarke, N. D. (2002). *Biochemistry*. W.H. Freeman and Company. ISBN 0-7167-3051-0.
24. Holland, P. M.; Abramson, R. D.; Watson, R.; Gelfand, D. H. *PNAS* **1991**, *88*, 7276.
25. Waga, S.; Stillman, B. *Annual Review of Biochemistry* **1998**, *67*, 721.
26. Brown, N. C. *J. Mol. Biol.* **1971**, *59*, 1.
27. Lodish, H.; Berk, A.; Zipursky, S. L.; Matsudaira, P.; Baltimore, D.; Darnell, J. *Molecular Cell Biology*. 4th edition. New York: W. H. Freeman; 2000.
28. Zaret, K. S.; Sherman, F. *Cell* **1982**, *28*, 563.

29. Yoshizawa, S.; Fourmy, D.; Puglisi, J. D. *Science* **1999**, 285, 1722.
30. David-Cordonnier, M.-H.; Laine, W.; Gaslonde, T.; Michel, S.; Tillequin, F.; Koch, M.; Léonce, S.; Pierre, A.; Bailly, C. *Current Medicinal Chemistry-Anti-Cancer Agents* **2004**, 4, 83.
31. Bleckburn, G. M.; Gait, M. N. *Nucleic Acids in Chemistry and Biology*, IRL Press, New York, 1990, pp. 297–332.
32. Graves, D. E.; Velea, L. M. *Curr. Org. Chem.* **2000**, 4, 915.
33. Ihmels, H.; Otto, D. *Top Curr. Chem.* **2005**, 258, 161.
34. Chaires, J. B. *Archives of Biochemistry and Biophysics* **2006**, 453, 26.
35. Lerman, L. *J. Mol. Biol.* **1961**, 3, 18-IN14.
36. Suh, D.; Chaires, J. B. *Bioorg. Med. Chem.* **1995**, 3, 723.
37. Chaires, J. B. *Biopolymers* **1997**, 44, 201.
38. Friedman, R. A.; Manning, G. S. *Biopolymers* **1984**, 23, 2671.
39. Manning, G.S. *Q. Rev. Biophys.* **1978**, 11, 179.
40. Chatteraj, M.; King, B. A.; Bublitz, G. U.; Boxer, S. G. *Proc. Natl. Acad. Sci. U.S.A.* **1996**, 93, 8362.
41. Liu, X.; Diao, H.; Nishi, N. *Chem. Soc. Rev.* **2008**, 37, 2745.
42. Zimmer, C.; Wahnert, U. *Prog. Biophys. Mol. Bid.* **1986**, 47, 31.
43. Tse, W. C.; Boger, D. L. *Chem. Biol.* **2004**, 11, 1607.
44. Kopka, M. L.; Yoon, C.; Goodsell, D.; Pjura, P.; Dickerson, R. E. *Proc. Natl. Acad. Sci. USA* **1985**, 82, 1376.
45. Dervan, P. B. *Science* **1986**, 232, 464.

46. Streltsov, S.; Sukhanova, A.; Mikheikin, A.; Grokhovsky, A.; Zhuze, A.; Kudelina, I.; Mochalov, L.; Oleinikov, V.; Jardillier, J.-C.; Nabiev, I. *J. Phys. Chem. B* **2001**, *105*, 9643.
47. Joshi, H.; Sengupta, A.; Gavvala, K.; Hazra, P. *RSC Adv.* **2014**, *4*, 1015.
48. Murphy, C. J.; Arkin, M. R.; Jenkins, Y.; Ghatlia, N. D.; Bossmann, S. H.; Turro, N. J.; Barton, J. K. *Science* **1993**, *262*, 1025.
49. www.madsci.org/posts/archives/2010-03/1268774308.Gb.r.html
50. www.mun.ca/biology/scarr/MGA2_02-07.html
51. Chaires, J. B. *Archives of Biochemistry and Biophysics* **2006**, *453*, 26
52. SantaLucia Jr., J. *Proc. Natl. Acad. Sci. USA* **1998**, *95*, 1460.
53. Chaires, J.B. *Biopolymers* **1997**, *44*, 201.
54. Spolar, R. S.; Record Jr., M. T. *Science* **1994**, *263*, 777.
55. Manning, G.S. *Q. Rev. Biophys.* **1978**, *11*, 179.
56. Rauf, S.; Gooding, J. J.; Akhtar, K.; Ghauri, M. A.; Rahman, M.; Anwar, M. A.; Khalid, A. M. *J. Pharm. Biomed. Anal.* **2005**, *37*, 205.
57. Berkel, G. J. V. *Eur. J. Mass Spectrom.* **2003**, *9*, 539.
58. Yamashita, M.; Fenn, J.B. *J. Phys. Chem.* **1984**, *88*, 4451.
59. Karas, M.; Backmann, D.; Bahr, U.; Hillenkamp, F. *Int. J. Mass Spectrom. Ion Process.* **1987**, *78*, 53.
60. Powers, R.; *J. Struct. Func. Genom.* **2002**, *2* 113.
61. Tse, W. C.; Boger, D. L. *Acc. Chem. Res.* **2004**, *37*, 61.
62. Eriksson, M.; Norde'n, B. *Methods Enzymol.* **2001**, *340*, 68.
63. Rizzo, V.; Schellman, J. A. *Biopolymers* **1984**, *23*, 435.

64. Norde'n, B.; Kurucsev, T. *J. Mol. Recognit.* **1994**, *7*, 141.
65. Armitage, B. *Top Curr. Chem.* **2005**, *253*, 55.
66. Tanious, F. A.; Ding, D.; Patrick, D. A.; Bailly, C.; Tidwell, R. R.; Wilson, W. D. *Biochemistry* **2000**, *39*, 12091.
67. Wilson, W. D.; Barton, H. J.; Tanious, F. A.; Kong, S. B.; Strekowski, L. *Biophysical Chemistry* **1990**, *35*, 227.
68. Suh D. Oh Y. K.; Chaires, J. B. *Process Biochem.* **2001**, *37*, 521.
69. Long, E. C.; Barton, J. K. *Acc. Chem. Res.* **1990**, *23*, 273.
70. Narayanan, A.; Varnavski, O. P.; Swager, T. M.; Goodson, T. J. *Phys. Chem. C* **2008**, *112*, 881
71. Drobizhev, M.; Makarov, N. S.; Tillo, S. E.; Hughes, T. E.; Rebane, A. *Nat. Methods* **2011**, *8*, 393.
72. Zipfel, W. R.; Williams, R. M.; Webb, W. W. *Nat. Biotechnol.* **2003**, *21*, 1369.
73. Spangler, C. *J. Mat. Chem.* **1999**, *9*, 2013.
74. Fisher, W. G.; Partridge, W. P.; Dees, C.; Wachter, E. A. *Photochem. Photobiol.* **1997**, *66*, 141.
75. Wang, Y.; Clark, T. B.; Goodson, T. *J. Phys. Chem. B* **2010**, *114*, 7112.
76. Clark, T. B.; Zi'olkowski, M.; Schatz, G. C.; Goodson III, T. J. *Phys. Chem. B* **2014**, *118*, 2351.
77. McLean, A. M.; Socher, E.; Varnavski, O.; Clark, T. B.; Imperiali, B.; Goodson III, T. *J. Phys. Chem. B* **2013**, *117*, 15935.
78. Means, A.; VanBerkum, M.; Bagchi, I. *Pharmacol. Ther.* **1991**, *50*, 255.
79. Black, D. J.; Tran, Q.-K.; Persechini, A. *Cell Calcium* **2004**, *35*, 415.

80. Hanahan, D.; Weinberg, R. A. *Cell* **2000**, *100*, 57.

Chapter 2

Experimental Instrumentation and Techniques

In this chapter, the experimental setups and procedures used in the dissertation are discussed in detail. Common spectroscopic techniques were employed to investigate the materials and biological-based systems including UV-Vis absorption, steady-state fluorescence, and circular dichroism. Steady-state spectroscopy was used as an initial examination and diagnostic of the systems. Ultrafast nonlinear spectroscopy was further utilized to gain a deeper understanding of the materials and biological-based interactions including two-photon absorption (TPA), fluorescence upconversion, and time-correlated single-photon counting (TCSPC). TPA was implemented as a new methodology to determine the DNA-binding modes of small organic molecules. Fluorescence upconversion and TCSPC were employed to examine the excited state dynamics of the DNA-binding molecules. The culture and imaging of mammalian cells will discuss in significant detail. This was a major contribution to our research group because it will allow future researchers to correlate their ultrafast nonlinear techniques towards bio-imaging applications in live cells.

2.1 An Overview and Introduction of Ultraviolet–Visible Spectroscopy and Single-Photon Excited Fluorescence

Steady-state spectroscopy is commonly used to optically characterize materials, which include absorption and fluorescence.^{1–3} In steady-state spectroscopy, the samples are continuously irradiated with a beam of light. In other words, the excited states are continuously formed and eliminated in which a steady-state is reached. Steady-state spectroscopy provides information in regards to the initial investigation of the system and/or material prior to a further examination by ultrafast nonlinear spectroscopy.

Absorption remains one of the most common spectroscopic techniques because of its accuracy and simplicity. The absorption of energy occurs between the closely spaced rotational vibrational energy levels of the excited state. The absorbance spectrum can be used as a quantitative tool to determine the concentration of a material as well as a qualitative guide to identify the “fingerprint” of a material.^{4–6} The absorbance is the logarithm of the ratio of incident to transmitted radiant energy or light through a given material or system.⁷ The absorbance is measured using UV-Vis absorption spectroscopy, which is governed by Beer-Lambert’s law⁸ as given by

$$A = \log\left(\frac{I_0}{I}\right) = \varepsilon \cdot [c] \cdot l \quad (2.1)$$

where A is the absorbance, I is the intensity of light absorbed, ε is the molar extinction coefficient, $[c]$ is the concentration, and l is the path length. It is important to note that absorbance is dimensionless. The wavelength of light absorbed can be translated to the amount of energy required to excite the molecule from the ground state to the excited state. In general, the absorption in the UV range results in a $\pi \rightarrow \sigma^*$ whereas the absorption in the visible to near IR range is due to the $\pi \rightarrow \pi^*$.^{9,10} Shifts in the absorption spectrum

can provide information with respect to environmental changes in the system. Additionally, changes in the absorption spectrum can provide details about sample and/or material degradation.

In terms of collecting an absorption spectrum experimentally, an Agilent Model 8341 spectrophotometer equipped with deuterium and tungsten lamps was employed, allowing for the absorption spectrum to be collected over a wide range (200 – 1100 nm). Quartz cuvettes supplied by Starna were utilized in all experiments with a path length of 1 cm. The solvent was used as a blank to avoid potential artifacts.

Another steady-state process is the emission of a molecule. The fluorescence process is governed by three processes including excitation (absorption), vibrational relaxation, and emission.¹¹⁻¹⁴ When a molecule is excited by the absorption of photons, the electron relaxes back to the ground state, resulting in fluorescence or the release of photons (radiative decay), which is generally lower in energy (longer wavelength). The emission of most molecules is typically inefficient due to other competing mechanisms, such as non-radiative decay where the energy released is in the form of phonons or more commonly known as heat. The fluorescence of a molecule can be quantified by the quantum yield, which is determined by the ratio of number of photons emitted by the number of photons absorbed with a maximum value of 1 (or 100%). The quantum yield can be calculated with the use of an integrating sphere⁸ or the comparative method.¹⁵ Without the use of an integrating sphere, the comparative method cannot determine the absolute quantum yield, but can provide an efficient means to calculate the quantum yield.^{16,17} A standard is required to calculate the quantum yield by the comparative

method. The quantum yield of a given sample can be calculated using the following equation¹⁸

$$\Phi_x = \Phi_{Std} \frac{Grad_x \eta_x^2}{Grad_{std} \eta_{std}^2} \quad (2.2)$$

where Φ is the quantum yield, η is the refractive index of the solvent, and $Grad$ is the slope obtained from plotting the integrated fluorescence versus absorbance at different concentrations. When measuring the quantum yield, it is important to keep the optical density below 0.10 to avoid reabsorption and internal filter effects.

In terms of measuring the fluorescence spectrum experimentally, a Fluoromax-2 fluorimeter equipped with a Xenon light source was used to collect the emission and excitation spectra. A photomultiplier tube (PMT) with diffraction grating was utilized to collect the counts or emission at a single wavelength. Quartz cells manufactured by Starna were used for all experiments with 1 cm path lengths. The emission was collected 90° from the excitation source.

2.2 An Overview of Circular Dichroism Spectroscopy to Investigate the DNA-Binding Interactions of Small Organic Molecules

Circular dichroism has been used to investigate the chirality of molecules,¹⁹ secondary structures of peptides,²⁰ and DNA-binding interactions of various molecules.²¹⁻²⁴ When polarize light passes through a material or system, the rate of absorption of left and right circularly polarized light may differ. CD is the differential absorption of left and right circularly polarized light as given by

$$\Delta A = (A_L - A_R) \cdot [c] \cdot l \quad (2.3)$$

where ΔA is the difference in the absorption between the left (A_L) and right (A_R) polarized light, $[c]$ is the concentration, and l is the path length. CD is commonly represented as ellipticity, which is the angle whose tangent is the ratio of the minor to the major axis of the ellipse. This can be expressed by

$$\theta = 3298.2 \cdot \Delta\varepsilon \quad (2.4)$$

where θ is the ellipticity and $\Delta\varepsilon$ is the change in the molar extinction coefficient. The units of ellipticity are $\text{deg}\cdot\text{cm}^2\cdot\text{dmol}^{-1}$.

Optical activity arises when there are parallel molecular magnetic and electronic transition dipole moments that can couple with the electric field of a circularly polarized light source.^{21,25,26} An induced circular dichroism (ICD) signal is observed when an achiral molecule binds to chiral DNA due to a nondegenerate coupling of the binding molecule with the DNA-base transitions.²⁴ In general, a strong positive ICD signal is observed when the dipole is polarized perpendicular to the long axis of the pocket, which is a characteristic feature of a groove binding molecule. Contrarily, an intercalator has a weak negative ICD signal when the transition dipole of the binding molecule is polarized along the long axis of the binding pocket or parallel to the nucleobases.^{27,28}

The use of CD can be ambiguous when determining the DNA-binding mode of small organic molecules. It has been reported that the common methodologies to evaluate the DNA-binding mode must be made with caution because a combination of select methods only provides sufficient information to determine the DNA-binding mode.^{29,30} The dipole moment of the binding molecule must be known in order to determine the DNA-binding mode with CD. This is a major issue when examining the DNA-binding mode with solely the use of CD.

2.3 An Introduction and Overview of Two-Photon Absorption Spectroscopy

Two-photon absorption (TPA) has been widely used to examine the fundamentals of the excited state as well as correlating structure-function relationships in organic molecules.³¹⁻³⁴ As a result, two-photon spectroscopy has been increasingly utilized as a tool for investigating environmental changes, charge transfer character, and application towards fluorescence imaging.³⁵⁻³⁸ Two-photon excited fluorescence (TPEF) has been employed in confocal microscopy, which offers several advantages over traditional one-photon excited fluorescence. TPEF demonstrates superior spatial resolution because the TPA process is quadratically power dependent. Additionally, the excitation wavelength is in the near-infrared (IR), leading to reduced photodamage and autofluorescence. The excitation for TPEF is confined to a small volume in a focal plane, which results in reduced photobleaching as well as deeper tissue penetration capabilities for imaging applications.³⁹⁻⁴³

Maria Göppert-Mayer theoretically proposed the idea of two-photon absorption in the 1930's.⁴⁴ This was experimentally confirmed decades later with the invention of the laser. Pulsed lasers can deliver a high density of photon with a high peak power, which is necessary for TPA since it requires a high density of photons to enable simultaneous absorption of two photons. With the use of pulsed lasers, the TPA cross-section can be determined. TPA cross-sections have units of $\text{cm}^4 \cdot \text{s} \cdot \text{photon}^{-1}$, which is also reported as Göppert-Mayer (GM) with $1 \text{ GM} = 10^{-50} \text{ cm}^4 \cdot \text{s} \cdot \text{photon}^{-1}$.

The TPA cross-section was determined by employing the TPEF method.⁴⁵ The fluorescence intensity is monitored as a function of power, which allows for the calculation of the TPA cross-section. This method is more accurate and easily

accomplished as compared to the z-scan method. Intrinsically, TPEF is similar to one-photon excited fluorescence (OPEF) with the exception that TPEF requires the simultaneous absorption of two-photons with half the energy as compared to OPEF.⁴⁶

The Jabolonski diagram of OPEF and TPEF is shown in Figure 2.1.

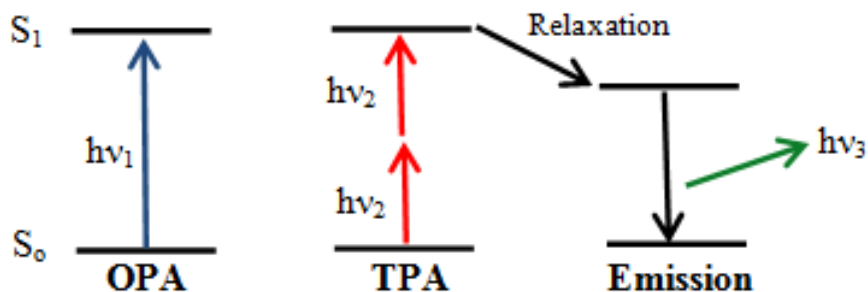


Figure 2.1. Jabolonski diagram representing one-photon absorption (OPA), two-photon absorption (TPA), and the emission process.

In this work, the TPA cross-sections were measured utilizing the TPEF method as described above. Two-photon spectroscopy was performed using a Kapteyn Murnane Laboratories diode-pumped mode-locked Ti:sapphire laser with pulses of ~ 30 fs. The laser head (Millennia) was supplied by Spectra Physics. Typical output power from the cavity was 200 – 250 mW. All emission scans were recorded at 800 nm excitation, scanning from 350 – 750 nm. An Ocean Optics spectrometer was used to monitor the wavelength. The two prisms located within the cavity were utilized to adjust the mode-lock and beam quality. The input power from the laser was varied by utilizing a variable neutral density filter. The fluorescence was collected perpendicular to the incident beam. A focal-length plano-convex lens was used to direct the fluorescence into a monochromator whose output was coupled to a photomultiplier tube. The photon-counting unit was manufactured by Hamamatsu, which was used to convert the photons

into counts. The multi-meter was used to convert the input mV to mW by obtaining a Keithley plot. Coumarin 307 ($(\phi\delta)_{800\text{ nm}} = 15\text{ GM}$) dissolved in methanol was used as a standard.⁴⁵ The TPA set-up is shown in Figure 2.2.

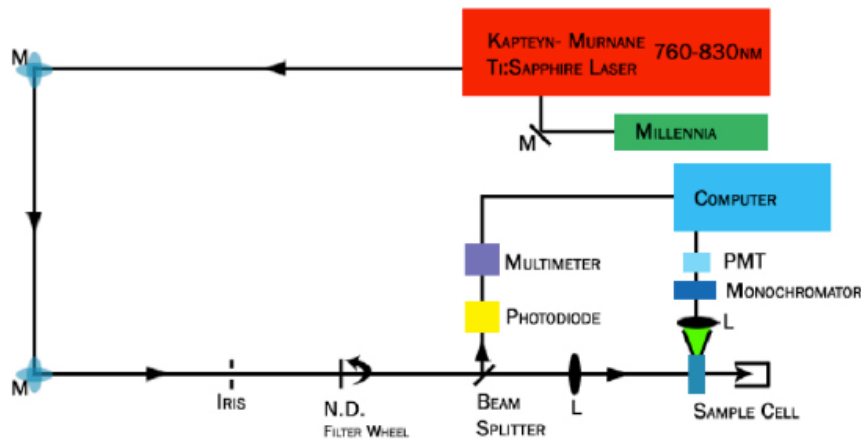


Figure 2.2. TPA set-up in our laboratory.

The equation used to calculate the TPA cross-section will be derived. The TPEF signal can be used to calculate the TPA cross-section with the following mathematical equation as given by

$$F(t) = \frac{1}{2} \eta \delta [c] n \frac{g_p}{\pi f \lambda \tau} \phi \langle P(t) \rangle^2 \quad (2.5)$$

where $F(t)$ is the TPEF photons collected per second, η is fluorescence quantum yield, δ is the TPA cross-section of the sample, $[c]$ is the concentration, n is the refractive index of the solvent, g_p is the shape factor of the pulsed laser (0.664 for Gaussian shape), f is the frequency of the laser (75×10^6 pulses/sec in our case), λ is the excitation wavelength, τ is the pulse durations, ϕ is the collection efficiency, and $\langle P(t) \rangle$ is the input intensity.

Equation 2.5 can be simplified by using a standard to calculate the TPA cross-section of a given sample. The standard is used to determine the collection efficiency.

Additionally, the values associated with the laser parameters are not needed when comparing against a known standard. As a consequence, the equation to calculate the TPA cross-section can be derived accordingly. By taking the logarithm of Equation 2.5, the equation can be simplified as

$$\log[F(t)] = 2 \log[\langle P(t) \rangle] + \log\left[\frac{1}{2}\eta\delta[c]n\frac{g_p}{\pi f\lambda\tau}\phi\right] \quad (2.6)$$

Therefore, the logarithm plot of the fluorescence intensity versus the power should give a slope of 2 since Equation 2.6 can be transcribed into the form $y = mx + b$. The slope of 2 confirms a two-photon excitation process rather than a one-photon excitation process.

Since the sample and standard both exhibit a slope of 2, the following equation is true:

$$m_{std}x_{std} = m_{samp}x_{samp} \quad (2.7)$$

The values or variables are substituted into Equation 2.5 to give the following:

$$2 \log[\langle P(t) \rangle]_{samp} = 2 \log[\langle P(t) \rangle]_{std} \quad (2.8)$$

$$\log[F(t)_{samp}] - b_{samp} = \log[F(t)_{std}] - b_{std}; \quad b = \log\left[\frac{1}{2}\eta\delta[c]n\frac{g_p}{\pi f\lambda\tau}\phi\right] \quad (2.9)$$

By substituting in the values, a relationship between the standard and sample can be established. It is important to note the b in Equation 2.9 can be ascribed to the y-intercept.

Equation 2.9 is further manipulated to give the following:

$$\log[F(t)_{samp}] - \log[F(t)_{std}] = b_{samp} - b_{std} \quad (2.10)$$

$$\log\left[\frac{F(t)_{samp}}{F(t)_{std}}\right] = b_{samp} - b_{std} \quad (2.11)$$

$$\frac{F(t)_{samp}}{F(t)_{std}} = 10^{(b_{samp}-b_{std})} \quad (2.12)$$

Equation 2.12 simplifies to $F(t) = b$ with $b = \frac{1}{2}\eta\delta[c]n\frac{g_p}{\pi f\lambda\tau}\phi$ when the logarithm power is equal to 0. This can be substituted into Equation 2.12 to give the following:

$$\frac{\frac{1}{2}\eta_{samp}\delta_{samp}[c]_{samp}n_{samp}\cdot\frac{g_p}{\pi f\lambda\tau}\phi}{\frac{1}{2}\eta_{std}\delta_{std}[c]_{std}n_{std}\cdot\frac{g_p}{\pi f\lambda\tau}\phi} = 10^{(b_{samp}-b_{std})} \quad (2.13)$$

$$\frac{\eta_{samp}\delta_{samp}[c]_{samp}n_{samp}}{\eta_{std}\delta_{std}[c]_{std}n_{std}} = 10^{(b_{samp}-b_{std})} \quad (2.14)$$

$$\delta_{samp} = \frac{10^{(b_{samp}-b_{std})}\cdot\delta_{std}\eta_{std}[c]_{std}n_{std}}{\eta_{samp}[c]_{samp}n_{samp}} \quad (2.15)$$

Equation 2.13 is simplified to give Equation 2.15 as the final expression to calculate the TPA cross-section of a given sample. The quantum yield, concentration, and refractive index of the solvent can be easily determined. The y-intercept or b value is determined by plotting the log-log plot of the fluorescence intensity-power. The log-log plot may not have an exact slope of 2 due to artifacts in the measurement, such as the residual light from the environment. As consequence, the slope needs to be corrected to give a slope of 2. This was done by manually subtracting counts from the fluorescence intensity. Furthermore, the TPA action cross-section can be determined by multiplying the TPA cross-section by the quantum yield. The action cross-section provides information about the two-photon excited fluorescence brightness, which is an important property for bio-imaging applications.

2.4 An Introduction and Overview of Time-Resolved Fluorescence Upconversion

In order to investigate the fluorescence dynamics of a molecule or system, fluorescence upconversion can be employed. Fluorescence upconversion has resolution on the femtosecond to picosecond time scale, which allows for the examination of electronic processes in the excited state. This technique can be used to gain detailed information relative to charge-transfer and energy migration.⁴⁷⁻⁴⁹ Additionally, time-

resolved spectroscopy is widely a used technique to study to the function and structure of macromolecules, including peptides and proteins.^{33,50–53}

Polarization measurements can be obtained by a Berek compensator. The polarization of the excitation source can be altered as either parallel ($I_{//}$) or perpendicular (I_{\perp}). Fluorescence anisotropy can provide detailed information about the system, such as the directionality^{11,54} of a material as well as about the shape, size, and dynamics of biological molecules.^{55–60} The fluorescence anisotropy can be calculated as given by⁶¹

$$r(t) = \frac{I_{//} - G \cdot I_{\perp}}{I_{//} + 2G \cdot I_{\perp}} \quad (2.16)$$

where $r(t)$ is the anisotropy and G is the correction factor. Anisotropy is a dimensionless quantity that relates the ratio of the difference in the polarized intensity with the overall intensity.¹¹ The maximum initial anisotropy value that can be achieved with a one-photon process is 0.40. In other words, no depolarization from the excitation to the emission between the dipoles is noted. The initial anisotropy can be calculated by the following⁶²:

$$r_o = \frac{2}{5} \left(\frac{2 \cos^2 \theta - 1}{2} \right) \quad (2.17)$$

Where r_o is the initial anisotropy and θ is the angle between the absorption and emission transition dipoles. The initial anisotropy will change as the excitation wavelength is varied because anisotropy measurements are wavelength dependent.

The fluorescence upconversion setup used in our laboratory is shown in Figure 2.3. A Millennia was used to produce a 532 nm light source. The light source was directed into a Tsunami manufactured by Spectra Physics containing a Ti:sapphire crystal to produce a mode-locked 800 nm light source with pulses of ~120 fs and repetition rate of 82 MHz. A FOG-100 system supplied by CDP, Inc. was used for the fluorescence upconversion measurements. The 800 nm light source is directed to a dichromic mirror. The residual

800 nm is passed to the variable delay line to produce a gate pulse, allowing for time-resolved measurements with a resolution of ~ 200 fs. The 800 nm light source is up-converted to 400 nm through second harmonic generation with the use of a beta-barium borate (BBO) crystal to produce the excitation source. A rotating cell holder with an optical path of 1 mm containing two quartz lens with a Teflon spacer was used to reduce photo-degradation.

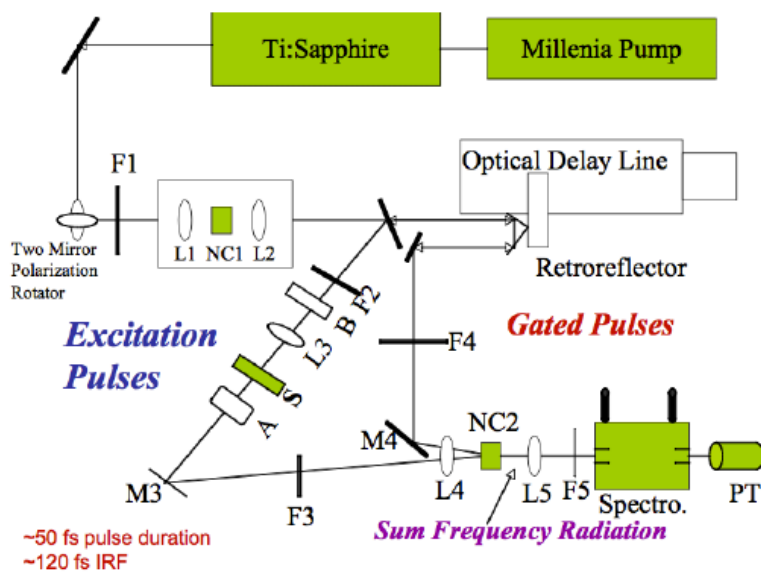


Figure 2.3. Fluorescence upconversion set-up in our laboratory.

The fluorescence was collected by focusing the emission on a second BBO crystal in which there is overlap between the emission and gate pulse that has passed through the delay line. A sum frequency radiation is generated, which combines the emission and gate pulse at 300 – 400 nm.⁶³ This signal is further focused and directed into a monochromator where it is detected by a photomultiplier tube (PMT). From the delay line, one step is equivalent to 6.25 femtoseconds with a range of approximately 1

nanosecond.⁶⁴ This allows for the time-resolved investigation of fluorescence dynamics in the femtosecond to picosecond time regime. It is important to check for photo-degradation by measuring the absorption spectrum before and after the experiment since this can cause artifacts in the data.

2.5 An Introduction and Overview of Time-Correlating Single-Photon Counting

Time-correlated single-photon counting (TCSPC) can be employed to examine the fluorescence decay on the nanosecond timescale. The principles described in fluorescence upconversion are applicable. Unlike fluorescence upconversion, TCSPC does not depend on a delay line for time-resolved measurements. Instead, TCSPC is an electronic process based on the repetitive collection of single photons over many different excitations.⁶⁵ This technique requires a high repetitive light source to accumulate a sufficient number of photons.⁶⁶ In order for time-resolved measurements, a time reference is necessary to sort the detected photons into bins.⁶⁷ This is achieved by taking the difference between the emission and reference pulse detection times. The reference pulse signal is converted to an electrical process or growing voltage by using a time-to-amplitude converter (TAC).^{68,69} This signal is then abrupt once the emission pulse is detected, which stops the growing voltage. The difference in the signal and emission pulses results in a signal that is guided to a multichannel analyzer or analog to digital converter (ADC). A quantitative value is assigned and recorded, which is sorted into the appropriate bin. This process or cycle is repeated until the distribution of photons relative to their bin assignment produces the fluorescence lifetime.

The TCSPC set-up is presented in Figure 2.4. It is important to note that the electronic components required for TCSPC must have sufficient processing speed in order to measure the fluorescence decay accurately. Therefore, the system is designed to minimize late response by measuring a single photon per excitation cycle, which allows for a dead time between the detection of photons. The quality of the detectors and ADC are critical for the time-resolution. Thus, it is important to use equipment that has sufficient processing speed. A Kapteyn Murnane Laboratories diode-pumped mode-locked Ti:sapphire laser with pulses of ~ 30 fs and repetition rate of 90 MHz was used as discussed earlier. The laser is tunable from 780 – 830 nm, which can produce an excitation wavelength of 390 – 415 nm through second harmonic generation. Single-photon excitation can be achieved by directing the pulsed laser through a BBO to generate a 400 nm excitation source. Two-photon excitation can be obtained by removing the BBO. The intensity of the excitation source can be altered with the use of a neutral density filter. The SYNC reference signal is produced by reflecting a small portion of the 800 nm beam towards a silicon photodiode with a glass slide. It is important to use an oscilloscope to monitor the amplitude of the reflected beam. The position of the photodiode must be adjusted until an amplitude of 1 W is achieved. A polarizer is placed after the second harmonic generation of the 400 nm excitation beam and emission of the sample. The polarizer can be adjusted to the magic angle of 54.7° with respect to the vertical polarization of the excitation beam, which allows for fluorescence decay measurements with distinct polarization.⁷⁰ In addition, the polarizers can be adjusted for anisotropy measurements.

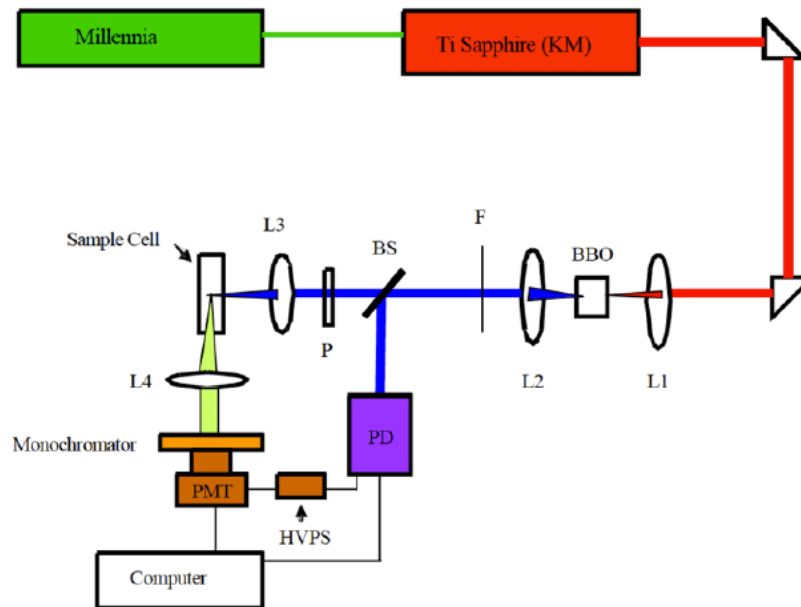


Figure 2.4. TCSPC setup in our laboratory.

The fluorescence of the sample is collected perpendicular to the excitation beam. A focusing lens is used to direct the emission towards a monochromator where the detected emission wavelength is specified. A PMT is used to detect the emission and transmit the signal into the computer with an interface card supplied by Time Harp. PicoQuant software was utilized to display and analyze the data collected from the experiment. The instrument response function (IRF) was collected by using a scattering medium, such as milk or mixing gold colloidal particles with NaCl.⁵⁵ The IRF was reported to have a value of approximately 300 ps. The average excitation power used was less than 10 mW at 400 nm.

2.6 An Introduction and Overview of Confocal Microscopy to Image Live Cells

Fluorescence microscopy has a broad range of applications due to the sensitivity as well as its ability to provide information about biological-related processes.^{41,71–85} Additionally, fluorescence microscopy is nondestructive and noninvasive, thus fluorescence microscopy can be applied to live specimens.⁸⁶ As a result, cellular and biochemical processes can be investigated at biologically relevant conditions. Fluorescence microscopy techniques that exhibit high spatial and temporal resolution have been employed to examine biological processes. In this work, confocal (single-photon and multi-photon) and fluorescence lifetime imaging microscopy (FLIM) were utilized. Confocal microscopy is an optical imaging technique that provides high spatial resolution and contrast by using a spatial pinhole at the confocal plane to avoid and minimize out-of-focus light.⁸⁷ Additionally, confocal microscopy can be used to reconstruct 3-D structures from the collected images.⁸⁸ Confocal microscopy offers several advantages over traditional wide-field microscopes as the excitation source is focused on a specific position of specimen rather than the entire specimen.⁸⁹ On the other hand, the emission close to the focal plane can be detected while eliminating out-of-focus signal with the use of confocal microscopy.⁹⁰ The images obtained from scanning the specimen are called optical sections, which refers to the noninvasive method to collect the image using focused light rather than sectioning the sample by physical means.⁹¹ A representation of wide-field vs pointing scanning of specimens is depicted in Figure 2.5.

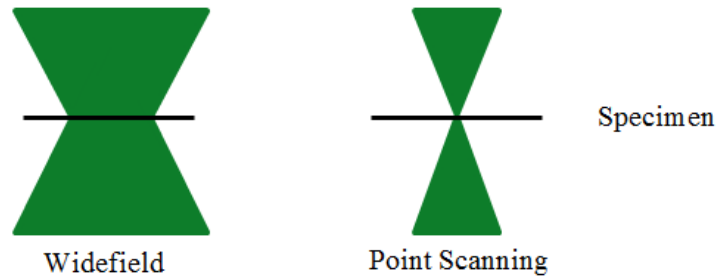


Figure 2.5. Representation of wide-field vs point scanning of a specimen.

A diagram representation of confocal microscopy is shown in Figure 2.6. A tunable excitation source produced from a light source passes through an aperture then a beam splitter.⁸⁸ The excitation light is then focused at the focal plane where the specimen is located. The beam splitter acts a dichromatic mirror for the emission wavelength and transparent for the excitation wavelength. However, the dichromatic mirror can behave vice versa if the position of the excitation source and detector are switched. The specimen is excited then the emission is directed back towards the dichromatic mirror, which directs the emission towards another aperture. The fluorescence that arrives at the detector comes predominately from a narrow focus plane to improve z-resolution. This allows for superior resolution as compared to conventional microscopy. To increase resolution, multi-photon excitation can be used to excite the sample.⁹² It is important to note that multi-photon confocal microscopy does not require a pinhole aperture.

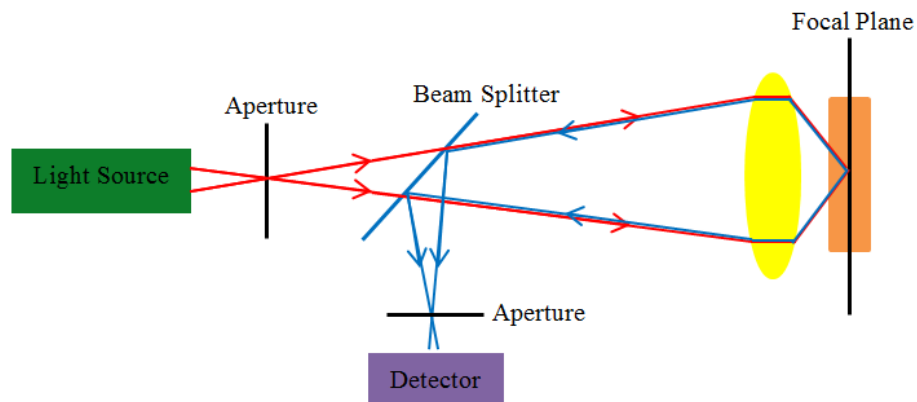


Figure 2.6. Diagram representation of confocal microscopy.

Fluorescence lifetime imaging microscopy (FLIM) is an imaging technique that is based on the differences in the fluorescence lifetime or exponential fluorescence decay rate. The fluorescence lifetime of the fluorophore is used to yield the image rather than the intensity. In other words, the images are shown in pseudo-color that correlates to a given lifetime. FLIM produces images with the intensity in each pixel determined by the fluorescence lifetime. As a result, fluorophores with similar emission wavelengths, but varying fluorescence lifetimes can be differentiated. An advantage of FLIM is that the fluorescence image produced is dependent on the environment of the fluorophore instead of its concentration.⁸⁴ Thus, molecular effects can be examined independently of the concentration of the fluorophore. FLIM can provide information that is inaccessible with steady-state fluorescence microscopy techniques. In this work, FLIM requires the use of a pulsed-laser as the excitation source and is based on time-correlated single-photon counting (TCSPC) or a time-domain method as given in Figure 2.7. The FLIM images are produced from well-defined planes rather than out-of-focus fluorescence to reduce

unwanted fluorescence. FLIM based on TCSPC exhibits high time resolution as well as high photon efficiency and lifetime accuracy.^{93,94}

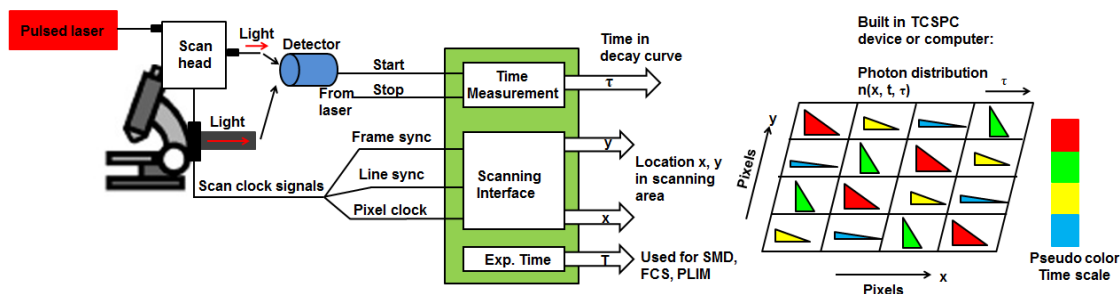


Figure 2.7. Principle of FLIM based on TCSPC.

The imaging experiments were carried out on Leica Inverted SP5X Confocal Microscope System equipped with a 10X – 100X objective. The 100X objectives was used with oil immersion, which provides a medium (high refractive index) to increase resolution. It is important to use the oil immersion correctly as it will result in spherical aberration if used incorrectly. Avalanche diode detectors were used to increase sensitivity and resolution when capturing and collecting images. A 405 nm diode (UV excitation), multi-line argon laser (470-670 nm), and Spectra Physics Mai-Tai two-photon tunable (640-1040 nm) laser were used as the excitation wavelength source. The power of the laser was adjusted to 5 – 10 % to reduce cell apoptosis. It is important to minimize exposure times especially when using the multi-photon excitation source. Picoquant SMD fluorescent lifetime imaging module (FLIM) is integrated into the Leica software. An Acousto Optical Beam Splitter (AOBS) was utilized to replace beam splitters and fluorescent filters in the light path. The microscope is equipped with five photomultiplier tubes (PMT) to allow the detection of emission, which is tunable to a specific or desired

wavelength. A motorized X, Y, Z stage allows for precise control of the position of the sample.

When operating the confocal microscope located in the Microscopy and Imaging Analysis (MIL) Core at the University of Michigan, it is important to turn on the equipment in the proper order. The equipment is labeled 1 – 7, which should be turned on in the following series (1 through 7). If multi-photon is utilized, turn on the equipment labeled 8 and 9 as well. Click on the LASF icon on the computer to start the software. When a window asking to initialize the stage appears, click no. Once the software has loaded, click laser and turn on the necessary excitation source (405 diode, argon laser, multi-photon, white light) under configuration. Select the desired magnification objective lens (10x – 100x). Note that 40x and higher requires oil immersion whereas the other objective lens do not. Place the sample on the stage located on the microscope. The x and y direction of the stage can be adjusted using the hand wheel. Focus the cells under bright field mode. Additionally, the cells can be focused under the bright field using UV excitation fluorescence. On equipment #1, open the shutter and turn on the 405 nm diode to excite the sample. Select the background by pressing the GFP or BRG button, which turns the background green or red, respectively allowing for better contrast. Click the z button on the hand wheel to adjust and focus in the z-direction. Once focused, turn on the selected excitation source for single photon and adjust the power to 5 – 10 % and open the shutter. Click pinhole and airy 1 before the imaging experiments. The pinhole controls the amount of light that is directed into the detector. Select detector 1 and adjust the collected emission wavelength range. In my case, HyD1 was used for the imaging experiments. It is important to turn off the other detectors that are not in use. The color of

the fluorescence can also be adjusted by clicking properties. Adjust the resolution to 1024 x 1024 pixels and the number of scans to 6. Click the live button to visualize and observe the cells. The z-direction or focus can be adjusted to improve the image quality. The gain and intensity can also be adjusted to optimize fluorescence and image quality. Once you are ready to capture the image, click the capture button. The image will be captured. Be sure to save the file into your folder as well as the image by clicking “export as” and saving as a TIF file. A distance key can also be added to the image if desired. This can be achieved by clicking the scale button located on the right computer monitor. Right click with the mouse and click capture image, which will allow the scale to be visualized in the image. The fluorescence and background contrast can be adjusted by moving the contrast scale located on the right computer monitor. If the images are fuzzy or blurry, the objectives may have to be cleaned with methanol. It is important to not saturate the intensity of the image. This can be done by clicking the button that changes the scanning abilities in the software located on the right computer monitor (icon on the top left hand corner). If the cell or any part of the screen is blue, this indicates the intensity is too high. You do not want blue or high intensity spots in the images. With regards to the multi-photon imaging experiments, the wavelength can be adjusted. Be sure the pulse icon is on before starting. Turn on the gate (right column to 1), gain to 30%, power to 10%, and open the shutter. In order to acquire images via FLIM, the second computer next to the computer monitors needs to be powered on. Additionally, the Pico Quant instruments need to be turned on. The sample will be excited with the pulsed laser (two-photon excitation). The two monitors on the top row control the FLIM software. It is important to click the SymPho Time (Pico Harp) software then start a new workspace to begin. In

the Leica software, open the FLIM wizard set-up on the top left hand margin. This will allow you to setup the parameters. Once it is setup, you can select to either collect the fluorescence lifetime for a given time or until a certain amount of counts are reached per pixel. It is critical to keep the photons per second below 1000 counts/sec as it will saturate the image. This can be achieved by reducing the laser power and/or gain. Click collect image and wait for the collection to complete. Once the image is collected, use the Pico Harp software to fit the fluorescence lifetime. It important to fit the exponential decay with bi- or tri-exponential fit. This will correlate the fluorescence lifetime to an image color. The pseudo-color within the image will correspond to the fluorescence lifetime. The FLIM images can be viewed by clicking the tau icon. The time resolution on the FLIM is on the order of picoseconds to nanoseconds. After the imaging experiments, the shut-down procedure is important. Turn off the laser(s) and switch the objective back to 10X in the Leica Software. If oil immersion is used, clean the objectives with the lens paper before switching the objective back to 10X. When powering down, follow the instructions on the wall located behind the computer. It is important to turn off the numbered equipment in the proper order to avoid damage. Be sure to give the laser(s) 10 min to cool down prior to turning off the remaining equipment. This is listed on the instructions. If FLIM is used, shut down the computer and the Pico Quant instruments. The microscope located in the MIL core is shown in Figure 2.8.

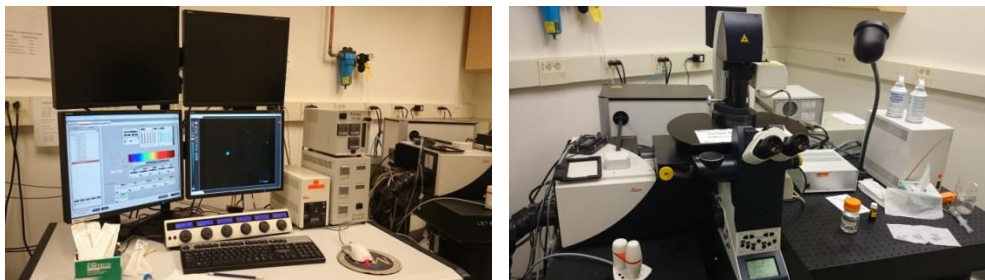


Figure 2.8. Inverted confocal microscope located in the MIL Core at the University of Michigan.

2.7 Summary and Standard Operating Procedures to Culture Mammalian Cells

The examination of biological-based systems plays an important role in drug research develop and development. *In vivo* experiments are conducted in the entire or whole animal/plant. In contrast, *in vitro* studies are performed in solution or in cells cultured with medium. In order to examine systems at physiologically relevant conditions, experiments can be conducted *in vitro*, which offers several advantages. Living organisms have extremely convoluted functional systems that consist of many complex structures and compounds. Because of this complexity, there is a significant barrier when examining systems at biologically relevant conditions. The main advantage of *in vitro* experiments is that it simplifies the system, thus, bypassing the complex barrier. Another advantage is that the studies can be used to examine human cell lines without exposing humans to potential carcinogenic and/or toxic compounds. An additional advantage is that human cell lines can be used directly.⁹⁵ In other words, no translation from animal to human is necessary. Finally, *in vitro* studies can be tuned towards automation processes, which is essential for high through-put screening for pharmaceutical testing.^{36,96–103}

In order to culture mammalian cells while avoiding contamination, it is critical to practice aseptic technique. It is critical to use protective wear (goggles, gloves, lab coat)

at all times when handling cells.¹⁰⁴ Before working in the laminar flow hood, wash hands with soap and warm water. A laminar flow hood equipped with a high-efficiency particulate arrestance (HEPA) filter is required to prevent contamination from airborne particles and aerosols.¹⁰⁵ It is important to locate the hood away from windows, doors, and other equipment with no foot traffic as well as keeping the hood uncluttered as it can hinder the flow of air. When handling cells, it necessary to turn the UV lamp for at least 30 min to sterilize the surface. Once completed, the laminar flow should be established for at least 20 min prior to working in the hood. It is critical to clean the hood with 70% ethanol before and after usage. Be sure to spray all containers entering the hood with 70% ethanol before placing it in the hood. All cell culture containers (pipettes, flasks, petri dishes, centrifuge tubes, etc.) should be purchased sterilized by gamma-irradiation. Always spray your hands with 70% ethanol while wearing gloves before placing them in the hood. It should be emphasized to never pour solutions and always pipette the solution as pouring can cause contamination. If for some reason you have to place the cap of a container down, never place it facing down.¹⁰⁶ After you are done working in the laminar flow hood, wipe the surface down with ethanol and turn on the UV light. The equipment required for culturing cells is shown in Figure 2.9.

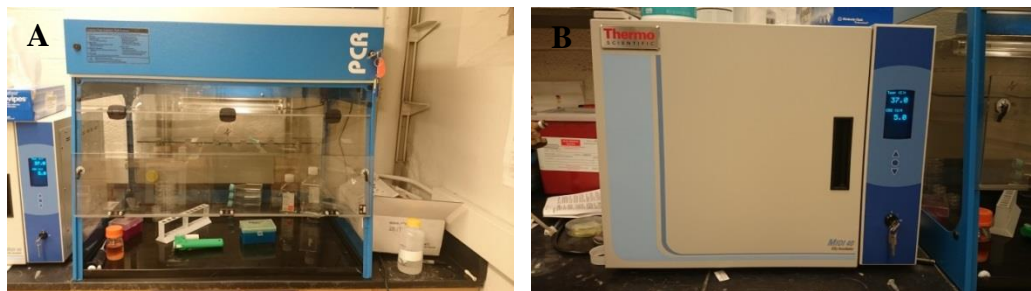


Figure 2.9. (A) Laminar flow hood and (B) CO₂ incubation oven in our laboratory.

The cells were cultured with Dulbecco's Modified Eagle Medium (DMEM) with 10% fetal bovine serum (FBS), 100 units of penicillin, and 100 µg/ml streptomycin. DMEM was purchased with phenol red, which allows for easy monitoring of the pH of the medium. The cells should be grown in medium with a pH of 7.0 – 7.4.¹⁰⁵ FBS provides the essential growth factors for proper cell growth. Penicillin and streptomycin are used as antibiotics to prevent bacterial contamination. The cells must be grown at conditions of 37 °C with 5% CO₂ and high humidity. CO₂ is necessary to prevent the medium from becoming too basic as CO₂ (slightly acidic) is absorbed into the medium.¹⁰⁶ This is important to maintain the pH of the medium. The temperature must be kept at 37 °C for optimal cell growth. The incubation oven should be cleaned with ethanol prior to use. The water dish located inside the incubation oven should be replaced every other week. Be sure to clean the metal dish with ethanol before use. It is critical to use sterilize water and place the water dish under the UV lamp for at least 1 h prior to placing the dish back in the hood. The water dish is a major site for contamination so it is crucial to keep it clean and replace the water frequently.¹⁰⁴

It is important to preserve the cells using a liquid nitrogen freezer (-120 to -130 °C). The cells should be placed into working medium (DMEM with 10% FBS) and 5% DMSO with about 10⁵ cells/mL.¹⁰⁵ The cells should be placed in a cryogenic tube and frozen at 1 °C/min until -80 °C then placed at -120 °C. In order to thaw the cells, the cells must be removed from the liquid nitrogen freezer then immediately placed in a 37 °C water bath for 1 – 2 min. It is important to move as quickly as possible as DMSO is toxic and results in cell apoptosis. Once the cells are thawed, place the solution into 10 mL of working medium in a 15 mL centrifuge tube then centrifuge at 125 x g for 5 min. The

cells will be located at the bottom of the centrifuge tube as a beige color. Aspirate the medium then place 10 mL of new working medium into the centrifuge tube. Resuspend the cells by gently mixing the cells using the 15 mL pipette. Place the cells in a T-flask (75 cm²). These flasks are coated with poly-lysine to facilitate and promote cell adherence. Poly-lysine is positively charged, which promotes adherence of the cells since the cell membrane is negatively charged. Gently rock the flask back and forth to eventually distribute the cells. Do not rock the flask in a stirring motion as it can cause the cells to aggregate. Incubate the cells in the CO₂ oven with the proper conditions as discussed above. It is important to replenish the medium every 1 – 3 days. With the use of phenol red, the pH can be monitored by the color of medium: yellow pH 6.0 – 6.5, orange 6.6 – 6.9, orange/pink 7.0 – 7.4, pink/purple 7.5 – 8.0.¹⁰⁷ The medium should be changed immediately if it is orange to yellow in color. The cells will take approximately 4 – 7 days to reach 70 – 90 % confluency during the first passage. A microscope is required to observe the cells during this period. It is important to be gentle with the cells as it is the most sensitive period of the cells.

Once the cells have reached 70 – 80 % confluency, passaging (splitting or subculturing) of the cells is necessary. Remove the medium and wash the cells with sterile PBS containing no ions. Remove the PBS then add 2 – 3 mL of 0.25% (w/v) Trypsin-0.53 mM EDTA solution to cover the cells.¹⁰⁸ Trypsin is a serine protease that is used to hydrolyze the proteins (peptide bonds) keeping the cells adhered to the surface, thus detaching the cells from the surface. Place the cells into the CO₂ oven for 2 – 5 min to increase the Trypsin activity or until the cells start to dislodge from the surface. Longer exposure time is required for cells that are difficult to remove from the surface of the

flask. Add 6 – 8 mL of working medium to neutralize the Trypsin solution. It is important to not expose the cells to the Trypsin solution too long as it is very toxic. Gently mix the cells into the medium using the pipette. Subculture ratios of 1:2 to 1:10 are recommended.^{105,106} The cells will reach 70 – 90 % confluency in 3 – 5 days at a 1:10 split. Cells should be discarded after 30 – 50 splits as the genetics can alter. After working in the hood, the flasks and pipettes should be placed in a bleach bath (10 – 20 % bleach) for at least 1 d prior to disposal. Medium or water that came in contact with the cells should be disposed in a container containing concentrated bleach. This container can be poured down the sink after sitting for at least 30 minutes.

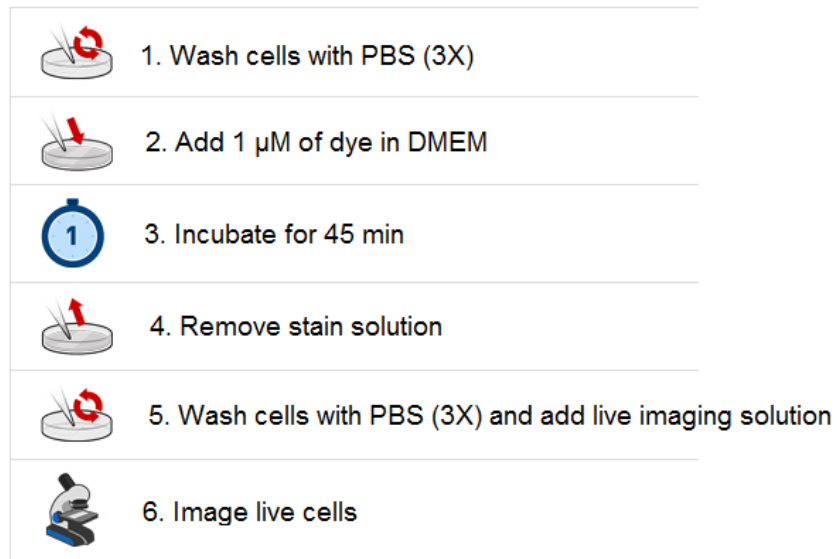


Figure 2.10. Standard operating procedure to stain cells with fluorescent nuclear dyes.

The fluorescent nuclear dyes were imaged *in vitro* by fluorescence confocal microscopy. This was accomplished by incubating the cells with 1 – 5 μ M of dye in DMEM for 30 – 60 min. The cells were washed with PBS (3X) to remove excess dye.

Live cell imaging solution was used as the physiological medium for the imaging experiments, which also provides image clarity with high signal-to-noise ratio. This solution offers several advantages over standard buffer, such as PBS or HEPES. Cells apoptosis begins after 30 min in common buffers whereas the live imaging solution provides high cell viability for up to 4 h when exposed to ambient conditions for extended periods of time. It is important to monitor cell viability if the dye exhibits high cytotoxicity. This can be done by employing a cell counting unit or hemocytometer along with trypan blue, which is a stain that is used to label non-living cells. The dye works by staining the cells blue since the cell wall has been disrupted. Live cells will not stain blue as the dye cannot penetrate the cell wall. It is important that at least 70 – 80 % of the cells are viable when performing imaging experiments. The protocol is summarized in Figure 2.10.

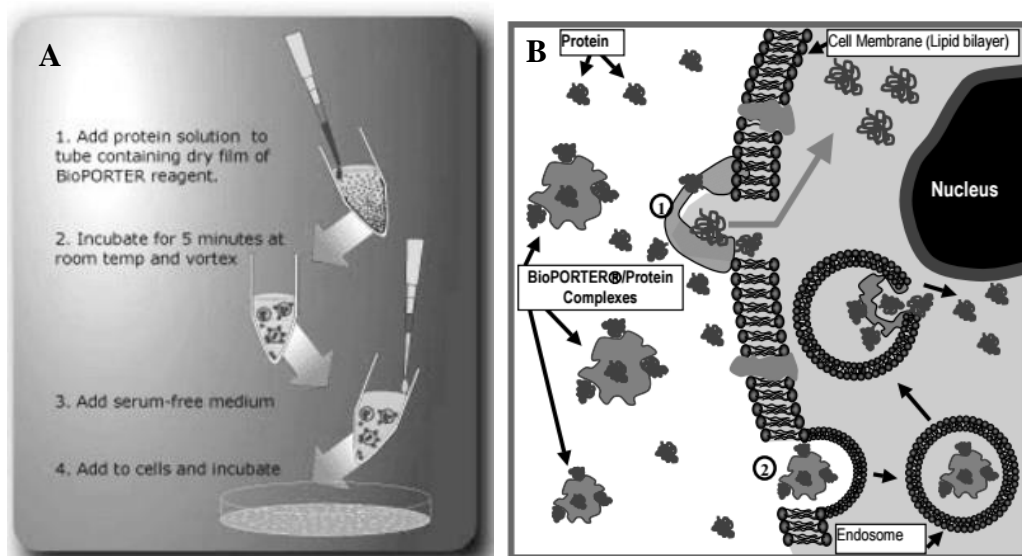


Figure 2.11. (A) Simplified directions to use BioPORTER peptide delivery kit. (B) Summary of how the BioPORTER reagent works.

Transfection experiments are required for the delivery of macromolecules, such as DNA, peptides, and proteins into live cells. The transfection kit used in this work was supplied by BioPORTER.¹⁰⁹ The kit uses a lipid-based reagent for protein and peptide delivery, which allows for a quick delivery into the cell. The delivered peptides retain their structure and function while minimizing adverse effects on the cell. The protocol for the transfection of peptides and/proteins is easy to follow. 250 μL of methanol or chloroform was added to the vial containing the BioPORTER reagent. It is important to use sterile solvent or sterile filter the solvent by using a 0.22 μm filter. The solution was vortexed for 10 – 20 sec. 2.5 μL of BioPORTER reagent solution was added to centrifuge tube. The solvent was allowed to evaporate in the laminar flow hood for 2 h to produce a thin film of transfection reagent. If larger amounts of transfection reagent are used, longer evaporation time is required. 10 – 25 μL of the protein or peptide (100 $\mu\text{g}/\text{ml}$) was added to the centrifuge tube containing the BioPORTER reagent. The solution was mixed using a pipette and allowed to incubate at room temperature for 3 – 5 min. The solution was then diluted with 250 of μL DMEM (serum-free, antibiotic-free). It is important to not include FBS or antibiotics during the transfection process as it can hinder the transfection efficiency. The solution was then added to the cells and incubated in the CO_2 oven at 37 $^\circ\text{C}$ for 4 h. The cells were washed with PBS to remove excess dye-transfected complex prior to imaging. The BioPORTER kit is detailed in Figure 2.11.

In this work, the cells were imaged live in optical imaging wells. The cells were not fixed because it can alter cells and/or tissue as well as the fluorescence dynamics cannot be observed with continuous real-time analysis. The optical imaging wells were supplied by MatTek Corporation. 35 mm imaging wells coated with poly-lysine with a glass

thickness of No. 1.5 were used for all imaging experiments. The cells were plated by a 1:5 dilution (1.25 – 1.5 mL) 24 h prior to conducting the imaging experiments. It is critical to plate or seed the cells with the proper density. If the cells are too dense, it can cause variation in the transfection process. It is important to note that the transfection kits are generally toxic, resulting in cell apoptosis. Therefore, it is critical to use the proper cell density (60 – 70 % confluent).

References

1. Vogel, H. J. *Calcium-Binding Protein Protocols*; Humana Press: New Jersey, 2002; Vol. 173.
2. Weljie, A. M.; Vogel, H. J. *Methods Mol. Biol.* **2002**, *173*, 75.
3. www.photobiology.info/Nonell_Viappiani.html
4. Bakker, J. M.; Aleese, L. Mac; Meijer, G.; von Helden, G. *Phys. Rev. Lett.* **2003**, *91*, 203003.
5. Okamoto, H.; Tasumi, M. *Chem. Phys. Lett.* **1996**, *256*, 502.
6. Dalrymple, B. E.; Duff, J. M.; Menzel, E. R. *SPIE/SPSE Technical Symposium East*; Freeman, C., Nudelman, S., Richmond, J. C., Eds.; International Society for Optics and Photonics, 1977; pp 118–125.
7. *Encyclopedia of Life Sciences*; John Wiley & Sons, Ltd: Chichester, UK, 2001.
8. Porrès, L.; Holland, A.; Pålsson, L.-O.; Monkman, A. P.; Kemp, C.; Beeby, A. J. *Fluoresc.* **2006**, *16*, 267.
9. www.2.chemistry.msu.edu/faculty/reusch/VirtTxtJml/Spectrpy/UV-Vis/spectrum.htm

10. www.teaching.shu.ac.uk/hwb/chemistry/tutorials/molspec/uvvisab1.htm
11. Lakowicz, J. R. Principles of fluorescence spectroscopy; Springer: New York (2006).
12. *Practical Fluorescence, Second Edition*; CRC Press, 1990.
13. Espósito, B. P.; Epsztejn, S.; Breuer, W.; Cabantchik, Z. I. *Anal. Biochem.* **2002**, *304*, 1.
14. Mohammed, G. H.; Binder, W. D.; Gillies, S. L. *Scand. J. For. Res.* **2008**, *10*, 383.
15. Bensasson, R.; Goldschmidt, C. R.; Land, E. J.; Truscott, T. G. *Photochem. Photobiol.* **1978**, *28*, 277.
16. Rurack, K.; Spieles, M. *Anal. Chem.* **2011**, *83*, 1232.
17. Chen, R. F. *Anal. Lett.* **1967**, *1*, 35.
18. [www.horiba.com/fileadmin/uploads/Scientific/Documents/Fluorescence/quantum yieldstrad.pdf](http://www.horiba.com/fileadmin/uploads/Scientific/Documents/Fluorescence/quantum_yieldstrad.pdf)
19. Polavarapu, P. L. *Chirality* **2008**, *20*, 664.
20. Kelly, S.; Price, N. *Curr. Protein Pept. Sci.* **2000**, *1*, 349.
21. Eriksson, M.; Nordén, B. *Methods Enzymol.* **2001**, *340*, 68.
22. Kubista, M.; Aakerman, B.; Norden, B. *J. Phys. Chem.* **1988**, *92*, 2352.
23. Schipper, P. E.; Nordén, B.; Tjerneld, F. *Chem. Phys. Lett.* **1980**, *70*, 17.
24. Nordén, B.; Kurucsev, T. *J. Mol. Recognit.* **1994**, *7*, 141.
25. Hiort, C.; Norden, B.; Rodger, A. *J. Am. Chem. Soc.* **1990**, *112*, 1971.
26. Becker, H.-C.; Nordén, B. *J. Am. Chem. Soc.* **1997**, *119*, 5798.
27. Chaires, J. B.; Waring, M. J., Eds.; Academic Press: New York; Vol. 340, pp

- 68–98 (2001).
28. Mazur, S.; Tanious, F. A.; Ding, D.; Kumar, A.; Boykin, D. W.; Simpson, I. J.; Neidle, S.; Wilson, W. D. *J. Mol. Biol.* **2000**, *300*, 321.
29. Suh, D.; Chaires, J. B. *Bioorg. Med. Chem.* **1995**, *3*, 723.
30. Long, E. C.; Barton, J. K. *Acc. Chem. Res.* **1990**, *23*, 271.
31. Narayanan, A.; Varnavski, O. P.; Swager, T. M.; Goodson, T. *J. Phys. Chem. C* **2008**, *112*, 881.
32. Laine, R. M.; Sulaiman, S.; Brick, C.; Roll, M.; Tamaki, R.; Asuncion, M. Z.; Neurock, M.; Filhol, J.-S.; Lee, C.-Y.; Zhang, J.; Goodson, T.; Ronchi, M.; Pizzotti, M.; Rand, S. C.; Li, Y. *J. Am. Chem. Soc.* **2010**, *132*, 3708.
33. Clark, T. B.; Ziolkowski, M.; Schatz, G. C.; Goodson, T. *J. Phys. Chem. B* **2014**, *118*, 2351.
34. Varnavski, O. P.; Goodson, T.; Mohamed, M. B.; El-Sayed, M. A. *Phys. Rev. B* **2005**, *72*, 235405.
35. Drobizhev, M.; Makarov, N. S.; Tillo, S. E.; Hughes, T. E.; Rebane, A. *Nat. Methods* **2011**, *8*, 393.
36. Drobizhev, M.; Stepanenko, Y.; Rebane, A.; Wilson, C. J.; Screen, T. E. O.; Anderson, H. L. *J. Am. Chem. Soc.* **2006**, *128*, 12432.
37. Drobizhev, M.; Tillo, S.; Makarov, N. S.; Hughes, T. E.; Rebane, A. *J. Phys. Chem. B* **2009**, *113*, 855.
38. Drobizhev, M.; Tillo, S.; Makarov, N. S.; Hughes, T. E.; Rebane, A. *J. Phys. Chem. B* **2009**, *113*, 12860.
39. Dumat, B.; Bordeau, G.; Faurel-Paul, E.; Mahuteau-Betzer, F.; Saettel, N.; Metge,

- G.; Fiorini-Debuisschert, C.; Charra, F.; Teulade-Fichou, M.-P. *J. Am. Chem. Soc.* **2013**, *135*, 12697.
40. Kim, H. M.; Cho, B. R. *Chem. Rev.* **2015**, *115*, 5014.
41. Abbotto, A.; Baldini, G.; Beverina, L.; Chirico, G.; Collini, M.; D'Alfonso, L.; Diaspro, A.; Magrassi, R.; Nardo, L.; Pagani, G. A. *Biophys. Chem.* **2005**, *114*, 35.
42. Theer, P.; Hasan, M. T.; Denk, W. *Opt. Lett.* **2003**, *28*, 1022.
43. McLean, A. M.; Socher, E.; Varnavski, O.; Clark, T. B.; Imperiali, B.; Goodson, T. *J. Phys. Chem. B* **2013**, *117*, 15935.
44. Göppert-Mayer, M. *Ann. Phys.* **1931**, *401*, 273.
45. Xu, C.; Webb, W. W. *J. Opt. Soc. Am. B* **1996**, *13*, 481.
46. Pawlicki, M.; Collins, H. A.; Denning, R. G.; Anderson, H. L. *Angew. Chem. Int. Ed. Engl.* **2009**, *48*, 3244.
47. Lahankar, S. A.; West, R.; Varnavski, O.; Xie, X.; Goodson, T.; Sukhomlinova, L.; Twieg, R. *J. Chem. Phys.* **2004**, *120*, 337.
48. Varnavski, O.; Goodson, T. *Chem. Phys. Lett.* **2000**, *320*, 688.
49. Varnavski, O. P.; Ostrowski, J. C.; Sukhomlinova, L.; Twieg, R. J.; Bazan, G. C.; Goodson, T. *J. Am. Chem. Soc.* **2002**, *124*, 1736.
50. Xu, J.; Knutson, J. R. *Methods Enzymol.* **2008**, *450*, 159.
51. Wang, Y.; Clark, T. B.; Goodson, T. *J. Phys. Chem. B* **2010**, *114*, 7112.
52. Zhang, L.; Kao, Y.-T.; Qiu, W.; Wang, L.; Zhong, D. *J. Phys. Chem. B* **2006**, *110*, 18097.
53. Michalet, X.; Weiss, S.; Jäger, M. *Chem. Rev.* **2006**, *106*, 1785.

54. Jablonski, A. *Bull. Acad. Pol. Sci., Ser. sci. math. astr. phys* **1960**.
55. Ryderfors, L.; Mukhtar, E.; Johansson, L. B.-Å. *Chem. Phys. Lett.* **2005**, *411*, 51.
56. Kuśba, J.; Lakowicz, J. R. *J. Chem. Phys.* **1999**, *111*, 89.
57. Chib, R.; Raut, S.; Sabnis, S.; Singhal, P.; Gryczynski, Z.; Gryczynski, I. *Methods Appl. Fluoresc.* **2014**, *2*, 015003.
58. Stsiapura, V. I.; Maskevich, A. A.; Kuzmitsky, V. A.; Uversky, V. N.; Kuznetsova, I. M.; Turoverov, K. K. *J. Phys. Chem. B* **2008**, *112*, 15893.
59. Swaminathan, R.; Hoang, C. P.; Verkman, A. S. *Biophys. J.* **1997**, *72*, 1900.
60. Brüsweiler, R.; Liao, X.; Wright, P. E. *Science* **1995**, *268*, 886.
61. www.horiba.com/fileadmin/uploads/Scientific/Documents/Fluorescence/Anisotropy_FL-3.pdf
62. Goodson, T. *Annu. Rev. Phys. Chem.* **2005**, *56*, 581.
63. Xu, J.; Knutson, J. R. *Methods Enzymol.* **2008**, *450*, 159.
64. www.cdpsystems.com/fog100.html
65. Becker, W.; Bergmann, A.; Hink, M. A.; König, K.; Benndorf, K.; Biskup, C. *Microsc. Res. Tech.* **2004**, *63*, 58.
66. O'Connor, D. *Time-correlated single photon counting*; Academic Press, 2012.
67. www.picoquant.com/images/uploads/page/files/7253/technote_tcspc.pdf
68. Coleman, P. G.; Griffith, T. C.; Heyland, G. R. *Appl. Phys.* **1974**, *5*, 223.
69. Davidson, F. *J. Appl. Phys.* **1968**, *39*, 62.
70. Chang, M. C.; Courtney, S. H.; Cross, A. J.; Gulotty, R. J.; Petrich, J. W.; Fleming, G. R. *Instrum. Sci. Technol.* **2008**, *14*, 433.
71. Suzuki, T.; Fujikura, K.; Higashiyama, T.; Takata, K. *J. Histochem. Cytochem.*

- 1997**, 45, 49.
72. Ploeger, L. S.; Dullens, H. F. J.; Huisman, A.; van Diest, P. J. *Biotech. Histochem.* **2008**, 83, 63.
73. Juette, M. F.; Gould, T. J.; Lessard, M. D.; Mlodzianoski, M. J.; Nagpure, B. S.; Bennett, B. T.; Hess, S. T.; Bewersdorf, J. *Nat. Methods* **2008**, 5, 527.
74. Gläser, K.; Wilke, K.; Wepf, R.; Biel, S. S. *Skin Res. Technol.* **2008**, 14, 324.
75. Nie, S.; Chiu, D.; Zare, R. *Science* **1994**, 266, 1018.
76. Mank, M.; Santos, A. F.; Drenth, S.; Mrcic-Flogel, T. D.; Hofer, S. B.; Stein, V.; Hendel, T.; Reiff, D. F.; Levelt, C.; Borst, A.; Bonhoeffer, T.; Hübener, M.; Griesbeck, O. *Nat. Methods* **2008**, 5, 805.
77. Ricard, C.; Coles, J.; Serduc, R.; Sanden, B. Van Der; Verant, P.; Vial, J.-C. Academic press Elsevier 2009, pp 1221–1229.
78. Kanony, C.; Åkerman, B.; Tuite, E. *J. Am. Chem. Soc.* **2001**, 123, 7985.
79. Lichtman, J. W.; Conchello, J.-A. *Nat. Methods* **2005**, 2, 910.
80. Wilson, J. N.; Wiggenius, J.; Pitter, D. R. G.; Qiu, Y.; Abrahamsson, M.; Westerlund, F. *J. Phys. Chem. B* **2013**, 117, 12000.
81. Hiraoka, Y.; Sedat, J. W.; Agard, D. A. *Biophys. J.* **1990**, 57, 325.
82. Gordon, G. W.; Berry, G.; Liang, X. H.; Levine, B.; Herman, B. *Biophys. J.* **1998**, 74, 2702.
83. Huang, B.; Bates, M.; Zhuang, X. *Annu. Rev. Biochem.* **2009**, 78, 993.
84. Becker, W. *J. Microsc.* **2012**, 247, 119.
85. Chaigneau, E.; Oheim, M.; Audinat, E.; Charpak, S. *Proc. Natl. Acad. Sci. U. S. A.* **2003**, 100, 13081.

86. www.physics.emory.edu/faculty/weeks//confocal
87. Paddock, S. W. *Mol. Biotechnol.* **2000**, *16*, 127.
88. Smith, C. L. *Curr. Protoc. Mol. Biol.* **2008**, *Chapter 14*, Unit 14.11.
89. Webb, R. H. *Reports Prog. Phys.* **1996**, *59*, 427.
90. www.microscopyu.com/articles/confocal/confocalintrobasics.html
91. Conchello, J.-A.; Lichtman, J. W. *Nat. Methods* **2005**, *2*, 920.
92. Diaspro, A.; Corosu, M.; Ramoino, P.; Robello, M. *Microsc. Res. Tech.* **1999**, *47*, 196.
93. Ballew, R. M.; Demas, J. N. *Anal. Chem.* **1989**, *61*, 30.
94. Philip, J.; Carlsson, K. *J. Opt. Soc. Am. A* **2003**, *20*, 368.
95. Antibodies, N. R. C. (US) C. on M. of P. M. *Monoclonal Antibody Production*; National Academies Press: Washington, D.C., 1999.
96. Ozbal, C. C.; LaMarr, W. A.; Linton, J. R.; Green, D. F.; Katz, A.; Morrison, T. B.; Brennan, C. J. H. *Assay Drug Dev. Technol.* **2004**, *2*, 373.
97. Wan, H.; Holmen, A. *Comb. Chem. High Throughput Screen.* **2009**, *12*, 315.
98. Fastrez, J. *Mol. Biotechnol.* **1997**, *7*, 37.
99. Giuliano, K. A.; Haskins, J. R.; Taylor, D. L. *Assay Drug Dev. Technol.* **2003**, *1*, 565.
100. Gill, S.; Gill, R.; Lee, S. Sen; Hesketh, J. C.; Fedida, D.; Rezazadeh, S.; Stankovich, L.; Liang, D. *Assay Drug Dev. Technol.* **2003**, *1*, 709.
101. Hamid, R.; Rotshteyn, Y.; Rabadi, L.; Parikh, R.; Bullock, P. *Toxicol. In Vitro* **2004**, *18*, 703.
102. Hägg, M.; Bivén, K.; Ueno, T.; Rydlander, L.; Björklund, P.; Wiman, K. G.;

- Shoshan, M.; Linder, S. *Invest. New Drugs* 20, 253.
103. Gabelica, V.; De Pauw, E.; Rosu, F. *J. Mass Spectrom.* **1999**, 34, 1328.
104. www.level.com.tw/html/ezcatfiles/vipweb20/img/img/20297/intro_animal_cell_culture.pdf
105. www.qiagen.com/us/resources/molecular-biology-methods/animal-cell-culture/
106. www.abcam.com/index.html?pageconfig=resource&rid=11453
107. www.olszta.com/ph&ureacolorcards
108. www.atcc.org/products/all/CCL-2.aspx#culturemethod
109. www.genlantis.com/bioporter-reagent.html

Chapter 3

Two-Photon Spectroscopy as a New Sensitive Method for Determining the DNA Binding Mode of Fluorescent Nuclear Dyes

3.1 Original Publication Information

A majority of this chapter was published as the following document:

Doan, P.; Pitter, D.; Kocher, A.; Wilson, J. N.; Goodson III, T. “Two-Photon Spectroscopy as a New Sensitive Method for Determining the DNA Binding Mode of Fluorescent Nuclear Dyes” *J. Am. Chem. Soc.* **2015**, *137*, 9198.

Modifications were made to the original document to adapt the context to this form. The original manuscript and supporting information have been combined.

3.2 Abstract

A new optical strategy to determine the binding modes (intercalation vs groove binding) of small fluorescent organic molecules with calf thymus DNA was developed using two-photon absorption (TPA) spectroscopy. Two-photon excited emission was utilized to investigate newly synthesized donor-acceptor-donor π -system chromophores, which bind to DNA. The results show that TPA cross-sections are able to differentiate the fine details between the DNA binding modes. Groove binding molecules exhibit an enhanced TPA cross-section due to the DNA electric field induced enhancement of the

transition dipole moment while intercalative binding molecules exhibit a decrease in the TPA cross-section. Remarkably, the TPA cross-section of **1** is significantly enhanced (13.6-fold) upon binding with DNA. The sensitivity of our TPA methodology is compared to circular dichroism (CD) spectroscopy. TPA demonstrates superior sensitivity by more than an order of magnitude at low DNA concentrations. This methodology can be utilized to probe DNA interactions with other external molecules such as proteins, enzymes, and drugs.

3.3 Introduction

Fluorescent molecular nuclear dyes have been widely used in cellular biology with potential applications in forensic, diagnostic and bioanalytical analysis.¹ Fluorophores that display enhanced fluorescence upon binding with DNA have been utilized in fluorescence microscopy as well as quantifying nucleic acids in gel electrophoresis and flow cytometry.² The binding interactions of external molecules with DNA often results in a significant change in their properties, which has an important impact on physiological functions.³ Thus, the binding mode is a crucial parameter for drugs targeted at DNA. DNA binding molecules interact with DNA through intercalation or groove binding as represented in Figure 3.1, respectively. Common effects of DNA intercalative drugs inhibit cell growth, cell transformation and cell death, which have applications as antitumor, antibacterial, and anti-parasitic agents.⁴ Another class of drugs interact with DNA through a groove binding mechanism. Several groove binding drugs act by interfering with cellular processes, which target enzyme and protein access to DNA.⁵ The mechanism of binding is key to the performance of both DNA-targeted therapies and

fluorescent probes. While basic design principles are proposed, the binding modes of many dyes cannot be unambiguously assigned based either on their structure, or through the use of many well-established spectroscopic techniques. Therefore, distinguishing between an intercalator and groove binder is critical for the design of DNA-targeted drugs and fluorescent probes.

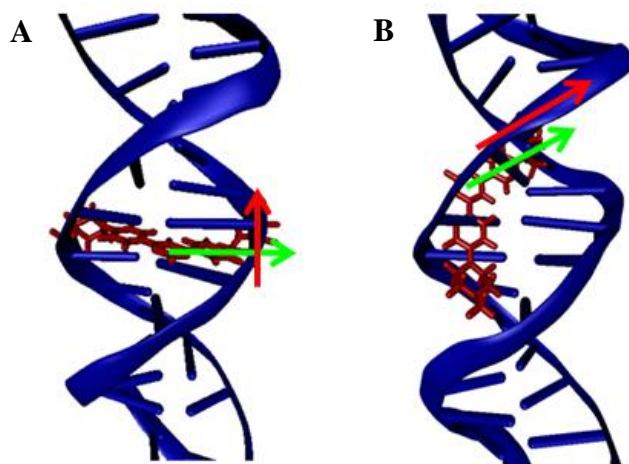


Figure 3.1. (A) Intercalative and (B) groove binding modes. Orientation of the $S_0 \rightarrow S_1$ transition dipole is shown in green. The DNA electric field is shown in red.

Qualitative methods have been employed to elucidate the binding modes of external molecules to DNA.³ However, a combination of select methods must be used to determine the DNA binding mode with certainty.⁶ New methodologies with high sensitivity are of interest to investigate the DNA binding modes. Nonlinear spectroscopy methods, such as TPA provide a powerful tool to examine the photophysical properties of fluorescent organic molecules in biological systems.⁷ Hence, TPA can be used with high sensitivity to understand the changes in the chromophore DNA binding environment, charge transfer character, and excited-dipoles.⁸ We present the first results of two-photon

spectroscopy to diagnose the DNA binding modes of small fluorescent molecules with calf thymus dsDNA (ctDNA). The change in the TPA cross-section was investigated to assess the binding mode based on the DNA electric field induced perturbation of the dye's transition dipole. A series of dyes (Figure 3.2) were investigated to demonstrate our methodology. These fluorophores illustrate a general scaffold for DNA binding dyes, which include linear, crescent, or planar structural motifs.

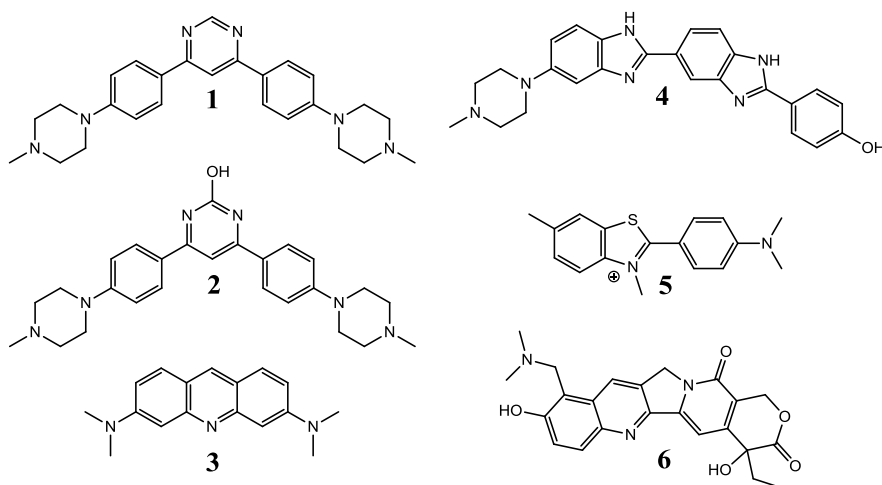
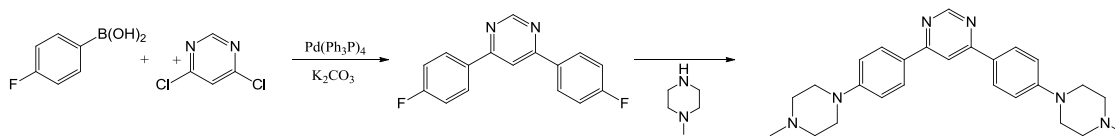


Figure 3.2. Chemical structures of 4,6-bis(4-(4-methylpiperazin-1-yl)phenyl) pyrimidine (**1**), 4,6-bis(4-(4-methylpiperazin-1-yl)phenyl) pyrimidin-2-ol (**2**), acridine orange (**3**), Hoechst 33258 (**4**), thioflavin t (**5**), and topotecan (**6**).

Reaction of 4,6-bis(4-fluorophenyl)pyrimidine⁹ with *N*-methylpiperazine by nucleophilic aromatic substitution afforded **1** with an overall yield of 41%. The reaction is shown in scheme 3.1. The Biginelli reaction of 4-(4-methyl-1-piperazinyl) benzaldehyde, 4-(4-methyl-1-piperazinyl) acetophenone and urea yielded **2**.¹⁰

Scheme 3.1. Synthesis of **1**.



It has been reported that the TPA cross-section of fluorophores can change in different environmental conditions. It has been shown that the local electric fields have an influence on the TPA cross-section.¹¹ The TPA cross-sections of triphenylamines with *N*-methyl benzimidazolium moiety terminated branched dyes have been investigated, and it was reported that the TPA cross-section enhances about 10-fold upon groove binding with DNA.^{12,40} We also present a TPA cross-section enhancement for the characterization of groove binding molecules similar to Dumat *et al.*¹² However, we attribute the TPA cross-section change due to the DNA electric field influence on the dipole of the binding molecule. Based on the orientation of the binding agent relative to the DNA helical axis, the change in the TPA cross-section is analyzed to determine the DNA binding mode. A groove binding molecule will have a dipole oriented more parallel to the DNA electric field resulting in an enhanced TPA cross-section upon binding. Contrarily, an intercalating agent will have a dipole aligned more perpendicular to the DNA electric field leading to a decreased TPA cross-section upon binding. A groove binding molecule will exhibit an increased induced dipole while an intercalating molecule will have a decreased induced dipole due to the DNA electric field perturbation. It is important to note that the TPA cross-sections are an ensemble average for the given system. This allows for the investigation of DNA-dye interactions at various DNA-to-dye ratios. Notably, this was observed for the intercalating dyes.

3.3 Experimental

Materials. All chemicals and solvents were obtained from commercial suppliers and used without further purification, unless otherwise indicated. Calf thymus DNA (ctDNA), [poly(dA-dT)]₂, [poly(dG-dC)]₂, and topotecan were purchased from Sigma Aldrich and used as received.

Sample Preparation. Stock solutions of the dye (500 μM) were prepared by dissolving in DMSO then sonicated for 15 min. Once prepared, the samples were stored in the absence of light at 25 °C. Samples were prepared in PBS (1X) by diluting the stock solution of dye. A stock solution of DNA (1000 μM) was prepared by dissolving the DNA in PBS (1X) for 24 h at 4 °C with occasional stirring prior to use. The DNA base pairs concentration of the polynucleotides were determined using molar extinction coefficients: $\epsilon_{260} = 13,500 \text{ M}^{-1} \text{ cm}^{-1}$ for ctDNA,¹³ $\epsilon_{262} = 6600 \text{ M}^{-1} \text{ cm}^{-1}$ for [poly(dA-dT)]₂,¹⁴ and $\epsilon_{254} = 8400 \text{ M}^{-1} \text{ cm}^{-1}$ for [poly(dG-dC)]₂.¹⁵ Once prepared, the nucleic acids were stored at 4 °C. Measurements were performed with [dye] = 5 μM. Topotecan-DNA complexes were prepared 72 hours and stored at 25 °C before optical measurements.

Quantum Yield Measurements. The fluorescence quantum yields were measured using the Williams comparative method. The optical density was measured below 0.10 to avoid reabsorption and internal filter effects. The absorption and fluorescence were measured for four samples with decreasing concentrations. The quantum yield was calculated using the following equation

$$\Phi_x = \Phi_{Std} \frac{Grad_x}{Grad_{Std}} \frac{\eta_x^2}{\eta_{Std}^2} \quad (2.16)$$

where Φ is the quantum yield, η is the refractive index of the solvent, and $Grad$ is the slope obtained from plotting the fluorescence versus absorbance. The quantum yields

were measured for **1** and **2** using Coumarin 307 ($\Phi = 0.56$)¹⁶ dissolved in methanol as the standard; **3** using Coumarin 153 ($\Phi = 0.54$)¹⁷ dissolved in methanol as the standard; **4**, **5**, and **6** using Coumarin 30 ($\Phi = 0.35$)¹⁸ dissolved in methanol as the standard. The quantum yields were measured at the maximum absorption for each complex. Extra precaution was taken when measuring the quantum yields as it can significantly influence the TPA cross-section.

Steady-State Measurements. Absorption spectra were measured on an Agilent 8341 spectrophotometer. Emission spectra were collected on a Fluoromax-2 fluorimeter with slits set at 3 nm and an integration time of 0.100 s. CD spectra were measured on an Aviv model 202 circular dichroism spectrometer using a wavelength step of 1 nm and a bandwidth of 1.0 nm. The CD scans were averaged with $n = 3$. Quartz cells with 10 mm path lengths were used for all measurements. All optical measurements were carried out at 25 °C.

Two-Photon Absorption (TPA). Two-photon spectroscopy was performed using a Kapteyn Murnane Laboratories diode-pumped mode-locked Ti:sapphire laser with pulses of ~30 fs. All emission scans were recorded at 800 nm excitation, scanning from 350 – 750 nm. TPA cross-sections were measured utilizing the two-photon excited fluorescence (TPEF) method.¹⁹ The input power from the laser was varied using a variable neutral density filter. The fluorescence was collected perpendicular to the incident beam. A focal-length plano-convex lens was used to direct the fluorescence into a monochromator whose output was coupled to a photomultiplier tube. A counting unit was used to convert the photons into counts. Coumarin 307 dissolved in methanol was used as a standard ($(\phi\delta)_{800\text{ nm}} = 15\text{ GM}$).¹⁹

Disadvantages of TPA. There are several drawbacks when using TPA. First, the quantum yield is required to calculate the TPA cross-section by the TPEF method. Inaccurate quantum yield measurements can significantly influence the TPA cross-section, therefore affecting the results. In order to measure the TPA cross-section accurately, the quantum yield must be measured with precaution. It is important to use proper technique and keep the optical density below 0.10 to avoid reabsorption and internal filter effects. The quantum yield and TPA measurements were conducted with three trials and averaged to give a TPA cross-section value. Another disadvantage of TPA is that it is a destructive technique since a high density of photons is required for two-photon excitation. It is important to monitor the degradation of the sample by measuring the absorption and fluorescence before and after the experiment. Sample degradation can be reduced by minimizing the output power used to excite the sample. Finally, the TPEF technique cannot be used if the sample does not display two-photon excited fluorescence. In this case, a nonlinear transmission method, such as Z-scan would have to be employed to measure the TPA cross-section. Measurements using the TPEF technique are more accurate and precise than nonlinear transmission techniques. When using a nonlinear transmission technique, there will be more variation in the TPA data. Such variations can be reduced by minimizing false nonlinear optical processes including thermal lensing as well as stimulated emission and scattering.²⁰

Synthesis. 4,6-Bis(4-fluorophenyl)pyrimidine²¹ (450 mg, 1.68 mmol), Cs₂CO₃ (1 g, 3.0 mmol), *N*-methylpiperazine (3.0 mL, 27.0 mmol) and 1.0 mL of DMSO were placed in a 15 mL pressure tube with a stir bar, then heated at 90 °C for 96 h. The progress of the reaction was monitored every 12 h by TLC until the 4,6-bis(4-

fluorophenyl)pyrimidine and mono-substituted product were completely consumed. The cooled, crude reaction mixture was poured into 100 mL of water, extracted with 3 x 50 mL of EtOAc and 1 x 50 mL of CH₂Cl₂. The organic fractions were combined with the solvents removed under reduced pressure; as the volume reduced, a yellow precipitate was observed. This was collected by filtration to yield 298 mg of **1** (41% yield). mp 468 - 472 °C (decomp.); IR ν_{max} (cm⁻¹): 2967.25, 2930.95, 2840.30, 27966.66, 1606.34, 1570.55, 1499.84, 1223.38, 816.92, 792.64; ¹H NMR (500 MHz, DMSO-*d*₆, TFA): δ 2.896 (s, 6H), 3.151 (broad s, 8H), 3.542 (broad s, 4H), 4.053 (broad s, 4H), 7.129-7.147 (d, 4H, *J* = 9 Hz), 8.262-8.280 (d, 4H, *J* = 9 Hz), 8.382 (s, 1H), 9.085 (s, 1H), 10.539 (broad s, 2H); ¹³C NMR (500 MHz, DMSO-*d*₆, TFA): δ 42.52, 45.01, 52.47, 110.22, 115.46, 117.73, 127.26, 128.95, 151.89, 163.18; HR-ESI (Q-TOF) *m/z*: calcd for C₁₅H₂₁N₂O₂⁺ [M+H]⁺ calcd 429.2761, found 429.2754.

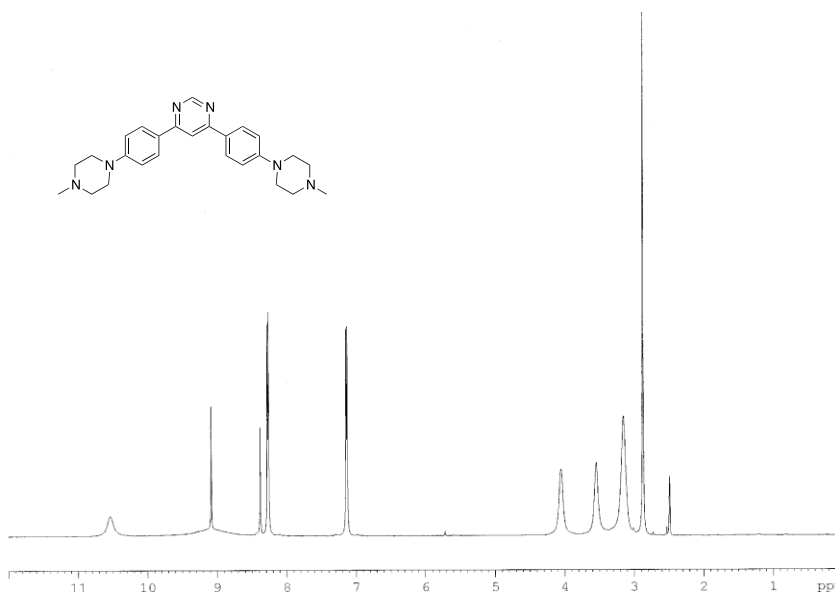


Figure 3.3. ¹H-NMR of **1**.

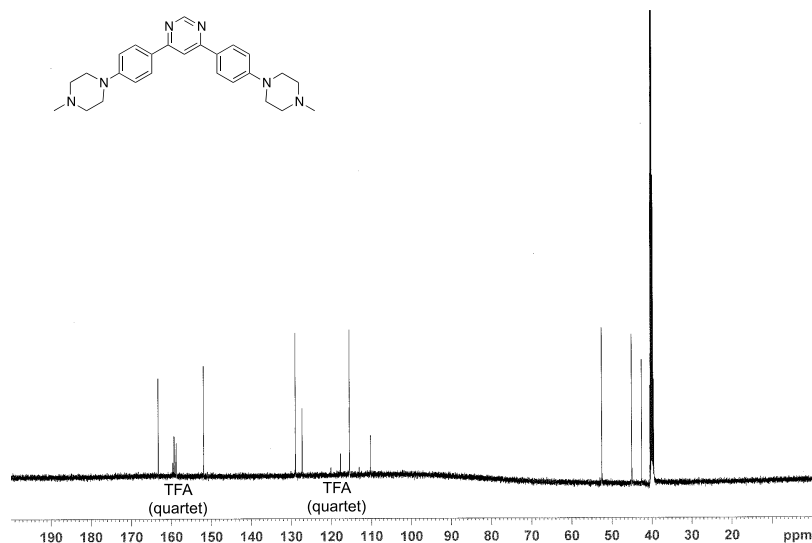


Figure 3.4. ^{13}C -NMR of **1**.

3.5 Results and Discussion

To demonstrate our methodology, acridine orange (**3**) and Hoechst 33258 (**4**) were used as standards. It is important to note that **3** has been reported as a DNA intercalator²⁴ and **4** has been reported as a DNA groove binder.²⁵ The steady-state absorption and emission are shown in Figure 3.5. The fluorescence quantum yield of the dyes is summarized in Table 3.1. A red-shift in the absorption spectra was noted as DNA concentration increased, which is due to the dye binding with DNA. The fluorescence increased 2.1 fold upon binding with DNA at 624 μM for **3**. The TPA cross-sections were measured utilizing the two-photon excited fluorescence (TPEF) method.²⁶ For **3** (Figure 3.6), a decrease in the TPA cross-section was observed as the DNA concentration was increased. This can be rationalized by the orientation of **3** upon intercalating to DNA. The dipole of **3** is oriented more perpendicular to the DNA electric field (parallel to the bases) leading to a reduction in the induced dipole. The decreasing trend is evident of a DNA

intercalative binding mode resulting in lengthening and unwinding of the DNA helix.⁶ Important driving factors for intercalation include π -stacking, dispersive interaction, dipole-dipole interaction, and electrostatic factors with the aromatic nucleobases in DNA.²⁷ The TPA cross-section was also measured in the presence of [poly(dG-dC)]₂. The results confirm that the decreasing TPA cross-section trend is directly related to **3** intercalating at GC base pairs. It was previously reported that **3** intercalates at GC-rich sequences,²⁸ which corresponds with our results. Interestingly, the TPA cross-section increased from 0.11 to 0.13 GM when the DNA concentration was increase to 4 μ M. This observation can be explained by the dye-dye interaction when DNA is introduced to the system, which was also observed at 7 μ M of DNA using CD.²⁹ The dyes form ordered aggregates at the surface of DNA resulting in an enhanced dipole, which influences the TPA cross-section.

Table 3.1. Fluorescence quantum yield of dyes at various DNA concentrations.

DNA (μ M)	1	2	3	4	5
0	0.009	0.003	0.29	0.012	0.29
2	0.029	0.008	0.31	0.018	0.24
4	0.034	0.017	0.30	0.045	0.24
7	0.048	0.033	0.47	0.082	0.23
14	0.087	0.052	0.41	0.14	0.23
32	0.19	0.11	0.42	0.30	0.21
63	0.28	0.18	0.51	0.41	0.22
125	0.37	0.25	0.66	0.46	0.22
250	0.44	0.30	0.73	0.47	0.22
624	0.47	0.36	0.66	0.45	0.21

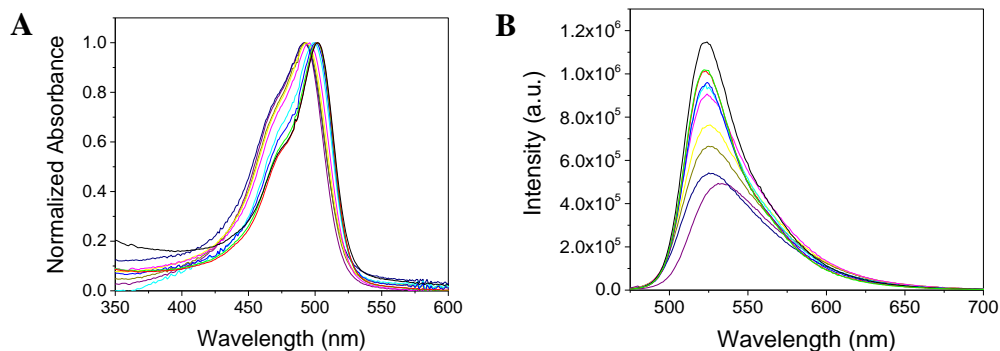


Figure 3.5. (A) Absorption and (B) emission spectra of **3**. Measurements were conducted at different DNA (base pairs) concentrations with units of μM (0, purple; 2, navy; 4, dark yellow; 7, yellow; 14, magenta; 32, cyan; 63, blue; 125, green; 250, red; 624, black).

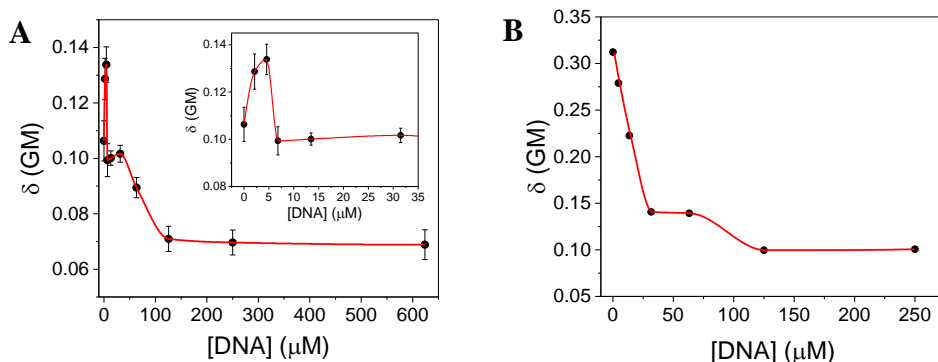


Figure 3.6. (A) TPA cross-section of **3** ($5 \mu\text{M}$) plotted as a function of DNA (base pairs) concentration. Inset graph: Enlargement at low DNA concentration. Results are the mean with \pm SD ($n = 3$). (B) TPA cross-section plotted in the presence of $[\text{poly}(\text{dG-dC})]_2$. The red line is to guide the eye.

As shown in Figure 3.7, the absorption and emission displayed shifts as the DNA concentration increased for **4**, which is due to the dye binding with DNA Presented in Figure 3.8, an increasing TPA cross-section trend was observed for **4** with increasing DNA concentrations. A TPA cross-section enhancement of 6.9-fold was observed upon binding with DNA. The dipole of **4** is oriented more parallel to the DNA electric field

when bound resulting in an enhanced TPA cross-section. The increasing trend indicates a DNA groove binding mode, which is characterized by little to no perturbation of the DNA structure.³⁰ Groove binding molecules require conformational flexibility that allows the molecule to fit into the groove and functional groups that interact with the nucleobases with minimal steric hinderance.³ Moreover, the TPA cross-section of **4** was measured in the presence of [poly(dA-dT)]₂. A TPA cross-section enhancement of 7.4 fold was observed upon binding at AT base pairs. The findings confirm the TPA cross-section enhancement is directly related to **4** groove binding at AT-rich sequences. **4** was reported to groove bind along the AT sequences while occupying four base pairs³¹ through van der Waals and hydrogen bonding interactions.³²

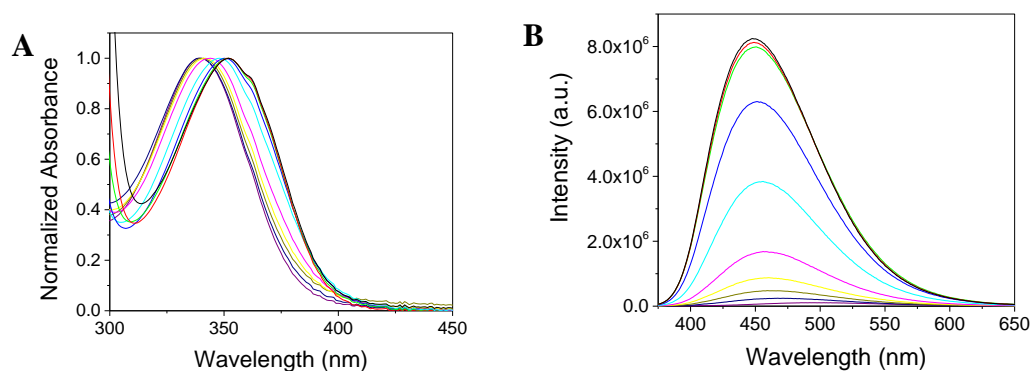


Figure 3.7. (A) Absorption and (B) emission spectra of **4**. Measurements were conducted at different DNA (base pairs) concentrations with units of μM (0, purple; 2, navy; 4, dark yellow; 7, yellow; 14, magenta; 32, cyan; 63, blue; 125, green; 250, red; 624, black).

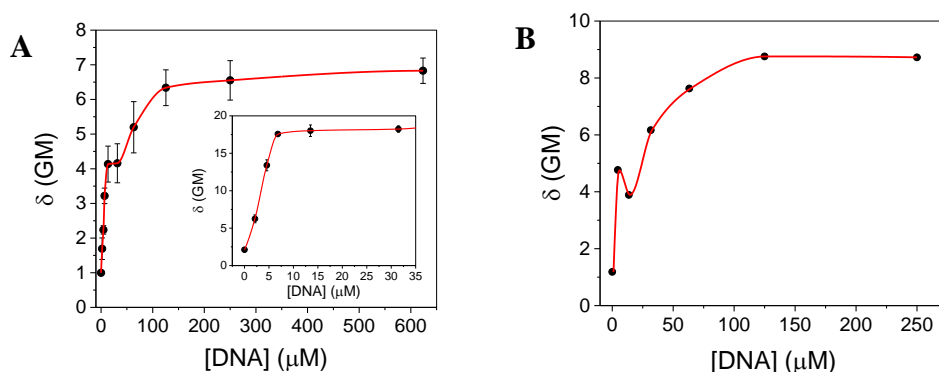


Figure 3.8. (A) TPA cross-section of **4** (5 μM) plotted as a function of DNA (base pairs) concentration. Inset graph: Enlargement at low DNA concentration. Results are the mean with \pm SD ($n = 3$). (B) TPA cross-section plotted in the presence of $[\text{poly}(\text{dA-dT})]_2$. The red line is to guide the eye.

CD measurements were applied to compare with the TPA analysis. Positive and negative induced circular dichroism (ICD) signals were observed near 480 nm and 465 nm, respectively for **3**. The CD spectra are shown in Figure 3.9. The positive band is due to the interaction between the transition dipoles of two or more ordered dyes and reduces when DNA concentrations are increased.²⁹ The negative ICD signal near 465 nm is attributed to the intercalated dye.³³ Contrarily, a strong positive ICD signal was observed at approximately 360 nm for the interaction of **4** with DNA (see Supporting Information). The positive band is attributed to **4** groove binding with DNA³⁴ as presented in Figure 3.9B.

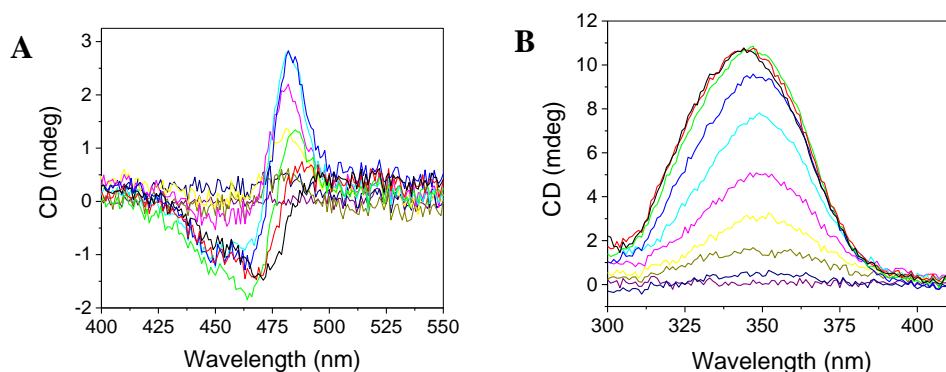


Figure 3.9. CD spectra of (A) **3** and (B) **4** at different DNA concentrations. Measurements were conducted at different DNA (base pairs) concentrations with units of μM (0, purple; 2, navy; 4, dark yellow; 7, yellow; 14, magenta; 32, cyan; 63, blue; 125, green; 250, red; 624, black).

TPA was employed to study the binding mode of thioflavin t (**5**). It was previously reported that **5** intercalates with dsDNA.³⁵ **5** undergoes a twisted internal charge-transfer (TICT), which is responsible for the quenched fluorescence in the absence of DNA. When bound with DNA, the internal rotation of the dye is restricted due to steric hindrance resulting in enhanced fluorescence.³⁶ Presented in Figure 3.10, the decreasing trend is indicative of an intercalative binding mode. This suggests the dipole of **5** is oriented more perpendicular with the DNA electric field upon binding. **5** had a TPA cross-section of 40.0 GM in the absence of DNA. The TPA cross-section decreased to 11.4 GM at 624 μM of DNA. The decrease in the TPA cross-section can be attributed to the DNA electric field induced perturbation of the dye's transition dipole rather than the conformational change of the dye upon intercalation since **1**, **2**, and **4** undergo a conformational change upon groove binding. Similar to **3**, the TPA cross-section increased at low DNA concentrations. The TPA cross-section increased to 53.7 GM at 4 μM of DNA, which can be attributed to the formation of dimers that bind at the DNA

grooves under excess dye conditions.³⁷ Furthermore, CD was used to compare with the TPA experiments. However, an ICD signal was not detected at our experimental conditions. This demonstrates TPA is more sensitive at low dye concentrations as compared to CD. Bathochromic shifts of 8 and 48 nm were observed in the absorption and emission spectra, respectively at 624 μM of DNA indicating the dye is bound with DNA as presented in Figure 3.11.

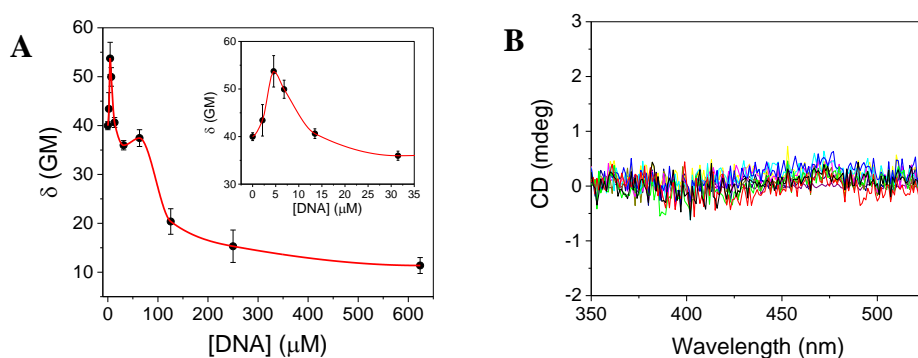


Figure 3.10. (A) TPA cross-section of **5** (5 μM) plotted as a function of DNA (base pairs) concentration. Inset graph: Enlargement at low DNA concentration. Results are the mean with \pm SD ($n = 3$). The red line is to guide the eye. (B) CD spectra of **5** at different DNA concentrations. Measurements were conducted at different DNA (base pairs) concentrations with units of μM (0, purple; 2, navy; 4, dark yellow; 7, yellow; 14, magenta; 32, cyan; 63, blue; 125, green; 250, red; 624, black).

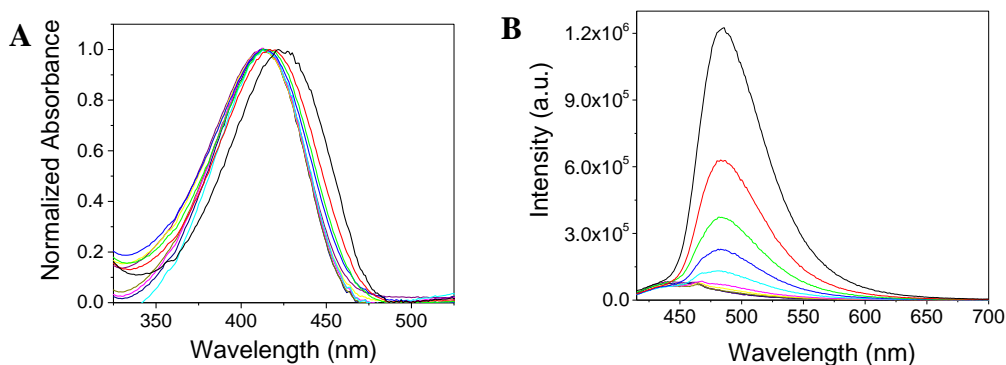


Figure 3.11. (A) Absorption and (B) emission spectra of **5** at different DNA concentrations. Measurements were conducted at different DNA (base pairs) concentrations with units of μM (0, purple; 2, navy; 4, dark yellow; 7, yellow; 14, magenta; 32, cyan; 63, blue; 125, green; 250, red; 624, black).

The binding mode of topotecan (**6**), a clinically approved anti-cancer drug, was investigated using TPA. There has been controversy regarding the binding mode of **6**. The binding mechanism is of interest because therapeutic importance can be improved. Yang *et al.* reported an intercalating binding mode in the absence of topoisomerase I.³⁸ However, Streltsov *et al.*³⁹ and Joshi *et al.*⁴⁰ concluded **6** binds to DNA through a groove binding mechanism. Our TPA analysis suggests **6** groove binds with DNA as shown in Figure 3.13. The TPA cross-section enhancement can be attributed to **6** groove binding at GC-rich sequences.^{38,40} Quenching in the steady-emission was noted as presented in Figure 3.12. This can be ascribed to the photoinduced electron transfer (PET) between the drug and DNA nucleobases.³¹ A TPA cross-section enhancement of 1.5-fold was observed upon binding with DNA. This can be attributed to the orientation of the binding agent relative to the DNA helical axis. **6** was reported to be oriented nearly 55° to the DNA helical axis, which is approximate to a groove binder (<55°), but less than a classical intercalator (62-76°).^{38,40} Comparatively, **4** had a TPA cross-section enhancement of 6.9-fold with a 45° angle of orientation.⁴¹ The difference in the TPA cross-section enhancement at low and high DNA concentrations can be attributed to the DNA electric field induced enhancement of the transition dipole. The low TPA cross-section enhancement suggests the binding angle of topotecan is between an intercalator and groove binder. A larger TPA cross-section enhancement is expected if the dipole of the binding molecule is oriented more parallel with the DNA electric field. Interestingly, an ICD signal was not detected at our experimental conditions of 5 μM. This indicates that our approach is more sensitive at both low DNA and drug concentration.

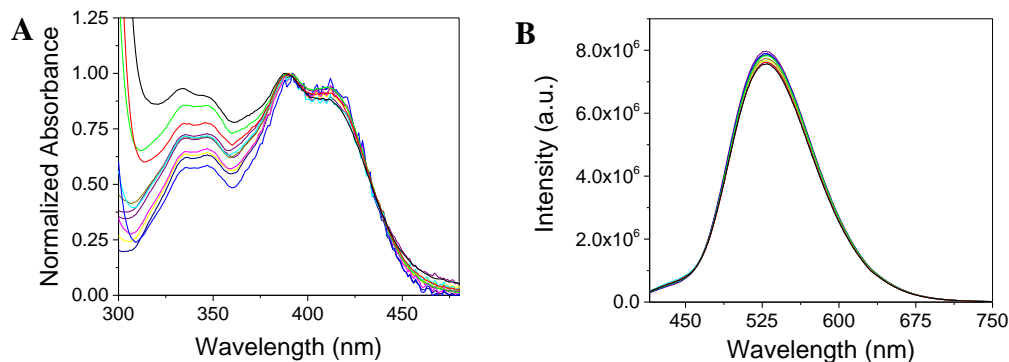


Figure 3.12. (A) Absorption and (B) emission spectra of **6**. Measurements were conducted at different DNA (base pairs) concentrations with units of μM (0, purple; 2, navy; 4, dark yellow; 7, yellow; 14, magenta; 32, cyan; 63, blue; 125, green; 250, red; 624, black).

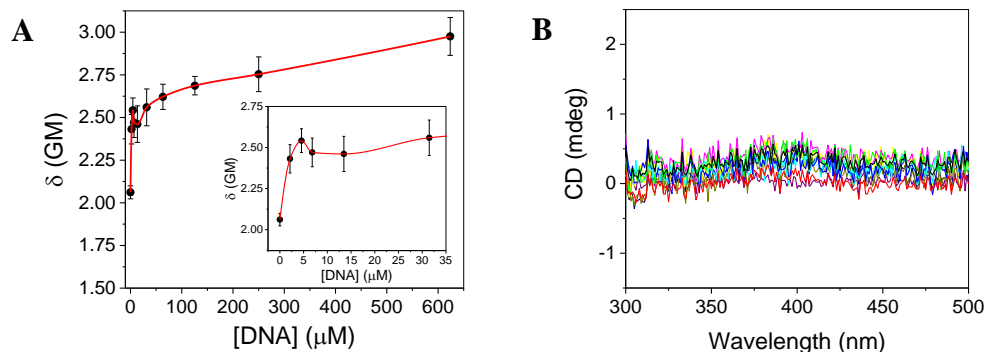


Figure 3.13. (A) TPA cross-section of **6** ($5 \mu\text{M}$) plotted as a function of DNA (base pairs) concentration. Inset graph: Enlargement at low DNA concentration. Results are the mean with \pm SD ($n = 3$). The red line is to guide the eye. (B) CD spectra of **6** at different DNA concentrations. Measurements were conducted at different DNA (base pairs) concentrations with units of μM (0, purple; 2, navy; 4, dark yellow; 7, yellow; 14, magenta; 32, cyan; 63, blue; 125, green; 250, red; 624, black).

The binding mode of **1** was investigated. Shown in Figure 3.14, a red-shift was observed in the absorption spectra whereas the fluorescence increased with increasing DNA concentrations suggesting that the dye is binding with DNA. Furthermore, the binding mode was studied utilizing TPA and CD. The TPA cross-section of the unbound

dye was 2.1 GM. Shown in Figure 3.15, the TPA cross-section increased to 28.7 GM at 624 μM of DNA. A significant TPA cross-section enhancement of 13.6-fold was observed upon binding with DNA, which was the largest enhancement noted. The TPA cross-section enhancement suggests **1** undergoes a groove binding mechanism in the presence of DNA. The crescent shape of **1** allows the molecule to groove bind at AT-rich sequences. Furthermore, CD was used to investigate the system. **1** exhibits a positive ICD signal near 370 nm in the presence of DNA, which is consistent of a groove binding mode (Figure 5B). The positive band corresponds to the $S_0 \rightarrow S_1$ transition, which suggests the transition dipole of **1** is oriented along the groove.⁴² Interestingly, a weak negative band is observed near 325 nm at 32 μM of DNA or greater. The bisignate ICD signal is attributed to the formation of dimers at the surface or in the groove of DNA.⁴³ In agreement with CD, the TPA cross-section enhancement indicates the transition dipole of **1** is oriented more parallel to the DNA electric field.

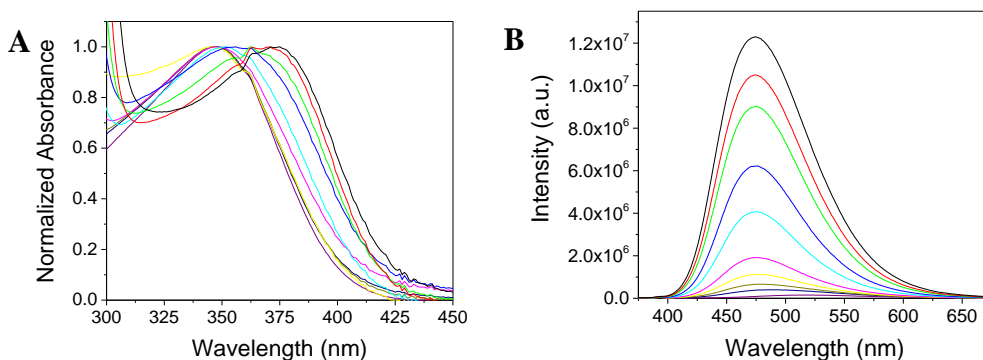


Figure 3.14. (A) Absorption and (B) emission spectra of **1**. Measurements were conducted at different DNA (base pairs) concentrations with units of μM (0, purple; 2, navy; 4, dark yellow; 7, yellow; 14, magenta; 32, cyan; 63, blue; 125, green; 250, red; 624, black).

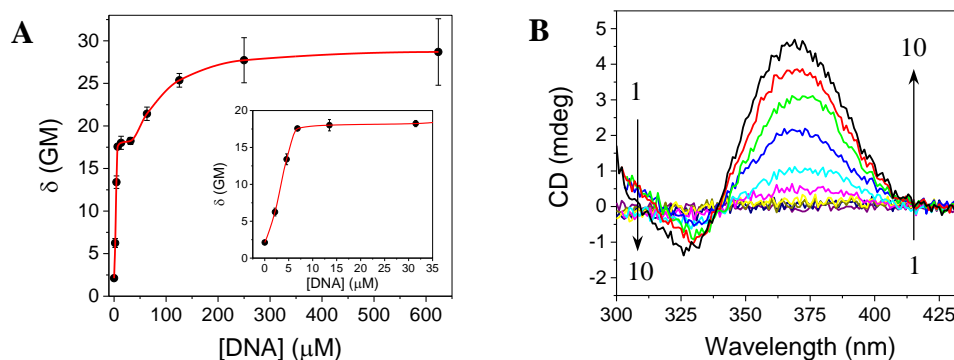


Figure 3.15. (A) TPA cross-section of **1** (5 μM) plotted as a function of DNA (base pairs) concentration. Inset graph: Enlargement at low DNA concentration. Results are the mean with \pm SD ($n = 3$). The red line is to guide the eye. (B) CD spectra at different DNA concentrations. 1 \rightarrow 10 represents DNA (base pairs) concentrations 0, 2, 4, 7, 14, 32, 63, 125, 250, 624 μM , respectively.

The binding mode of **2** was examined. The steady-state absorption and emission spectra are shown in Figure 3.16. As expected, a red-shift in the absorption and emission spectra was noted as the DNA concentration increased indicating the dye is binding with DNA. Moreover, TPA and CD were used to investigate the binding interactions. Presented in Figure 3.17A, the TPA cross-section is plotted as a function of DNA concentration. The TPA cross-section increased from 3.4 to 14.0 GM from 0 to 624 μM of DNA. A TPA cross-section enhancement of 4.1-fold was observed. Comparing with **1**, this suggests a larger TPA cross-section enhancement is observed when a less electron withdrawing central core is incorporated into the donor-acceptor-donor π -system. In addition, the hydroxyl substituent from **2** may interact with the DNA nucleobases and surrounding water molecules resulting in a lower TPA cross-section enhancement.⁴⁴ The increasing trend suggests **2** interacts with DNA though a groove binding mechanism. Moreover, CD was used to examine the binding mode of **2** (Figure 3.17B). A positive ICD signal was recorded in the presence of DNA near 400 nm, which corresponds to the

$S_0 \rightarrow S_1$ transition. The negative band at approximately 350 nm corresponds to the $S_0 \rightarrow S_2$ transition. **2** was previously reported to groove bind with DNA using linear dichroism (LD),¹⁰ which agrees with the TPA analysis. Additionally, it was shown that **2** interacts with DNA through hydrogen bonding interactions at the AT base pairs, occupying three base pairs. However, the fluorescence is nearly quenched from GC sequences, which is most likely due to PET from guanine to the excited chromophore.⁴⁵

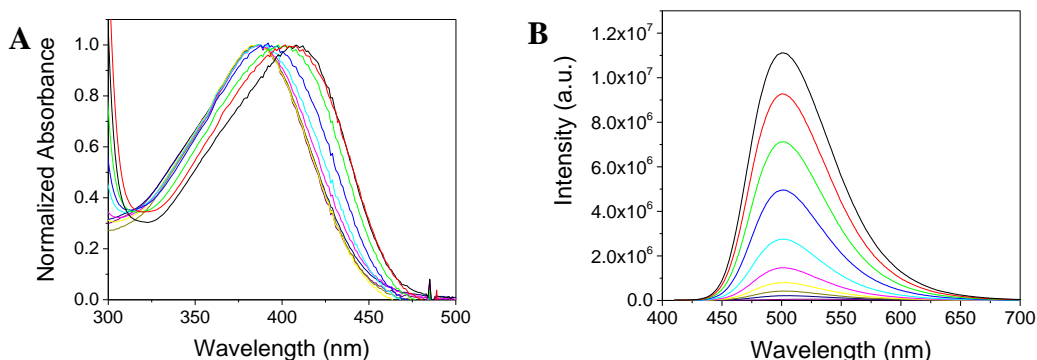


Figure 3.16. (A) Absorption and (B) emission spectra of **2**. Measurements were conducted at different DNA (base pairs) concentrations with units of μM (0, purple; 2, navy; 4, dark yellow; 7, yellow; 14, magenta; 32, cyan; 63, blue; 125, green; 250, red; 624, black).

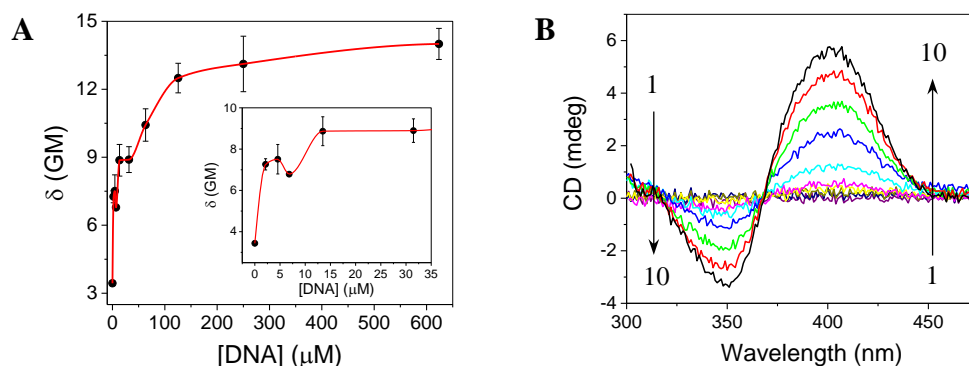


Figure 3.17. (A) TPA cross-section of **2** ($5 \mu\text{M}$) plotted as a function of DNA (base pairs) concentration. Inset graph: Enlargement at low DNA concentration. Results are the mean with \pm SD ($n = 3$). The red line is to guide the eye. (B) CD spectra at different DNA concentrations. 1 \rightarrow 10 represents DNA (base pairs) concentrations 0, 2, 4, 7, 14, 32, 63, 125, 250, 624 μM , respectively.

A direct comparison of TPA and CD demonstrates superior sensitivity compared to CD. It is important to note an ICD signal was not observed for **5** and **6**, however a change was detected utilizing TPA. This indicates our method has superior sensitivity at low dye and DNA concentrations. Moreover, an ICD signal was not observed at DNA concentrations less than 7 μM for **1** – **3**. However, an ICD signal was detected at 4 μM of DNA for **4**. TPA detected a significant environmental change in the presence of 2 μM of DNA for all compounds, which demonstrates the methodology has potential use at biologically relevant concentrations while avoiding problems with background absorption of common buffers.⁴⁶ For example, the TPA cross-section increased from 2.1 to 6.2 GM when DNA concentrations were increased to 2 μM for **1**. The findings are significant as it suggests two-photon spectroscopy can provide detail information at dilute concentrations of DNA and differentiate between the DNA binding modes of external molecules, which are inaccessible with single-photon excited fluorescence. Furthermore, two-photon excitation microscopy (TPEM) can be used for cellular studies. Since the TPA process is quadratically intensity dependent, TPEM can provide superior spatial resolution with reduced photobleaching and photodamage as well as autofluorescence for bioimaging at low concentrations.

3.6 Conclusion

In summary, we developed a new highly sensitive methodology to diagnose the DNA binding mode of external molecules. This report is the first example that applied TPA cross-section changes to determine the DNA binding mode of fluorescent nuclear dyes and DNA-targeted drugs. The TPA cross-sections of intercalating and groove binding

dyes are influenced by the electric field of the DNA backbone upon binding. An increasing trend is indicative of a groove binding mode while a decreasing trend suggests an intercalative binding mode. Moreover, a comparison of our TPA studies with CD demonstrates TPA exhibits superior sensitivity at DNA concentrations of 4 μM and lower by more than an order of magnitude. This work may facilitate the biological studies of DNA interactions with other external molecules as well as applications for bioimaging.

References

1. Wang, J. *Nucleic Acids Res.* **2008**, *28*, 3011.
2. Benveniste, A. L.; Creeger, Y.; Fisher, G. W.; Ballou, B.; Waggoner, A. S.; Armitage, B. A. *J. Am. Chem. Soc.* **2007**, *129*, 2025.
3. Ihmels, H.; Otto, D. *Top. Curr. Chem.* **2005**, *258*, 161.
4. Berman, H. M.; Young, P. R. *Ann. Rev. Biophys. Bioeng.* **1981**, *10*, 87.
5. Mukherjee, A.; Lavery, R.; Bagchi, B.; Hynes, J. T. *J. Am. Chem. Soc.* **2008**, *130*, 9747.
6. Suh, D.; Chaires, J. B. *Bioorg. Med. Chem.* **1995**, *3*, 723.
7. (a) Clark, T. B.; Ziolkowski, M.; Schatz, G. C.; Goodson III, T. *J. Phys. Chem. B* **2014**, *118*, 2351. (b) Bhaskar, A.; Ramakrishna, G.; Haley, M. M.; Goodson III, T. *J. Am. Chem. Soc.* **2006**, *128*, 13972. (c) McLean, A. M.; Socher, E.; Varnavski, O.; Clark, T. B.; Imperiali, B.; Goodson III, T. *J. Phys. Chem. B* **2013**, *117*, 15935. (d) Wang, Y.; Clark, T. B.; Goodson, T. *J. Phys. Chem. B* **2010**, *114*, 7112.

8. (a) Wang, Y.; He, G. S.; Prasad, P. N.; Goodson, T. *J. Am. Chem. Soc.* **2005**, *127*, 10128. (b) Flynn, D. C.; Ramakrishna, G.; Yang, H. B.; Northrop, B. H.; Stang, P. J.; Goodson III, T. *J. Am. Chem. Soc.* **2010**, *132*, 1348.
9. (a) Wheelhouse, R. T.; Jennings, S. A.; Phillips, V. A.; Pletsas, D.; Murphy, P. M.; Garbett, N. C.; Chaires, J. B.; Jenkins, T. C. *J. Med. Chem.* **2006**, *49*, 5187. (b) Qing, F.-L.; Wang, R.; Li, B.; Zheng, X.; Meng, W.-D. *J. Fluorine Chem.* **2003**, *120*, 21.
10. Pitter, D. R.; Wigenius, J.; Brown, A. S.; Baker, J. D.; Westerlund, F.; Wilson, J. N. *Org. Lett.* **2013**, *15*, 1330.
11. (a) Drobizhev, M.; Makarov, N. S.; Tillo, S. E.; Hughes, T. E.; Rebane, A. *Nat. Methods* **2011**, *8*, 393. (b) Drobizhev, M.; Tillo, S.; Makarov, N. S.; Hughes, T. E.; Rebane, A. *J. Phys. Chem. B* **2009**, *113*, 12860. (c) Bairu, S.; Ramakrishna, G. *J. Phys. Chem. B* **2013**, *117*, 10484.
12. Dumat, B.; Bordeau, G.; Faurel-Paul, E.; Mahuteau-Betzer, F.; Saettel, N.; Metge, G.; Fiorini-Debuisschert, C.; Charra, F.; Teulade-Fichou, M.-P. *J. Am. Chem. Soc.* **2013**, *135*, 12697.
13. Malak, H.; Castellano, F. N.; Gryczynski, I.; Lakowicz, J. R. *Biophys. Chem.* **1997**, *67*, 35.
14. Inman, R. B.; Baldwin, R. L. *J. Mol. Biol.* **1962**, *5*, 172.
15. Wells, R. D.; Larson, J. E.; Grant, R. C.; Shortle, B. E.; Cantor, C. E. *J. Mol. Biol.* **1970**, *54*, 465.
16. Reynolds, G. A.; Drexhage, K. H. *Opt. Comm.* **1975**, *13*, 222.
17. Rurack, K.; Spieles, M. *Anal. Chem.* **2011**, *83*, 1232.

18. Jones II, G.; Jackson, W. R.; Choi, C.; Bergmark, W. R. *J. Phys. Chem.* **1985**, *89*, 294.
19. Xu, C.; Webb, W. W. *J. Opt. Soc. Am. B* **1996**, *13*, 481.
20. Oulianov, D. A.; Tomov, I. V.; Dvornikov, A. S.; Rentzepis, P. M. *Opt. Commun.* **2001**, 191, 235.
21. (a) Wheelhouse, R. T.; Jennings, S. A.; Phillips, V. A.; Pletsas, D.; Murphy, P. M.; Garbett, N. C.; Chaires, J. B.; Jenkins, T. C. *J. Med. Chem.* **2006**, *49*, 5187.
(b) Qing, F.-L.; Wang, R.; Li, B.; Zheng, X.; Meng, W.-D. *J. Fluorine Chem.* **2003**, *120*, 21.
22. (a) Takashima, S. *J. Mol. Bio.* **1963**, *7*, 455. (b) Saxena, V. K.; Van Zandt, L. L. *Phys. Rev. A* **1992**, *45*, 7610.
23. (a) Stigter, D. *Biophys. Chem.* **2002**, *101*, 447. (b) Stigter, D.; Bustamante, C. *Biophys. J.* **1998**, *75*, 1197. (c) Ferree, S.; Blanch, H. W. *Biophys. J.* **2003**, *85*, 2539.
24. Armstrong, R. W.; Kurucsev, T.; Strauss, U. P. *J. Am. Chem. Soc.* **1970**, *92*, 3174.
25. Furse, K. E., Corcelli, S. A. *J. Am. Chem. Soc.* **2008**, *130*, 13103.
26. Xu, C.; Webb, W. *J. Opt. Soc. Am. B* **1996**, *13*, 481.
27. Reynisson, J.; Schuster, G. B.; Howerton, S. B.; Williams, L. D.; Barnett, R. N.; Cleveland, C. L.; Landman, U.; Harrit, N.; Chaires, J. B. *J. Am. Chem. Soc.* **2003**, *125*, 2072.
28. Nafisi, S.; Saboury, A. A.; Keramat, N.; Neault, J. F.; Tajmir-Riahi, H. A. *J. Mol. Struct.* **2007**, *827*, 35.
29. Zama, M.; Ichimura, S. *Biopolymers* **1970**, *9*, 53.

30. Mallena, S.; Lee, M. P.; Bailly, C.; Neidle, S.; Kumar, A.; Boykin, D. W.; Wilson, W. D. *J. Am. Chem. Soc.* **2004**, *126*, 13659.
31. Fornander, L. H.; Wu, L.; Billeter, M.; Lincoln, P.; Nordén, B. *J. Phys. Chem. B* **2013**, *117*, 5820.
32. Wan, K. X.; Shibue, T.; Gross, M. L. *J. Am. Chem. Soc.* **2000**, *122*, 300.
33. Mason, S. F., McCaffery, A. J. *Nature* **1964**, *204*, 468.
34. Willis, B.; Arya, D. P. *Biochemistry* **2006**, *45*, 10217.
35. (a) Cañete, M.; Villanueva, A.; Juarranz, A.; Stockert, J. C. *Cell Mol. Biol.* **1987**, *33*, 191. (b) Zsila, F. *Int. J. Biol. Macromol.* **2015**, *72*, 1034. (c) Murudkar, S.; Mora, A. K.; Jakka, S.; Singh, P. K.; Nath, S. *J. Photoch. Photobio. A* **2014**, *295*, 17.
36. Stsiapura, V. I.; Maskevich, A. A.; Kuzmitsky, V. A.; Turoverov, K. K.; Kuznetsova, I. M. *J. Phys. Chem. A*, **2007**, *111*, 4829.
37. Biancardi, A.; Biver, T.; Burgalassi, A.; Mattonai, M.; Secco, F.; Venturini, M. *Phys. Chem. Chem. Phys.* **2014**, *16*, 20061.
38. Yang, D.; Strode, J. T.; Spielmann, H. P.; Wang, A. H. J.; Burke, T. G. *J. Am. Chem. Soc.* **1998**, *120*, 2979.
39. Streltsov, S.; Sukhanova, A.; Mikheikin, A.; Grokhovsky, A.; Zhuze, A.; Kudelina, I.; Mochalov, L.; Oleinikov, V.; Jardillier, J.-C.; Nabiev, I. *J. Phys. Chem. B* **2001**, *105*, 9643.
40. Joshi, H.; Sengupta, A.; Gavvala, K.; Hazra, P. *RSC Adv.* **2014**, *4*, 1015.
41. Moon, J. H.; Kim, S. K.; Sehlstedt, U.; Rodger, A.; Norden, B. *Biopolymers* **1996**, *38*, 593.

42. Wilson, W. D.; Tanious, F. A.; Ding, D.; Kumar, A.; Boykin, D. W.; Colson, P.; Houssier, C.; Bailly, C. *J. Am. Chem. Soc.* **1998**, *120*, 10310.
43. Seifert, J.; Connor, R.; Kushon, S. A.; Wang, M.; Armitage, B. A. *J. Am. Chem. Soc.* **1999**, *121*, 2987.
44. Liu, Z.; Shao, P.; Huang, Z., Liu; B., Chen, T.; Qin, J. *Chem. Commun.* **2008**, *19*, 2260.
45. Wilson, J. N.; Wigenius, J.; Pitter, D. R.; Qiu, Y.; Abrahamsson, M.; Westerlund, F. *J. Phys. Chem. B* **2013**, *117*, 12000.
46. Greenfield, N. J. *Nat. Protoc.* **2007**, *1*, 2876.

Chapter 4

A New Design Strategy to Tailor the DNA-Binding Mechanism of Small Organic Molecules and Drugs

4.1 Original Publication Information

A majority of this chapter was published as the following document:

Doan, P.; Pitter, D.; Kocher, A.; Wilson, J. N.; Goodson III, T. “A New Design Strategy to Tailor the DNA-Binding Mechanism of Small Organic Molecules and Drugs”

Modifications were made to the original document to adapt the context to this form.

The manuscript has been submitted to *Nature Chemistry*.

4.2 Abstract

The classical model for DNA groove binding molecules states that groove binding molecules should adopt a crescent shape that closely matches the helical groove of DNA. We present a new design strategy that does not obey this classical model. The DNA-binding mechanism was investigated by synthesizing and examining a series of novel fluorescent nuclear dyes as fluorescent probes for the detection of nucleic acids. This study has led to the emergence of structure-property relationships of DNA-binding molecules that possess a crescent or V-shaped donor-acceptor-donor motif. The findings

reveal that the structure of these fluorophores can be designed to either intercalate or groove bind with calf thymus dsDNA by structurally modifying the electron accepting properties of the central heterocyclic accepting core. This is the first example that has demonstrated an induced change in the DNA-binding mode for crescent shaped DNA-binding molecules. Moreover, the results indicate that increasing conjugation length between the electron donating arms and electron accepting core does not induce a change in the DNA-binding mode. This suggests that the electron accepting properties of the central heterocyclic core is the key factor in the DNA-binding mechanism. The fluorophores were characterized by steady-state and ultrafast nonlinear spectroscopies as well as electronic structure calculations. The fluorophores are nearly quenched in buffered aqueous solution, however, display a high degree of turn on/off sensitivity upon DNA binding with a fluorescence enhancement of up to 74-fold as well as a Stokes shift of up to 9320 cm^{-1} . Furthermore, these fluorophores exhibit a two-photon absorption (TPA) cross-section enhancement of up to 13.6-fold upon binding with DNA. Bio-imaging experiments were carried out in live HeLa cells to evaluate the performance of these fluorophores utilizing two-photon excited fluorescence confocal microscopy. This report represents a new strategy for the design and development of therapeutics aimed at DNA.

4.3 Introduction

Fluorophores are valuable in many fields including, nanoscience, biochemistry, and energy conversion.¹ Fluorescent nuclear dyes have become important tools in cellular biology as well as for the detection and characterization of nucleic acids. Additionally,

fluorescent nuclear dyes have been widely employed in flow cytometry,² cellular imaging, and the quantification of nucleic acids in gel electrophoresis.³ Fluorophores that can be used for DNA quantification offer several advantages. For example, fluorescent detection of DNA is approximately 100 to 1000 times more sensitive than traditional absorption techniques.⁴ Moreover, fluorescent nuclear dyes are not generally affected by contaminants, such as proteins and enzymes. Fluorophores that display enhanced fluorescence upon binding with DNA are of considerable interest. However, there remains limitations with several commercially available fluorescent dyes used for imaging and detection purposes including Hoechst 33242 and 4',6-diamidino-2-phenylindole (DAPI). These limitations include insufficient photostability, high energy excitation wavelengths, and poor water solubility that lead to the formation of non-fluorescent aggregates.^{2,5,6,7} Furthermore, there are drawbacks with fluorescent nuclear dyes that possess low cell permeability and high toxicity.^{8,9}

Small organic DNA-binding molecules can interact with DNA predominately through an intercalating or groove binding mechanism.¹⁰ In general, intercalating molecules have planar aromatic rings incorporated into the structure that bind with DNA by inserting between the DNA nucleobases to form a binding pocket. Lengthening, unwinding, and distortion of the DNA helical axis are most prominent upon intercalation,¹¹ which requires important driving factors, such as π -stacking, dipole-dipole interaction, electrostatic factors, and dispersive interaction with the aromatic nucleobases in DNA.¹² On the other hand, groove binding is characterized by little to no perturbation in the DNA structure. Groove binding molecules generally contain unfused-aromatic structures with terminal basic functions.¹³ Additionally, groove binding molecules require

conformational flexibility that allows the molecule to fit into the DNA groove and functional groups that interact with the nucleobases through H-bonding and/or van der Waals interactions with minimal steric hinderance.¹⁰ Groove depth, groove width, electrostatic potential, and floor functionality are structural features found to be critical for groove binding recognition.¹⁴ The DNA-binding interactions of small organic molecules can provide valuable information towards the development of highly sensitive probes for DNA detection as well as the means for the design of therapeutics targeted at DNA. For example, common effects of DNA intercalative drugs inhibit cell growth, cell transformation, and cell death, which have applications as antitumor, antibacterial, and anti-parasitic agents¹⁵ while common effects of groove binding drugs interfere with cellular processes by targeting enzyme and protein access to DNA.¹⁶ Hence, structure-property relationships are of considerable interest to guide in the design of small organic molecules in which the DNA-binding mechanism can be modified and tailored. These relationships will contribute to the development of therapeutics aimed at DNA.

Several common methods have been employed to examine the DNA-binding interactions of small organic molecules including circular dichroism. However, these techniques cannot provide information accessible with ultrafast nonlinear spectroscopy. Therefore, ultrafast nonlinear spectroscopy has been widely utilized to investigate structure-property relationships of organic molecules.¹⁷⁻¹⁹ Additionally, two-photon excited fluorescence (TPEF) has been used to study the fundamentals of the excited state as well as correlating structure-function relationships.²⁰⁻²⁴ As a result, two-photon spectroscopy has been increasingly utilized as a tool for investigating environmental changes, charge transfer character, and application towards fluorescence imaging.²⁵

Furthermore, ultrafast time-resolved spectroscopy has been employed to study the photophysical properties of fluorescent organic molecules in biological systems.^{26–29} Thus, ultrafast nonlinear spectroscopy provides a power tool to develop structure-property relationships of small organic DNA-binding molecules.

In this article, we report the first design strategy for DNA-binding molecules that possess a crescent or V-shaped donor-acceptor-donor motif in which the DNA-binding mode can be tailored. According to the classical model for DNA binding, molecules that adopt a crescent or curved scaffold can groove bind with DNA because the complex can closely fit or match the groove of the DNA helix.³⁰ The combined approach utilizing ultrafast nonlinear and steady-state spectroscopies along with electronic structure calculations were employed to examine the structure-property relationships of these fluorophores. Herein, the results reveal that an induced change in the DNA-binding mode can be achieved by modifying the electron accepting properties of the central heterocyclic core of the fluorophore. Altering conjugation length between the electron donating arms and electron accepting core did not induce a change in the DNA-binding mode, suggesting that the central heterocyclic core plays an important role in the DNA-binding mechanism. The impact of this work is significant as the design strategy can be applied towards the development of therapeutics targeted at DNA.

4.4 Experimental

Materials. Chemicals and solvents were obtained from commercial suppliers and used without further purification, unless otherwise indicated. HeLa cells (CCL-2) were purchased from ATCC and used as received. Fetal bovine serum (FBS),

penicillin/streptomycin (10,000 U/ml), and Live Cell Imaging Solution were provided by Life Technologies. Dulbecco's Modified Eagle Medium (DMEM) was supplied by Corning. Calf thymus dsDNA was purchased from Sigma Aldrich. A stock solution of calf thymus dsDNA (1 mM) was prepared by dissolving DNA in PBS (1X) for 24 h at 4 °C with occasional stirring prior to use. A stock solution of fluorophore (500 μM) was constructed in DMSO. Samples were prepared in PBS (1X) by diluting the stock solution. Measurements for the DNA system were performed with [fluorophore] = 5 μM and [DNA] = 100 μM, unless otherwise indicated.

Synthesis. **1** and **5** were synthesized previously.³¹ Reaction of 4,6-bis(4-fluorophenyl)pyrimidine^{32,33} with *N*-methylpiperazine by nucleophilic aromatic substitution afforded **4** with an experimental yield of 41%.³⁴ **2**, **3**, **6**, and **7** were synthesized elsewhere.³⁵

Synthesis of [2-[2,6-bis[(1E)-2-(4-methylpiperazin-1-yl)phenyl]ethenyl]-4H-pyran-4-ylidene]-propanedinitrile (8): 0.17 g (1.0 mmol) of 2-(2,6-dimethyl-4H-pyran-4-ylidene)-propanedinitrile, 0.45 g (2.2 mmol) of 4-(4-methyl-1-piperazinyl)-benzaldehyde, 2.40 g (19.0 mmol) of TMS-Cl, and 10 ml of anhydrous dimethylformamide were mixed in a 25 mL pressure tube with a magnetic stir bar. After heating at 90 °C for 48 h, the reaction was cooled to room temperature and poured into a chilled solution of 1 M NaOH; the resulting dark red precipitate was isolated by suction filtration and rinsed with water. The filtrate was crystallized twice from methanol and dried in an oven to yield 0.23 g (42%) of **8** as a deep red powder. m.p: 296-298 °C; IR ν_{\max} (cm⁻¹): 2791.64, 2204.35, 1635.96, 1595.66, 1537.87, 1487.56, 1331.44, 1188.29, 1138.23, 828.66; ¹H NMR (500 MHz, DMSO-*d*₆), δ (ppm): 2.22 (3H, s), 2.43 (broad s, 8H), 3.29 (broad s,

8H), 6.73 (2H), 6.98-7.00 (d, 4H, $J = 10$ Hz), 7.11-7.14 (d, 2H, $J = 15.0$ Hz), 7.65-7.68 (d, 2H, $J = 15.0$ Hz), 7.67-7.69 (d, 4H, $J = 8.6$ Hz); ^{13}C NMR (125 MHz, DMSO- d_6 , TFA), δ (ppm): 42.51, 44.95, 52.46, 55.34, 106.46, 115.07, 116.61, 117.40, 126.56, 130.17, 138.05, 151.08, 156.52, 159.96; HR-ESI (Q-TOF) m/z : calc'd for $\text{C}_{34}\text{H}_{37}\text{N}_6\text{O}^+$ ($\text{M}+\text{H}^+$): 545.7105, found: 545.3012.

Absorption and Fluorescence. Absorption spectra were measured on an Agilent 8341 spectrophotometer. Emission spectra were collected on a Fluoromax-2 fluorimeter with slits set at 4 nm and an integration time of 0.100 s. Fluorescence quantum yields were obtained for **1** and **3** using Coumarin 153 dissolved in methanol; **2** using Rhodamine B dissolved in water; **4** and **6** using cresyl violet dissolved in methanol; **5** and **8** using Rhodamine 6G dissolved in water; **7** using Coumarin 30 dissolved in methanol as the fluorescence standards.

Circular Dichroism (CD). CD spectra were recorded on an Aviv model 202 circular dichroism spectrometer using a wavelength step of 1.0 nm and a bandwidth of 1.0 nm. CD scans were averaged with $n = 3$. Quartz cells with 10 mm path lengths were used for all measurements. All optical measurements were carried out at 25 °C under N_2 .

Two-Photon Absorption (TPA). Two-photon spectroscopy was performed using a Kapteyn Murnane Laboratories diode-pumped mode-locked Ti:sapphire laser with pulses of ~30 fs. All emission scans were recorded at 800 nm excitation. TPA cross-sections were measured utilizing the two-photon excited fluorescence (TPEF) method.³⁶ A variable neutral density filter was used to control the input power from the laser. The fluorescence was collected perpendicular to the incident beam. A focal-length plano-convex lens was utilized to direct the fluorescence into a monochromator whose output

was coupled to a photomultiplier tube. A counting unit was utilized to convert the photons into counts. Coumarin 307 dissolved in methanol was used as a standard ($(\phi\delta)_{800\text{ nm}} = 15\text{ GM}$).³⁶

Fluorescence Lifetime Measurements. The time-correlated single-photon counting (TCSPC) system has been described in detail elsewhere.³⁷ A Kapteyn Murnane Laboratories (KML) mode-locked Ti:sapphire laser system (90 MHz) delivering ~ 30 fs output pulses at 800 nm was used as the excitation source. Second harmonic generation in a β -barium borate (BBO) crystal was used to convert the 800 nm pulsed light to 400 nm excitation pulses. The fluorescence was collected at the maximum emission to a right angle excitation and detected by a photomultiplier tube (PMT) module coupled to a monochromator. A time to amplitude converter (TAC) was used to create time resolution. TimeHarp 200 (PicoQuant) software was implemented for the TCSPC measurements. Fluorescence anisotropy measurements were carried out by recording the fluorescence with a polarizer oriented parallel or perpendicular with respect to the excitation source.

The fluorescence upconversion setup used for time-resolved measurements has been reported previously.³⁸ A Tsunami Ti:sapphire laser operated at 800 nm with 120 fs pulses and a repetition rate of 82 MHz was utilized to produce an excitation wavelength of 400 nm using a BBO crystal. The gate pulse was directed to a delay line while the excitation light was upconverted to excite the samples using a FOG-100 system. Fluorescence anisotropy measurements were collected by changing the polarization of the excitation source utilizing a Berek compensator. All samples were placed in a 1 mm thick rotating sample cuvette.

Electronic Structure Calculations. The electronic structure calculations were carried out utilizing General Atomic and Molecular Electronic Structure System (GAMESS) software.^{39,40} The configuration interaction singles (CIS) approach was implemented in the calculations. The CIS method utilizes the restricted Hartree-Fock (RHF) theory generating singly excited determinants of configuration of interaction expansions. The CIS approach offers several advantages of calculating the excited states as well as the optimization of the selected state. The first excited state was optimized. 6-31G was used as the basis set. Hückel was employed as the initial molecular orbital guess. The calculations were performed on the free fluorophore in the absence of DNA. Avogadro was used to optimize the configuration of the molecule.⁴¹ The molecular orbitals were visualized using Gabedit Software.⁴²

Cell Culture and Fluorescence Microscopy. HeLa cells were cultured in DMEM (with phenol red) supplemented with 10% dialyzed FBS serum, 100 units of penicillin, and 100 µg/ml streptomycin in a humid incubator at 37 °C and 5% CO₂. Prior to imaging, the cells were seeded in a 35 mm glass bottom dish supplied by MatTek. The cells were incubated for 24 h or until a monolayer was visible at 60 – 70% confluency. The working medium was removed and 2 µM of fluorophore in DMEM (serum-free) was added to the imaging dish and incubated for 1 h. The medium was removed and the cells were washed with PBS to remove excess fluorophore. Live Cell Imaging Solution was used as the physiological medium during the imaging experiments.

The imaging experiments were carried out on a Leica Inverted SP5X Confocal Microscope System equipped with a 10X – 100X objective. Avalanche diode detectors were used when capturing and collecting images. A 405 nm diode (UV excitation), multi-

line argon laser (470 – 670 nm), and Spectra Physics Mai-Tai two-photon tunable laser (640 – 1040 nm) were used as the excitation wavelength source. The excitation power was adjusted to 5 – 10 % to reduce cell apoptosis. An Acousto Optical Beam Splitter (AOBS) was utilized to replace the beam splitters and fluorescent filters in the light path. The microscope was equipped with five photomultiplier tubes (PMT). A motorized X, Y, Z stage allows for precise control of the position of the sample.

4.5 Results

Design. The fluorophores (Figure 4.1) were designed with three key elements: **(i)** Recognition units were incorporated into the pendant arms of the fluorophores. Because DNA is a polyanionic molecule, cationic recognition arms are necessary for the fluorophore to electrostatically interact with the DNA backbone, which plays an important role in the formation of DNA-drug complexes.⁴³ *N*-methylpiperazine was selected because protonation of the pendant arms is achieved at physiological conditions.⁴⁴ **(ii)** The pendant aryl arms were designed to control the optical switching of fluorescence. Quenching is noted when the pendant arms are allowed free rotation in the absence of DNA, resulting in an ultrafast non-radiative deactivation. The pendant arms of the fluorophores are restricted of rotation when bound with DNA, which leads to a planar conformation. As a consequence, a large fluorescence enhancement originates from the loss of rotation of the pendant arms due to the constrictive DNA environment as well as a reduction in the non-radiative deactivation pathways upon binding with DNA. **(iii)** The donor-acceptor-donor π -system motif is responsible for the optical properties.⁴⁵ The incorporation of heterocyclic cores with varying electron accepting properties into the

conjugated π -system leads to an enhancement in the photophysical properties, which allows for a variety of molecular designs.

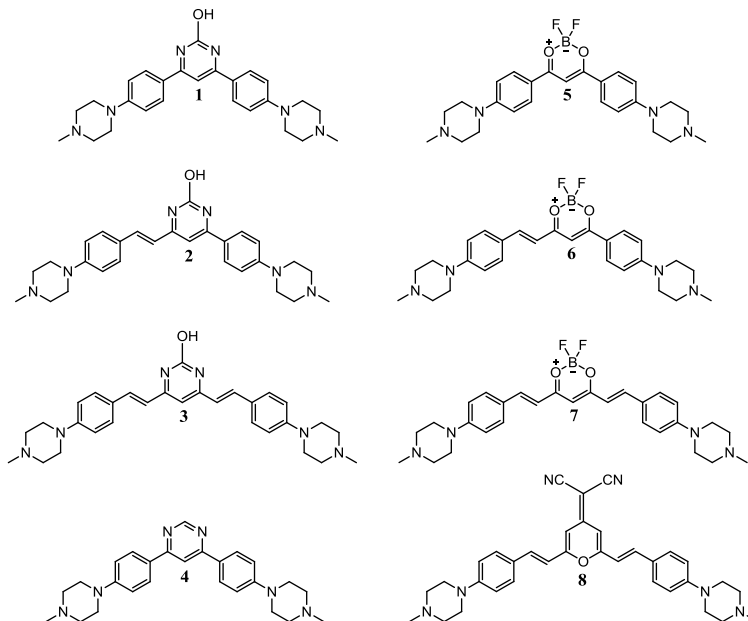


Figure 4.1. Chemical structures of the fluorescent nuclear dyes. The fluorophores adopt a donor-acceptor-donor motif with varying conjugation length between the electron donor arms and electron acceptor core.

UV-Vis Absorption. The steady-state absorption spectra of the fluorophores in the absence of DNA are presented in Figure 4.2a. As expected, the fluorophores (**1**, **4**, **5**) with shorter conjugation length displayed the shortest wavelength absorption maxima while the fluorophores (**3**, **7**, **8**) with increased conjugation length on both pendant arms exhibited the longest wavelength absorption maxima. The fluorophores displayed a single absorption band, which can be attributed to the $\pi - \pi^*$ transition. In the case of the fluorophores with a difluoroboron β -diketonate or dicyanomethylene pyran heterocyclic core (**5** – **8**), a second less intense absorption band at a higher energy wavelength was noted, which can be ascribed to the $n - \pi^*$ transition. Interestingly, **7** had the broadest absorption band with a bathochromic shift of 63 nm compared to **5**. The broad absorption

band is similar to the case where the closely spaced vibrational energy levels are due to the increase in conjugation length and electron accepting abilities of the heterocyclic core.⁴⁶

A direct comparison of the fluorophores with (**3**, **7**, **8**) and without (**1**, **4**, **5**) increased conjugation length on the pendant arms will allow us to assess the effect of the electron accepting abilities of the heterocyclic central core relative to the absorption spectra in the absence of DNA. The fluorophores (**1**, **4**, **5**) without increased conjugation length on both pendant arms will be discussed first. As expected, the addition of an electron donating hydroxyl substituent to the pyrimidine core (**1**) resulted in a bathochromic shift of 39 nm compared to **4**. The shift can be ascribed to both the electron accepting properties of the core as well as the increase in conjugation length. Comparing with **4**, a bathochromic shift of 124 nm was achieved by replacing the pyrimidine core with a difluoroboron β -diketonate core as demonstrated with **5**. The fluorophores with increased conjugation length on both pendant arms were also investigated (**3**, **7**, **8**). **3** exhibited a maximum absorption band near 435 nm. **8** displayed a bathochromic shift of 20 nm compared to **3** while **7** exhibited a bathochromic shift of 80 nm relative to **8**. The pyrimidinol core displayed the weakest electron accepting properties followed by the dicyanomethylene pyran core. The difluoroboron β -diketonate core possessed the strongest electron accepting properties.⁴⁷

The absorption spectra of the fluorophores were also examined in the presence of DNA (Figure 4.2b). Bathochromic shifts of 2 – 4 nm were observed in the absorption maxima upon DNA binding for the fluorophores (**1**, **4**, **5**) without increased conjugation length on both pendant arms, which was the smallest shift noted. Interestingly, the

fluorophores (**3**, **7**, **8**) with increased conjugation length on both pendant arms exhibited the largest bathochromic shifts of 12 – 20 nm upon complexing with calf thymus dsDNA. It remains unclear on why this phenomenon is observed. Thus, it is reasonable to suggest that the difference in the absorption shift upon binding with DNA can be directly related to the conjugation length. The fluorophores with increased conjugation length on the pendant arms exhibit more conformational isomers compared to the fluorophores without increased conjugation length. A larger bathochromic shift is observed since the fluorophores with increased conjugation length on both pendant arms resulted in a larger reduction of conformational isomers upon complexing with DNA. The bathochromic shift can also be ascribed to the change in the environment of the fluorophore when bound with DNA.⁴⁸ Upon complexing with DNA, the fluorophore displaces water molecules, leading to a more hydrophobic environment that prevents fluorescence quenching and provides steric protection.^{49,50}

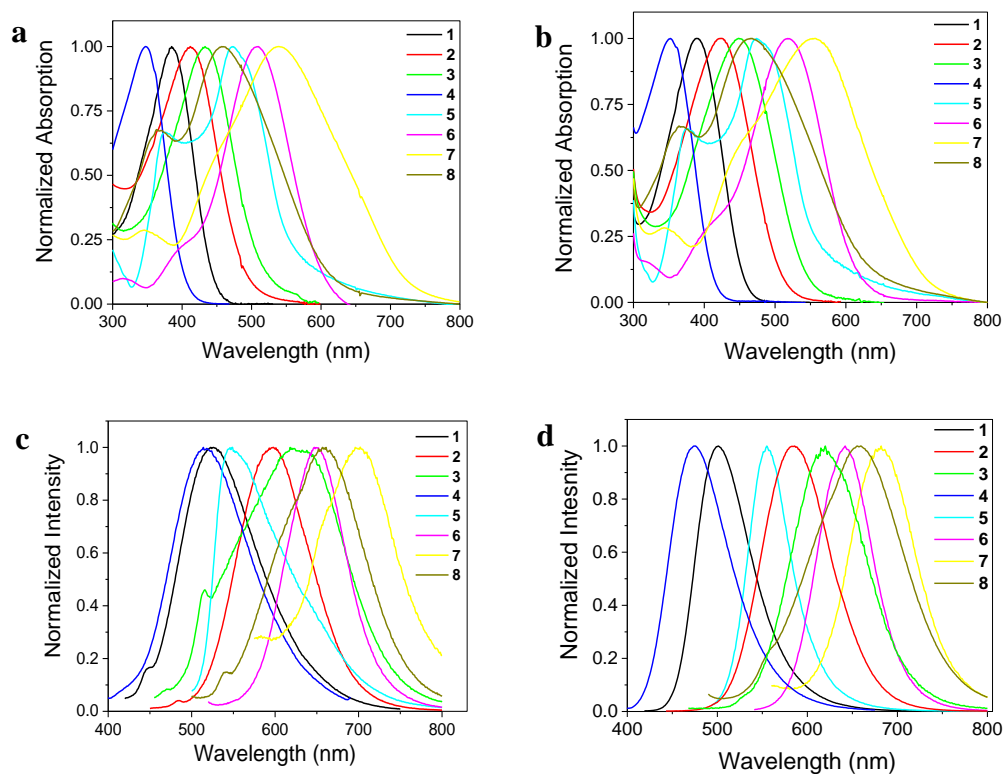


Figure 4.2. Steady-state spectra of the fluorophores. Normalized absorption spectra of the fluorescent nuclear dyes in the (a) absence and (b) presence of DNA. Normalized emission spectra of the fluorescent nuclear dyes in the (c) absence and (d) presence of DNA.

Steady-State Fluorescence. The emission spectra of the fluorophores were investigated in the absence of DNA (Figure 4.2c). The fluorophores displayed weak fluorescence in buffered aqueous solution with the fluorescence quantum yield ranging on the order of 10^{-4} to 10^{-2} . In particular, the fluorophores with increased conjugation length on both pendant arms exhibited the lowest quantum yields. Similar to the absorption spectrum, shifts in the emission band were also noted by varying the conjugation length and electron accepting properties of the heterocyclic core. By comparing **1**, **4**, and **5**, the difluoroboron β -diketonate core possesses the most electron

accepting abilities, leading to the most bathochromically shifted maximum emission band near 549 nm as noted for **5**. It has been reported that the vacant p-orbital from the boron atom overlaps with the conjugated moiety, which leads to a decrease in the lowest unoccupied molecular orbital (LUMO), resulting in a bathochromic shift in both the absorption and emission spectra.^{51,52} A similar trend was also observed by comparing **3**, **7**, and **8**. The results indicate that the optical properties of the fluorophores can be finely tuned by varying the electron accepting properties of the central heterocyclic core as well as the conjugation length. The modifications in the optical properties can be directly attributed to the change in the highest occupied molecular orbital (HOMO) and/or LUMO. By comparing the fluorophores that possess the same electron donating pendant arms, the incorporation of a stronger electron accepting core decreases the LUMO energy, resulting in a bathochromic shift.³¹ Likewise, increasing conjugation length on the pendant arms led to an increase in the energy of the HOMO. As a consequence, a bathochromic shift was observed because the molecule exhibits delocalization.⁵³

Presented in Figure 4.2d, the emission spectra of the fluorophores were examined in the presence of DNA. With the exception of **8**, the fluorophores displayed a fluorescence fold increase of up to 74-fold as well as narrowing of the emission band upon binding with DNA. The broader emission band can be attributed to a large distribution of conformational isomers of the free fluorophore in solution.⁴⁸ In particular, the emission band of **3** is broad compared to the remaining complexes. It is important to note that the small peak near 515 nm arises from the Raman scattering of solvent. The broadening of the emission band is ascribed to several equilibrated excited state rotational conformational isomers of the unbound fluorophore.⁴⁸ In the presence of DNA, the broad

emission band was not observed. Narrowing of the emission band implies that the fluorophore adopts a more planar conformation upon binding with DNA, which restricts free rotation of the pendant arms. As a consequence, there is a reduction of conformational isomers as well as a fluorescent enhancement, which was shown in a previous report.³¹

Table 4.1. Summary of steady-state properties of the fluorophores in the absence of DNA. Measurements were conducted with [fluorophore] = 5 μ M in PBS.

Compound	$\lambda_{\text{max, abs}}$ (nm)	$\lambda_{\text{max, em}}$ (nm)	Stokes Shift (cm^{-1})	ϵ ($\text{M}^{-1} \text{cm}^{-1}$)	Φ
1	387	523	6720	36,500	0.005
2	415	598	7370	37,400	0.012
3	435	619	6680	36,600	7×10^{-4}
4	348	514	9320	39,900	0.006
5	472	549	2970	29,000	0.009
6	508	647	4230	43,000	0.005
7	535	696	4320	27,200	2×10^{-4}
8	455	661	6850	42,500	0.002

Table 4.2. Summary of steady-state properties of the fluorophores in the presence of DNA. Measurements were conducted with [fluorophore] = 5 μ M and [DNA] = 100 μ M in PBS.

Compound	$\lambda_{\text{max, abs}}$ (nm)	$\lambda_{\text{max, em}}$ (nm)	Stokes Shift (cm^{-1})	ϵ ($\text{M}^{-1} \text{cm}^{-1}$)	Φ	Fluorescence Fold Increase
1	389	501	5790	32,700	0.14	73.8
2	423	586	6490	30,100	0.15	31.2
3	448	620	6140	26,300	0.02	61.1
4	352	476	7400	29,600	0.10	29.0
5	474	555	3180	23,800	0.06	28.5
6	521	642	3590	44,600	0.18	39.3
7	555	682	3310	32,900	0.007	33.7
8	467	659	5260	29,200	0.004	1.3

Trends in the Stokes shift were observed when the electron accepting properties of the central core and conjugation length on the pendant arms were varied. In the case of the fluorophores with the difluoroboron β -diketonate heterocyclic core, they displayed the smallest Stokes shift. Notably, **5** had the lowest Stokes shift of 2970 and 3180 cm^{-1} in the absence and presence of DNA, respectively. On the other hand, **4** exhibited the largest Stokes shift of 9320 and 7400 cm^{-1} in the absence and presence of DNA, respectively. The Stokes shift decreased as the electron accepting properties of the central core increased for the bound fluorophore regardless of conjugation length. Interestingly, the Stokes shift increased when conjugation length was extended to a single pendant arm. For example, **1** displayed a Stokes shift of 5790 cm^{-1} in the presence of DNA. Increasing conjugation length to a single pendant arm resulted in an enhanced Stokes shift of 6490 cm^{-1} as observed with **2**. This trend was also observed in the case of the fluorophores with a difluoroboron β -diketonate heterocyclic core.

Circular Dichroism (CD) Spectroscopy. CD has been used to study the function and interactions of DNA complexes in buffered aqueous solution.⁵⁴⁻⁵⁷ Optical activity arises when there are parallel molecular magnetic and electronic transition dipole moments that can couple with the electric field of a circularly polarized light source.^{54,55} An induced circular dichroism (ICD) signal is noted when a achiral molecule binds to chiral DNA due to a nondegenerate coupling of the chromophore with the DNA-base transitions.⁵⁵ In general, a strong positive ICD signal is observed when the dipole of the fluorophore is polarized perpendicular to the long axis of the pocket, which is a characteristic feature of a groove binding molecule. On the contrary, an intercalator has a

weak negative ICD signal when the transition dipole of the fluorophore is polarized along the long axis of the binding pocket or parallel to the nucleobases.^{58,59}

CD was employed to gain an insight on the DNA-binding mechanism of the fluorophores. The CD spectra in the presence of DNA are presented in Figure 4.3. With the exception of **8**, an ICD signal was detected, which confirms DNA-dye binding interactions. A positive ICD signal was observed for **1 – 4**, which suggests that the fluorophores are groove binding with DNA. Additionally, this indicates that the transition dipole of the fluorophore is oriented along the groove.⁶⁰ Interestingly, a bisignate ICD signal was observed for **1 – 7**, which is due to the interactions between the fluorophore that reflect excitonic coupling in dimers or aggregates formed at the groove or surface of DNA.⁵⁹ **1** and **4** were previously found to groove bind with DNA, which corresponds with the results.³⁴ The heterocyclic core allows the fluorophore to interact with the DNA nucleobases required for groove binding. The pyrimidine core can act as an H-bonding donor site whereas the hydroxyl substituent on the pyrimidine core can act as an H-bonding donor/acceptor site for **1 – 3**. In a previous report, **1** was found to groove bind at AT-rich sequences. However, the fluorescence is nearly quenched from GC sequences, which is likely due to the photoinduced electron transfer (PET) from guanine to the excited chromophore.⁶¹

The CD spectra were investigated in case of the fluorophores with a difluoroboron β -diketonate core (**5 – 7**). **5** was previously reported to intercalate with DNA utilizing linear dichroism (LD).³¹ Unexpectedly, **5** exhibited a strong positive ICD band near 475 nm, which suggests that the fluorophore is groove binding with DNA. However, when a positive ICD signal arises from an intercalator, this indicates that the transition dipole is

oriented along the long axis of DNA whereas a negative ICD signal is observed when the transition dipole is aligned perpendicular with the long axis.⁶² Based on the CD results, it is reasonable to suggest that the transition dipole of **5** – **7** is oriented parallel with the long axis of DNA. However, it is difficult to determine the DNA-binding mode based solely on CD.

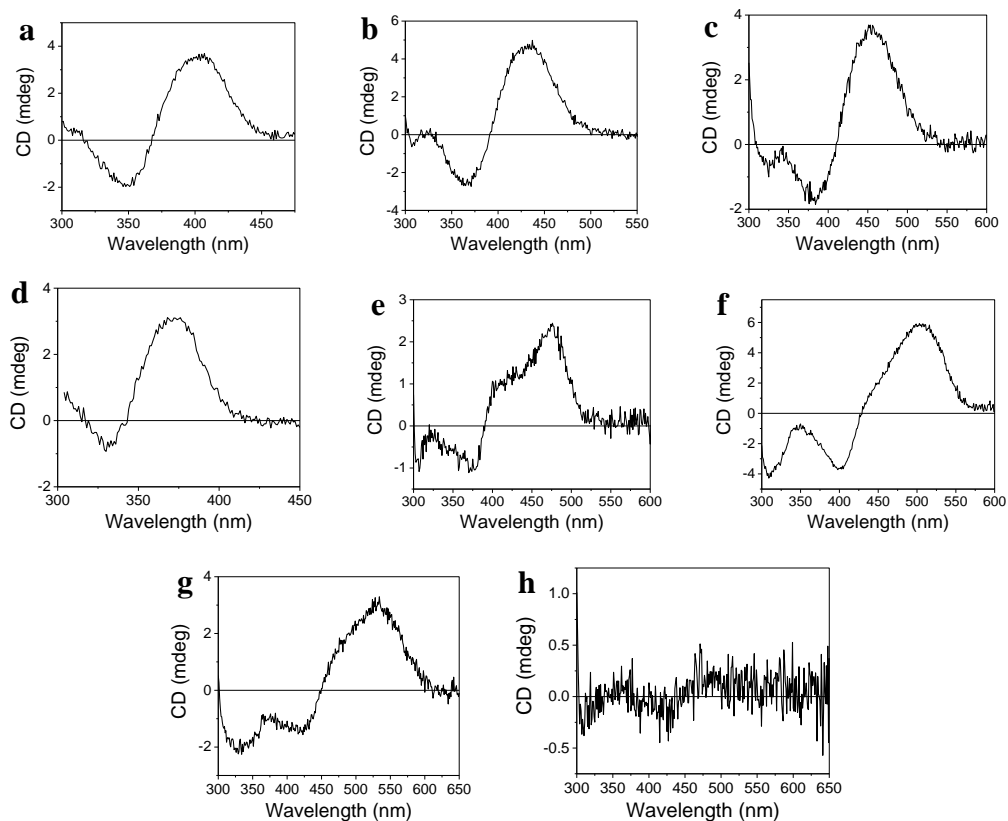


Figure 4.3. CD spectra. Evidence of DNA-binding interactions for (a) **1**, (b) **2**, (c) **3**, (d) **4**, (e) **5**, (f) **6**, (g) **7**. (h) An ICD signal was not detected for **8**, which indicates that the molecule is neither intercalating nor groove binding with DNA. Measurements were conducted at [fluorophore] = 5 μ M and [DNA] = 100 μ M.

Two-Photon Absorption (TPA). Summarized in Table 4.3, the TPA cross-sections (δ) of the unbound fluorophores were examined. The TPA cross-section increased as conjugation length increased in the case of the fluorophores with the same central core.

For example, the TPA cross-section of **1** was 3.4 GM. Increasing conjugation length to a single pendant arm resulted in a TPA cross-section of 6.1 GM as detailed with **2** while increasing conjugation length to both pendant arms led to a TPA cross-section of 66.8 GM as shown with **3**. A similar trend was also noted for **5 – 7**. Interestingly, there was a significant enhancement in the TPA cross-section when a stronger electron accepting core was incorporated into the structure in the case of the fluorophores with increased conjugation length on a single pendant arm. For instance, **2** had a TPA cross-section of 6.1 GM. A dramatic increase in the TPA cross-section was found by replacing the hydroxypyrimidine core with a difluoroboron β -diketonate core as demonstrated with **6**, which displayed a TPA cross-section of 37.5 GM. The findings suggest that the electron accepting properties of the core and conjugation length play an important role in the TPA cross-sections of the unbound fluorophore.

Table 4.3. TPA cross-section (δ) of fluorescent nuclear dyes in the absence of DNA. The TPA cross-sections were measured with an excitation wavelength of 800 nm in PBS.

Compound	Φ	δ (GM)
1	0.005	3.4
2	0.012	6.1
3	7×10^{-4}	66.8
4	0.006	2.1
5	0.009	1.4
6	0.005	37.5
7	2×10^{-4}	50.6
8	0.002	87.6

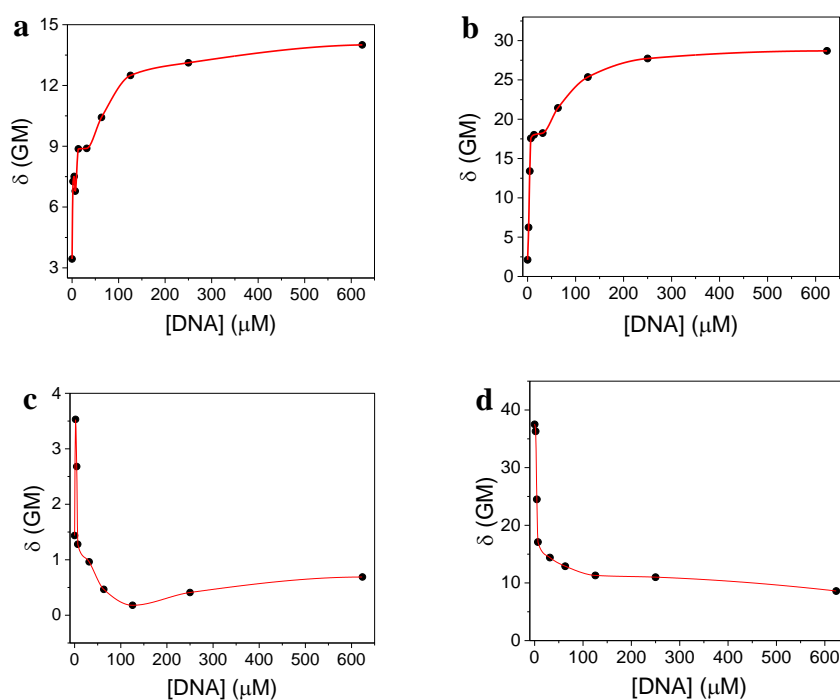


Figure 4.4. TPA cross-section (δ) plotted as a function of DNA concentration. The TPA cross-section was measured for (a) **1**, (b) **4**, (c) **5**, (d) **6** with [fluorophore] = 5 μM at increasing DNA concentrations to determine the DNA-binding mode. The red line is to guide the eye

TPA was employed to assess the DNA-binding mode as described in a previous report where an overall increasing or decreasing trend in the TPA cross-section indicates a groove binding or intercalating binding mode, respectively.³⁴ The TPA cross-sections were plotted as a function of DNA concentration as given in Figure 4.4. **1** and **4** were previously found to display an increasing TPA cross-section trend, suggesting a groove binding mode.³⁴ The increasing TPA cross-section trend suggests that the dipole of the fluorophore is oriented more parallel with the DNA electric field, which is indicative of a groove binder. It is reasonable to suggest that these fluorophores are binding at the minor groove because it has been reported that large molecules tend to bind at the major groove while small molecules bind at the minor groove of DNA.⁶³ Interestingly, the TPA cross-

section enhancement of **4** is significantly greater than **1**. **1** exhibited a TPA cross-section enhancement of 4.1-fold whereas **4** displayed a TPA cross-section enhancement of 13.6-fold upon binding with DNA. Since the structures are nearly identical, this can be attributed to the hydroxyl substituent on the heterocyclic core of **1**. It has been shown that intermolecular interactions can influence the TPA cross-section.⁶⁴⁻⁶⁶ Additionally, it has been reported that H-bonding interactions and aggregation can reduce the TPA cross-section of V-shaped hydroxypyrimidine complexes.⁶⁷ Hence, the difference in the TPA cross-section enhancement upon binding with DNA is directly related to the hydroxyl substituent on **1** interacting with the DNA nucleobases and/or surrounding water molecules.

5 was previously shown to intercalate with DNA utilizing LD.³¹ It has been reported that CD cannot determine the binding mode of an intercalator unambiguously without the orientation of the transition dipole moment being known.¹⁰ In order to determine the DNA-binding mode unambiguously, TPA was employed. Our TPA results indicate that both **5** and **6** intercalate with DNA as observed with the decreasing TPA cross-section trend. For example, **6** had a TPA cross-section of 37.5 GM in the absence of DNA. The TPA cross-section decreased to 8.6 GM at 624 μM of DNA. The overall decreasing TPA cross-section trend suggests that the transition dipole of both **5** and **6** is oriented more perpendicular to the DNA electric field, which is indicative of an intercalating binding mode. Interestingly, the TPA cross-section of **5** increased from 1.4 to 3.5 GM when the DNA concentration was increased from 0 to 2.1 μM . This can be directly attributed to the fluorophore stacking or aggregating at the surface of DNA at high dye-to-DNA ratios.⁶⁸ This provides an example in which CD cannot determine the binding mode of an

intercalator unambiguously. Based on our findings, we can conclude that **5** and **6** intercalate with DNA, which does not necessarily agree with the CD interpretation.

Time-Resolved Fluorescence. The fluorescence lifetime of the fluorophores in the absence of DNA was investigated to gain a better understanding on the excited-state dynamics as presented in Figure 4.5. Since the fluorophores exhibit a single emission band, the fluorescence dynamics of the fluorophores were measured at the maximum emission band. The fluorophores displayed a two-component decay, suggesting that multiple excited states exist. The fluorescence lifetimes are summarized in Table 4. The multi-exponential decay indicates that there are two deactivation pathways, which includes the emission from the locally excited (LE) state and the intramolecular charge transfer between the fluorescent LE state to the non-fluorescent twisted intramolecular charge transfer (TICT) state (LE \rightarrow TICT transition) by twisting of the molecular moieties.⁶⁹ The short component is likely due to an intramolecular charge transfer from the fluorescent LE to the non-fluorescent TICT state. When the pendant arms are allowed free rotation, the rate of the LE \rightarrow TICT transition process may compete with other radiative and non-radiative processes.⁷⁰ By hindering this process or restricting the pendant arms, the LE \rightarrow TICT transition is suppressed, leading to an enhanced emission and a longer decay rate. Interestingly, the short component of fluorophores is near 2 ps with the exception of **8**. Because of this, it is also reasonable to suggest that the fast component may also be attributed to the photoisomerization of the fluorophore. It has been reported that photoisomerization of *cis*-stilbene is 1 ps in *n*-hexane.⁷¹ This indicates that the photoisomerization activation barrier is minimal. The longer component is not likely due to solvent or vibrational relaxation, but to the excited-state population

dynamics of the free fluorophore. In other words, this is attributed to the population decay of the charge transferred state coupled with the triplet state.⁷² The predominant long component can be attributed to the LE state or the deactivation of the LE state to the ground state.

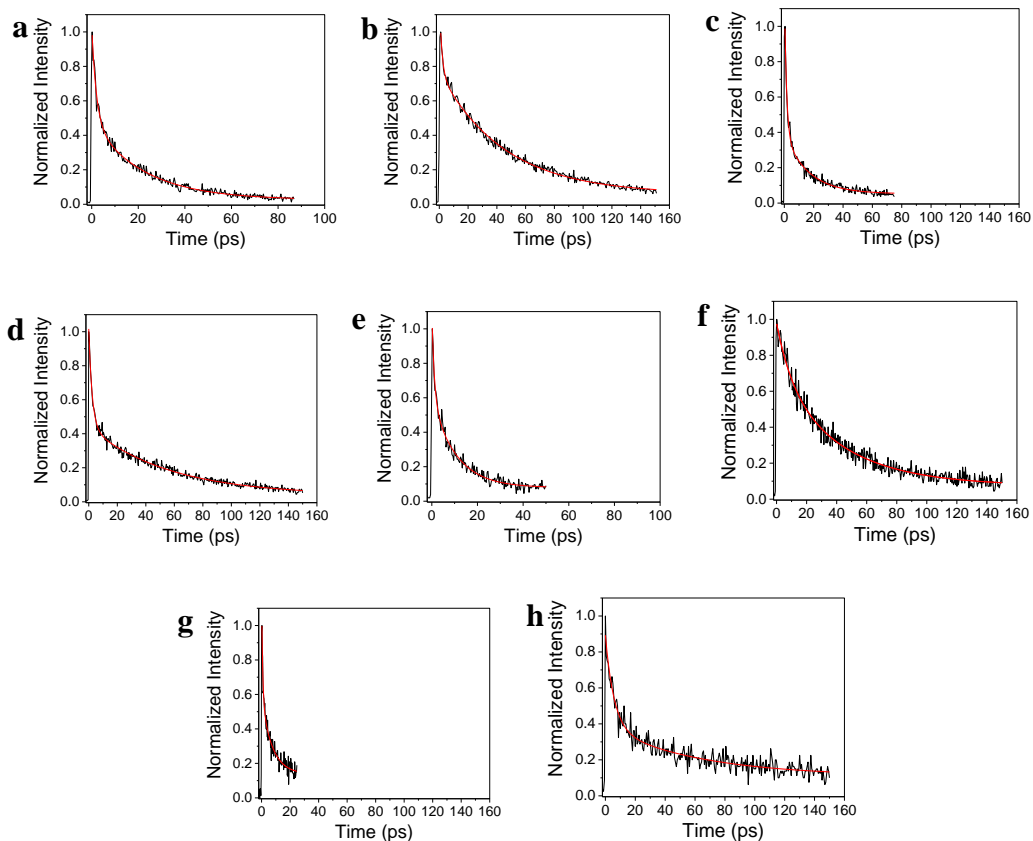


Figure 4.5. Fluorescence lifetime dynamics. Fluorescence upconversion of (a) **1**, (b) **2**, (c) **3**, (d) **4**, (e) **5**, (f) **6**, (g) **7**, (h) **8** in the absence of DNA.

Table 4.4. Summary of fluorescence lifetime data in the absence of DNA. The fluorescence lifetime values were fitted to the equation $y(t) = A_1e^{-t/\tau_1} + A_2e^{-t/\tau_2}$.

Compound	A_1	τ_1 (ps)	A_2	τ_2 (ps)
1	0.55	2.0	0.45	22.3
2	0.38	1.7	0.62	45.1
3	0.71	1.4	0.29	16.4
4	0.62	2.3	0.38	30.6
5	0.50	1.1	0.50	10.6
6	0.32	2.4	0.68	43.3
7	0.58	0.8	0.42	7.4
8	0.56	4.0	0.44	27.3

The fluorescence decay dynamics were investigated to analyze the effect of conjugation length. Increasing π -conjugation length to one pendant arm led to a longer-lived fluorescence lifetime as observed with **2** and **6**. For example, **2** exhibited a long component of 45.1 ps, which was the longest lifetime noted. The longer-lived fluorescence lifetime can be directly ascribed to the asymmetrical configuration of the fluorophore. The fluorophores have two charge transfer excited states that are different in energy due to the asymmetric pathway. Thus, there is an increase in the ICT character due to the asymmetric structural configuration. It has been previously reported that the fluorescence lifetime increases as the ICT character is increased, which corresponds with our results.⁶⁹ The shortest lifetimes were observed for the fluorophores with increased π -conjugation length on both pendant arms. These observations are consistent in the case of the fluorophores that possess a pyrimidinol or difluoroboron β -diketonate core. **3** exhibited a long component of 16.4 ps while **7** had a long component of 7.4 ps. The low quantum yield and fast decay of **3** and **7** can be directly related to the increase in conjugation length on both pendant arms. Increasing conjugation length results in the delocalization of the excited state. Photoinduced alterations in the dipole occur when the

π -conjugated system connecting the donor and acceptor moieties is lengthened.⁷³ The insertion of double bonds between the donor and acceptor moieties leads to a decrease in the overall aromaticity of the system, resulting in a reduced band gap.⁷⁴ Additionally, this leads to an increase in the rigidification of the fluorophore. As a consequence, a faster fluorescence lifetime is observed.

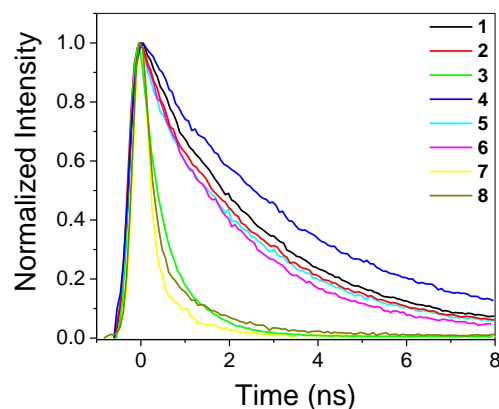


Figure 4.6. Fluorescence lifetime dynamics of fluorescent nuclear dyes in the presence of DNA.

Table 4.5. Summary of fluorescence lifetime data in the presence of DNA. The fluorescence lifetime values were fitted to the equation $y(t) = A_1 e^{-t/\tau_1}$.

Compound	τ (ns)
1	2.59
2	2.37
3	0.60
4	3.40
5	2.28
6	2.14
7	0.34
8	0.46

TCSPC was employed because of the increase in the fluorescence lifetime of the DNA bound fluorophore (Figure 4.6). A single-component decay in the nanosecond time

range was noted with the exception of the fluorophores with increased conjugation length on both pendant arms. The fluorescence lifetime in the presence of DNA is summarized in Table 4.5. In order to assess the effect of conjugation length, the pyrimidinol (**1** – **3**) and difluoroboron β -diketonate (**5** – **7**) fluorophores were studied. In both cases, the fluorophores without increased conjugation length exhibited the longest lifetimes. The fluorophores with increased conjugation length on a single pendant arm displayed a slight decrease in the fluorescence lifetime. Interestingly, a sub-nanosecond decay was observed for the fluorophores with increased conjugation length on both pendant arms. For instance, **1** exhibited a fluorescence lifetime of 2.59 ns while **2** displayed a single-component lifetime of 2.37 ns. Increasing conjugation length on both pendant arms resulted in a lifetime decay of 0.60 ns as shown with **3**.

The fluorescence dynamics of the DNA bound fluorophore were examined to analyze the effect of varying the electron accepting properties of the central heterocyclic core. The fluorophores (**1**, **4**, **5**) without increased conjugation length exhibited fluorescence lifetimes greater than 2 ns. **5** had a slightly faster decay than **1** with a fluorescence lifetime of 2.28 ns, suggesting that the incorporation of a more electronegative core leads to a faster decay. **4** exhibited a single exponential decay of 3.40 ns, which was the longest lifetime observed. Interestingly, **4** had a lower quantum yield ($\Phi = 0.10$) as compared to **1** ($\Phi = 0.14$), but the lifetime was predominantly longer. As discussed above, the addition of the hydroxyl substituent to the pyrimidine core contributes to the significant change in the fluorescence lifetime by interacting with the DNA nucleobases and/or surrounding water molecules. The fluorophores (**3**, **7**, **8**) with increased conjugation length on both pendant arms displayed a fluorescence lifetime in the sub-nanosecond time scale.

Similarly, a stronger electron accepting core resulted in a faster fluorescence lifetime as noted above. The low quantum yield and short lifetime can be attributed to the fluorophore not tightly binding with DNA. As a consequence, the pendant arms are not as restricted. Furthermore, the fluorophore is exposed to more surrounding water molecules, which can interact with the bound fluorophore. **8** was not compared since the results indicate that the fluorophore does not bind with DNA. The findings suggest that incorporating a stronger electron accepting core results in a faster decay for the DNA bound fluorophore regardless of conjugation length.

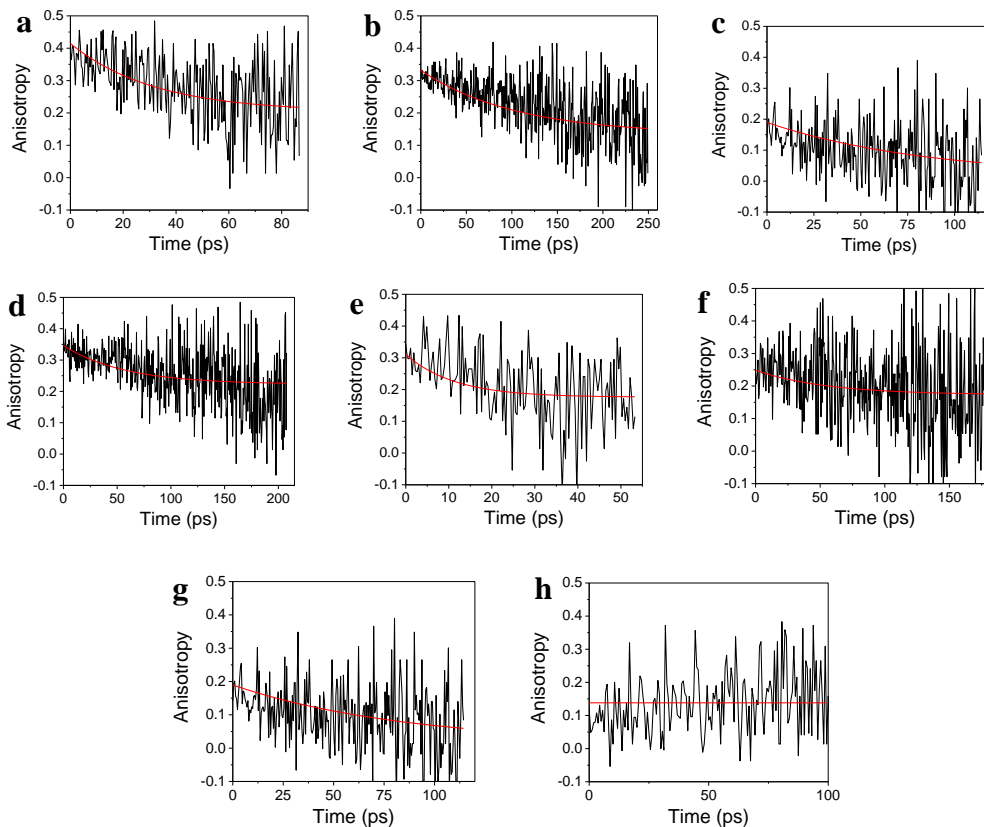


Figure 4.7. Fluorescence anisotropy in the absence of DNA for (a) **1**, (b) **2**, (c) **3**, (d) **4**, (e) **5**, (f) **6**, (g) **7**, (h) **8**.

To further understand the fluorescence dynamics of the unbound fluorophores, ultrafast fluorescence anisotropy decay measurements were conducted as shown in Figure 4.7. The rotational anisotropy decay values are summarized in Table 4.6. Anisotropy measurements can provide detailed information about the directionality of the material. A higher anisotropy suggests that the material is more symmetrical and less freely moving.⁵³ Interestingly, the anisotropy value decreased as conjugation length increased. This indicates that the highest symmetry and lowest direction dependence is observed for the fluorophores without increased conjugation length regardless of the accepting properties of the central heterocyclic core. This observation can also be attributed to the increase in rotational diffusion and/or energy transfer processes.⁷⁵ Specifically, the fluorophores with increased conjugation length reorient faster after excitation. Anisotropy values can also provide information about the transition dipole of the fluorophore. A high anisotropy (near 0.40) indicates that the emission is not delocalized and is subsequent from localized transition dipoles,⁷⁶ which was noted for **1** (0.39). With the exception of **8**, the fluorophores exhibit anisotropy decay in the absence of DNA. This suggests that the angle between the absorption and emitting dipoles does not change during intersystem crossing for **8**.⁷⁶ In other words, the emission from **8** has equal intensities along the different axes of polarization.

Table 4.6. Rotational anisotropy decay. The rotational correlation decay parameters of the fluorophores are given in the absence and presence of DNA.

Compound	Absence of DNA		Presence of DNA	
	τ (ps)	r_0	τ (ps)	r_0
1	31.8	0.39	5194	0.19
2	104.0	0.31	2020	0.16
3	85.4	0.19	4880	0.17
4	57.3	0.35	5806	0.27
5	11.3	0.34	452	0.05
6	24.7	0.25	1079	0.03
7	85.4	0.12	2200	0.11
8	N/A	0.12	2276	0.07

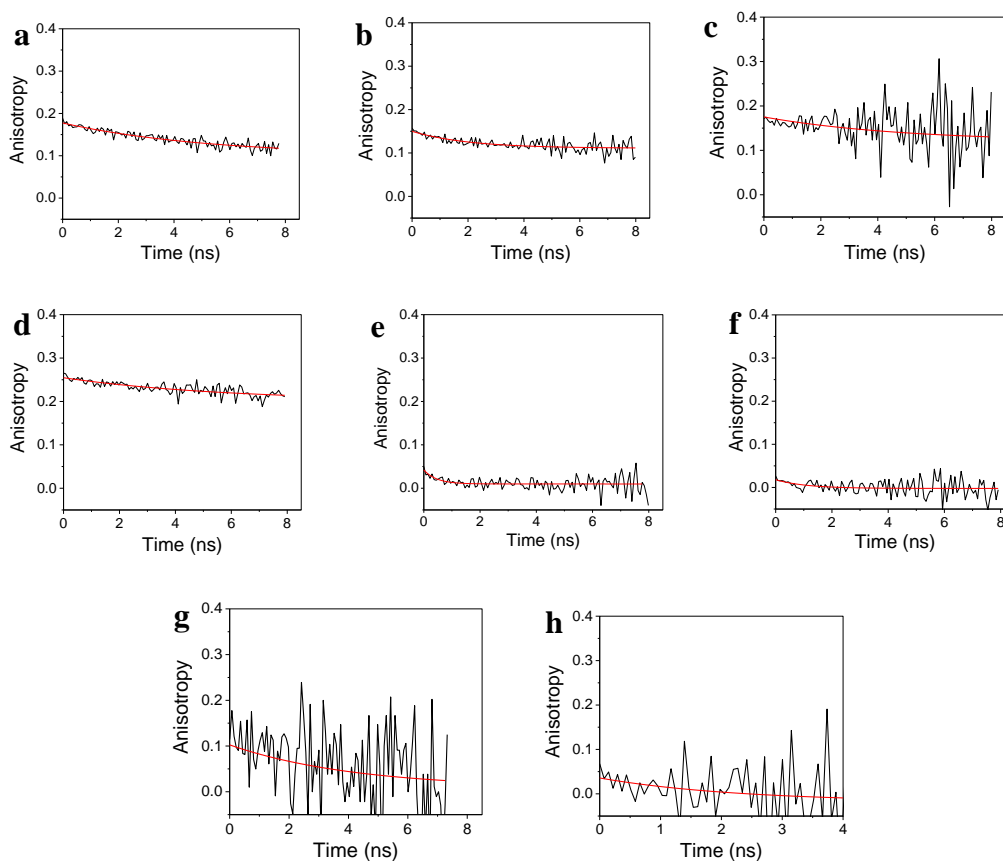


Figure 4.8. Fluorescence anisotropy in the presence of DNA for (a) **1**, (b) **2**, (c) **3**, (d) **4**, (e) **5**, (f) **6**, (g) **7**, (h) **8**.

The DNA-binding interactions of the bound fluorophores were investigated by polarized excitation measurements. Time-resolved anisotropy can provide important information about the shape, size, and dynamics of biological molecules.⁷⁷ A change in the depolarization is observed when a small molecule binds to a macromolecule, such as DNA. The bound fluorophore exhibits different excited states that lead to different depolarization times. The rotational correlation times of the bound fluorophore were longer than the local motion of the free fluorophore under the same conditions, indicating a restricted tumbling motion. Both groove binding and intercalation inhibit the rapid tumbling motion of the binding molecule.⁷⁸ Fluorescence anisotropy was utilized to investigate the fluorophores bound with DNA. The values are summarized in Table 6. The rotational correlation times of the bound fluorophore were longer than the local motion of the free fluorophore under the same conditions, indicating a restricted tumbling motion as presented in Figure 4.8. For example, **1** had an anisotropic decay of 31.8 ps in the absence of DNA while the anisotropic decay was 5.2 ns when bound with DNA. Interestingly, **1** – **4** displayed high residual anisotropy whereas the remaining fluorophores showed rapid anisotropy decay.

The high residual anisotropy of **1** – **4** suggests that the fluorophores exhibit highly restricted rotation upon binding with DNA. This can be ascribed to the fluorophore tightly binding at the groove of DNA. The locking of the fluorophore is due to the protonated *N*-methylpiperazine recognition units electrostatically interacting with the negatively charged DNA helix. In addition, the heterocyclic core of the fluorophore undergoes intermolecular interactions with the DNA nucleobases to further stabilize the binding molecule. It is important to note that high residual anisotropy was not observed

for **5** – **7**, which indicates that the fluorophores are less restricted upon binding. By comparing with the groove binding fluorophores, this can be directly related to the DNA-binding mechanism of the fluorophore as they were found to intercalate with DNA by implementing our TPA methodology. The rapid anisotropic decay can be attributed to the wobbling of the fluorophore at the intercalating site, indicating a less restricted motion.^{79,80} Poor intermolecular interactions required for intercalation, such as π -stacking, between the DNA nucleobases and the intercalating fluorophore can contribute to the wobbling of the bound fluorophore.

Electronic Structure Calculations. GAMESS Software was implemented to examine the electronic structure of the fluorophores in the absence of DNA. Calculations were carried out in the gaseous state. Geometry optimization was performed by Avogadro Software. The CIS method was implemented in this work. 6-31G and Hückel were used as the basis set and initial molecular orbital guess, respectively. Presented in Table 4.7, the molecular orbitals (MO) of the free fluorophores were investigated.

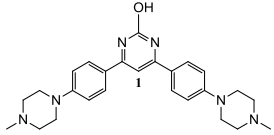
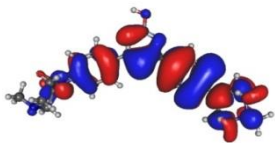
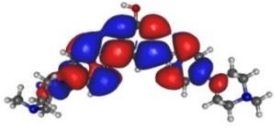
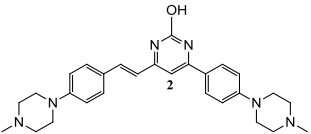
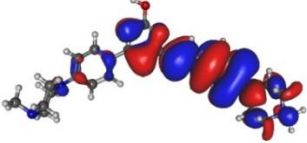
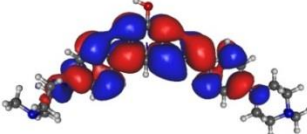
One can gain an insight on the charge transfer character by examining the electronic structure of a molecule. In the case of the fluorophores with the pyrimidinol core (**1** – **3**), the HOMO was mainly localized on a single pendant arm whereas the LUMO was mostly localized on the central heterocyclic core, which indicates that the HOMO \rightarrow LUMO absorption transition exhibits ICT character. This was also noted for **4** and **8**. Interestingly, the distribution of the MO differed in the case of the fluorophores with the difluoroboron β -diketonate core (**5** – **7**). The HOMO was more delocalized over the entire molecule while the LUMO was localized on the central heterocyclic core and/or a single pendant arm. This suggests that the complexes with an uneven distribution of the HOMO

exhibit a stronger ICT character. In other words, the fluorophores with the difluoroboron β -diketonate core exhibit a weaker ICT character compared to the remaining fluorophores. The difference in the localization of the HOMO can be directly related to the electron accepting properties of the central core. By structurally modifying the central core of the fluorophore with a stronger electron accepting moiety, the energy of the LUMO is decreased. Furthermore, mixing between the accepting core and donating arms is observed in the case of the difluoroboron β -diketonate fluorophores because there is a reasonable energy match between the HOMO of the moieties. As a consequence, this leads to delocalization throughout the molecule and a bathochromic transition⁴⁷. In the case of the remaining fluorophores, the energy match is poor between the electron donating arms and electron accepting core. As a result of this, the HOMO is more localized on a single pendant arm, leading to greater ICT character.

The electronic structure calculations were analyzed to further understand the DNA-binding mechanism of the fluorophores. It has been reported that intercalators exhibit large charge delocalization and polarizability.⁸¹ Additionally, intercalation is accompanied by the interaction between the HOMO of the DNA base pairs and LUMO of the binding molecule, which contributes to the selectivity of the DNA-binding mechanism.⁸² Interestingly, the groove-binding molecules (**1** – **4**) displayed strong delocalization of the LUMO over the entire molecule whereas the LUMO was more localized on a single pendant arm in the case of the intercalating molecules (**5** – **7**). This suggests that the localization of the LUMO plays an important role in the DNA-binding mode. The localization and lower energy of the LUMO promotes intercalation because the binding molecule can accept electrons from the DNA base pairs.⁸³ In other words,

there is mixing between the LUMO of the intercalating molecule and HOMO of the DNA base pairs, which stabilizes the complex. It is important to note that the groove binding molecules exhibit greater localization of the HOMO on a single pendant arm whereas the HOMO of the intercalating molecules is more delocalized over the entire molecule. This implies that the DNA-binding molecules with localization of the HOMO on a single pendant arm groove bind with DNA while delocalization of the HOMO results in intercalation, which remains unclear in our case. It has been reported that the HOMO of water is a large contributor to the stabilization of H-bonding interactions.⁸⁴ Therefore, it is reasonable to suggest that groove binding of the fluorophores is partially governed by the localization of the HOMO on a single pendant arm as it stabilizes the binding molecule at the DNA helical groove by promoting favorable interactions, such as H-bonding.

Table 4.7. Molecular orbitals diagrams. The electronic structures of the unbound fluorescent nuclear dyes were calculated by GAMESS in the gaseous state.

Chemical Structure	HOMO	LUMO
 <p style="text-align: center;">1</p>		
 <p style="text-align: center;">2</p>		

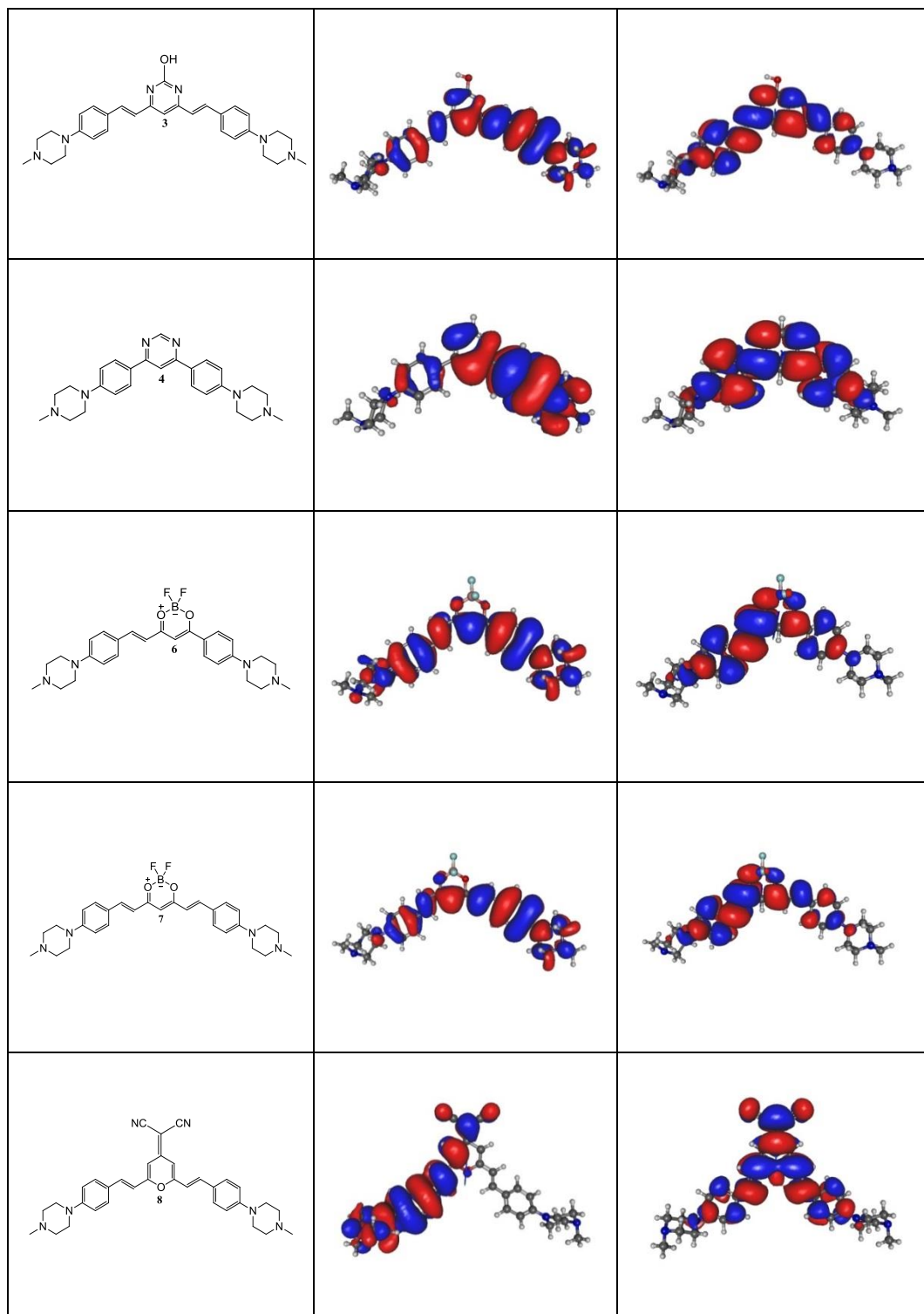


Table 4.8. Experimental TPA cross-sections (δ) and electronic properties of the unbound fluorophore. Electronic calculations were implemented by GAMESS to obtain the ground state and transition state dipoles of the fluorophores in the gaseous state.

Compound	δ (GM)	Ground state dipole (D)	Transition state dipole (D)
1	3.4	0.52	8.85
2	6.1	0.51	10.46
3	66.8	0.46	11.12
4	2.1	0.56	8.31
5	1.1	1.92	9.77
6	21.7	2.25	10.06
7	50.6	2.41	11.59
8	87.6	2.81	8.34

The ground state and transition state dipole moments were obtained by the electronic structure calculations. The fluorophores with weaker electron accepting properties (**1 – 4**) had ground state dipoles ranging from 0.46 – 0.56 D. On the other hand, the fluorophores with stronger electron accepting properties (**5 – 8**) had ground state dipoles ranging from 1.92 – 2.81 D. The transition dipole of the fluorophore increased as conjugation length increased. For instance, the transition dipole of **1** was 8.85 D. Increasing conjugation length to single pedant arm resulted in a transition dipole of 10.46 D as noted with **2** whereas increasing conjugation length on both arms led to a transition dipole of 11.12 as observed with **3**. A similar trend was also recorded in the case of the fluorophores with the difluoroboron β -diketonate heterocyclic core.

Live Cell Imaging. To explore the utility of the fluorescent nuclear dyes, a series of imaging experiments were carried out using confocal fluorescence microscopy. The fluorophores demonstrated a dramatic increase in the fluorescence upon binding with DNA, which makes them suitable for bioimaging applications. Cellular uptake of the

fluorophore was verified by confocal microscopy. The fluorophores displayed excellent cellular uptake with low cytotoxicity. No cell morphology or viability changes were found during the experiments. Single-photon fluorescence confocal microscopy was utilized to image the fluorescent nuclear dyes (Figure 4. 9). **1**, **2**, and **4** demonstrated distinguishable nuclei staining with high selectivity for DNA with less pronounced staining of the cytoplasm. The images displayed specific staining of DNA localized in the cell nucleus with a high signal-to-noise ratio. **3** also exhibited high selectivity for DNA localized in the nucleus; however, staining of the cytoplasm was more pronounced. To confirm these observations, the cells were also stained with 1 μM of **3**. Staining of the cytoplasm was also noted at the lower fluorophore concentration.

5 – **8** showed vastly different staining trends as the fluorophore was mainly localized in the cytoplasm. This is likely due to the increase in the electron accepting properties of the heterocyclic core, causing the fluorophore to penetrate the nucleus membrane with lower efficiency. From the steady-state studies, **8** was not expected to label the nuclei with a high fluorescent enhancement. It should be emphasized that localized bright spots were observed in the cytoplasm, which is likely attributed to direct staining of organelles. It was previously reported that cationic molecules can be used as fluorescent probes for lysosomes, endoplasmic reticulum, cell membrane, and mitochondria.⁸⁵ Therefore, these bright spots localized in the cytoplasm may constitute as labeled organelles, such as lysosomes⁸⁶ or mitochondria.⁸⁷

Presented in Figure 4.10, two-photon excited microscopy (TPEM) was utilized to image the fluorophores in live HeLa cells. TPEM offers several advantages over traditional one-photon fluorescence microscopy (OPEM) as it demonstrates superior

spatial resolution and sensitivity because the TPA process is quadratically power dependent. For example, the features of a single cell are remarkably pronounced by TPEM as compared to OPEM as illustrated in Figure 4.11. A significant portion of the fluorescence collected with single-photon microscopy arises from autofluorescence due to the higher energy excitation wavelength. Autofluorescence is less pronounced with TPEF since the excitation wavelength is near the IR range, which also minimizes photodamage. The excitation for TPEF is confined to a small volume in a focal plane, leading to reduced photobleaching as well as deeper tissue penetration capabilities for imaging applications.⁸⁸ Thus, fluorophores that exhibit TPA properties are of interest. **1**, **2**, and **4** displayed optical properties that are promising as biological markers utilizing TPEM. The labeled nuclei are less pronounced with single-photon confocal microscopy whereas the contrast and resolution is more dramatic by TPEM. Cell permeable small organic molecules that can target specific DNA sequences and interfere with gene expression are important for drug research and development.⁸⁹ Hence, imaging of such processes with high spatial resolution is of considerable interest.

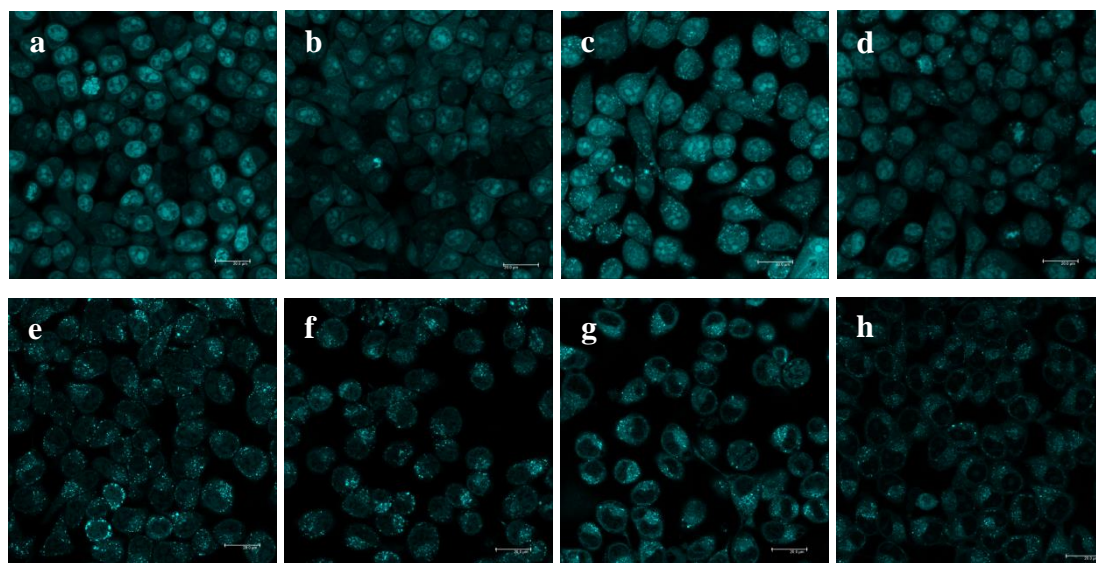


Figure 4.9. Single-photon excited fluorescence confocal microscopy images of (a) **1**, (b) **2**, (c) **3**, (d) **4**, (e) **5**, (f) **6**, (g) **7**, (h) **8**. The cells were incubated at 2 μM of fluorophore for 1 h. Bar: 20 μm .

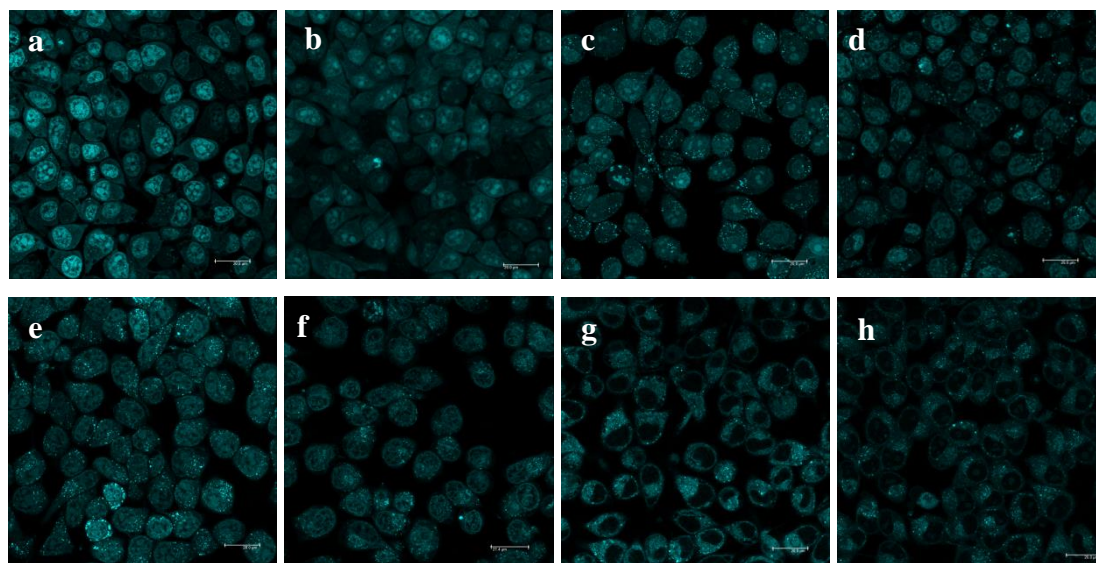


Figure 4.10. Two-photon excited fluorescence confocal microscopy images of (a) **1**, (b) **2**, (c) **3**, (d) **4**, (e) **5**, (f) **6**, (g) **7**, (h) **8**. The cells were incubated at 2 μM of fluorophore for 1 h. $\lambda_{\text{ex}} = 800 \text{ nm}$. Bar: 20 μm .

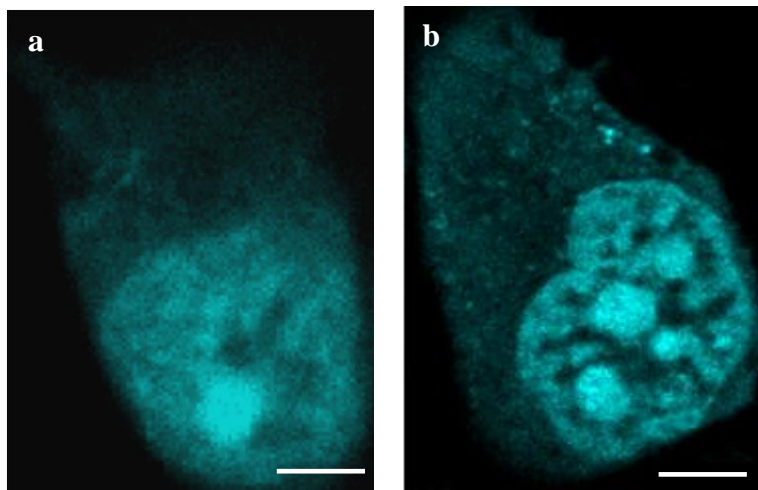


Figure 4.11. Two-photon excited fluorescence confocal microscopy images of a single HeLa cell. (a) One-photon and (b) two-photon excited fluorescence confocal microscopy images of cells stained with **1**. Bar: 5 μm .

4.5 Discussion

The fluorophores displayed a high turn-on sensitivity upon binding with DNA. In the non-planar conformation, fluorescence quenching is predominant because electronic coupling of the donor pendant arms and acceptor heterocyclic core is not as effective due to poor overlapping between the π -orbitals.⁹⁰ Upon binding with DNA, the fluorophore undergoes a conformational change to the planar configuration where overlapping of the π -orbitals is maximized, leading to enhanced fluorescence.⁹¹ The conformational change enhances the coupling between the transition dipole of the fluorophore and internal charge transfer in each pedant arm, causing enhanced fluorescence.⁹⁰ The increase in fluorescence can be attributed to the inhibition of ultrafast isomerization of the fluorophore.⁹² This fluorescent turn-on mechanism is a key element in the molecular design of the fluorophores. With the exception of **8**, a dramatic fluorescence fold increase was noted upon binding with calf thymus dsDNA. It has been reported that the charge transfer state of the fluorophore is stabilized in polar solvents.³¹ Thus, fluorescence

quenching is observed in the absence of DNA due to the free rotation in the pendant arms.

The Stokes shift is a critical property for biological applications. Stokes shifts greater than 80 nm are of considerable interest because the reabsorption of photons is minimized,¹ which have applications in quantitative determination, bioimaging, and fluorescence assay.^{91,93} Moreover, there are disadvantages of fluorophores with low Stokes shifts, such as self-quenching and measurement error by both excitation and scattering light.⁹⁴ The results imply that a stronger electron accepting central core leads to a smaller Stokes shift regardless of the conjugation length. In addition, increasing conjugation length on a single pendant arm resulted in a larger Stokes shift. This is significant as it indicates that the Stokes shift of a fluorophore can be tailored. The smaller Stokes shift of **5** can be directly related to the electron accepting properties of the difluoroboron β -diketonate heterocyclic core. Such inclusions lead to a smaller geometry relaxation of the molecular framework when excited.⁹⁵ The geometry of the S_1 state is more similar to the geometry of the S_0 state. Hence, the emission energy is not significantly lower than the excitation energy, which results in a reduced Stokes shift. On the contrary, **4** had the largest Stokes shift. The large Stokes shift of **4** indicates a large vibrational, electronic, and geometric difference in the excited state reached immediately after absorption.^{91,96}

The optical properties of the fluorophores were further examined by investigating the excited-state dynamics utilizing time-resolve spectroscopy. Emission dynamics can be utilized to understand the fluorophore as the fluorescence lifetime is sensitive to the environment and local motion of the fluorophore.⁷⁵ As shown in the results, the

fluorescence lifetime decreases as the electron accepting properties of the core is increased in the case of the fluorophores without increased conjugation on the pendant arms. It is important to note that the fluorescence lifetime did not always correlate with the quantum yield. For example, **5** displayed the fastest lifetime (10.6 ps) although the quantum yield ($\Phi = 0.009$) was the largest while **4** exhibited a significantly longer lifetime (30.6 ps), but yielded a slightly lower quantum yield ($\Phi = 0.006$). The incorporation of a difluoroboron β -diketonate core led to a faster fluorescence lifetime regardless of conjugation length. This can be rationalized due to the increase in the competing radiative pathways because of the stronger electron acceptor core. Since the fluorescence lifetime increases with increasing ICT character,⁶⁹ the difluoroboron β -diketonate core likely causes a weaker ICT, leading to a faster fluorescence decay. Interestingly, **8** did not follow the trend. It is also important to note that increasing conjugation length on a single pendant arm resulted in a longer-lived fluorescence lifetime as shown with both **2** and **6**. These observations can be explained by the electronic structure calculations.

The trends in the excited-state dynamic studies can be rationalized by interpreting the electronic structure calculations. As noted, in the case of the fluorophores with the same structural motif, a decrease in the fluorescence lifetime was observed as the electron accepting properties of the central heterocyclic core was enhanced with the exception of **8**. This can be explained by the ICT character of the molecule, which is due to the relaxation of the excited state by twisting of a single bond between the donor and acceptor moieties. It has been reported that ICT states may lead to charge separation by structural reorganization, which is an irreversible process.⁹⁷ Additionally, maximum

charge separation occurs between the donor and acceptor moieties of a molecule because of minimum overlap of the orbitals.⁶⁹ The difference in the charge separation affects ICT character, which can influence the fluorescence lifetime as shown in the results. By comparing the fluorophores without increased conjugation length on the pendant arms, **4** displayed the longest fluorescence lifetime while **5** exhibited the fastest fluorescence lifetime. Illustrated in the electronic structure calculations, the HOMO of **4** was mainly localized on a single pendant arm whereas the HOMO was more delocalized for **5**, which indicates that **4** exhibits more ICT character. As a result, the fluorophore with greater ICT character will exhibit a longer fluorescence lifetime.

Although the central core of **3** is a weaker electron acceptor, **8** surprisingly displayed the longest long-lived fluorescence decay in the case of the fluorophores that possess increased conjugation length on both pendant arms. Represented in the electronic structure calculations, **8** exhibited significant ICT character as the HOMO was localized on a single pendant arm, which explains the fluorescence lifetime results. Dicyanomethylene pyran derivatives have been extensively studied as dopants for organic light emitting diodes (OLED).⁹⁸⁻¹⁰⁰ **8** is a symmetric derivative of 4-(dicyanomethylene)-2-methyl-6-(4-dimethylaminostyryl)-4H-pyran (DCM), which is a well-known laser dye. The dicyano group possesses strong electron accepting properties. Additionally, the pyran ring is electron deficient, which can act as an auxiliary acceptor.¹⁰¹ The symmetric structure of **8** indicates that it has two ICT routes. This infers that **8** has two excited states with similar energy levels. The low quantum yield of **8** ($\Phi = 0.002$) suggests that the fluorescence emission solely originates from the ICT from the donor to the acceptor moieties.¹⁰² Upon excitation, the first locally excited state is

reached, which is non-emissive. The ICT state is then reached, which leads to enhanced charge separation.¹⁰³ The electronic structure calculations correlated with the experimental data, which implies that both enhanced ICT character and charge separation lead to a longer fluorescence lifetime.

While increasing conjugation length between the donor pendant arms and acceptor central core led to a bathochromic shift in the absorption, the TPA cross-section of the unbound fluorophores increased with increasing conjugation length. The increase in the TPA cross-section was more than an order of magnitude greater when comparing the fluorophores containing the same electron accepting core with and without increased conjugation length on both pendant arms. These implications suggest that the transition dipole increases with increasing conjugation length, which can be rationalized by the electronic structure calculations. Summarized in Table 4.6, the ground state and transition dipole moments were calculated. It has been reported that the TPA cross-section is dependent on the transition dipole moment of a molecule.¹⁰⁴ In the case of the fluorophores that possess a pyrimidinol and difluoroboron β -diketonate core, the transition dipole increased with increasing conjugation length. It has been shown that, in general, extending π -conjugation leads to a larger TPA cross section.¹⁰¹ Additionally, it has been previously reported that molecules with a donor- π -acceptor- π -donor motif exhibit high TPA activity.^{17,105,106} This suggests that there is stronger electronic coupling between the pendant arms and central heterocyclic core for the fluorophores that possess increased conjugation length, which gives rise to a larger TPA cross-section.^{107,108} Interestingly, the TPA cross-section of **8** was more than a magnitude higher than **4** although the calculated transition dipoles were similar. However, the ground state dipole

of **4** and **8** were significantly different. It has been reported that TPA cross-section is dependent on the nature of the ground state and excited state.¹⁰⁹ Therefore, the difference in the TPA cross-section between **4** and **8** can be attributed to the ground state and transition dipole moments as well as the conjugation length. Moreover, the steady-state absorption spectra can serve as an effective representation relative to the TPA cross-sections. As detailed in Figure 2A, **8** demonstrated greater absorption at 400 nm compared to **4**. The TPA cross-section measured at 800 nm is attributed to the $S_0 \rightarrow S_1$ electronic transition for **4**. On the contrary, the TPA cross-section of **8** is due to the $S_0 \rightarrow S_n$ electronic transition. This assignment seems probable because **8** exhibited a bimodal absorption band with the higher energy absorption band near 400 nm whereas **4** displayed a single absorption band. Hence, it is likely that these electronic transitions are also contributing to the dramatic contrast in the TPA cross-sections.

CD spectroscopy was employed to investigate the DNA-binding interactions of the fluorophores. Overall, the positive ICD bands correspond well with the absorption bands, which can be assigned to the transition along the long axis of the molecule.⁶¹ Interestingly, all the fluorophores displayed a bisignate shape in the presence of DNA with the exception of **8**. Because of this, it is difficult to determine the DNA-binding mode with solely the use of CD. A major issue with CD is that the DNA-binding mode cannot be determined unambiguously without the inclusion of other techniques.¹⁰ In previous reports, it has been noted that the common methodologies, such as CD and LD, to evaluate the DNA-binding must be made with caution because a combination of selected methods only provides sufficient information to determine the DNA-binding mode.^{11,110,111} In particular, the direction of the transition dipole must be known in order

to provide detailed information regarding the orientation of the fluorophore relative to the DNA structure by CD.⁶ In order to better understand the DNA-binding mechanism, our developed TPA methodology was implemented.

The DNA-binding mode of the fluorophores that possess a difluoroboron β -diketonate core could not be determined unambiguously by only CD. Therefore, TPA was employed to investigate the DNA-binding mechanism. TPA can provide valuable information that is inaccessible with steady-state spectroscopy. The TPA cross-section is directly proportional to the square of the transition dipole moment and change of the static dipole moment after excitation. Hence, TPA can detect changes in environmental conditions, charge transfer character, and excited-dipoles with high sensitivity.²⁵ Many factors play an important role on the TPA cross-section, such as conjugation length, molecular planarity, efficiency of intramolecular charge transfer (ICT), vibronic coupling, properties of charge transfer network, and electron donating and accepting properties.^{17,112} In our previous report, it was shown that the local DNA electric field can influence the transition dipole of the binding molecules, which affects the TPA cross-section of the fluorophore upon DNA binding.³⁴ As shown in the results, **5** and **6** displayed an overall decreasing TPA cross-section trend as the concentration of DNA was increased, indicating that the fluorophores are intercalating with DNA. This is critical as it illustrates a major drawback of CD to determine the DNA-binding mode of small organic molecules whereas our TPA approach can determine the DNA-binding mode unambiguously. This is important if the direction of the transition dipole of the fluorophore is unknown since it is required to assess the DNA-binding mode by CD. Another issue with CD is that the signal indicative of an intercalating binding mode may

not be observed because a stronger, more intense signal due to other interactions, such as aggregation, can overwhelm the intercalating signal.¹¹³

Based on the results, it was confirmed that an induced change in the DNA-binding mode can be achieved by varying the electron accepting properties of the central heterocyclic core while conjugation length between the electron donor arms and electron acceptor core did not influence the DNA-binding mode. This is significant as crescent shaped DNA-binding molecules have been reported to groove bind with DNA because they can match the curvature of the DNA groove for binding.³⁰ Herein, we demonstrated that crescent shaped molecules can bind with DNA through intercalation, which does not obey the classical model for groove binding. This is in strong contrast to other intercalative binding molecules as they generally adopt planar structural scaffolds. The induced change in the DNA-binding mode can be explained by the charge-transfer interactions between an intercalator and DNA nucleobases. Previous calculation studies have shown that intercalators, such as ethidium bromide, are good electron acceptors that exhibit large charge delocalization while DNA base pairs are good electron donors.⁸¹ As the electron accepting properties of the central heterocyclic core is increased, we observe an induced change in the DNA-binding mode from groove binding to intercalation by modifying the hydroxypyrimidine to a difluoroboron β -diketonate central core. This implies that intercalating molecules are not only stabilized by interactions, such as electrostatic and dispersion interactions, but also charge-transfer contributions.⁸¹ Charge-transfer reactions can occur over short distances (on the order of Angstroms),¹¹⁴ which provide evidence of charge-transfer interactions between the DNA nucleobases and intercalating fluorophore. This is significant as it suggests that the DNA-binding mode

can be tailored by modifying the electron accepting properties of the central heterocyclic core. Based on these conclusions, one would elucidate that **8** would bind with DNA through intercalation. Although the electron accepting properties of the central core is increased for **8**, the experimental data indicates that the fluorophore does not bind with DNA.

The findings substantiate that **8** is neither intercalating nor groove binding with DNA. Narrowing of the emission band was not noted as well as a low fluorescence enhancement (1.3-fold) in the presence of DNA support the claim that **8** is not binding with DNA. Moreover, an ICD signal was not detected for **8** in the presence of DNA. This implies that the fluorophore is not binding with DNA, but rather electrostatically interacting with DNA. This was further supported by the anisotropy data as **8** exhibited a rotational correlational time of 2.3 ns in the presence of DNA, suggesting some sort of interaction between the fluorophore and DNA. The *N*-methylpiperazine recognition units can electrostatically interact with the negatively charged DNA helical axis. The results confirm that the dicyanomethylene pyran core is responsible for **8** not binding with DNA since **3** and **7** were found to bind with DNA. The required interactions for DNA-binding with the DNA nucleobases, such as van der Waals and/or hydrogen bonding interactions, is directly due to the dicyanomethylene pyran preventing these interactions. It has been reported that the orientation of a molecule upon binding with DNA can be directly related to the electrostatic and steric effects.⁸¹ Thus, the dicyanomethylene substituent may undergo steric hindrance with the DNA nucleobases, which does not allow the fluorophore to fit in the groove or pocket of DNA.

The performance of the fluorophores was evaluated by carrying out a series of bio-imaging experiments. Several TPA active molecules are not biocompatible due to poor water solubility or form non-fluorescent aggregates in aqueous solution. Therefore, water soluble DNA-binding fluorophores that demonstrate TPA properties are consequently rare.¹¹⁵ Water soluble fluorophores that exhibit TPA properties with large upconversion fluorescence yields have attracted considerable interest in the development of fluorescent probes towards biological applications. The results indicate that **1** is the most suitable for biological applications because of the reasonable Stokes shift (5790 cm^{-1}) and large fluorescence fold increase (74-fold) upon binding with DNA. Additionally, **1** was previously reported to exhibit low cytotoxicity, sufficient photostability, and possess high water solubility.³¹ Based on the bio-imaging experiments, **1** displayed a high signal-to-noise ratio as well as low cytoplasm staining. The staining of the nuclei was pronounced and distinguishable compared to the remaining fluorophores. Consequently, **1** offers significant advantages over commercial fluorescent nuclear dyes. Although **4** demonstrated the largest TPA cross-section enhancement upon binding with DNA, the staining contrast between the nuclei and cytoplasm was not as predominant. In addition, an issue with **4** is that the maximum absorption is near 352 nm in the presence of DNA. As a consequence, **4** requires a higher energy excitation wavelength, which is undesirable for bio-imaging applications requiring single-photon excitation. In particular, **1** demonstrated promising bio-imaging properties, suggesting that it can be used as an invaluable tool to detect and monitor regions of DNA, which opens further applications.

4.6 Conclusion

In summary, we developed a design strategy that allows tailoring of the DNA-binding mode by investigating a series of novel fluorescent nuclear dyes that exhibit high turn on/off sensitivity upon binding with DNA. Steady-state spectroscopy, nonlinear ultrafast spectroscopy, and electronic structure calculations were employed to examine the optical properties and DNA-binding interactions of the fluorophores. The findings imply that the optical properties can be finely tuned by varying the conjugation length as well as the electron accepting properties of the central heterocyclic core. Moreover, bio-imaging experiments were carried out to evaluate the performance of the fluorophores by confocal fluorescence microscopy in which **1** was found to possess excellent properties towards bio-imaging applications.

By investigating the DNA-binding mechanism, a structure-property relationship was established for DNA-binding molecules that adopt a crescent donor-acceptor-donor motif. The results reveal that the DNA-binding mode can be tailored by implementing structural modifications to the central heterocyclic core. This was achieved by simply replacing the central heterocyclic core from a pyrimidine-based moiety with a difluoroboron β -diketonate moiety, which induced a change in the DNA-binding mode from groove binding to intercalation, respectively. While increasing conjugation length between the electron donating arms and electron accepting core of the fluorophore did not induce a change in the DNA-binding mode, this implies that the central heterocyclic core plays a critical role in the DNA-binding mechanism. This is the first report that has demonstrated structure-property relationships for a design strategy where the DNA-binding mode can be tailored in the case of DNA-binding molecules that possess a

crescent donor-acceptor-donor motif. The impact of this work opens new strategies for the design and development of therapeutics targeted at DNA as their performance is dependent on the DNA-binding mechanism.

References

1. Araneda, J. F.; Piers, W. E.; Heyne, B.; Parvez, M.; McDonald, R. *Angew. Chem. Int. Ed. Engl.* **2001**, *50*, 12214.
2. Suzuki, T.; Fujikura, K.; Higashiyama, T.; Takata, K. *J. Histochem. Cytochem.* **1997**, *45*, 49.
3. Jin, L.-T.; Choi, J.-K. *Electrophoresis* **2004**, *25*, 2429.
4. Kapuscinski, J. *Biotech. Histochem.* **1995**, *70*, 220.
5. Gläser, K.; Wilke, K.; Wepf, R.; Biel, S. S. *Skin Res. Technol.* **2008**, *14*, 324.
6. Armitage, B. A. In DNA binders and related subjects. Springer Berlin Heidelberg. pp. 55–76 (2005).
7. Kanony, C.; Åkerman, B.; Tuite, E. *J. Am. Chem. Soc.* **2001**, *123*, 7985.
8. Nocker, A.; Sossa-Fernandez, P.; Burr, M. D.; Camper, A. K. *Appl. Environ. Microbiol.* **2007**, *73*, 5111.
9. Zhao, H.; Traganos, F.; Dobrucki, J.; Wlodkovic, D.; Darzynkiewicz, Z. *Cytometry. A* **2009**, *75*, 510.
10. Ihmels, H.; Otto, D. *Top Curr. Chem.* **2005**, *258*, 161.
11. Suh, D.; Chaires, J. B. *Bioorg. Med. Chem.* **1995**, *3*, 723.
12. Chattoraj, M.; King, B. A.; Bublitz, G. U.; Boxer, S. G. *Proc. Natl. Acad. Sci. U. S. A.* **1996**, *93*, 8362.

13. Welch, J. J.; Rauscher, F. J.; Beerman, T. A. *J. Biol. Chem.* **1994**, *269*, 31051.
14. Tse, W. C.; Boger, D. L. *Chem. Biol.* **2004**, *11*, 1607.
15. Berman, H. M.; Young, P. R. *Annu. Rev. Biophys. Bioeng.* **1981**, *10*, 87.
16. Mukherjee, A.; Lavery, R.; Bagchi, B.; Hynes, J. T. *J. Am. Chem. Soc.* **2008**, *130*, 9747.
17. Albota, M. *et al. Science* **1988**, *281*, 1653.
18. Wang, Y.; He, G. S.; Prasad, P. N.; Goodson, T. *J. Am. Chem. Soc.* **2005**, *127*, 10128.
19. Bhaskar, A. *et al. J. Am. Chem. Soc.* **2006**, *128*, 11840.
20. Narayanan, A.; Varnavski, O. P.; Swager, T. M.; Goodson, T. *J. Phys. Chem. C* **2008**, *112*, 881.
21. Yan, X.; Goodson, T.; Imaoka, T.; Yamamoto, K. *J. Phys. Chem. B* **2005**, *109*, 9321.
22. Laine, R. M. *et al. J. Am. Chem. Soc.* **2010**, *132*, 3708.
23. Varnavski, O. P.; Goodson, T.; Mohamed, M. B.; El-Sayed, M. A. *Phys. Rev. B* **2005**, *72*, 235405.
24. Ramakrishna, G.; Bhaskar, A.; Goodson, T. *J. Phys. Chem. B* **2006**, *110*, 20872.
25. Drobizhev, M.; Makarov, N. S.; Tillo, S. E.; Hughes, T. E.; Rebane, A. *Nat. Methods* **2001**, *8*, 393.
26. Clark, T. B.; Orr, M. E.; Flynn, D. C.; Goodson, T. *J. Phys. Chem. C* **2001**, *115*, 7331.
27. McLean, A. M. *et al. J. Phys. Chem. B* **2013**, *117*, 15935.
28. Clark, T. B.; Ziółkowski, M.; Schatz, G. C.; Goodson, T. *J. Phys. Chem. B* **2014**,

118, 2351.

29. Wang, Y.; Clark, T. B.; Goodson, T. *J. Phys. Chem. B* **2010**, *114*, 7112.
30. Munde, M. *et al. J. Am. Chem. Soc.* **2007**, *129*, 13732.
31. Pitter, D. R. G. *et al. Org. Lett.* **2013**, *15*, 1330.
32. Wheelhouse, R. T. *et al. J. Med. Chem.* **2006**, *49*, 5187.
33. Qing, F.; Wang, R.; Li, B.; Zheng, X.; Meng, W.-D. *J. Fluor. Chem.* **2003**, *120*, 21.
34. Doan, P. H.; Pitter, D. R. G.; Kocher, A.; Wilson, J. N.; Goodson III, T. *J. Am. Chem. Soc.* **2015**, *137*, 9198.
35. Pitter, D. R. G.; Brown, A. S.; Baker, J. D.; Wilson, J. N. *Org. Biomol. Chem.* **2005**, *13*, 9477.
36. Xu, C.; Webb, W. W. *J. Opt. Soc. Am. B* **1996**, *13*, 481.
37. Lahankar, S. A. *et al. J. Chem. Phys.* **2004**, *120*, 337.
38. Varnavski, O.; Goodson, T. *Chem. Phys. Lett.* **2000**, *320*, 688.
39. Furgal, J. C.; Goodson III, T.; Laine, R. M. *Dalton Trans.* **2016**, *45*, 1025.
40. Schmidt, M. W. *et al. J. Comput. Chem.* **1993**, *14*, 1347.
41. Hanwell, M. D. *et al. J. Cheminform.* **2012**, *4*, 4.
42. Allouche, A.-R. *J. Comput. Chem.* **2001**, *32*, 174.
43. Strekowski, L.; Wilson, B. *Mutat. Res.* **2007**, *623*, 3.
44. Biros, S. M. *et al. Bioorg. Med. Chem. Lett.* **2007**, *17*, 4641.
45. Ellinger, S. *et al. Chem. Mater.* **2001**, *23*, 3805.
46. Feit, M. D. *J. Chem. Phys.* **1983**, *78*, 301.
47. Xu, S. *et al. Inorg. Chem.* **2013**, *52*, 3597.

48. Cosa, G.; Focsaneanu, K.-S.; McLean, J. R. N.; McNamee, J. P.; Scaiano, J. C. *Photochem. Photobiol.* **2007**, *73*, 585.
49. Furse, K. E.; Corcelli, S. A. *J. Am. Chem. Soc.* **2008**, *130*, 13103.
50. Reynisson, J. *et al.* *J. Am. Chem. Soc.* **2003**, *125*, 2072.
51. Matsumi, N.; Chujo, Y. *Polym. J.* **2007**, *40*, 77.
52. Miyata, M.; Chujo, Y. *Polym. Bull.* **2003**, *51*, 9.
53. Kuśba, J.; Lakowicz, J. R. *J. Chem. Phys.* **1999**, *111*, 89.
54. Eriksson, M.; Nordén, B. *Methods Enzymol.* **2001**, *340*, 68.
55. Nordén, B.; Kurucsev, T. *J. Mol. Recognit.* **1994**, *7*, 141.
56. Rizzo, V.; Schellman, J. A. *Biopolymers* **1984**, *23*, 435.
57. Kubista, M.; Aakerman, B.; Norden, B. *J. Phys. Chem.* **1988**, *92*, 2352.
58. Tanious, F. A. *et al.* *Biochemistry* **2000**, *39*, 12091.
59. Seifert, J. L.; Connor, R. E.; Kushon, S. A.; Wang, M.; Armitage, B. A. *J. Am. Chem. Soc.* **1999**, *121*, 2987.
60. Wilson, W. D. *et al.* *J. Am. Chem. Soc.* **1998**, *120*, 10310.
61. Wilson, J. N. *et al.* *J. Phys. Chem. B* **2013**, *117*, 12000.
62. Garbett, N. C.; Ragazzon, P. A.; Chaires, J. B. *Nat. Protoc.* **2007**, *2*, 3166.
63. Corradini, R.; Sforza, S.; Tedeschi, T.; Marchelli, R. *Chirality* **2007**, *19*, 269.
64. Woo, H. Y. *et al.* *J. Am. Chem. Soc.* **2005**, *127*, 14721.
65. Drobizhev, M. *et al.* *J. Am. Chem. Soc.* **2006**, *128*, 12432.
66. Ogawa, K.; Ohashi, A.; Kobuke, Y.; Kamada, K.; Ohta, K. *J. Am. Chem. Soc.* **2003**, *125*, 13356.
67. Liu, Z. *et al.* *Chem. Commun.* **2008**, 2260.

68. Zama, M.; Ichimura, S. *Biopolymers* **1970**, *9*, 53.
69. Grabowski, Z. R.; Rotkiewicz, K.; Rettig, W. S *Chem. Rev.* **2003**, *103*, 3899.
70. Stsiapura, V. I. *et al. J. Phys. Chem. B* **2008**, *112*, 15893.
71. Todd, D. C. *et al. J. Chem. Phys.* **1990**, *93*, 8658.
72. Banerjee, D.; Pal, S. K. *Chem. Phys. Lett.* **2006**, *432*, 257.
73. Blanchard-Desce, M.; Wortmann, R.; Lebus, S.; Lehn, J.-M.; Krämer, P. *Chem. Phys. Lett.* **1995**, *243*, 526.
74. Roncali, J. *Macromol. Rapid Commun.* **2007**, *28*, 1761.
75. Lakowicz, J. *Principles of Fluorescence Spectroscopy*; 3rd ed.; Springer Science Business Media: New York, 2006; pp 47, 243, 358– 359, 588.
76. Flynn, D. C. *et al. J. Am. Chem. Soc.* **2010**, *132*, 1348.
77. Chib, R. *et al. Methods Appl. Fluoresc.* **2014**, *2*, 1.
78. Abdel-Mottaleb, M. S. A.; Sherief, A. M. K.; Ismaiel, L. F. M., De Schryver, F. C.; Vanderauweraer, M. A. *J. Chem. Soc. Faraday Trans.* **1989**, *85*, 1779.
79. Magde, D.; Zappala, M.; Knox, W. H.; Nordlund, T. M. *J. Phys. Chem.* **1983**, *87*, 3286.
80. Millar, D. P.; Robbins, R. J.; Zewail, A. H. *Proc. Natl. Acad. Sci. U. S. A.* **1980**, *77*, 5593.
81. Řeha, D. *et al. J. Am. Chem. Soc.* **2002**, *124*, 3366.
82. Nakatani, K.; Matsuno, T.; Adachi, K.; Hagihara, S.; Saito, I. S. *J. Am. Chem. Soc.* **2001**, *123*, 5695.
83. Tan, L.-F. *et al. Polyhedron* **2007**, *26*, 5458.
84. Umeyama, H.; Morokuma, K. *J. Am. Chem. Soc.* **1977**, *99*, 1316.

85. Haugland, R. P. Handbook of fluorescent probes and research chemicals, 9th edn. Molecular Probes, Eugene (2002).
86. Horobin, R. W.; Stockert, J. C.; Rashid-Doubell, F. *Histochem. Cell Biol.* **2006**, *126*, 165.
87. Leung, C. W. T. *et al. J. Am. Chem. Soc.* **2013**, *135*, 62.
88. Dumat, B. *et al. J. Am. Chem. Soc.* **2013**, *135*, 12697.
89. Belitsky, J. M.; Leslie, S. J.; Arora, P. S.; Beerman, T. A.; Dervan, P. B. *Bioorg. Med. Chem.* **2002**, *10*, 3313.
90. Pond, S. J. K. *et al. J. Phys. Chem. A* **2002**, *106*, 11470.
91. Peng, X. *et al. J. Am. Chem. Soc.* **2005**, *127*, 4170.
92. Fürstenberg, A. *et al. J. Am. Chem. Soc.* **2006**, *128*, 7661.
93. Xue, L.; Liu, C.; Jiang, H. *Chem. Commun.* **2009**, 1061.
94. Zhou, Y.; Xiao, Y.; Chi, S.; Qian, X. *Org. Lett.* **2008**, *10*, 633.
95. Chen, Y.; Zhao, J., Guo; H.; Xie, L. *J. Org. Chem.* **2012**, *77*, 2192.
96. Achelle, S. *et al. J. Org. Chem.* **2009**, *74*, 3711.
97. Ghosh, R.; Palit, D. K. *J. Phys. Chem. A* **2015**, *119*, 11128.
98. Xie, Z. Y.; Hung, L. S.; Lee, S. T. *Appl. Phys. Lett.* **2001**, *79*, 1048.
99. Feng, J. *et al. Appl. Phys. Lett.* **2002**, *81*, 2935.
100. Qiao, J. *et al. Appl. Phys. Lett.* **2002**, *81*, 4913.
101. Shao, P. *et al. Opt. Mater.* **2006**, *29*, 337.
102. Guo, Z.; Zhu, W.; Tian, H. *Chem. Commun.* **2012**, *48*, 6073.
103. Bourson, J.; Valeur, B. *J. Phys. Chem.* **1989**, *93*, 3871.
104. Pawlicki, M.; Collins, H. A.; Denning, R. G.; Anderson, H. L. *Angew. Chem. Int.*

- Ed. Engl.* **2009**, *48*, 3244.
105. Hrobáriková, V. *et al.* *J. Org. Chem.* **2010**, *75*, 3053.
106. Badaeva, E. A.; Timofeeva, T. V.; Masunov, A.; Tretiak, S. *J. Phys. Chem. A* **2005**, *109*, 7276.
107. Katan, C. *et al.* *J. Phys. Chem. A* **2005**, *109*, 3024.
108. Katan, C., Tretiak, S. & Even, J. *SPIE Photonics Europe* **2010**, 7712, 7123D.
109. Goodson, T. G. *Acc. Chem. Res.* **2005**, *38*, 99.
110. Long, E. C.; Barton, J. K. *Acc. Chem. Res.* **1990**, *23*, 271.
111. Suh, D.; Oh, Y.-K.; Chaires, J. B. *Process Biochem.* **2001**, *37*, 521.
112. Reinhardt, B. A. *et al.* *Chem. Mater.* **1998**, *10*, 1863.
113. Wilson, W. D.; Barton, H. J.; Tanious, F. A.; Kong, S. B.; Streckowski, L. *Biophys. Chem.* **1990**, *35*, 227.
114. Ly, D.; Sanii, L.; Schuster, G. B. *J. Am. Chem. Soc.* **1999**, *121*, 9400.
115. Abbotto, A. *et al.* *Biophys. Chem.* **2005**, *114*, 35.

Chapter 5

Photophysical Investigation and Imaging of Sox-Based Fluorescence Chemosensor Peptide for Kinase Activity with Continuous Real-Time Analysis in Live Cells

5.1 Explanation

The objective of this project was to examine the activity of kinase enzymes with continuous real-time analysis in live cells. This project was done in collaboration with Prof. Barbara Imperiali at Massachusetts Institute of Technology. In order to accomplish this task, a custom fluorescent labeled peptide was implemented that allowed kinase activity to be monitored. This is the first example that has demonstrated a continuous real-time analysis of kinase activity in live cells. This work is significant as it allows for the study of kinase activity at physiological conditions, which is critical for drug research and development. Abnormal kinase activity has been associated with several disorders, such as cancer and diabetes. Therefore, it is important to better understand the activity of kinase enzymes because they are essential in nearly all biological processes. The work presented in this chapter is the preliminary results. The project will be resumed by a new graduate student.

5.2 Introduction

Signaling in biological systems is critical for many cellular and biological processes, which are regulated by protein phosphorylation. Such processes are complex and strategically orchestrated by diverse cellular species. More importantly, signaling cascades are important for cellular function, such as mediating cell proliferation and apoptosis.¹ The transmission of signal is continued through a series of biochemical changes within the cell or cell membrane. A major component of cellular signaling is to control and maintain normal physiological equilibrium within the cell. Thus, many diseases are directly related to an abnormal cellular signaling process. Because of their complexity, understanding these processes remains a challenge in biochemistry.

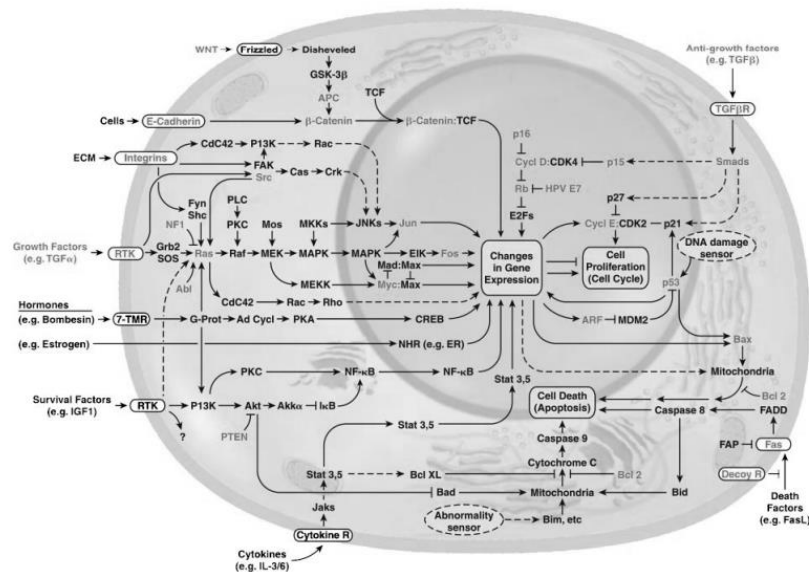


Figure 5.1. Signaling pathways of a cell.

In order to treat disorders and diseases, several biological and cellular processes have been examined. One process of considerable interest is targeting protein kinases, which

have become major targets for therapy. Kinases are enzymes that are responsible for phosphorylating peptides and proteins, which can modify their functions. It has been shown that protein phosphorylation regulates various cellular functions, such as cell proliferation, metabolism, motility, and apoptosis.² Therefore, disruption of protein phosphorylation can alter cellular functions, thus leading to severe disorders. Over 500 types of kinases are known to exist in the human genome in which 478 are typical and 40 are atypical.³ Typical kinases are divided into those that phosphorylate serine, threonine or tyrosine residues. On the other hand, atypical kinases have been reported to exhibit biochemical kinase activity, but lack sequence similarities to the conventional eukaryotic kinases.³ The phosphorylation process is essential for cellular communication and signaling. In particular, protein substrate phosphorylation can have pronounced effects on many biological and cellular processes. For example, phosphorylation can lead to enzyme activation and deactivation as well as the development of sites for other biological entities.² A major component of cellular signaling is to control normal physiological balance within the cell. Thus, many diseases are directly related to an abnormal cellular signaling process. Oncology drug discovery has significantly benefited from understanding kinase activity. In fact, kinase inhibitors are currently being studied as new therapeutics aimed at cancer.

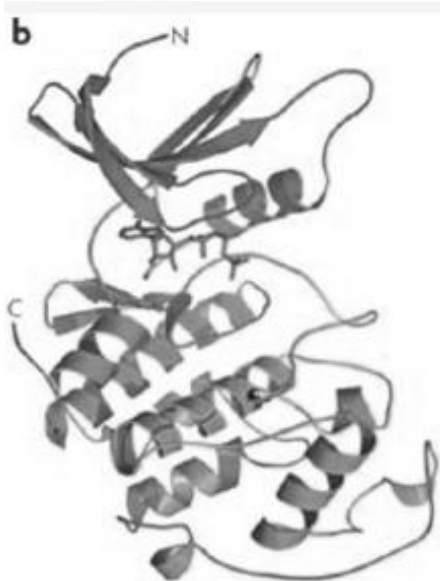


Figure 5.2. Cartoon representation of kinase enzymes.

In general, kinases consist of nearly 250 amino acids, which are composed of β -sheets at the N-terminus and α -helices (20 – 35 residues) at the C-terminus as illustrated in Figure 5.2.³ The phosphorylation of the peptide/protein substrate takes place at the phosphorylation-site or P-site. In order for the phosphorylation process to occur, ATP binds to the cleft between the β -sheets and α -helices in which the adenosine moiety is buried in the hydrophobic pocket with the phosphate moiety directed away from the enzyme. The protein prone to phosphorylation binds along the cleft at a specific site of residues. The γ -phosphate of ATP is then transferred to the amino acid undergoing phosphorylation (Ser, Thr, Tyr). In the active conformation, the α -helix packs against the N-terminal lobe and the aspartate of the DFG (Asp-Phe-Gly) motif chelates to Mg^{2+} to orientate ATP for phosphorylation as depicted in Figure 5.3. In the inactive conformation, this interaction is disrupted so that the phenylalanine of the DFG motif is directed towards the ATP site.⁴ The specificity of the kinase to phosphorylate a specific

residue is based on the depth of the catalytic cleft. Tyr-specific kinases have deeper catalytic clefts compared to Ser/Thr kinases. However, it is important to note that the P-site is not always specific. For example, there have been reports where Ser/Thr kinases phosphorylate Tyr residues whereas the opposite is consequently rare.⁵

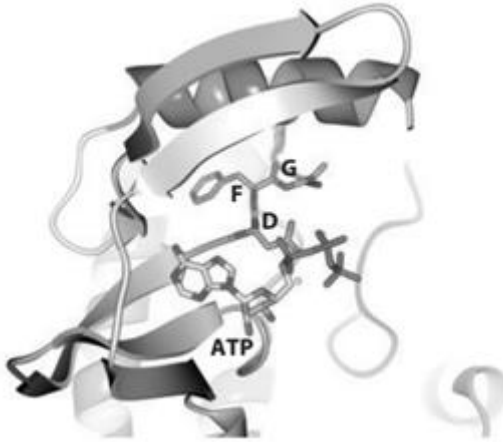


Figure 5.3. DFG motif location on kinase enzyme. These residues are responsible for preparing ATP for phosphorylation.

Peptide and protein phosphorylation is one of the most important and vital mechanism for cellular signaling and communication.⁶ Kinases are responsible for protein phosphorylation, which initiate and relay phosphorylation signals in intracellular pathways. This cycle is catalytic and very complex as detailed in Figure 5.4. Most kinases display specificity for the regions near the phosphorylation site or require recognition sites. The preference in recognition regions allows the kinase to fit and mold the region of the protein substrate. The transfer of the phosphoryl group is relatively simple, but is dependent on the correct orientation of the kinase, protein substrate, γ -phosphate of ATP, and hydroxyl substituent on the residue prepared for phosphorylation.⁴ Interestingly, it has been reported that Mg^{2+} is required for

phosphorylation to stabilize the negative charge that is developed the bridging oxygen.⁷ The transfer of the phosphoryl group is comprised of three steps: (i) orientation of the kinase and protein substrate; (ii) nucleophilic attack by the substrate hydroxyl substituent; (iii) acid catalysis for the proton transfer.⁴ The kinase activity is very complex, but was simplified for our purpose. In fact, many human diseases, especially cancer, are associated with abnormal protein phosphorylation.⁸ Hence, understanding kinase activity or protein phosphorylation is important for the development of therapeutic drugs. Additionally, kinase inhibitors are of interest for the development of cancer related drugs.⁹ In order to investigate protein kinase activity, sensors provide a means to elucidate protein-kinase interactions and allow for screening of potential therapeutics.

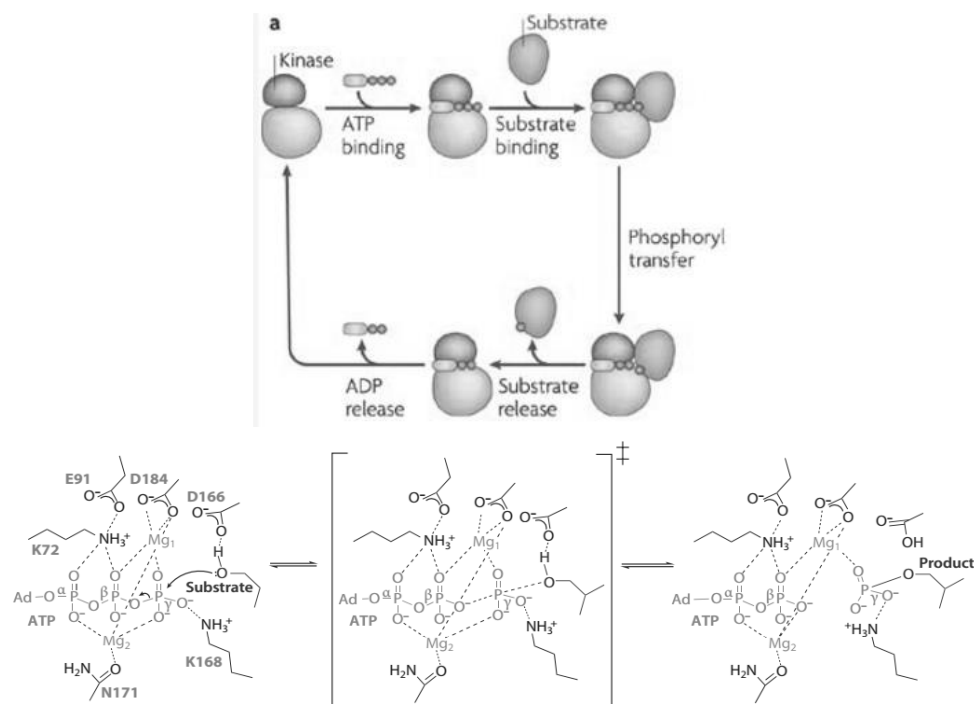


Figure 5.4. (Top) Catalytic cycle of kinase phosphorylation of peptide/protein substrate and (bottom) simplified schematic diagram of protein kinase mechanism.

Traditional methods have been employed to examine protein kinase activity, such as the use of radioactive-based assays where the phosphoryl transfer from [γ - ^{32}P]ATP to a substrate or protein is quantified by scintillation counting. An issue with this approach is that it requires handling of radioactive material and is not practical for high-throughput applications. Another limitation is that the method is a discontinuous assay, meaning that it cannot be used for real-time analysis. Furthermore, radioactive-based assays require significantly lower concentrations of ATP (10 – 50 μM), which reduces the activity of most kinases, leading to poorer resolution and sensitivity as well as the loss of kinetic information.¹⁰ Understanding kinase activity at physiological conditions is critical for drug research and development. The process of employing such assays are time-consuming as require immunopurification of the kinase from cell lysates and the proper disposal of radioactive material.¹¹ Other approaches to monitor and examine kinase activity are of considerable interest.

Continuous fluorescence-based assays are desirable because they can extract information relative to kinase activity with continuous real-time analysis. These assays can be used for high-throughput screening and the detection of kinase activity in cell extracts as well as examining spatial and temporal localization of kinase activity *in vitro*.¹² Many continuous assays used to examine kinase activity have been reported, such as the use of fluorescence-based fluorophores adjacent to the phosphorylated residue¹³⁻¹⁵ that take advantage of the conformation change of the substrate upon phosphorylation.^{16,17} However, these assays demonstrate low fluorescence changes, limiting their applicability. Hence, there remains a considerable challenge for the

development of fluorescence-based assays that demonstrate high sensitivity to monitor kinase activity.

A chelation-sensitive fluorophore 8-hydroxy-5-(N,Ndimethylsulfonamido)-2-methylquinoline (Sox) integrated into a peptide substrate via solid-phase peptide synthesis (SPPS) was previously reported for the detection of divalent metals.¹⁸ The Sox fluorophore demonstrates significant fluorescence enhancement in the presence of a divalent metal based on chelation enhanced fluorescence (CHEF). The Sox fluorophore or residue was used to develop a fluorescence-based approach to monitor kinase phosphorylation.¹² This versatile chemosensing strategy is utilized for the detection of serine, threonine, and tyrosine phosphorylation located on the N- or C-terminus of the kinase recognition motifs. The kinase recognition motifs can be tuned to target specific kinases. The Sox residue is separated from the amino acid prone to phosphorylation by a β -turn sequence, which generally consists of two or three residues. Upon phosphorylation, the turn sequence promotes a chain reversal in the peptide backbone, which allows the chelation between the Sox fluorophore and phosphorylated residue introduced by the kinase with the divalent metal resulting in fluorescence enhancement. The schematic representation of the Sox-labeled peptide is shown in Figure 5.5.

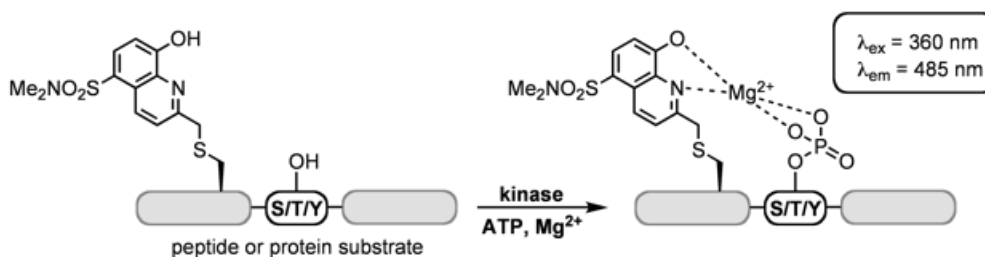


Figure 5.5. Schematic representation of Sox-labeled peptide for probing kinase activity.

In this work, we investigated the protein kinase activity utilizing a Sox-labeled peptide as a chemosensor. Steady-state and ultrafast nonlinear spectroscopies were employed to further examine the kinase activity. Additionally, we examined the kinase activity in live cells by conducting a series of bio-imaging experiments. The findings indicate that the Sox-labeled peptide can provide valuable information at physiological conditions.

5.3 Results and Discussion

The first step in this project was to investigate the steady-state properties of the Sox-peptide. We investigated the photophysical properties of the phosphorylated peptide (JNKP19). The absorption and emission spectra of JNKP19 in the absence and presence of Mg^{2+} are shown in Figure 5.6. In regards to the absorption spectra, a bathochromic shift approximately 50 nm was noted when Mg^{2+} was added to the system. This is due to energy transfer from the donor (Sox chromophore) to the acceptor (Mg^{2+}), which is typical of a donor-acceptor system. In terms of the emission spectra, the fluorescence was quenched in the absence of Mg^{2+} . In the presence of Mg^{2+} , a significant fluorescence enhancement was noted, which indicates that the Sox-peptide is highly sensitive. A fluorescence increase of over 30-fold was noted upon the addition of Mg^{2+} .

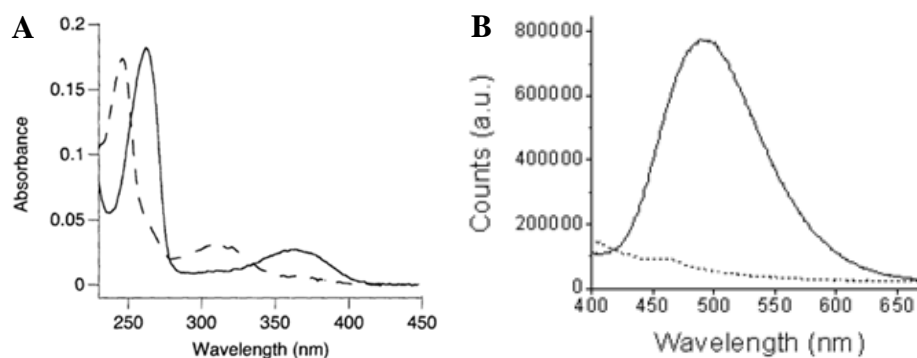


Figure 5.6. (A) Absorption and (B) emission spectra of JNKP19 in the absence (- - -) and presence (-) of 10 mM MgCl₂.

The fluorescence enhancement of the Sox fluorophore in the presence of a divalent metal, such as Mg²⁺ is due to the chelation enhanced fluorescence (CHEF) as summarized in Figure 5.7. In the absence of a divalent metal, the relaxation process of the electron in the excited state to its original ground state is prohibited. Instead, an electron from free receptor or lone pair is transferred to the ground state, resulting in quenched fluorescence. This event is also known as the photoinduced electron transfer (PET) effect. In the presence of a divalent metal, the quenching lone pair from the Sox fluorophore can chelate with the metal. As a result, the energy of the bound receptor or lone pair is reduced below the energy of the ground state of the fluorophore. In other words, the electron from the bound receptor cannot interfere with the relaxation process of the electron in the excited state, negating the PET effect. This allows the electron from the excited state to return back to the ground state, which results in fluorescence due to the CHEF effect.

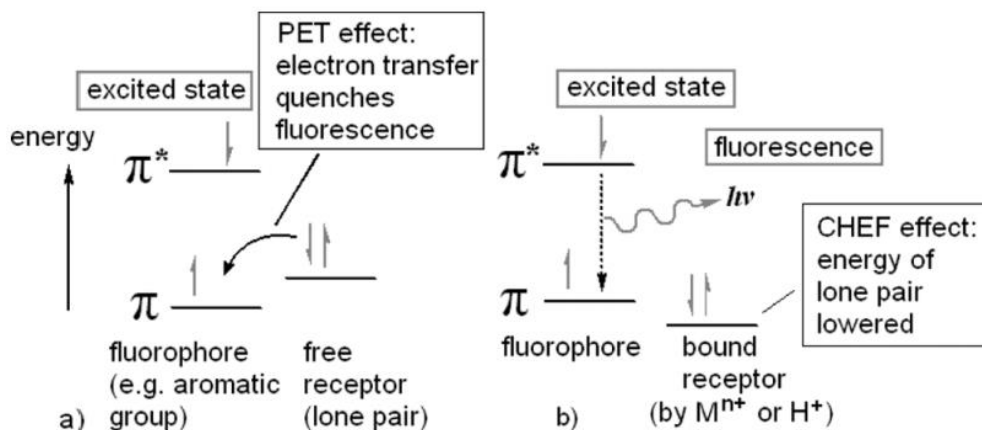


Figure 5.7. (a) Fluorescence quenched in the absence of a divalent metal due to the PET effect. (b) Fluorescence enhancement in the presence of a divalent metal due to the CHEF effect.

After our initial investigation, we examined the phosphorylation process of the kinase enzyme by employing the unphosphorylated Sox-labeled peptide (JNKS19). The steady-state spectra of JNKS19 and JNKP19 in the presence of 10 mM Mg²⁺ is presented in Figure 5.8. For JNKS19, a band near 320 nm was noted, which was not observed for JNKP19. This is likely due to the fluorophore chelating with Mg²⁺ in the absence of the phosphoryl. The chelation of the phosphoryl group contributes to a greater chelation enhancement of the Sox fluorophore, leading to the reduction of the absorption band near 320 nm for JNKS19. A fluorescence enhancement of approximately 5-fold was noted when the Sox labeled peptide is phosphorylated. This change in fluorescence will allow us to monitor the phosphorylation process.

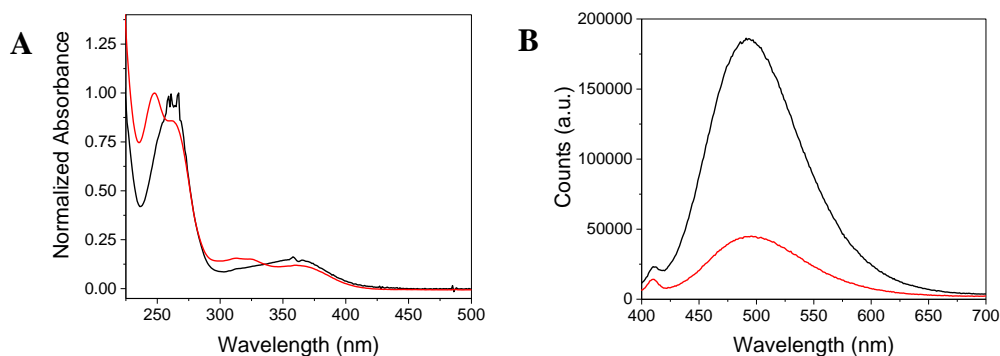


Figure 5.8. (A) Absorption and (B) emission spectra of JNKS19 (red) and JNKP19 (black) in the presence of 10 mM MgCl₂.

The phosphorylation process was monitored by employing JNKS19. The reaction was carried out at conditions of 50 mM Tris (pH 7.4), 10 mM MgCl₂, 1 mM EGTA, 2 mM DTT, 0.01% Brij-35P, 0.4 mM ATP, 2 μM JNKS19, and 0.2 ng/μL JNK2 recombinant enzyme. As shown in Figure 5.9, fluorescence measurements were collected every 5 min. The fluorescence did not change after 150 min, indicating that the peptide has become fully phosphorylated. This demonstrates that JNKS19 can be used as a kinase assay to monitor and detect kinase activity with continuous real-time analysis.

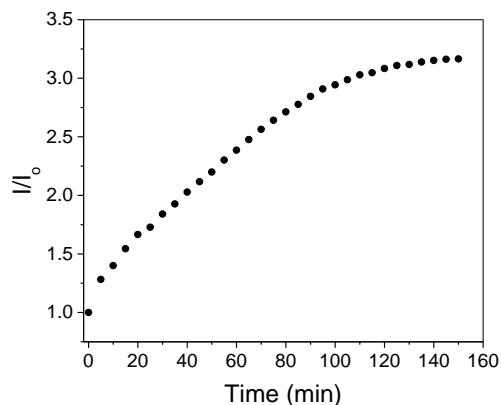


Figure 5.9. The fluorescence of JNKS19 was monitored as a function of time in the presence of JNK2, ATP, and MgCl₂.

After demonstrating that JNKS19 can be utilized to monitor kinase activity, our objective was to investigate kinase activity in live cells. In general, cell lysates or extracts are used to examine the activity of enzymes *in vitro*. However, there remain several limitations with this methodology. First, the addition or inclusion of inhibitors is required to improve sensitivity and specificity.¹⁰ Another issue using cell lysates is that the kinase activity cannot be monitored at physiological conditions. This is critical when examining newly developed drugs as its efficacy and activity can change if environmental conditions are varied. Finally, cell-based studies can simultaneously assay for compound characteristics, such as efficacy, toxicity, and cell permeability.

The first goal of this project was to transfect HeLa cells with a control fluorescein-labeled antibody to demonstrate our technique. This was accomplished by transfecting the cells using the BioPORTER transfection or protein delivery kit. 2.5 μL of transfection reagent was added to a centrifuge tube. The solvent was allowed to evaporate for 2 h to form a film. 10 μL of 100 ng/mL of the control fluorescein-labeled antibody was added and allowed to incubate at room temperature for 5 min. 250 μL of DMEM (serum-free and antibiotic-free) was added the centrifuge tube. The cells were incubated with the mixture for 4 h. The cells were imaged using confocal microscopy as shown in Figure 5.10. The cells exhibit little to no autofluorescence with an excitation wavelength of 490 nm. Clearly, fluorescence was detected after transfecting the cells with the control protein, verifying the successful transfection of the control fluorescein labeled protein.

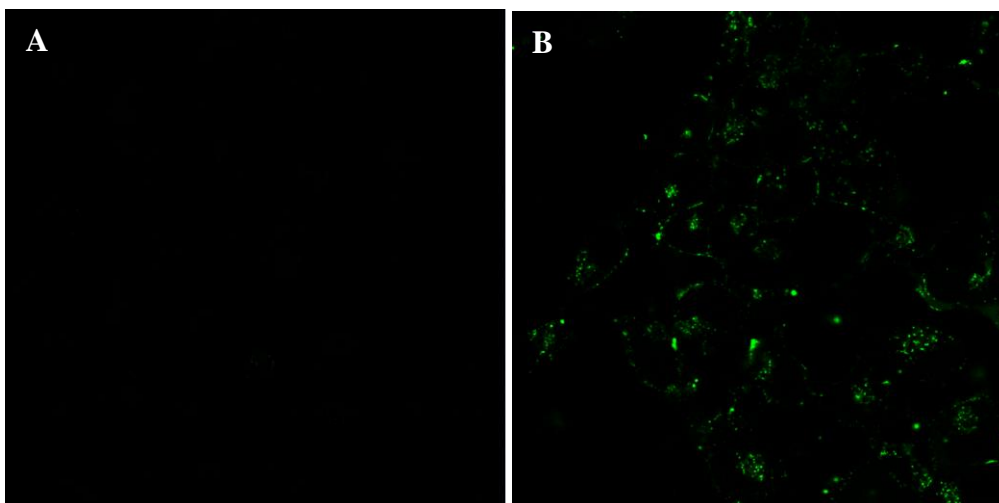


Figure 5.10. Confocal microscopy image of cells (A) before and (B) after transfection of fluoresceine labeled goat antibody. $\lambda_{\text{ex}} = 490 \text{ nm}$.

After demonstrating our transfection technique, JNKP19 was transfected into the cells as presented in Figure 5.11. It was rather difficult to determine if the peptide was successfully transfected due to the autofluorescence from the cells. There are several issues with the Sox-peptide. First, the excitation and emission wavelength is approximate to the organelles in the cells. The major contribution of autofluorescence is due to NAD(H) in the cytoplasm. Additionally, the granules are attributed to NAD(H) concentrated in the mitochondria.²⁰ Another issue with the Sox-labeled peptide is that it is dependent on the concentration of intracellular Mg^{2+} . Because of this, the sensitivity of the peptide was investigated at lower concentrations of Mg^{2+} (Figure 5.12). It is important to note that the fluorescence did not change significantly until 1 mM of MgCl_2 is reached. This indicates the Sox-peptide is not sensitive a sub-millimolar concentrations. It has been reported that the intracellular concentration of magnesium in live cells range from 5 – 20 mM with 1 – 5 % ionized or free magnesium.²¹ This suggests that the peptide is not sensitive at our experimental conditions. Thus, an increase in the

intracellular concentration of magnesium may be required to increase the sensitivity of the Sox-peptide.

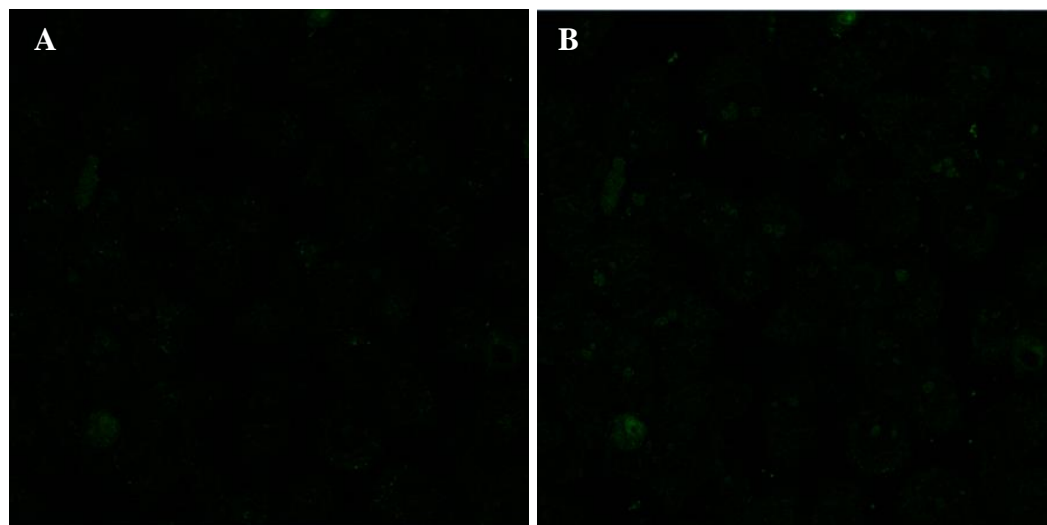


Figure 5.11. Confocal microscopy image of cells (A) before and (B) after transfection of JNKP19. $\lambda_{\text{ex}} = 780 \text{ nm}$.

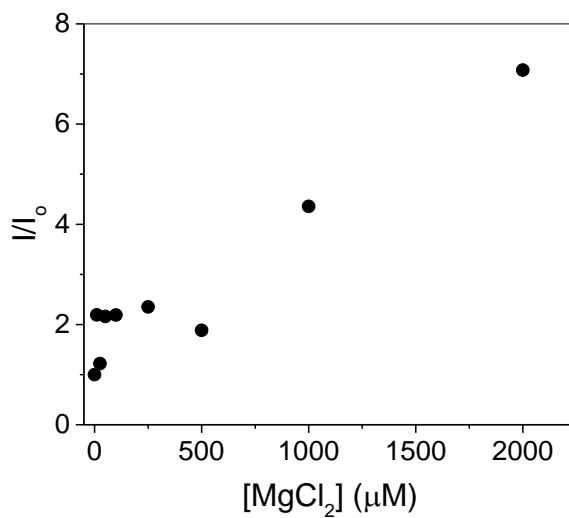


Figure 5.12. Fluorescence change of JNKP19 (5 μM) at varied concentrations of MgCl_2 .

Ionophores are chemical compounds used to transport ions across membranes, which work by reversibly binding with ions that are later transported in/out of the cell. There are two types of ionophores. First, carrier ionophores bind to specific ions while shielding its charge from the local environment, allowing the ions to bypass the membrane.²² Second, channel ionophores work by introducing a hydrophilic hole in the cell membrane that allows the ions to travel across the membrane.²³ In order to increase the intracellular concentration of ions within the cell, the medium must contain a higher concentration of ions than the cell. A23187 ionophore was used to increase the intracellular concentration of magnesium. This ionophore was selected because it has been extensively studied and exhibits low cytotoxicity. The ionophore forms stable 2:1 complexes with divalent metals, such as magnesium and calcium²⁴ to transport them across the membrane. In fact, the ionophore shields the charge of the ions, rendering them soluble in organic solvents. Although the ionophore increases the intracellular concentration of magnesium, there remain issues with the autofluorescence from the cells.

In order to distinguish between the Sox-peptide from the autofluorescence, fluorescence lifetime imaging microscopy (FLIM) was employed. As noted above, a majority of the autofluorescence is due to NAD(H). The fluorescence lifetime of JNKP19 was examined at various concentrations of MgCl₂ as shown in Figure 5.13. The fluorescence lifetimes are summarized in Table 5.1 The shorter component is relatively the same regardless of the concentration of MgCl₂, which is likely due to the non-chelated Sox-fluorophore. The longer component is attributed to the Sox-fluorophore bound with Mg²⁺. The longer component of JNKP19 is not significantly different than the autofluorescence from the cell until approximately 1 mM MgCl₂ is reached. This

suggests that FLIM can only be used to distinguish between the autofluorescence from the bound NAD(H) and JNKP19 if a high enough concentration of intracellular Mg^{2+} is achieved.

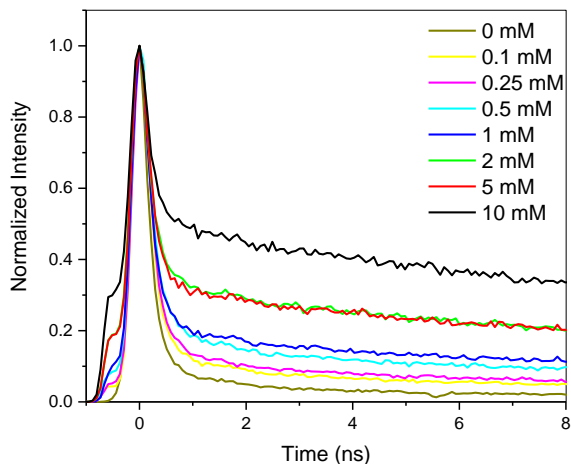


Figure 5.13. Fluorescence lifetime decay of JNKP19 at various concentrations of $MgCl_2$.

Table 5.1. Summarized fluorescent lifetime of JNKP19 at various concentrations of $MgCl_2$.

$[MgCl_2]$ (mM)	τ_1 (ns)	τ_2 (ns)
0	0.20	2.2
0.1	0.21	2.8
0.25	0.22	3.1
0.5	0.23	2.9
1	0.22	4.5
2	0.22	6.1
5	0.21	7.3
10	0.21	8.6

The FLIM images from the autofluorescence of the control cells were compared to the cells transfected with JNKP19. The lifetime distribution is nearly identical, which indicates that either the JNKP19 peptide was not delivered into the cell or the concentration of Mg^{2+} is not high enough to differentiate between the fluorescence

lifetimes. As a consequence, A23187 ionophore was employed to increase the intracellular concentration of divalent metals. Interestingly, small localized spots with a lifetime of nearly 2.2 ns were noted. The lifetime of the A23187 ionophore was found to be 2.4 ns by TCSPC. Hence, these localized bright spots are due to the A23187 ionophore. A notable shift in the distribution of the lifetime was observed when comparing the blank cells to the JNKP19 transfected cells in the presence of the ionophore. The average lifetime of the blank cells was nearly 2.0 ns while the average lifetime of the transfected cells was approximately 3.1 ns. In order to determine if the ionophore is causing an increase in the fluorescence lifetime, the cells were incubated in the presence of only the ionophore. The fluorescence lifetime of the cells containing only the ionophore was similar to cells transfected with JNKP19 and incubated with the ionophore. It is difficult to determine if JNKP19 was delivered into the cells.

It was reported that a majority of the autofluorescence from cells originates from NAD(P)H with a lifetime of 0.4 – 0.5 and 2.0 – 2.5 ns in the unbound and bound form, respectively.²⁵ The granules in the FLIM images from the autofluorescence are due to NAD(P)H found in the mitochondria.²⁶ Preliminary experiments were conducted before carrying out the FLIM experiments. The fluorescence lifetime of JNKP19 was measured at various concentrations of Mg^{2+} utilizing time-correlated single-photon counting (TCSPC). The long component increased from 2.9 ns to 4.5 ns when the concentration of $MgCl_2$ was increased from 0.5 mM to 1 mM. The short component of JNKP19 did not change significantly, regardless of the concentration of $MgCl_2$. This indicates that the short component is likely attributed to the non-chelated Sox-fluorophore. Based on the lifetimes of JNKP19, an ionophore will be required to increase the intracellular

concentration of divalent metals. The fluorescence lifetime of the A23187 ionophore was examined by employing TCSPC. A23187 ionophore exhibited a short and long component of 0.5 and 2.4 ns, respectively.

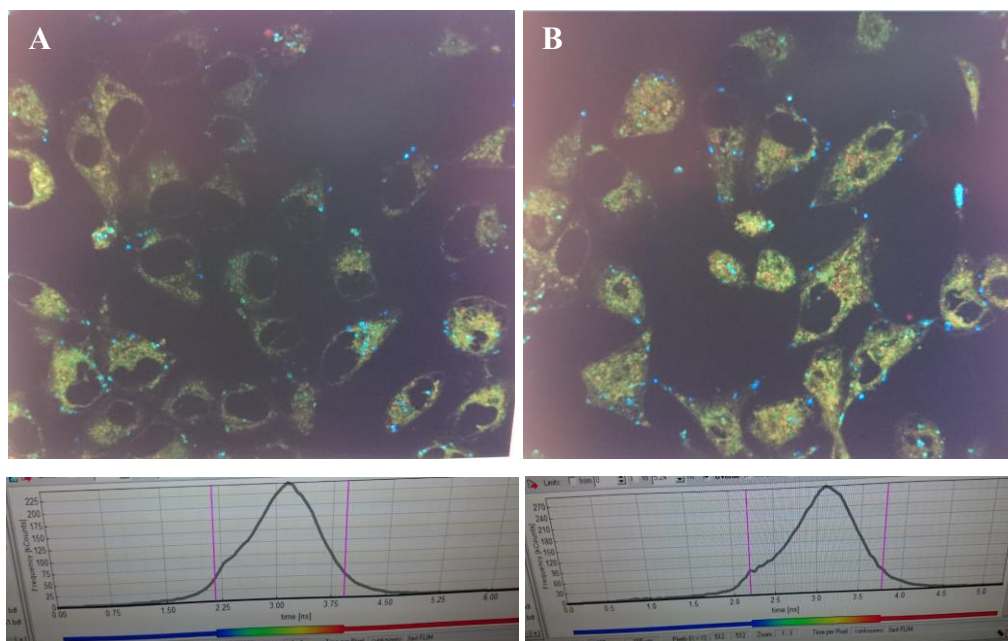


Figure 5.14. FLIM images of cells incubated with ionophore A23187 in the (A) absence and (B) presence of JNKP19. The cumulative histogram of fluorescence lifetime values are shown below the images.

In order to confirm the delivery of JNKP19 into the cell, FLIM imaging experiments were carried out with the cells incubated in the presence of the ionophore. We were concerned that an increase in divalent metals can interfere with other cellular processes, thus increasing the overall lifetime of the blank cell. The FLIM images of blank cells incubated with the ionophore are shown in Figure 5.14. Based on the images and fluorescence lifetime histogram distribution, it is difficult to determine if the Sox-peptide was successfully delivered into the cell. Because of this, we decided to move away from

using the ionophore as it may interfere with other biological processes. Ultimately, our objective was to monitor protein phosphorylation at physiological conditions, which will require the absence of an ionophore. As demonstrated, the ionophore can cause a significant change in the biological environment.

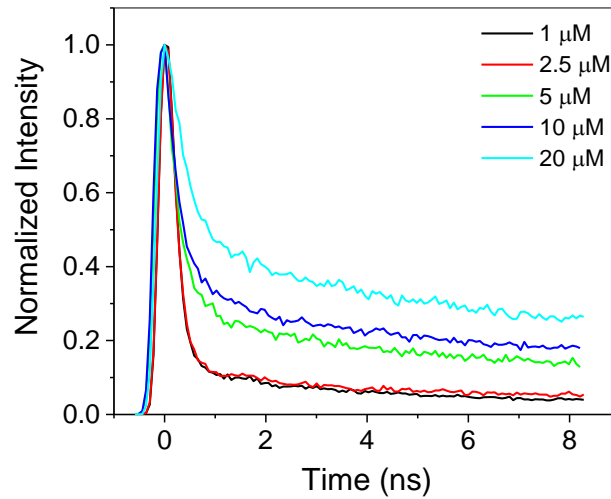


Figure 5.15. Fluorescence dynamics of JNKP19 at varying peptide concentrations. Experiments were carried out at pH = 7.4 and 1 mM MgCl₂.

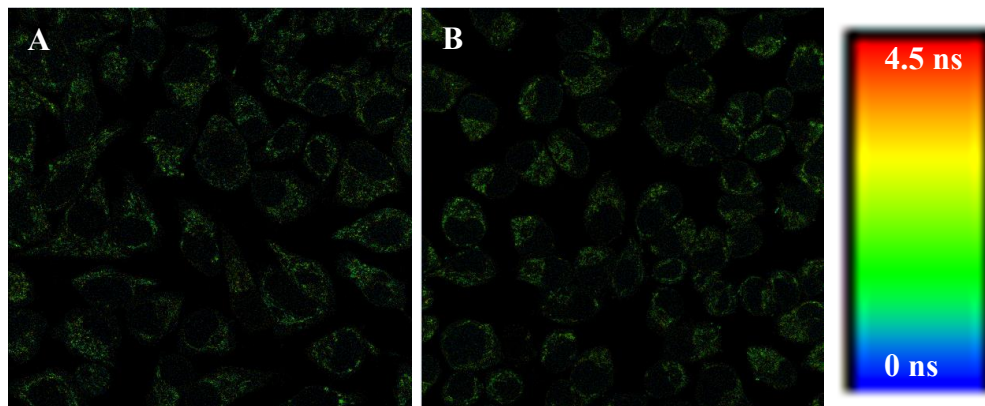


Figure 5.16. FLIM images of HeLa cells transfected (A) without and (B) with 16.6 μM JNKP19.

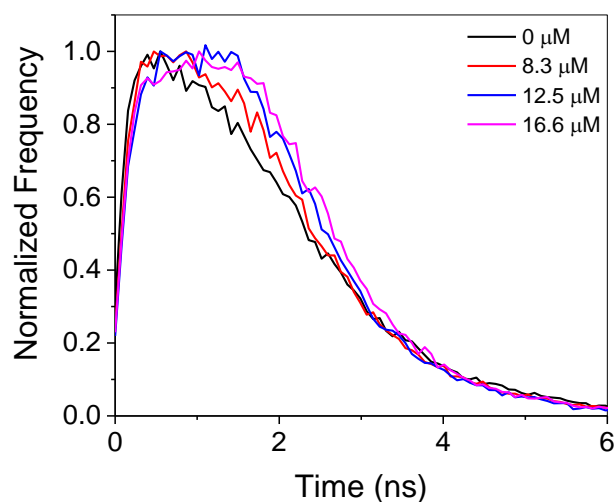


Figure 5.17. Cumulative histogram of fluorescence lifetime values of cells transfected with various concentrations of JNKP19.

A new approach was required to determine if JNKP19 was successfully delivered into the cells. Before the FLIM experiments were carried, the fluorescence lifetime of JNKP19 at varying concentrations was investigated by TCSPC as shown in Figure 5.15. It is important to note that the concentration of MgCl_2 was held constant at 1 mM with a pH of 7.4. Interestingly, the fluorescence lifetime increased with increasing peptide concentration, indicating that FLIM could be employed to determine if the peptide could be delivered into the cells. The cells were transfected with various concentrations of JNKP19 and imaged by FLIM as shown in Figure 5.16. However, it is difficult to determine if the peptide was delivered into the cell based on the pseudocolor lifetime distribution key. Because of this, the cumulative histogram of fluorescence lifetime obtained from the FLIM images were examined as presented in Figure 5.17. As illustrated, the fluorescence lifetime histogram shifts as the incubation concentration of JNKP19 is increased, indicating that the peptide is successfully transfected into the cells.

This demonstrates that the transfection kit was compatible with the Sox-peptide. This is significant as many peptide/protein transfection kits are not compatible with neutral peptides. Furthermore, this allows us to examine the kinase activity without disrupting physiological conditions. This is the first step that will allow us to examine the phosphorylation process or kinase activity in live cells with continuous real-time analysis.

5.4. Conclusion

Kinase enzymes are nearly essential in all biological processes since it's required for cellular communication. Several disorders, such as cancer, are associated with abnormal kinase activity. Hence, it is important to examine kinase activity for the development of therapeutics. The objective of this project was to examine kinase enzyme activity in live cells with continuous real-time analysis. Before we carried out such experiments, the steady-state properties of the Sox-peptide were investigated. The results indicate that the Sox-peptide is highly sensitive in the presence of divalent metals, such as Mg^{2+} . The next goal was to deliver the Sox-peptide into the cells. However, several issues were encountered. First, the excitation wavelength required caused a significant amount of autofluorescence when the bio-imaging experiments were carried out utilizing single-photon and two-photon excited fluorescence confocal microscopy. This caused challenges in determining if the Sox-peptide was successfully delivered into the cells. As a consequence, a new imaging technique was employed. FLIM was an excellent technique because it allowed us to differentiate between the autofluorescence and Sox-peptide fluorescence after transfection. The major accomplishment of this project is that we were able to confirm the delivery of the Sox-peptide into the cell by examining the

fluorescence lifetime histogram distribution. The results presented in this chapter are preliminary. The project will be continued by a future graduate student who will examine the kinase activity with continuous real-time analysis in live cells by employing the unphosphorylated Sox-peptide.

References

1. Chang, L.; Karin, M. *Nature* **2001**, *410*, 37.
2. Hanahan, D.; Weinberg, R. A. *Cell*, **2000**, *100*, 5.
3. Ubersax, J. A.; Ferrell Jr., J. E. *Nature Reviews Molecular Cell Biology* **2007**, *8*, 530.
4. Endicott, J. A.; Noble, M. E.; Johnson, L. N. *Annual Review of Biochemistry* **2012**, *81*, 587.
5. Zhu, H. *Nature Genet.* **2000**, *26*, 283.
6. Adams J. A. *Chem. Rev.* **2001**, *101*, 2271.
7. Cohen, P. *Nat. Rev. Drug Discov.* **2002**, *1*, 309.
8. Sridhar, R.; Hanson-Painton, O.; Cooper, D. R. *Pharm. Res.* **2000**, *17*, 1345.
9. Shults, M. D.; Janes, K. A.; Lauffenburger, D. A.; Imperiali, B. *Nature Methods* **2005**, *2*, 277.
10. Shults, M. D.; Carrico-Moniz, D.; Imperiali, B. *Anal. Biochem.* **2006**, *352*, 198.
11. Shults, M. D.; Imperiali, B. *J. Am. Chem. Soc.* **2003**, *125*, 14248.
12. Wright, D. E.; Noiman, E. S.; Chock, P. B.; Chau, V. *Proc. Natl. Acad. Sci. U.S.A.* **1981**, *78*, 6048.
13. McIlroy, B. K.; Walters, J. D.; Johnson, J. D. *Anal. Biochem.* **1991**, *195*, 148.

14. Post, P. L.; Trybus, K. M.; Taylor, D. L. *J. Biol. Chem.* **1994**, *269*, 12880.
15. Ohuchi, Y.; Katayama, Y.; Maeda, M. *Analyst* **2000**, *125*, 1905.
16. Zhang, J.; Ma, Y.; Taylor, S. S.; Tsien, R. Y. *Proc. Natl. Acad. Sci. U.S.A.* **2001**, *98*, 14997.
17. Shults, M. D.; Pearce, D. A.; Imperiali, B. *J. Am. Chem. Soc.* **2003**, *125*, 10591.
18. Lee, H.; Lee, H. S.; Reibenspies, J. H.; Hancock, R. D. *Inorg. Chem.* **2012**, *51*, 10904.
19. Bird, D. K.; Yan, L.; Vrotsos, K. M.; Eliceiri, K. W.; Vaughan, E. M.; Keely, P. J., White, J. G. Ramanujam, N. *Cancer Research* **2005**, *65*, 8766.
20. Jahnen-Dechent, W.; Ketteler, M. *Clinical Kidney Journal* **2012**, *5*, i3.
21. Pressman, B. C. *Annual Review of Biochemistry* **1976**, *45*, 501.
22. Spach, G.; Trudelle, Y.; Heitz, F. *Biopolymers* **1983**, *22*, 403.
23. Pfeiffer, D. R.; Reed, P. W.; Lardy, H. A. *Biochemistry* **1974**, *13*, 4007.
24. Schneckenburger, H.; Wagner, M.; Weber, P.; Strauss, W. S.; Sailer, R. *Journal of Fluorescence* **2004**, *14*, 649.
25. Niesner, R.; Peker, B.; Schlüsche, P.; Gericke, K. H. *ChemPhysChem* **2004**, *5*, 1141.

Chapter 6

Microporous Inorganic/Organic Hybrids via Oxysilylation of a Cubic Symmetry Nanobuilding Block [(HMe₂SiOSiO_{1.5})₈] with R_xSi(OEt)_{4-x}

6.1 Original Publication Information

A majority of this chapter was originally published as the following:

Pan, D.; Yi, E.; Doan, P.; Furgal, J. C.; Schwartz, M.; Clark, S.; Goodson III, T.; Laine, R. M. “Microporous Inorganic/Organic Hybrids via Oxysilylation of a Cubic Symmetry Nano-Building Block [(HMe₂SiOSiO_{1.5})₈] with R_xSi(OEt)_{4-x}” *J. Ceram. Soc. Jpn.* **2015**, *123*, 756.

Modifications were made to the original document to adapt to the context to this form. The data and results that I analyzed will be mainly discussed. The data collected from the other authors may not be included.

6.2. Abstract

Mesoporous copolymer gels were synthesized using B(C₆F₅)₃ Lewis acid catalyst to promote the Piers-Rubinsztajn of Q-type silsesquioxane with various ethoxysilanes to form 3-D network materials. The materials possessed high surface areas (> 700 m²/g) and thermal stability to 350 °C. Micropores of 0.6 – 2.0 nm as well as mesopores of 2 – 40 nm were noted. Changes in the reaction time and conditions did not significantly change

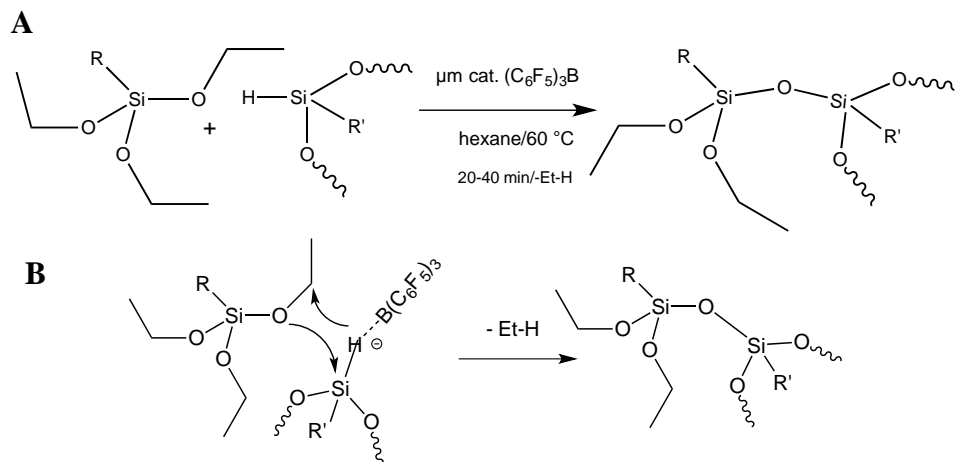
the characterization of the material. Smaller R groups gave higher specific surface areas (SSAs) than those with large R groups. Rigid, bridged compounds [(EtO)₃Si-R-Si(OEt)₃] (R = phenyl, biphenyl) offered high SSAs whereas flexible bridges [R = (CH₂)₂ or (CH₂)₈] gave reduced SSAs. The materials were characterized by Fourier–transform infrared spectroscopy (FTIR), thermal gravimetric analysis (TGA), and X-ray diffraction (XRD). Porosity and surface area analyses were done by Brunauer–Emmett–Teller (BET) method. Slow drying of the gels achieved monoliths whereas fast drying provided powders.

6.3 Introduction

Micro- (average pore sizes < 2 nm) and meso-porous (pores 2 – 50 nm) materials have been subjects of great interest for more than half a century because they offer many distinct properties with potential utility to diverse fields ranging from catalyst substrates, to bio-adsorbants, to drug storage and delivery, to remediation systems, to living cell containers, to gas sieving, to nano-reactors, to gas storage and vacuum insulation panel core materials.¹⁻³⁰

Over this period of time, researchers have developed diverse synthetic routes to micro- and meso-porous materials in the general categories of amorphous inorganics, amorphous organics and crystalline analogs including zeolites, metal organic framework (MOFs), and covalent organic framework (COFs). Most of these syntheses are aqueous in nature and require strongly basic environments, elevated temperatures, and relatively long reaction times. Only a small fraction of the reported synthetic methods rely on the formation of covalent bonds to build highly symmetrical 3-D porous structures.²⁵⁻³³

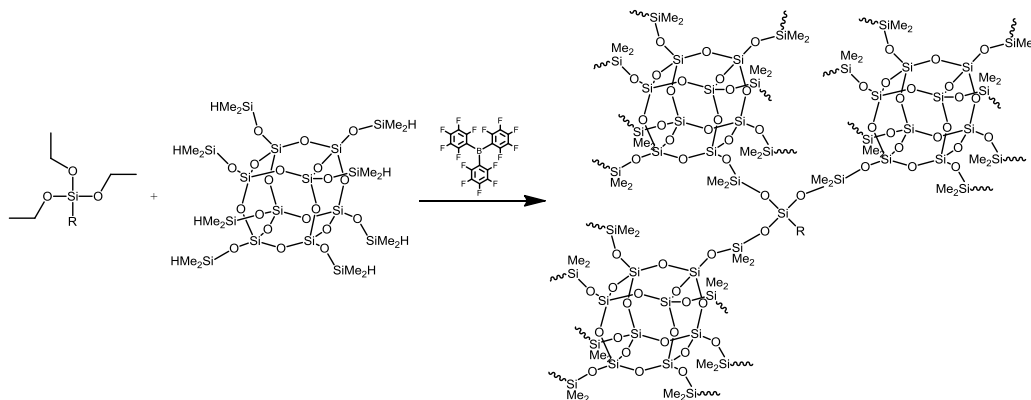
We report a method of synthesizing microporous hybrid materials with 3-D ordering using a new synthetic method based on the Piers-Rubinsztajn reaction, which we refer to here as oxysilylation as shown in Scheme 6.1A.³⁴⁻⁴⁵ In an oxysilylation reaction, Si-H bond is reacted with an alkoxy silane in the presence of catalytic amounts of $(C_6F_5)_3B$, generating a volatile alkane and a new Si-O-Si linkage. The proposed mechanism is shown in Scheme 6.1B.³⁸⁻⁴¹ Oxysilylation reactions can be carried out in hydrocarbon solvents at modest temperatures and short reaction times to provide an ordered, hydrophobic, microporous materials with high surface areas with the potential to be tailored so that multiple functionalities can be introduced.



Scheme 6.1. (A) Oxysilylation reaction with a catalytic amount of $(C_6F_5)_3B$. (B) Proposed mechanism of oxysilylation reaction.

A general synthesis of the porous materials is shown in Scheme 6.2. Various ethoxsilane species were reacted with octakis(dimethylsiloxy)octasilsesquioxane (OHS) to form the network polymer gels. A key to this reaction is to use molar amounts of catalyst $(C_6F_5)_3B$. Another advantage is that the leaving group is an alkane. Finally, the reactions can be carried out in low boiling solvents that are easily removed to give

microporous powders or monoliths. If one component is used in excess (e.g. OHS) then the material will contain reactive sites for the introduction of secondary and tertiary functional groups, providing a simple route to multiple types of materials for diverse applications.



Scheme 6.2. General oxysilylation reaction of OHS with $\text{RSi}(\text{OEt})_3$ with a catalytic amount of $(\text{C}_6\text{F}_5)_3\text{B}$.

6.4 Experimental

Copolymerization of OHS with TEOS. 1:1 molar equivalents of OHS:TEOS (Si-H/Si-OEt) were used. OHS (0.500 g, 3.94 mmol) was dissolved in 15 mL of hexane in a 25 mL round-bottom flask equipped with a magnetic stirrer. TEOS (0.206 g, 3.94 mmol) was added to the solution. The solution was stirred at 60 °C for 5 min. $\text{B}(\text{C}_6\text{F}_5)_3$ (3 mg, 7 μmol), dissolved in 500 μL of CH_2Cl_2 , is then added using a 1.0 mL syringe. A gel forms 1 – 2 min after addition of $\text{B}(\text{C}_6\text{F}_5)_3$. Aluminum foil was used to cover the neck of the round-bottom flask to reduce the drying rate. The gel was allowed to dry at 20 °C for 120 h. A 0.7 mm syringe needle was used to pierce a single hole through the foil. The gel was

dried at 20 °C for an additional 48 h. Significant shrinkage was observed upon drying. Single piece, glassy solids were obtained. Faster drying rates provide powders.

General copolymerization of OHS with RSi(OEt)₃ where R = Ph, vinyl, CH₃, (CH₂)₃Cl, (CH₂)₂CF₃, (CH₂)₈H. 1:1 molar equivalents of OHS:RSi(OEt)₃ (Si-H/Si-OEt) were used to prepare the gels. OHS (0.500 g, 3.94 mmol) was dissolved in 15 mL of hexane in a 25 mL round-bottom flask equipped with a magnetic stirrer. RSi(OEt)₃ (3.94 mmol) was added to the flask. The solution was stirred at 60 °C for 5 min. B(C₆F₅)₃ (3 mg, 7 μmol) was dissolved in 500 μL of CH₂Cl₂ then added to the resulting solution. The gel was dried as described above.

Fourier–transform infrared spectroscopy (FTIR). Diffuse reflectance Fourier transform (DRIFT) spectra were obtained using a Nicolet 6700 Series FTIR spectrometer (Thermo Fisher Scientific, Inc., Madison, WI). Optical grade KBr (International Crystal Laboratories, Garfield, NJ) was ground with 1.0 wt % of the sample to be analyzed. The ground powder was packed into a sample holder and leveled off with a glass plate to give a smooth surface. The FTIR sample chamber was purged continuously with N₂ prior to data acquisition. 64 scans were averaged for each spectrum in the range 4000 – 400 cm⁻¹ with a precision of ± 4 cm⁻¹.

Specific surface area (SSA) and porosity analyses were carried out using an ASAP 2020 sorption analyzer (Micromeritics Inc., Norcross, GA). Samples (100 mg) were degassed at 150 °C/10 h. Each analysis was run at –196 °C (77 K) with N₂. The SSAs were determined by the BET multipoint method using ten data points at relative pressures (P/P₀) of 0.05 – 0.30. The micropore size distribution was determined by the Horvath-

Kawazoe method. Data points were collected with low pressure incremental dose mode at $0 < P/P_0 \leq 0.1$.

Thermal gravimetric analysis (TGA). Thermal stabilities of materials under synthetic air were measured on a Q600 simultaneous TGA-DSC Instrument (TA Instruments, Inc., New Castle, DE). Before analysis, samples were ground into a powder and 15 – 25 mg were placed into alumina pans and then ramped from 25 to 1000 °C (10 °C/min). The air flow rate was 60 mL/min.

X-ray diffraction (XRD). XRD patterns were collected on a Rigaku Rotating Anode Goniometer (Rigaku Denki., LTD., Tokyo, Japan). The Jade Program 2010 (Version 1.1.5 Materials Data, Inc., Livermore CA) was used to determine the presence of crystallographic phases. XRD scans were made from 5° to 40° 2 θ , using a scan rate of 2° min⁻¹ in 0.01° increments and Cu K α radiation (1.541 Å) operating at 40 kV and 100 mA.

6.5 Results and Discussion

In this initial work, our objectives was to analyze a material with the basic nanobuilding block OHS, and study the oxysilylation reactions with Si(OEt)₄ to explore the range of conditions that can be used to produce microporous gels. We replaced Si(OEt)₄ with selected RSi(OEt)₃ and (EtO)₃Si-R-Si(OEt)₃ systems to identify sets of materials with a range of properties. This work is considered a prelude to using excess vinyl and/or -OSiMe₂H groups in oxysilylation, leaving these functionalities available for the introduction via hydrosilylation or oxysilylation of second and tertiary functional groups. However, it should also be possible to form catalyst particles within these microporous gels given that -OSiMe₂H groups are also potential points of reduction.

Therefore, we have established the groundwork for more complex studies. We begin with a detailed analysis of oxysilylation in a OHS: Si(OEt)₄ system with a 1 Si-H:1 Si-OEt ratio that results in micro/mesoporous gels and then introduce OHS:RSi(OEt)₃ systems with 1:1 Si-H:Si-OEt ratios. These gels were characterized by FTIR, TGA, N₂ absorption, and XRD.

The reactions were carried out in 15 mL of hexane where 5 μm mol (C₆F₅)₃B as a dichloromethane solution was added. Reactions were heated to 60 ° C with initiation typically observed within a few minutes as evidenced by the evolution of ethane bubbles. Caution should be used as these reactions can evolve gas violently especially if the alkoxy group is MeO.

Table 6.1. Specific conditions explored for the synthesis of the gels.

OHS:TEOS	Hexane Vol. (mL)	Temp (°C)	mg B(C ₆ F ₅) ₃ (μmol)	SSA (m ² /g)	Ave Pore Size (nm)
1:1	10	60	2.5 (4.89)	680	0.7
1:1	20	60	2.5 (4.89)	618	0.7
1:1	50	60	5.0 (9.78)	706	0.8

The resulting materials are relatively similar with roughly the same SSAs and average pore sizes regardless of the solvent volume or catalyst concentration. These results suggest that almost complete crosslinking despite the very low catalyst concentrations and solvent volume as suggested by the FTIR studies, which are discussed below. Thus, solvent does not influence the reaction rate or the extent to which the reaction reaches completion under these conditions. Note that the reactions can also be carried out in CH₂Cl₂. The reaction temperature must be limited to the boiling point of 40 °C. Reactions conducted in THF or EtOH are much slower as they are mild Lewis acids and

the reaction is difficult to drive to completion. However, the intermediate stages lead to materials that can be used to form coatings.⁶⁶

The recovered gels are hydrophobic as shown in Figure 6.1. Rapid drying leads to cracking driven by changes in osmotic pressure. Slowly dried samples retain the vessel shape whereas rapid drying leads to cracking driven by changes in osmotic pressure.

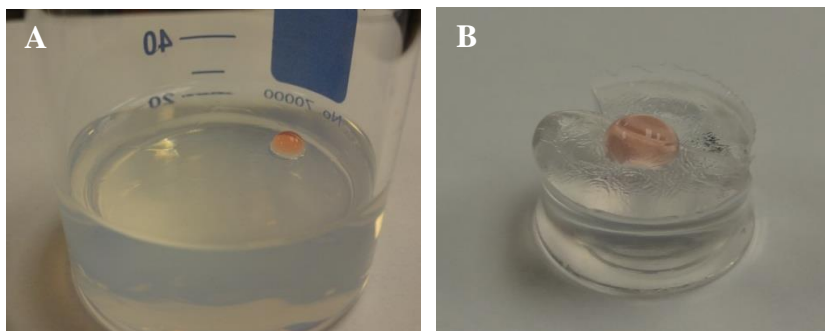


Figure 6.1. 1:1 OHS:TEOS (A) gel immediately after reaction and (B) after drying for 3 weeks.

The gels were characterized by FTIR. Figure 6.2 compares the FTIR of OHS with the reaction product obtained from the stoichiometric reaction of all the Si-H groups with an equal amount of Si-OEt at 60 °C in hexane. The key features of the product are the complete absence of $\nu\text{Si-H}$ and the appearance of a new $\nu\text{Si-O}$ band at 1040 cm^{-1} with retention of the original cage $\nu\text{Si-O}$ band at 1120 cm^{-1} . The FTIR spectrum of the final product is nearly identical to a typical FTIR spectrum of polydimethylsiloxane with the exception of the $\nu\text{Si-O}$ band at 1040 cm^{-1} .⁵² It is important to note that no $\nu\text{Si-OH}$ bands were observed. This indicates that there is no cleavage of the Si-O bonds, which is important for maintaining the structural composition.

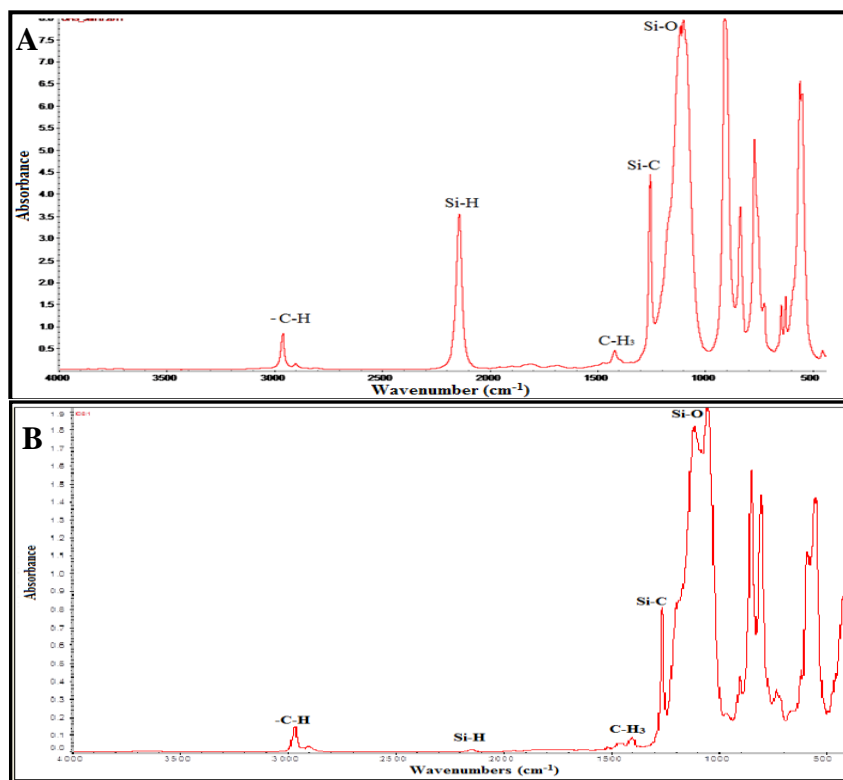


Figure 6.2. FTIR spectrum of (A) OHS and (B) 1:1 OHS:TEOS.

TGA was used to examine and characterize the dried gels. Shown in Figure 6.3, the TGA/DTA of the 1:1 OHS:TEOS product indicates an initial mass loss at 320 °C. The mass loss is associated with an exotherm, which is likely attributed to the oxidation of residual Si-H groups and the Si-Me groups. The ceramic yields (CY) are presented in Table 6.2 and 6.3. For the 1:1 OHS:TEOS material, the experimental CY was 85.5% with a theoretical CY of 90.6%. There are several reasons in which the experimental CY varies as compared to the theoretical CY. First, the residual ethoxy groups are not accounted for when calculating the theoretical CY; it is assumed that all the ethoxy groups have reacted. Another reason is that some of the starting material may be lost to sublimation; for instance, OHS sublimates at 280 °C. Finally, some of the polymer

fragments may leave as volatiles. It is worth noting that the mass loss continues to at least 800 °C. This is typical of hybrid materials that decompose into gaseous char and fragments. The char oxidizes at higher temperature in air, but remains relatively stable if heated under nitrogen.⁵³

Table 6.2. Selected properties for various gels, 1:1 OHS:RSi(OEt)₃ (Si-H/Si-OEt).

R	Density (g/cm ³)*	SSA (m ² /g)	Pore dia.(Å)	Max. pore volume (cm ³ /g)	Found CY (%)	Theor. CY (%)
OCH ₂ CH ₃	0.89 ± 0.08	665	7.2	0.28	85.5	90.6
CH ₃	1.05 ± 0.06	579	6.3	0.22	88.9	89.5
Ph	1.03 ± 0.09	452	5.9	0.18	75.6	79.1
(CH ₂) ₂ CF ₃	1.15 ± 0.08	141	N/A	N/A	74.0	76.2
Vinyl	1.09 ± 0.07	485	7.1	0.19	85.4	87.5
(CH ₂) ₃ Cl	1.17 ± 0.05	112	N/A	N/A	77.9	79.0
(CH ₂) ₈ H	N/A	6	N/A	N/A	71.4	74.1

* The value represents the average of 3 replicates ($n = 3$).

Table 6.3. Selected properties for various gels, 1:1 OHS:R[Si(OEt)₃]₂ (Si-H/Si-OEt).

R	Density (g/cm ³)*	SSA (m ² /g)	Pore dia. (Å)	Max. pore volume (cm ³ /g)	Found CY (%)	Theor. CY (%)
Benzene	0.91 ± 0.05	710	5.5	0.27	81.4	83.8
Biphenyl	0.96 ± 0.07	655	6.0	0.25	74.9	79.2
(CH ₂) ₂	0.94 ± 0.08	448	6.2	0.19	86.3	89.7
(CH ₂) ₈	1.07 ± 0.09	396	7.0	0.17	79.3	78.2

* The value represents the average of 3 replicates ($n = 3$).

XRD was utilized to characterize the periodicity of the dried gel. The XRD patterns of OHS and 1:1 OHS:TEOS are shown in Figure 6.3. The XRD suggests that the dried gel has some periodicity as evidenced by peaks at approximately 7.2, 17, and 23 °2θ. The XRD pattern for OHS showed peaks at 8.3, 18.9 and 24.4 °2θ which represented periodic distances of 1.1, 0.5 and 0.3 nm, respectively. They are tentatively assigned to the (100) or (010) (120) and (112) planes, respectively.⁶⁷ The broad peak at approximately 7.2 °2θ suggests that a larger unit cell of 1.3 nm arises from the incorporation of Si-O units to the

original OHS cell. The peak centered near $17^\circ 2\theta$ corresponds to the SQ cage, which has expanded with the addition of eight Si-O bonds, which indicates a distance near to 0.6 – 0.7 nm. The peak near $24^\circ 2\theta$ corresponds to the separation between faces of the cage.⁶⁷ It appears that there is some extended periodicity in the formed gel, which is not influenced by the varying conditions of the reaction.

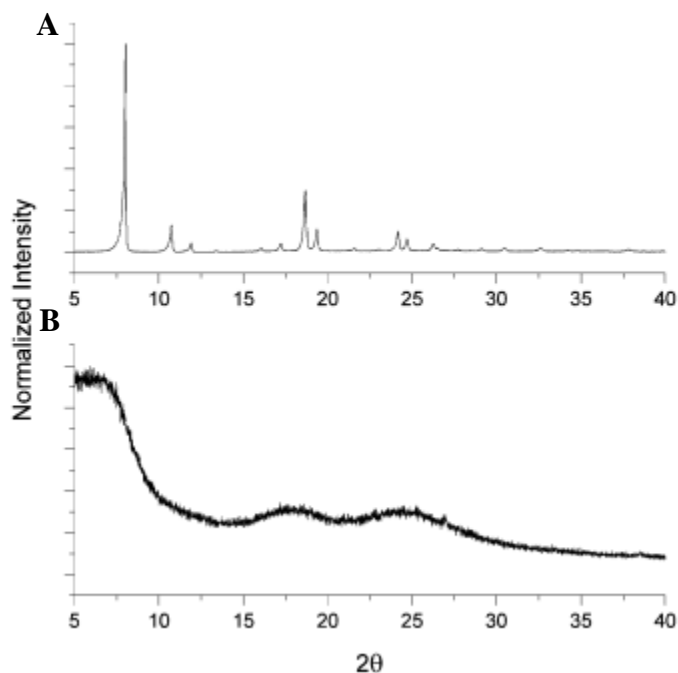


Figure 6.3. XRD pattern of (A) OHS and (B) 1:1 OHS:TEOS gel.

Highly periodic materials, such as zeolites, are generally prepared under hydrothermal conditions in which an equilibrium is established, allowing the defects to dissolved and removed to be replaced with more uniform and ordered structures over a period of time. Contrarily, the gels formed via oxysilylation are kinetic products. These materials are formed in minutes at room temperature. The byproduct of ethane gas removes the ability to form an equilibrium. Therefore, the defects or unordered structures

are retained due to the lack of mechanism to remove these defects. The periodic structures will display short ranged ordering as observed with other tethered cage structure systems.⁶⁹ Other methods, such as mass spectrometry, could not be employed to characterize the material due to the rapid polymerization reaction.

The surface area and porosity of the gels were analyzed utilizing the BET method. Pore sizes are classified into three classes, depending on the pore diameter (D); micropores ($D < 20 \text{ \AA}$), mesopores ($D = 20 - 500 \text{ \AA}$), macropores ($D > 500 \text{ \AA}$).⁵ The gels were found to have pore diameters of $6 - 7 \text{ \AA}$ as listed in Tables 6.2 and 6.3. Supercritical processing was not required to dry the gels in order to retain high specific surface areas (SSA). The porosity measurements were conducted from the adsorption stage to minimize hysteresis.

The SSA ranged from $6 - 665 \text{ m}^2/\text{g}$ with the gels containing the R-Si(OEt)₃ linkers. The trend on porosity and SSA were shown to be dependent on the flexibility of the R group on the linker. The gels containing the non-flexible functional groups (R = CH₃, Ph, vinyl) had SSA greater than $450 \text{ m}^2/\text{g}$. The linker with R = Me had the highest SSA of $579 \text{ m}^2/\text{g}$ among the R-Si(OEt)₃ linkers. Interestingly, the SSA decreased as the chain length increases from C₁ to C₈. For example, R = (CH₂)₇CH₃ offered the lowest SSA of $6 \text{ m}^2/\text{g}$. This is likely due to flexibility of the linker interfering with formation of the pores upon polymerization. The rigid linkers do not have the flexibility and stay in place, thus not affecting the formation of the pores.

Another interest was the effect on the SSA due to the size of the linkers for the bistriethoxysilane spacers, Si(OEt)₃-R-Si(OEt)₃. The gels containing the rigid linkers displayed higher SSA as compared to the linkers that were flexible. The SSA of gels with

rigid spacer had SSA greater than 650 m²/g. As the length of the rigid spacer increased, there was a decrease in the SSA. For example, the SSA decreased from 710 to 655 m²/g as the length of the linker was increased with R = phenyl to R = bisphenyl. This finding agreed with the work done by Oviatt *et al.*⁷¹ However, these finding was contrast with work done by Corriu *et al.*⁴⁰ in which the flexibility of the linker was not a factor in the porosity and SSA of the material.

6.6 Conclusion

In summary, we have demonstrated a new synthetic route to form network polymer gels through the oxysilylation reaction of cubic symmetry Q-type cages (OHS) with various ethoxysilane linkers. The materials were found to be hydrophobic with 3-D periodic microporous with high SSA and thermal stability. In addition, the gels were synthesized in mild conditions in the presence of a Lewis acid. The properties were investigated using a series of ethoxysilane linkers. It was found that more rigid structural elements gave higher SSA as compared to more flexible structural elements. Additionally, the gels displayed a short range of periodicity as evident from XRD. With the use of BET, it was reported that the diameter of the pore was, on average, 6 – 7 Å. Variation in the reaction conditions, such as solvent volume and catalyst concentration, did not change the properties of the final gels indicating that the reaction goes to completion as a kinetically favored product. The findings suggest that the gels can be easily functionalized to give materials towards other applications.

References

1. Flanigen, E. M.; Patton, R. L. Silica Polymorph and Process for Preparing Same. U.S. Patent 4,073,865, Feb. 14 (1978).
2. Flanigen, E. M.; Bennett, J. M.; Grose, R. W.; Cohen, J. P.; Patton, R. L.; Kirchner, R. M.; Smith, J. V. *Nature* **1978**, *271*, 512.
3. Barrer, R. M. "Hydrothermal Chemistry of Zeolites", Academic Press, London (1992).
4. Occelli, M. L.; Kessler, H. "Synthesis of Porous Materials", Marcel Dekker, New York (1997).
5. Naik, B.; Ghosh, N. N. *Recent Pat. Nanotechnol.* **2009**, *3*, 213.
6. Yanagisawa, T.; Shimizu, T.; Kuroda, K.; Kato, C. *Bull. Chem. Soc. Jpn.* **1990**, *63*, 988.
7. Kresge, C. T.; Leonowicz, M. E.; Roth, W. J.; Vartuli, J. C.; Beck, J. S. *Nature* **1992**, *359*, 710.
8. Beck, J. S.; Vartuli, J. C.; Roth, W. J.; Leonowicz, M. E.; Kresge, C. T.; Schmitt, K. D.; Chu, C. T-W.; Olson, D. H.; Sheppard, E. W.; McCullen, S. B.; Higgins, J. B.; Schlenker, J. L. *J. Am. Chem. Soc.* **1992**, *114*, 10834.
9. Inagaki, S.; Fukushima, Y.; Kuroda, K. *J. Chem. Soc. Chem. Commun.* **1993**, *8*, 680.
10. Inagaki, S.; Koiwai, A.; Suzuki, N.; Fukushima, Y.; Kuroda, K. *Bull. Chem. Soc. Jpn.* **1996**, *69*, 1449.
11. Bagshaw, S. A.; Prouzet, E.; Pinnavaia, T. J. *Science* **1995**, *269*, 1242.

12. Yaghi, O. M.; Li, H.; Davis, C.; Richardson, D.; Groy, T. L. *Acc. Chem. Res.* **1998**, *31*, 474.
13. Inagaki, S.; Guan, S.; Fukushima, Y.; Ohsuna, T.; Terasaki, O. *J. Am. Chem. Soc.* **1999**, *121*, 9611.
14. Ying, J. Y.; Mehnert, C. P.; Wong, M. S. *Angew. Chem., Int. Ed.* **1999**, *38*, 56.
15. Stein, A.; Melde, B. J.; Schroden, R. C. *Adv. Mater.* **2000**, *12*, 1403.
16. Schüth, F. *Chem. Mater.* **2001**, *13*, 3184.
17. Eddaoudi, M.; Moler, D. B.; Li, H.; Chen, B.; Reineke, T. M.; O’Keeffe, M.; Yaghi, O. M. *Acc. Chem. Res.* **2001**, *34*, 319.
18. Soler-Illia, G. J.; Sanchez, C.; Lebeau, B.; Patarin, J. *Chem. Rev.* **2002**, *102*, 4093.
19. Hartmann, M. *Chem. Mater.* **2005**, *17*, 4577.
20. Avnir, D.; Coradin, T.; Levc, O.; Livage, J. *J. Mater. Chem.* **2006**, *16*, 1013.
21. Vinua, A.; Moria, T.; Ariga, K. *Sci. Technol. Adv. Mater.* **2006**, *7*, 753.
22. Brodt, K. H.; Bart, G. C. J. *J. Therm. Insul. Build. Env.* **1994**, *17*, 238.
23. Caps, R.; Fricke, J. *Int. J. Therm.* **2000**, *21*, 445.
24. Brunner, S.; Simmler, H. *Vacuum* **2008**, *82*, 700.
25. Addicott, C.; Das, N.; Stang, P. J. *Inorg. Chem.* **2004**, *43*, 5335.
26. Seidel, S. R.; Stang, P. J. *Acc. Chem. Res.* **2002**, *35*, 972.
27. Mastalerz, M. *Angew. Chem., Int. Ed.* **2008**, *47*, 445.
28. Yang, H.-B.; Ghosh, K.; Arif, A. M.; Stang, P. J. *J. Org. Chem.* **2006**, *71*, 9464.
29. Yaghi, O. M.; Li, H.; Davis, C.; Richardson, D.; Groy, T. L. *Acc. Chem. Res.* **1998**, *31*, 474.
30. Yaghi, O. M.; Li, Q. *MRS Bull.* **2009**, *34*, 682.

31. Menzel, H.; Mowery, M. D.; Cai, M.; Evans, C. E. *Macromolecules* **1999**, *32*, 4343.
32. Morris, R. E. *J. Mater. Chem.* **2005**, *15*, 931.
33. Zhang, C.; Babonneau, F.; Bonhomme, C.; Laine, R. M.; Soles, C. L.; Hristov, H. A.; Yee, A. F. *J. Am. Chem. Soc.* **1998**, *120*, 8380.
34. Kim, Y.; Koh, K.; Roll, M. F.; Laine, R. M.; Matzger, A. J. *Macromolecules* **2010**, *43*, 6995.
35. Roll, M. F.; Kampf, J. W.; Kim, Y.; Yi, E.; Laine, R. M. *J. Am. Chem. Soc.* **2010**, *132*, 10171.
36. Wang, D.; Xue, L.; Li, L.; Deng, B.; Feng, S.; Liu, H.; Zhao, X. *Macromol. Rapid Commun.* **2013**, *34*, 861.
37. Wang, D.; Yang, W.; Li, L.; Zhao, X.; Feng, S.; Liu, H. *J. Mater. Chem. A* **2013**, *1*, 13549.
38. Peng, Y.; Ben, T.; Xu, J.; Xue, M.; Jing, X.; Deng, F.; Qiu, S.; Zhu, G. *Dalton Trans.* **2011** *40*, 2720.
39. Chaikittisilp, W.; Sugawara, A.; Shimojima, A.; Okubo, T. *Chem. Mater.* **2010**, *22*, 4841.
40. Corriu, R. J. P.; Moreau, J. J. E.; Thepot, P.; Man, M. W. C. *Chem. Mater.* **1992**, *4*, 1217.
41. Kim, Y.; Koh, K.; Roll, M. F.; Laine, R. M.; Matzger, A. J. *Macromolecules* **2010**, *43*, 6995.
42. Zhang, C.; Babonneau, F.; Bonhomme, C.; Laine, R. M.; Soles, C. L.; Hristov, H. A.; Yee, A. F. *J. Am. Chem. Soc.* **1998**, *120*, 8380.

43. Chaikittisilp, W.; Kubo, M.; Moteki, T.; Sugawara-Narutaki, A.; Shimojima, A.; Okubo, T. *J. Am. Chem. Soc.* **2011**, *133*, 13832.
44. Wang, S.; Tan, L.; Zhang, C.; Hussain, I.; Tan, B. *J. Mater. Chem. A* **2015**, *3*, 6542.
45. Wu, Y.; Wang, D.; Li, L.; Yang, W.; Feng, S.; Liu, H. *J. Mater. Chem. A* **2014**, *2*, 2160.
46. Wang, D. X.; Yang, W. Y.; Li, L. G.; Zhao, X.; Feng, S. Y.; Liu, H. Z. *J. Mater. Chem. A* **2013**, *1*, 13549.
47. Wang, D.; Xue, L.; Li, L.; Deng, B.; Feng, S.; Liu, H.; Zhao, X. *Macromol. Rapid Commun.* **2013**, *34*, 861.
48. Roll, M. F.; Kampf, J. W.; Kim, Y.; Yi, E.; Laine, R. M. *J. Am. Chem. Soc.* **2010**, *132*, 10171.
49. Alves, F.; Scholder, P.; Nischang, I. *ACS Appl. Mater. Interfaces* **2013**, *5*, 2517.
50. Wei, Z.; Luo, X.; Zhang, L.; Luo, M. *Microporous Mesoporous Mater.* **2014**, *193*, 35.
51. Raaijmakers, M. J. T.; Wessling, M.; Nijmeijer, A.; Benes, N. E. *Chem. Mater.* **2014**, *26*, 3660.
52. Jung, J. H.; Chou, K.; Furgal, J. C.; Laine, R. M. *Appl. Organomet. Chem.* **2013**, *27*, 666.
53. Laine, R. M. *J. Mater. Chem.* **2005**, *15*, 3725.
54. Rubinsztajn, S.; Cella, J. A. *Macromolecules* **2005**, *38*, 1061.
55. Chojnowski, J.; Rubinsztajn, S.; Cella, J.; Fortuniak, W.; Cypriak, M.; Kurjata, J.; Kaźmierski, K. *Organometallics* **2005**, *24*, 6077.

56. Rubinsztajn, S.; Cella, J. A. European Patent Application, General Electric, WO2005118682 (2005)
57. Rubinsztajn, S.; Cella, J. A. Silicone condensation reaction. US Patent 7064173, General Electric, USA (2006).
58. J. Chojnowski, J.; Fortuniak, W.; Kurjata, J.; Rubinsztajn, S.; Cella, J. A. *Macromolecules* **2006**, *39*, 3802.
59. Chojnowski, J.; Rubinsztajn, S.; Fortuniak, W.; Kurjata, J. *J. Inorg. Organomet. Polym. Mater.* **2007**, *17*, 173.
60. Chojnowski, J.; Rubinsztajn, S.; Fortuniak, W.; Kurjata, J. *Macromolecules* **2008**, *41*, 7352.
61. Kurjata, J.; Fortuniak, W.; Rubinsztajn, S.; Chojnowski, J. *Eur. Polym. J.* **2009**, *45*, 3372.
62. Kamino, B. A.; Grande, J. B.; Brook, M. A.; Bender, T. P. *Org. Lett.* **2011** *13*, 154.
63. Grande, J. B.; Fawcett, A. S.; McLaughlin, A. J.; Gonzaga, F.; Bender, T. P.; Brook, M. A. *Polymer* **2012**, *53*, 3135.
64. Grande, J. B.; Thompson, D. B.; Gonzaga, F.; Brook, M. A. *Chem. Commun.* **2010**, *46*, 4988.
65. Parks, D. J.; Blackwell, J. M.; Piers, W. E. *J. Org. Chem.* **2000**, *65*, 3090.
66. Cai, D.; Neyer, A.; Kuckuk, R.; Heise, H. M. *J. Mol. Struct.* **2010**, *976*, 274.
67. Takamura, N.; Viculis, L.; Zhang, C.; Laine, R. M. *Polym. Int.* **2007**, *56*, 1378.
68. Cordes, D. B.; Lickiss, P. D.; Rataboul, F. *Chem. Rev.* **2010**, *10*, 2081.
69. Wallace, W. E.; Guttman, C. M.; Antonucci, J. M. *Polymer* **2000**, *41*, 2219.

70. Gregg, S. J.; Sing, K. "Adsorption, Surface Area and Porosity", Acad. Press (1982).
71. Oviatt, Jr., H. W.; Shea, K. J.; Small, J. H. *Chem. Mater.* **1993**, 5, 943.
72. Snyder, J. R. *Chromatogr. J. Sci.* **1978**, 16, 223.

Chapter 7

Avoiding Carbothermal Reduction: Distillation of Alkoxysilanes from Biogenic, Green, and Sustainable Sources

7.1 Original

A majority of this chapter was published as the following document:

Laine, R. M.; Furgal, J. C.; Doan, P.; Pan, D. Popova, V. “Avoiding Carbothermal Reduction: Distillation of Alkoxysilanes from Biogenic, Green, and Sustainable Sources” *Angew. Chem. Int. Ed. Engl.* **2015**, *127*, 1.

Modifications were made to the original document to adapt the context to this form.

Data that was not published in the manuscript may also be discussed.

7.2 Abstract

We report here the first examples of base catalyzed depolymerization of silica to produce distillable spiroxiloxanes and alkoxysilanes in large quantities. Hindered diols, such as 2-methyl-2,4-pentanediol (b.p. 197 °C) or 2,2,4-trimethyl-1,3-pentane-diol (b.p. 232 °C) were reacted with a variety of silica sources including rice hull ash (RHA, ≈ 20 m²/g), vermiculite (4 m²/g), diatomaceous earth (20 m²/g DE), ashed rice hulls (A-RH, > 200 m²/g), or fumed silica (340 m²/g) in the presence of catalytic amounts of NaOH (10 mol % of SiO₂) to form spiroxiloxanes, (2-Me-2,4-pentanediolato)₂Si (**II**) and (2,2,4-

trimethyl-1,3-pentane-diolato)₂Si (**III**). Conversions of 5 – 98 % were obtained under standard conditions that were governed by surface area, crystallinity of the silica source, and distillation temperature. If ethylene glycol is used, a undistillable glycoxysilane is produced, Si(OCH₂CH₂OH)₄, which forms a polymeric material Si(OCH₂CH₂O)₂ upon heating and vacuum. Additionally, the material was mixed with EtOH in the presence of catalytic amount of acid gave Si(OEt)₄ with yields of 60% unoptimized. Similar conversion of **II** gave unoptimized 60 % yields of Si(OEt)₄.

The spiroxiloxanes and Si(OEt)₄ are hexane soluble. Therefore, solutions of Si(OEt)₄ or **II** and unreacted diol in hexane can be washed with water to remove starting diol to form pure **II**, which crystallizes at ambient temperatures and Si(OEt)₄ as a recovered liquid. Hexane solutions containing **III** and the starting diol were washed with MeOH followed by the removal of hexane to give pure **III**. All compounds can be distilled to produce higher purities. This process represents a green route for the production of alkoxysilanes, which can be used for precipitated silica, colloidal silica, fumed silica, and as precursors to compounds with Si-C bonds. These alkoxysiloxanes and spiroxiloxanes can be used to make high purity precipitated, colloidal and/or fumed silica directly from low cost biogenic silica sources. The process is described as renewable, sustainable, and has a minimal carbon footprint.

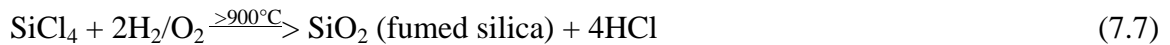
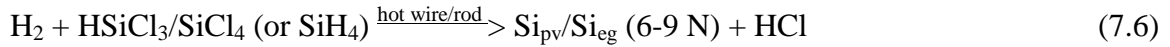
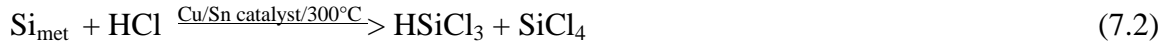
7.3 Introduction

We report the first example of the direct, base catalyzed depolymerization of silica by the reaction with hindered diols yielding spiroxiloxanes that can be distilled with in high purity. This work represents the culmination of over 80 years of literature efforts

targeting similar objectives. The spiro-siloxanes can be used to produce fumed, colloidal, or precipitated silica. Additionally, the spiro-siloxanes can be used as precursors for the formation of compounds containing Si-C bonds.

Although coal and crude oil make up less than 0.01 % of the Earth's crust, their utility to society is enormous given that they serve as the basis for much of the world's fuel, organic materials ranging from plastic bags to fibers for textiles, and food packaging to major components in flat panel displays. Contrarily, silicon lies in the same column just below carbon in the periodic chart, which offers many chemical bonding similarities. Silicon makes up more than 40 % of the Earth's minerals, and is less impactful on our society despite being important for applications ranging from solar cells to silicone rubbers.¹⁻⁴

Silicon-silicon and silicon-carbon double bonds are difficult to synthesize unless sterically stabilized and are not easily polymerized using the same chemistries as used for carbon. Additionally, the silicon-oxygen bond (534 KJ/mol) is one of the strongest bonds found in nature, which has a contribution to this problem. Thus, most Si containing compounds and materials are produced from Si_{met} , which is made by carbothermal reduction of silica with carbon in a high temperature and energy intensive process as shown in reactions (7.1) – (7.7).⁶⁻¹⁰ The higher purities required for photovoltaic (Si_{pv}) and electronic (Si_{eg}) grade silicon require additional processing steps, typically those of the Siemens process, reactions (5) and (6), which generate byproduct HCl, which is normally recycled.



All chlorosilanes and HCl gas are corrosive, toxic and polluting, such production processes including those used to produce fumed silica (reaction 7.7) require extensive safeguards adding to the overall cost of the final products. Because Si_{met} is a kinetic product, where SiC is the thermodynamic product, its synthesis requires electric arc furnace processing at 1900 °C adding to the overall cost for the production Si(OEt)_4 or Si(OMe)_4 .

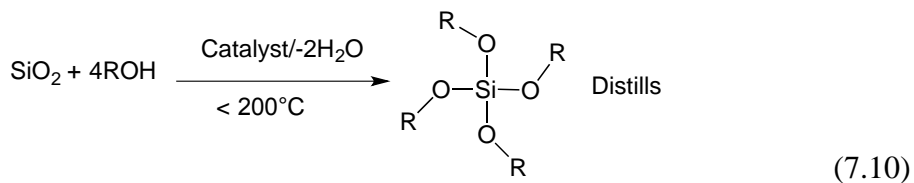
Precipitated silica is most commonly made through high temperature reactions of sand with sodium carbonate followed by the dissolution and precipitation with H_2SO_4 as given by



Each mole of Na_2SiO_3 produced results in one mole of CO_2 and requires one mole of H_2SO_4 producing one mole of precipitated silica and one mole of Na_2SO_4 , which must be

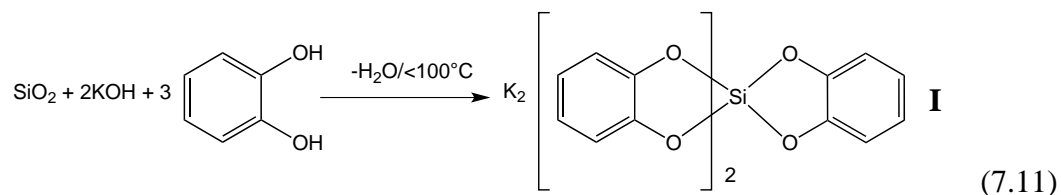
disposed. Therefore, the production of precipitated (ppt) silica, such as used as filler in polymers or as abrasives in toothpaste, requires high temperatures and generates unwanted byproducts, especially CO₂ and Na₂SO₄.¹¹ Reactions (7.1) – (7.7) start with SiO₂, which is reduced to Si_{met} and then re-oxidized back to some form of SiO₂. This approach is not cost effective because these processes are equipment and energy intensive.

In the early 1930's, repeated attempts were made to develop low temperature and cost effective methods to depolymerize silica in generating alternate routes to silicon containing compounds as well as precipitated silica. The success of such a process can be considered a "Grand Challenge" for silicon chemists as suggested by reaction (7.10). The idea of distilling the resulting product should allow the direct production of very high purity silicon containing materials including directly from any silica source at low temperatures, which significantly reduces cost. High purity silica can be used in several applications including edible products (e.g. toothpaste), polishing aids for planarizing silicon wafers, production of high purity silica for optical applications (lenses, gratings, photonic band gap materials), and the production of crucibles for growing electronics grade silicon boules.^{6,7,10}



In regards to the "Grand Challenge", research began with Rosenheim *et al.* (1931)¹² followed by Weiss *et al.* (1961),¹³ Frye (1964),¹⁴ Boer and Flynn (1968),^{15,16} Barnum

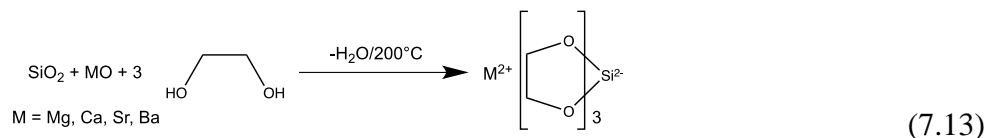
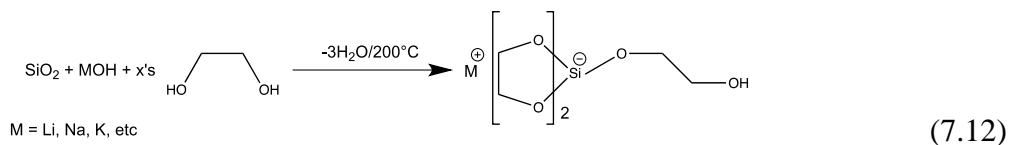
(1970),^{17,18} and Corriu (1986),^{19,20} to explore the depolymerization of SiO₂. This work here covers a wide variety of SiO₂ sources ranging from amorphous silica to quartz powder. These studies focused on reaction (11) or similar generating hexacoordinated triscatecholato Si, **I**.¹²⁻¹⁹



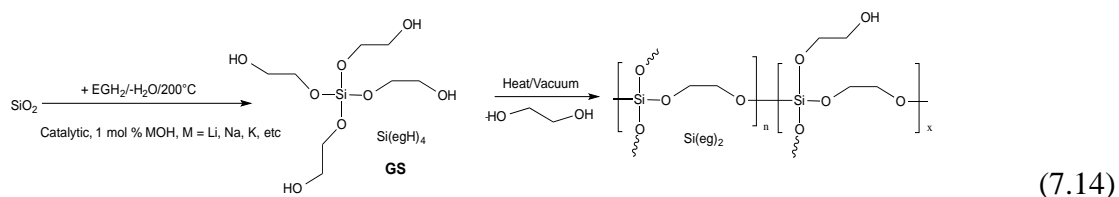
Silicon, unlike carbon, has the ability to form five and six bonds where the original Si-O bond strength of tetrahedral silicon is diminished, which is key to the success of the reaction. Unfortunately, **I** cannot be distilled. Additionally, **I** is highly stable in which it is water-soluble and has to be reacted with H₂SO₄ to produce precipitated silica. From a practical perspective, this process, while offering a low temperature route to precipitated silica, would require three moles of catechol per mole of precipitated silica or 330 g of catechol to produce 60 g of precipitated silica and 280 g of Na₂SO₄. This is unattractive due to the large amount of precursors required to yield a small amount of precipitated silica although no CO₂ would be produced.

A search for something more practical than catechol led us to try ethylene glycol to promote the depolymerization of silica as shown to reactions (7.12) and (7.13).^{21,22} The depolymerization mechanism builds on expansion of the coordination sphere around silicon. The pentacoordinated silicate of reaction (7.12) provided the basis for Herreros *et al.*²³ to determine that this compound is the primary intermediate in the ethylene glycol

mediated synthesis of silicalite zeolites. Likewise, it allowed Kinrade *et al.*²⁴ to propose a mechanism where sugars formed similar pentacoordinated silicates, allowing plants to transport silica within the plant as the basis for biosilification processes.

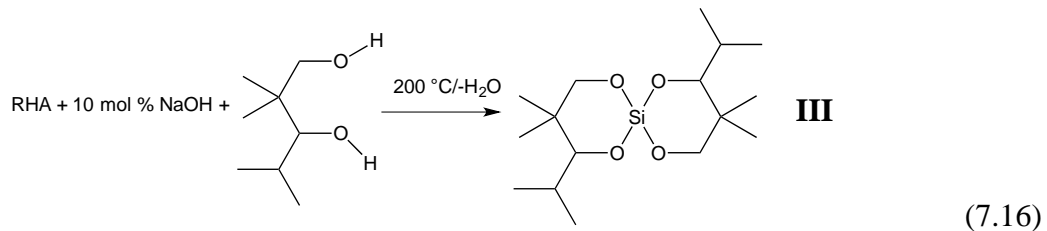
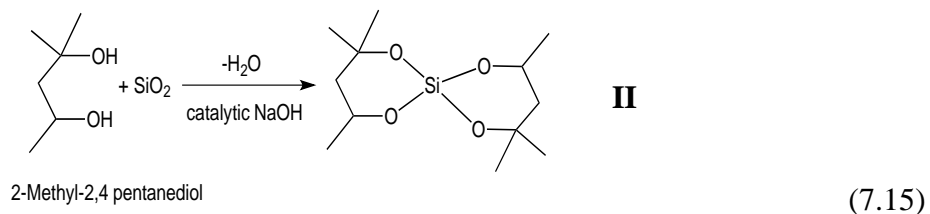


We were able to demonstrate the reaction (7.12) can be promoted catalytically using an alkali base as presented in reaction (7.13).^{25,26} These studies were done with fumed silica (SSA = 350 m²/g), which defeats the overall objective of the “Grand Challenge”. However, these studies were critical as they determined that reaction (7.14) is first order in base concentration and surface area, the activation energy for the reaction is approximately 60 kJ/mol, and the reaction is faster with amorphous rather than crystalline silica.²³ Unfortunately, the glycolatosiloxane (GS) product cannot be distilled as it forms polymers on heating resulting in purification difficulties.



Other amorphous silica sources with high surface areas, such as rice hull ash (RHA) and diatomaceous earth (DE) could be used as potential replacements for fumed silica.^{27,28} RHA is produced in 250k ton/yr quantities in the U.S. alone. Additionally, it is mainly amorphous and offers specific surface areas (SSA) of 20 m²/g. The samples used in our study were 90 wt % silica, 5 wt % carbon, and 5 wt % minerals that are easily removed by washing with dilute HCl.²⁹ In addition, we obtained a sample of rice hulls that had been ashed at ≥ 600 °C (A-RH) to produce a material that was > 95 wt % silica and with SSA of nearly 230 m²/g. DE is available from multiple commercial sources with a SSA ranging from 1 – 70 m²/g with an amorphous structure.

We report here the first examples of the synthesis of distillable spirosiloxanes directly from biogenic silica sources in the presence of a catalytic amount of base. Sterically hindered diols are key to the formation of spirosiloxanes.³⁰ 2-methyl-2,4-pentanediol is the hydrogenated product of base catalyzed acetone condensation and is the lowest cost diol available. This and 2,2,4-trimethyl-1,3-pentanediol permit extension of reaction (7.14) to (7.15) and (7.16).



7.4 Experimental

Materials. Chemicals and solvents were obtained from commercial suppliers and used without further purification, unless otherwise indicated. Fumed silica and Celite 545 filter aid were supplied by Wacker Chemie AG and Fisher Scientific, respectively. DE was manufactured by Safer Brand. RHA was supplied from Wadham Energy. Prior to use, DE and RHA were boiled with water, filtered, and dried. All other chemicals were purchased from Fisher Scientific and used as received. The A-RH was received from the J. Cervantes group of the University of Guanajuato, Mexico.

NMR analyses. ^1H , ^{13}C , and ^{29}Si NMR were measured in chloroform-*d* with TMS (0.00 ppm) as the internal reference on a Varian VNMRs 500 spectrometer. ^1H NMR spectra were collected at 500 MHz using a 7998.4 Hz spectral width, a pulse width of 45° , relaxation delay of 0.5 s, 65K data points. ^{13}C NMR spectra were collected at 100 MHz using a 25,000 Hz spectral width, a pulse width of 40° , relaxation delay of 1.5 s, and 75K data points. ^{29}Si NMR spectra were collected at 99.35 MHz using a 4960 Hz spectral width, a pulse width of 7° , a relaxation delay of 20 s, and 4K data points.

Mass spectroscopy (MS) analyses were conducted using a VG 70-250-S magnetic sector instrument (Waters) by electron impact ionization (EI). The instrument was calibrated with perfluorokerosene-H. The samples were conducted in EI mode at 70 eV electron energy with an ion source temperature of 240 °C. The mass range was scanned from 1000 to 35 m/z.

Electrospray ionization (ESI) was performed on an Agilent Q-TOF system with a dual ESI ion source. The mobile phase consisted of a 9:1 mixture of acetonitrile:water with 0.1% formic acid. Lock mass correction was used to obtain mass accuracy.

Matrix assisted laser desorption ionization time of flight (MALDI-TOF) was performed on a Micromass TofSpec-2E equipped with a 337 nm nitrogen laser in positive-ion reflectron mode using poly(ethylene glycol) as the calibration standard, dithranol as matrix, and AgNO₃ as ion source. Samples were prepared by mixing a solution of 5 parts matrix (10 mg/ml in THF), 5 parts sample (1 mg/ml in THF), and 1 part of AgNO₃ (2.5 mg/ml in water) and blotting the mixture on the target plate then air dried.

Thermal gravimetric analysis (TGA). Thermal stabilities of materials under synthetic air were measured on a Q600 simultaneous TGA-DSC Instrument (TA Instruments, Inc., New Castle, DE). Samples (15 – 25 mg) were placed into alumina pans and then ramped from 25 to 1000 °C (10 °C/min). The air-flow rate was 60 mL/min.

Synthesis of Spirosiloxane. The dissolution reaction was established by reacting of silica (0.33 moles) with NaOH (1.33 g, 0.03 moles) in 150 ml of diol in a distillation apparatus. The solution was heated 15 °C below the boiling point of the diol and stirred to promote complete dissolution. The reaction was stirred for 24 h to drive the reaction forward with the removal of water. Small amounts of water were collected (2 – 5 mL) via distillation. After 24 h, the diol was distilled to drive the reaction forward. 100 mL of diol was distilled then an additional 100 mL of diol was added to the reaction flask. A second distillation of 100 mL was undertaken after stirring for several hours. The dissolved silica remained in the reactor for EGH₂ and 1,4-butanediol since the spirosiloxane could not be distilled. The product was isolated by filtration.

Conversion of **II to Si(OEt)₄.** A 500 mL round-bottom flask was flame dried prior to the experiment. 25 mL of activated 4 Å molecular sieves, 10 g (0.038 mol) of **II** and 400

mL of dry 100 % ethanol were added to a 500 mL round-bottom flask equipped with a stir bar under nitrogen. The reaction was stirred 1 h prior to adding 2.5 mL (0.015 mol) of TFA. The reaction was allowed to stir at room temperature for 24 h under nitrogen. The contents in the reaction were then filtered to remove the molecular sieves and precipitated solids that formed during the course of the reaction. The filtrate was added to hexanes (400 mL) and washed with water (3 x 150 mL) to remove the diol and TFA. The hexanes solution was dried with Na_2SO_4 then filtered. The solvent was removed under reduced pressure to yield $\text{Si}(\text{OEt})_4$ (5.2 g, 65 %), which was characterized with NMR and EI-MS ($m/z = 208.1$).

Conversion of II to $\text{Si}(\text{OMe})_4$. A 500 mL round-bottom flask was flame dried prior to the experiment. 25 mL of activated 4 Å molecular sieves, 10 g (0.038 mol) of **II**, 200 mL of dry methanol, and dry hexanes were added to a 500 mL round-bottom flask equipped with a stir bar under nitrogen. The reaction mixture was allowed to stir for 1 h prior to adding 2.5 mL (0.015 mol) of TFA. The reaction was allowed to stir at room temperature for 24 h. The mixture was then poured into a separatory funnel and the two layers were separated. The methanol layer was discarded. The hexane layer was washed with water (3 x 300 mL) to remove unwanted diol and TFA. The solution was dried with Na_2SO_4 then filtered. Hexanes was removed under reduced pressure to yield $\text{Si}(\text{OMe})_4$ (3.0 g, 40 %), which was characterized using NMR and MS ($m/z = 153.1$).

Conversion of II to Precipitated Silica. **II** (10 g, 0.038 mol), 100 % ethanol (50 mL), H_2O (4 mL), and 12N HCl (2 mL) were added to a 250 mL round bottom flask equipped with magnetic stirrer. The reaction was allowed to stir at room temperature for

24 h. Na₂CO₃ was used to neutralize the reaction resulting in a transparent colloidal dispersion of silica particles.

7.5 Results and Discussion

Shown in Table 1, the characterization data and dissolution rate to dissolve a series of biogenic silica sources using diols ethylene glycol (EGH₂), 1,4-butane diol, 2-methyl-2,4-pentanediol, and 2,2,4-trimethyl-1,3-pentanediol. EGH₂ and 1,4-butane diol were not expected to form spiroxiloxanes whereas 2-methyl-2,4-pentanediol and 2,2,4-trimethyl-1,3-pentanediol were likely candidates. Two other hindered diols were also tried, which included 2-methyl-1,3-propanediol and 1,3-butanediol that yielded spiroxiloxanes, but did not distil. These were not fully characterized because of their tendency to gel, but ²⁹Si-NMR gave peaks in the 62-65 and 70-73 ppm regions that we have previously associated with simple spiroxiloxanes and ring opened polymer analogs.

Table 7.1. Percent SiO₂ depolymerization and characterization data given.

Diol (bp°C) SiO ₂	SSA m ² /g	EGH ₂ (197°)	HO(CH ₂) ₄ OH (235°)	2-methyl-2,4- pentanediol (197°)	2,2,4- trimethyl- 1,3- pentanediol (232°)
Celite	1	12%	13 %	4%	1.5%
Vermiculite	4	2.5	3	3	--
RHA	26	20	23	24	12
RHA	85	40 [†]		40 [†]	
DE	23	16	18	4	3
Fumed SiO ₂	350	98 ⁺	98 ⁺	98 ⁺	98 ⁺
A-RH	230			60	--
Mass Spec. ^{††}		Spiro 149, 80 % intensity ²³	Spiro 205, 15 % intensity	Spiro 260, I = 15% -CH ₃ 245 100%	Spiro 316, I = 7 % 273 (-Me ₂ CH) I = 30%
¹ H-NMR		Si(glycoxy) ₄ ²³ CH ₂ O 3.74 CH ₂ OH 3.94	CH ₂ O 3.41, CH ₂ 1.45 Si(OROH) ₄ CH ₂ O 3.70 CH ₂ 1.65	CHOH 4.20, CH ₂ 1.47, 1.64 CH ₃ 1.30, 1.24, 1.18 II	CHOH 3.7, CH ₂ OH, 3.32, CH 1.87 CH ₃ 0.73, 0.75, 0.95,

				$\underline{\text{C}}\text{H}_2\text{O}$ 4.30, $\underline{\text{C}}\text{H}_2$ 1.48, 1.66 $\underline{\text{C}}\text{H}_3$ 1.28, 1.22, 1.18,	III $\underline{\text{C}}\text{H}\text{O}$ 3.4, $\underline{\text{C}}\text{H}_2\text{O}$, 3.20, $\underline{\text{C}}\text{H}$ 1.59 $\underline{\text{C}}\text{H}_3$ 0.87, 0.88, 0.97,
^{13}C -NMR		Si(glycoxy)₄ ²³ $\underline{\text{C}}\text{H}_2\text{O}$ 3.74 $\underline{\text{C}}\text{H}_2\text{OH}$ 3.94	$\underline{\text{C}}\text{H}_2\text{O}$ 62.55 $\underline{\text{C}}\text{H}_2$ 29.84 Si(OROH)₄ $\underline{\text{C}}\text{H}_2\text{O}$ 64.80 $\underline{\text{C}}\text{H}_2$ 31.99	$\underline{\text{C}}(\text{Me})_2\text{OH}$ 71.56, $\underline{\text{C}}(\text{H},\text{Me})\text{OH}$ 65.64, $\underline{\text{C}}\text{H}_2$ 49.47 $(\underline{\text{C}}\text{H}_3)_2$ 31.82, 27.71, $\underline{\text{C}}\text{H}_3$ 24.31 II $\underline{\text{C}}(\text{Me})_2\text{OH}$ 74.63, 74.38 $\underline{\text{C}}(\text{H},\text{Me})\text{OH}$ 67.82, 67.60 $\underline{\text{C}}\text{H}_2$ 48.40, 48.32 $(\underline{\text{C}}\text{H}_3)_2$ 32.20, 27.98 $\underline{\text{C}}\text{H}_3$ 24.17	$\underline{\text{C}}\text{H}_2\text{OH}$, 83.11 $\underline{\text{C}}\text{H}\text{OH}$ 73.3, $\underline{\text{C}}$ 39.04, $\underline{\text{C}}\text{H}$ 29.08 $\underline{\text{C}}\text{H}_3$ 23.27, 19.66, 16.60, III $\underline{\text{C}}\text{H}\text{O}$ 82.52, $\underline{\text{C}}\text{H}_2\text{O}$ 69.17, $\underline{\text{C}}$ 40.80? $\underline{\text{C}}\text{H}$ 30.57 $\underline{\text{C}}\text{H}_3$ 23.11, 18.72, 15.16
^{29}Si -NMR		-82	-82	-82	-81.85

[†] 630 g RHA 75 wt % silica by TGA or 7.87 mol SiO₂, 7 l EGH₂, 10 mol % NaOH, 24 h distillation. ^{††} MALDI, EI, FABS, ²⁹Si NMR show GS is analogous to TEOS and Si(OBU-OH)₄ peak, spiroxiloxane shifted. ¹H, ¹³C NMRs suggest chirality in spiroxiloxanes, likely a racemic mixture.

The silica sources explored included RHA, DE, celite (low surface area DE), vermiculite (iron magnesium aluminosilicate with 10-12 wt % silica), ash rice hulls (A-RH), and fumed silica. All silica materials were first boiled in dilute HCl (24 h, 5 wt %), washed with water, acetone and then oven dried (115°C, 24 h) prior to use. The starting materials, isolated products and undissolved silica samples were characterized by mass spectroscopy, NMR, XRD, BET and TGA.

Table 7.1 presents the characterization data for the starting materials, the reaction products and coincidentally compares the extent of dissolution using standard conditions. The characterization spectra are shown in Figures 7.1 – 7.16. With the exception of vermiculite, all of the sources are amorphous silica. The XRD pattern of RHA is shown

in Figure 7.17. In general, the amount of SiO₂ that dissolves for all sources is directly related to specific surface areas, SSAs and reaction temperatures. Vermiculite's low silicon content and crystallinity are likely at least partially responsible for its poor dissolution rates.

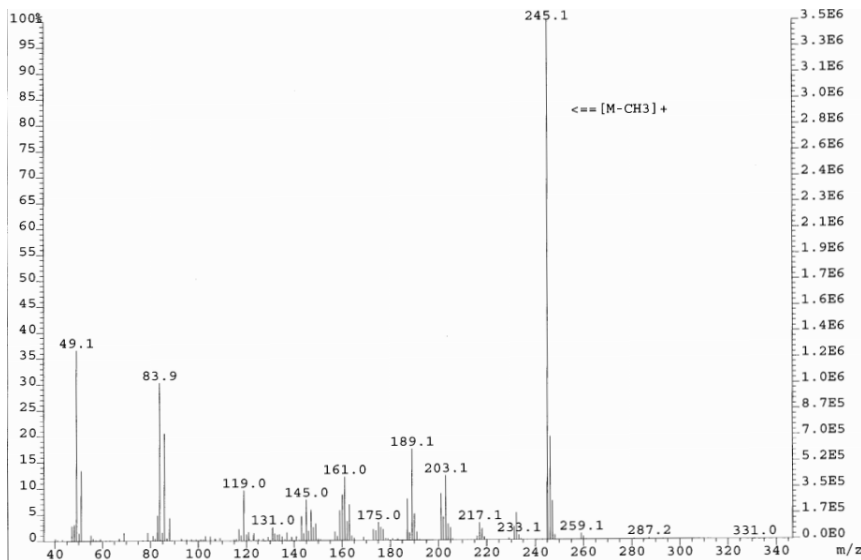


Figure 7.1. EI-MS of **II**.

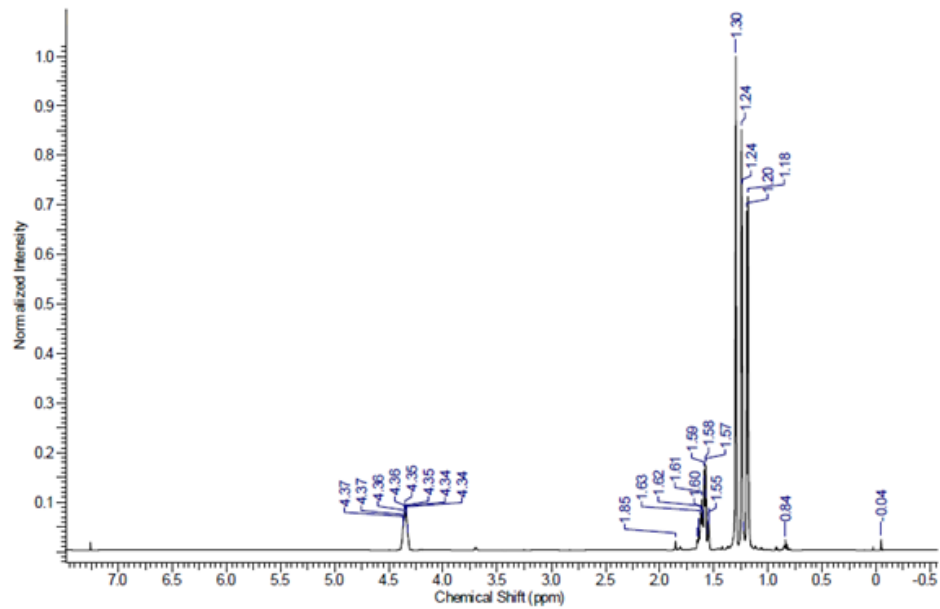


Figure 7.2. ^1H -NMR of II.

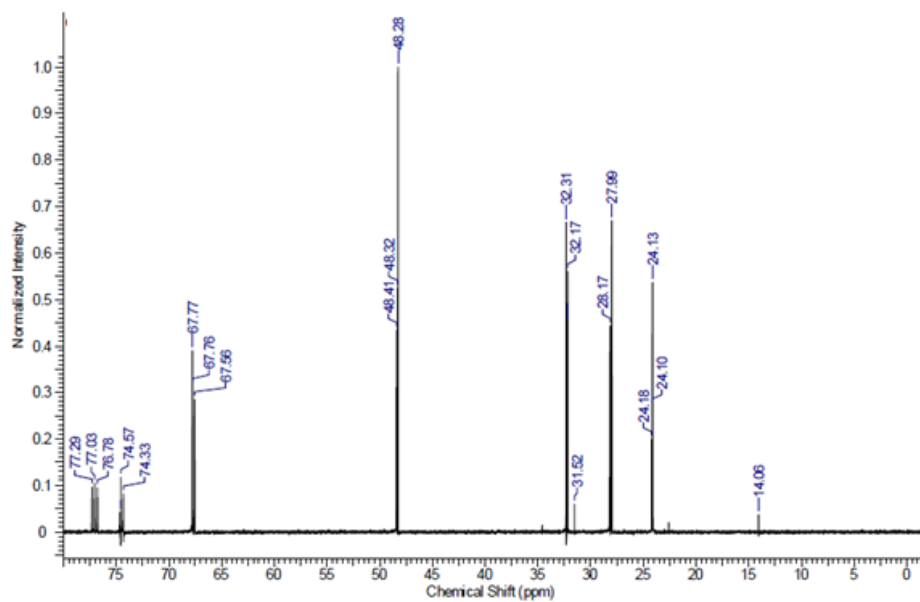


Figure 7.3. ^{13}C -NMR of II.

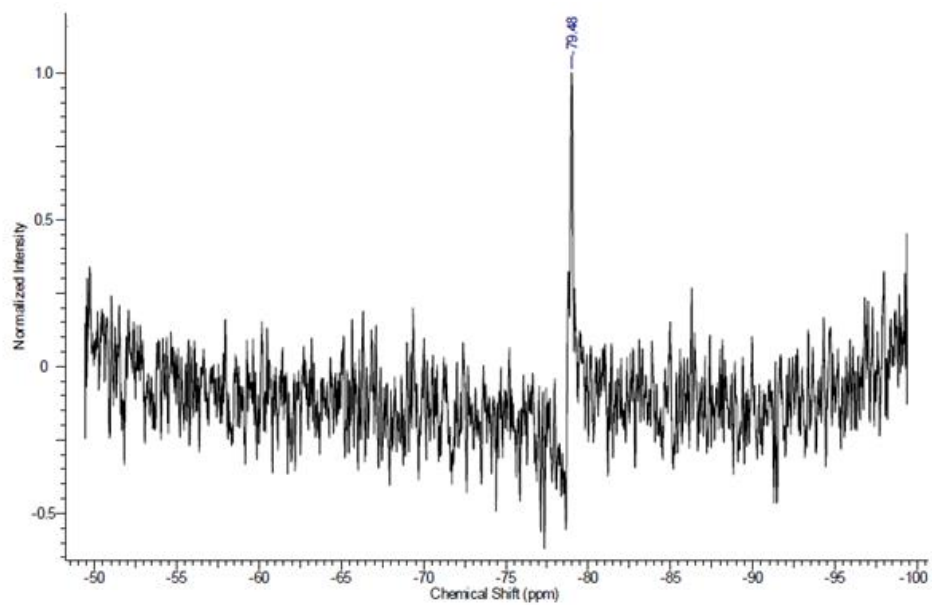


Figure 7.4. ^{29}Si -NMR of **II**.

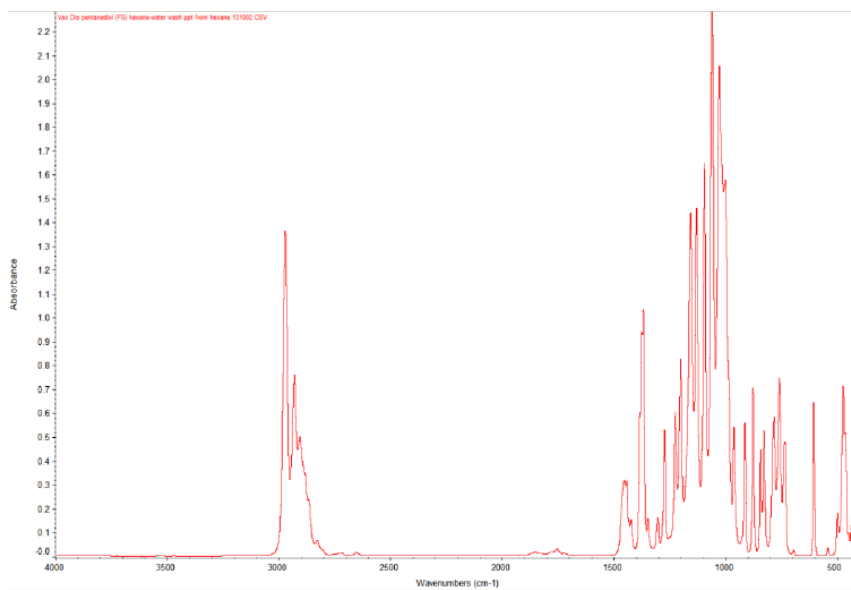


Figure 7.5. FTIR spectrum of **II**.

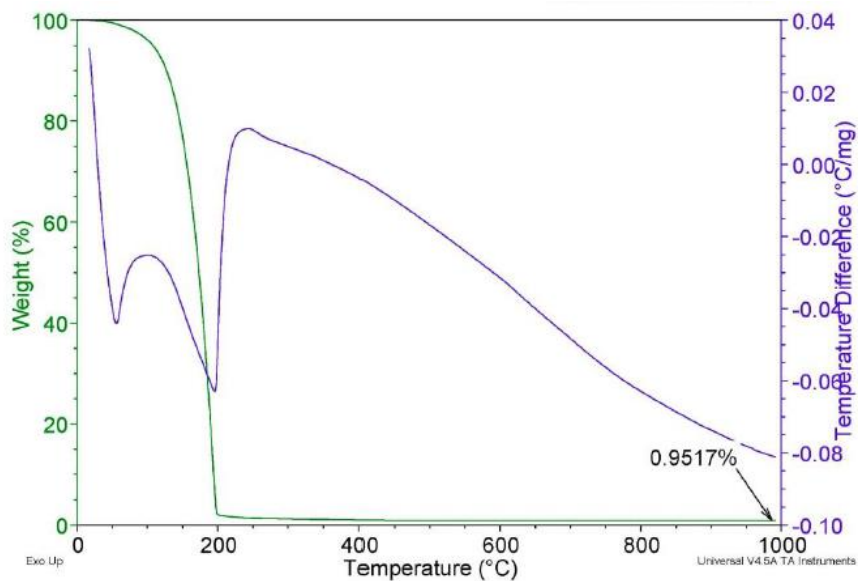


Figure 7.6. TGA of II.

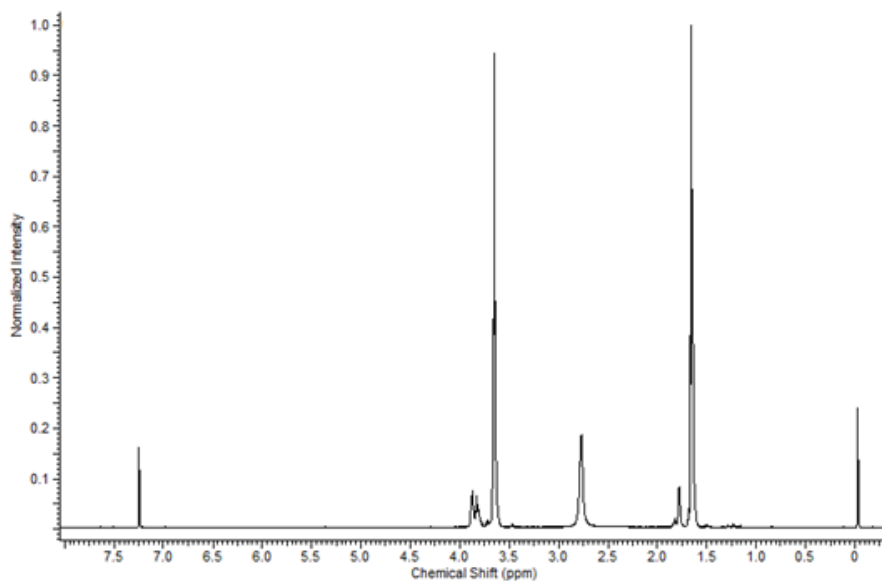


Figure 7.7. ¹H-NMR of spirosiloxane synthesized from 1,4-butanediol.

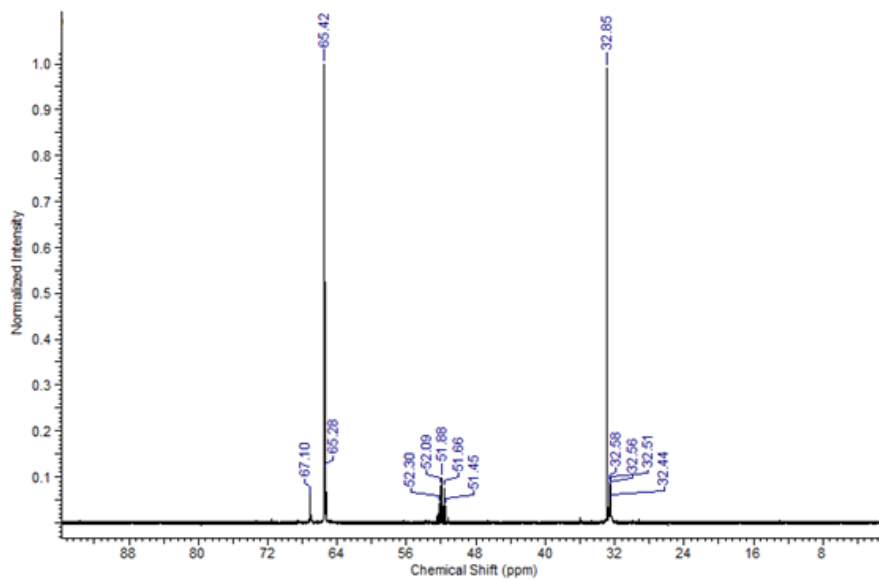


Figure 7.8. ^{13}C -NMR of spirosiloxane synthesized from 1,4-butanediol.

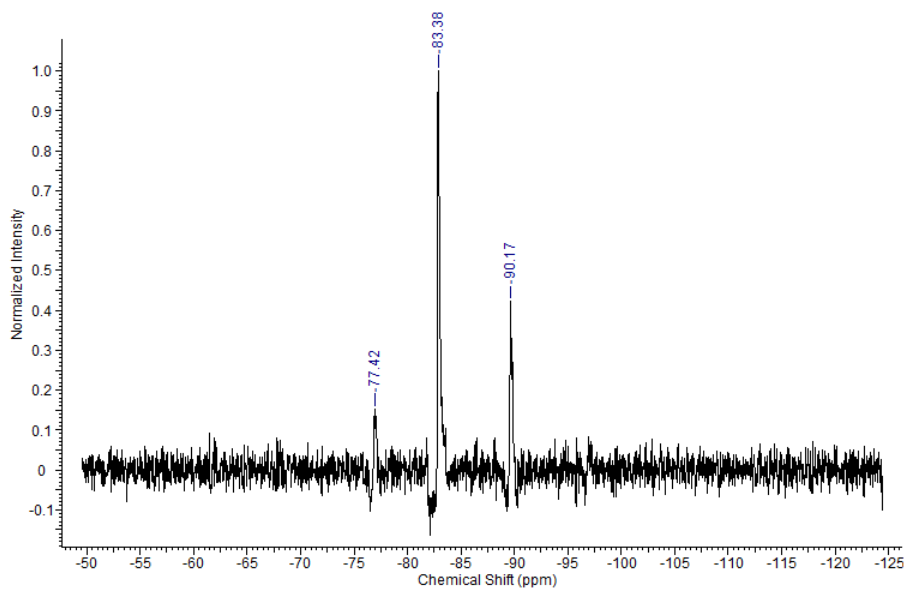


Figure 7.9. ^{29}Si -NMR of spirosiloxane synthesized from 1,4-butanediol.

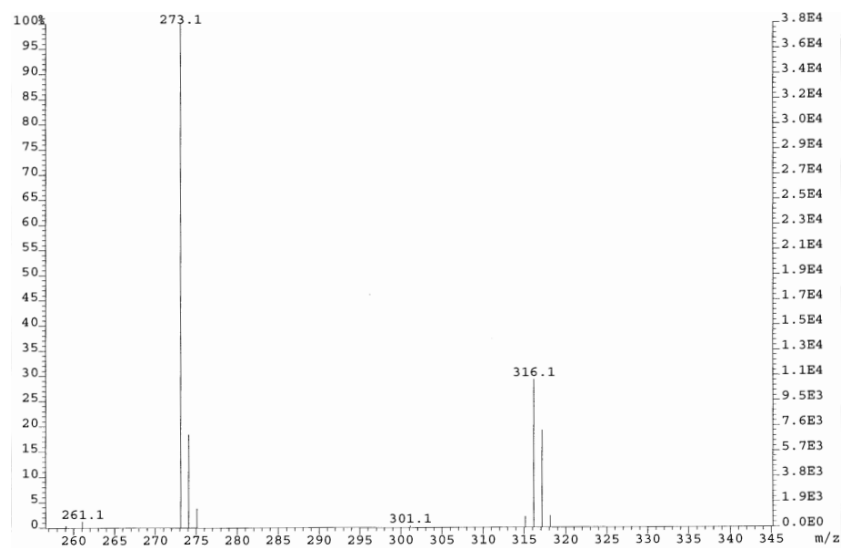


Figure 7.10. EI-MS of spiroisiloxane **III**.

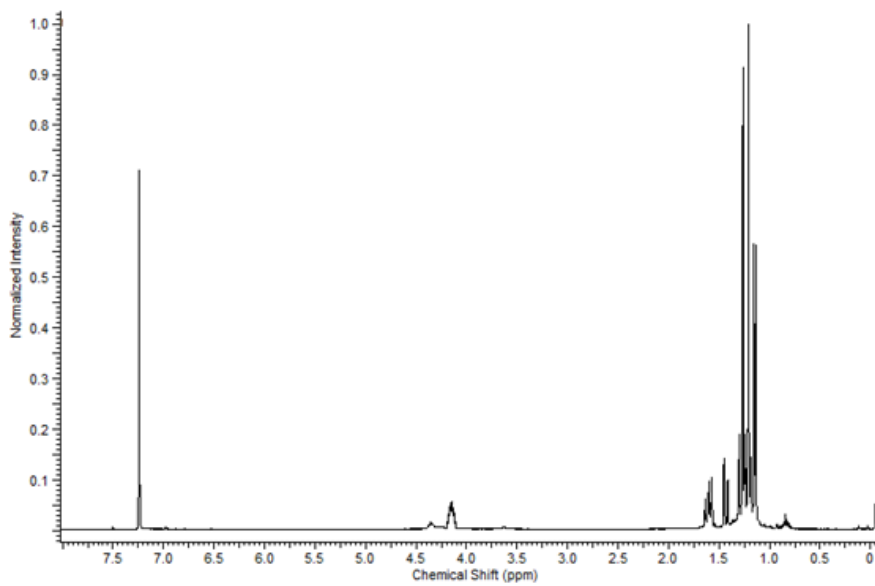


Figure 7.11. ¹H-NMR of **III**.

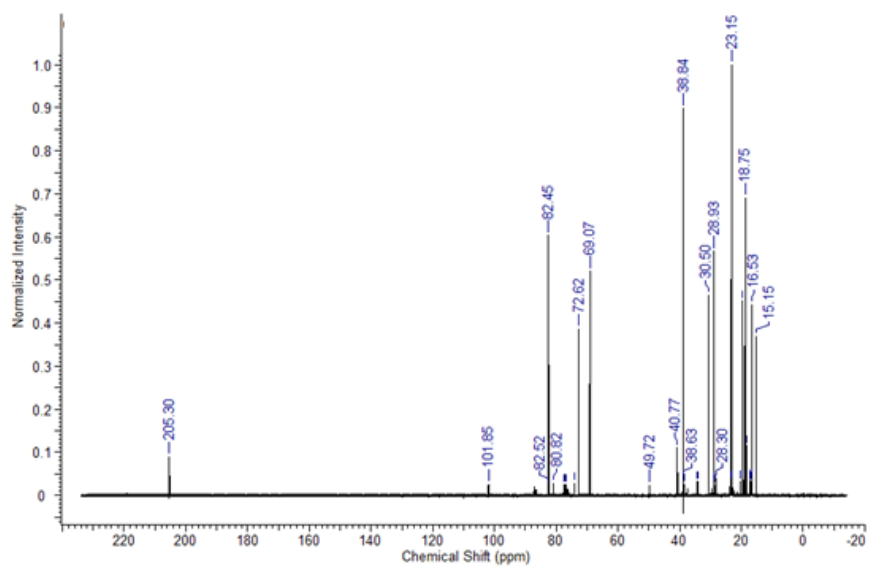


Figure 7.12. ^{13}C -NMR of III.

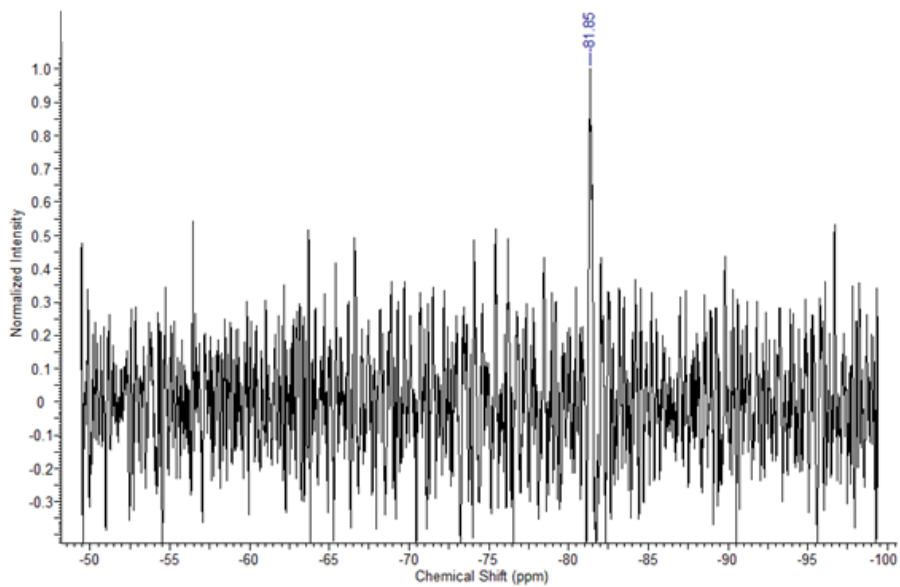


Figure 7.13. ^{29}Si -NMR of III.

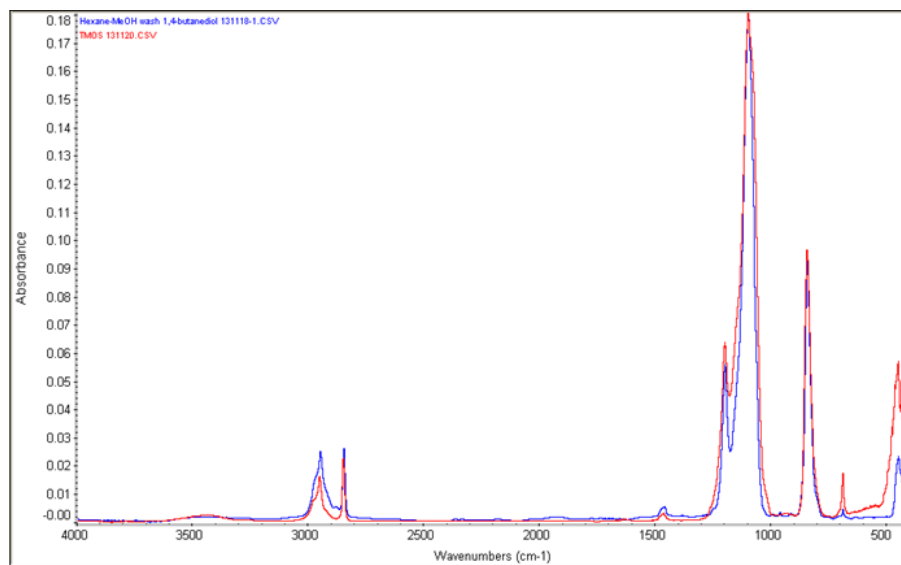


Figure 7.14. FTIR spectra of exchange reaction with MeOH and 1,4-butanediol spiroxiloxane is shown in blue. $\text{Si}(\text{OMe})_4$ is shown in red.

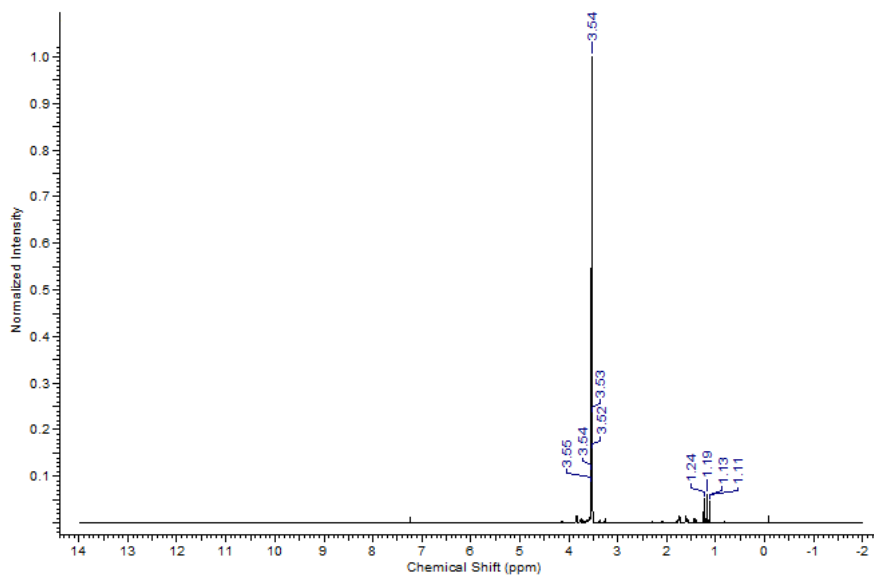


Figure 7.15. ^1H -NMR exchange reaction with MeOH and of spiroxiloxane synthesized from 1,4-butanediol.

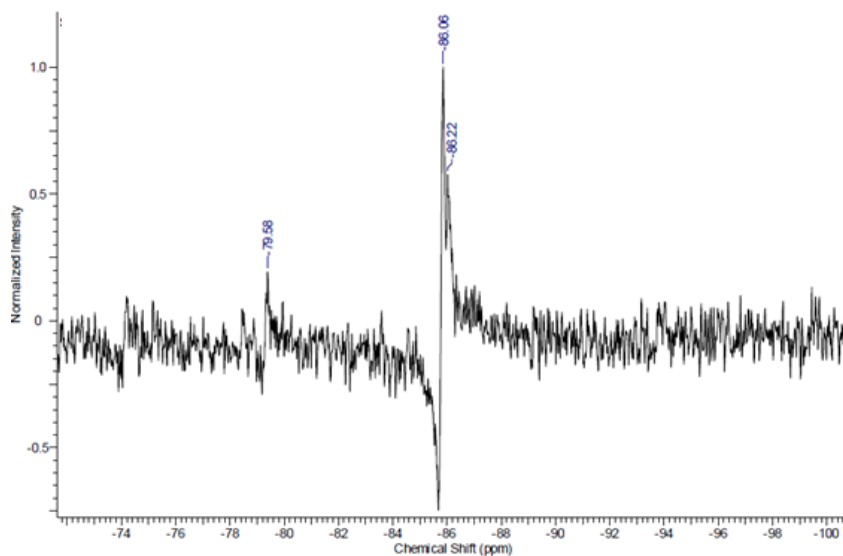


Figure 7.16. ^{29}Si -NMR exchange reaction with MeOH and of spirosiloxane synthesized from 1,4-butanediol.

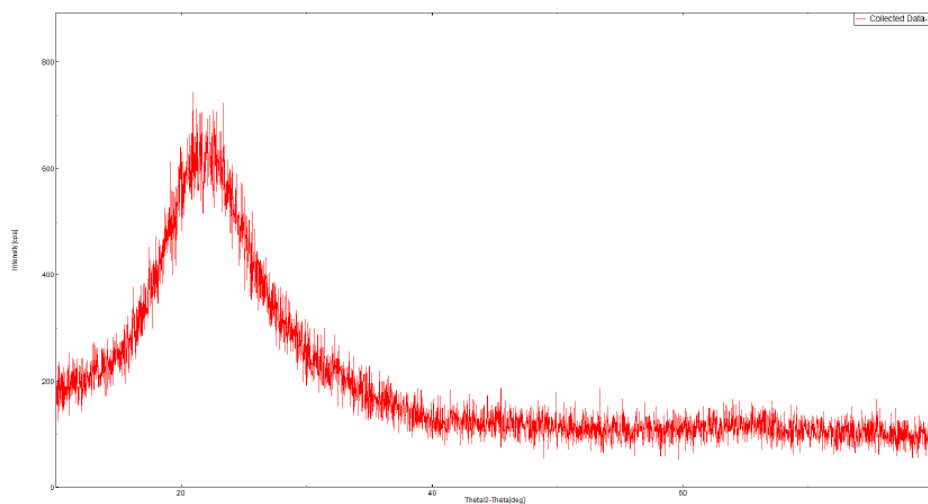


Figure 7.17. XRD pattern of RHA.

SiO_2 depolymerization in 1,4-butanediol was greater than in EGH_2 (b.p. $200\text{ }^\circ\text{C}$) as the boiling temperature is $40\text{ }^\circ\text{C}$ higher. The depolymerization rates for 2-methyl-2,4-pentanediol (b.p. $200\text{ }^\circ\text{C}$) are nearly the same as EGH_2 with the exception of celite and

diatomaceous earth in which the mass spectral analyses suggest that the diol “cracks” producing propanol as the major product rather than then **II**. Both DE and Celite likely have highly acidic sites that account for the observed cracking products. The ashed rice hulls gave the second highest dissolution under standard conditions, which is likely due to the SSA of approximately 230 m²/g. One experiment was conducted on a scale of 630 g of RHA (85 m²/g, 7.87 mol SiO₂), 10 mol % NaOH, 7 L of EGH₂. TGA determined the RHA contained 75 wt % silica content gave an approximately 40 % silica dissolution after 20 h of distillation as determined by TGA of the recovered RHA.

Vermiculite is a common aluminosilicate mineral with no free SiO₂ available for dissolution, however, some dissolution was noted. We have not characterized the product(s), although some alumina dissolution may occur concurrently given Al-EG complexes have been reported previously.³¹

The distillation of 2-methyl-2,4-pentanediol and **II** occur at nearly the same temperature making isolation and purification problematic. However, we found that both **II** and 2-methyl-2,4-pentanediol are hexane soluble with the diol also being water soluble. Thus, simply washing the hexane solutions of the recovered, distilled mixture or the reaction filtrate removes the diol and leaves pure **II**, which is easily recovered and can be redistilled at 200 °C to give higher purities. Removal of the hexane yields **II** as a liquid that slowly crystallizes upon cooling.

Compound **III** and the parent diol are also hexane soluble but the diol is not water soluble; however, **III** can be isolated simply by washing with MeOH. Both spiroxiloxanes can be distilled to higher purity. **II** and **III** are the first examples of a distillable form of

silica made at low temperatures directly from biogenic silica sources. This is significant as it is not energy intensive and does not require expensive equipment.

We explored the potential to use **II** as a precursor to Si(OEt)₄ (TEOS) and Si(OMe)₄ (TMOS) since TEOS and TMOS represent the optimal products. We found that it is easy to affect an exchange that provides TEOS and TMOS in 65 and 40 % yields, respectively via a simple acid catalyzed exchange reaction. This success prompted us to explore the direct synthesis of TEOS from Si(EG)₂ as shown in reaction (14). We report the successful synthesis of TEOS per reaction (17) again in unoptimized yields of 55 % using essentially the same conditions.

We explored the utility of using **II** and **III** to form pure precipitated silica. Mixing **II**, **III**, TEOS, or TMOS with water and catalytic amounts of HCl precipitates very fine silica particles at ambient conditions. This indicates that high purity precipitated silica can be easily produced without reverting to reactions (7.3), (7.8) or (7.9). If **II** dissolved in ethanol is acidified to pH 1 with HCl, precipitated silica is not observed as shown in Figure 7.18. However, the solution gels upon neutralization with Na₂CO₃. It appears that the diol stabilizes the colloid with the addition of ethanol resulting in precipitated silica.

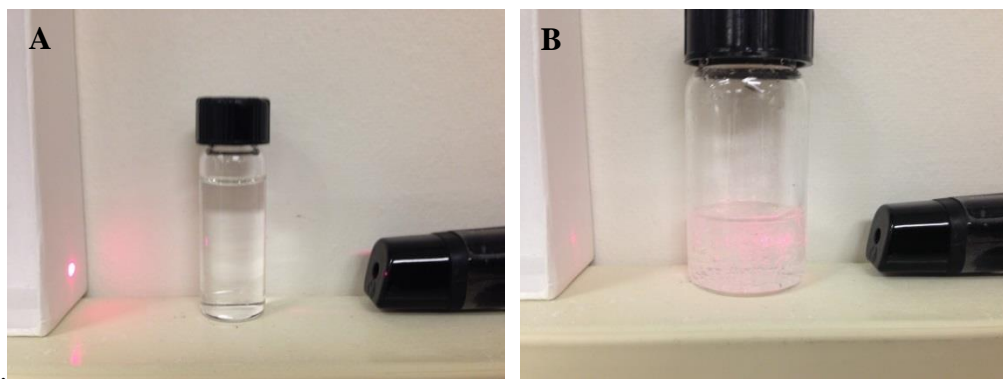


Figure 7.18. (A) Colloidal silica at pH 1 is transparent without scattering light. (B) A gel forms scattering light on neutralizing with Na_2CO_3 (pH 7, 30 min).

This approach provides a low-cost means of “petrifying wood”, which is infusing wood with a silicon material to produce a more flame retardant material. Moreover, the water-soluble diol can be recycled meaning this process is renewable. This approach requires only catalytic acid and does not produce CO_2 or Na_2SO_4 by-products making it a green and low cost route to produce high purity precipitated silica.

7.6 Conclusion

The work reported demonstrates the first examples of based catalyzed depolymerization of silica to form distillable and easily purified spiroxiloxanes. We also present the utility of this low cost and renewable approach as a potential route to the production of silicon compounds and their potential to serve as precursors for the formation of highly pure silicon-based materials, which does not require the production of metallurgical grade silicon, and corrosive and toxic SiCl_4 . Additionally, these low cost spiroxiloxanes can be used to produce flame retardant “petrified wood”. This process represents the first clear solution to the “Grand Challenge” of depolymerizing silica to

make high purity silicon containing materials using sustainable, green starting materials that does not produce byproducts CO₂ or Na₂SO₄ without the need for capital equipment or energy intensive processing.

References

1. Saga, T. *NPG Asia Mater.* **2010**, *2*, 96.
2. DeWolf, S.; Descoedres, A.; Holman, Z. C.; Ballif, C. *Green* **2012**, *2*, 7.
3. Shit, S. C.; Shah, P. *Natl. Acad. Sci. Lett.* **2013**, *36*, 355.
4. Concise Encyclopedia of High Performance Silicones, Eds. A. Tiwari, M. D. Soucek, Wiley 2014, ISBN: 978-1-118-46965-1.
5. Showell, G. A.; Mills, J. S. *DDT* **2003**, *8*, 551.
6. Silicon and Silicon Alloys, Chemicals and Metallurgical, V. Dosaj, M. Kroupa, R. Bitta in Kirk-Othmer Encyclopedia of Chemical Technology. John Wiley & Sons, Inc. online.
7. Kawamoto, H.; Okuwada, K. *Sci. Tech. Trends Quarterly Rev.* **2007**, *24*, 38.
8. Gurav, A.; Kodas, T.; Pluym, T.; Xiong, Y. *Aerosol Sci. Tech* **1993**, *19*, 411.
9. Okamoto, M.; Suzuki, E.; Ono, Y. *J. Catalysis* **1994**, *145*, 537.
10. Kirk-Othmer Encyclopedia of Chemical Tech., 5th Ed. Vol. 22, pp 365-547 (2007).
11. Falcone, J. "Silicon Compounds: Anthropogenic Silicas and Silicates," Kirk-Othmer Encyclopedia of Chemical Tech. DOI: 10.1002/0471238961.1925142006011203.a01.pub22005.
12. Rosenheim, A.; Raibmann, B.; Schendel, G. *Z. Anorg, Chem.* **1931**, *196*, 160.
13. Weiss, V. A.; Reiff, G.; Weiss, A. **1961**, *142*, 151.

14. Frye, C. L. *J. Am. Chem. Soc.* **1964**, *86*, 3170.
15. Boer, F. P.; Flynn, J. J.; Turley, J. W. *J. Am. Chem. Soc.* **1968**, *90*, 6973.
16. Flynn, J. J.; Boer, F. P. *J. Am. Chem. Soc.* **1969**, *91*, 5756.
17. Barnum, D. W. *Inorg. Chem.* **1970**, *9*, 1942.
18. Barnum, D. W. *Inorg. Chem.* **1970**, *11*, 1424.
19. A) Boudin, A.; Cerveau, G.; Chuit, C.; Corriu, R. J. P.; Reye, C. *Angew. Chem. Int. Ed.* **1986**, *25*, 474. B) Boudin, A.; Cerveau, G.; Chuit, C.; Corriu, R. J. P.; Reye, C. *Organometallics* **1988**, *7*, 1165.
20. A) Corriu, R. J. P.; Young, J. C. Chemistry of Organic Silicon Compounds, S. Patai, Z. Rappaport, eds. Ch. 20, Wiley, Chichester, 1989. B) Corriu, R. J. P. *Pure and Appl. Chem.* **1988**, *60*, 99.
21. Laine, R. M.; Blohowiak, K. Y.; Robinson, T. R.; Hoppe, M. L.; Nardi, P.; Kampf, J.; Uhm, J. *Nature* **1991**, *353*, 642.
22. Hoppe, M. L.; Laine, R. M.; Kampf, J.; Gordon, M. S.; Burggraf, L. W. *Angew. Chem. Int.* **1993**, *32*, 287.
23. Herreros, B.; Carr, S. W.; Klinowski, J. *Science* **1994**, *263* 1585.
24. Kinrade, S. D.; Del Nin, J. W.; Schach, A. S.; Sloan, T. A.; Wilson, K. L.; Knight, C. T. G. *Science* **1999**, *285*, 1542.
25. A) Cheng, H.; Tamaki, R.; Laine, R. M.; Babonneau, F.; Chujo, Y.; Treadwell, D. *J. Am. Chem. Soc.* **2000**, *122*, 10063. B) Laine, R. M.; Treadwell, D. R.; Mueller, B. L.; Bickmore, C. R.; Waldner, K. F.; Hinklin, T. *J. Chem. Mater.* **1996**, *6*, 1441.

26. Bickmore, C. R.; Hoppe, M. L.; Laine, R. M. "Processable Oligomeric and Polymeric Precursors to Silicates Prepared Directly from SiO₂, Ethylene Glycol and Base." in Synthesis and Processing of Ceramics: Scientific Issues, Mat. Res. Soc. Symp. Proc.; W.E. Rhine, T.M. Shaw, R.J. Gottschall, Y. Chen 249, 107 (1991).
27. www.enpowercorp.com/index.cfm?page=wadham
28. www.bugging-out.com/mineinfo.htm website for Diasource Inc.
29. Laine, R. M.; Krug, D. J.; Marchal, J. C.; McColm, A. "Low cost routes to high purity silicon and derivatives thereof" U.S. Patent 8475758 July 2, 2013.
30. Frye, C. L. *J. Org. Chem.* **1983**, 22, 2496.
31. A) Herreros, B. T.; Barr, L.; Klinowski, J. *J. Phys. Chem.* **1994**, 98, 738. B) Li, X.; Michaelis, V. K.; Ong, T.-C.; Smith, S. J.; McKay, I.; Müller, P.; Griffin, R. G.; Wang, E. N. *Cryst Eng Comm*, **2014**.
32. Boudin, A.; Cerveau, G.; Chuit, C.; Corriu, R. J. P.; Reye, C. *Angew. Chem. Int. Ed.* **1986**, 25, 4734.
33. Mcbee, E. T.; Roberts, C. W.; Judd, G. F.; Chao, T. S. *J. Am. Chem. Soc.* **1955**, 77, 1292.
34. George, P. D.; Sommer, L. H.; Whitmore, F. C. *J. Am. Chem. Soc.* **1955**, 77, 6647.
35. Tour, J. M.; John, J. A.; Stephens, E. B. *J. Organometallic Chem.* **1992**, 429, 301.
36. Silverman, G.; Rakita, P. Handbook of Grignard Reagents Marcel Dekker, 1996, 667-675.
37. Klovov, B. A. *Organic Process Research & Development* **2000**, 4, 49.

38. Jung, K.-H.; Kim, S.-Y.; Tan, W.; Shin, D.-S.; Ahn, C. *Bullet. Instit. Basic Sci.* **2005**, *17*, 79.
39. Laine, R. M.; Roll, M. F. *Macromolecules* **2011**, *44*, 1073.
40. Furgal, J. C.; Jung, J. H.; Goodson III, T.; Laine, R. M. *J. Am. Chem. Soc.* **2013**, *135*, 12259.
41. Jung, J. H.; Laine, R. M. *Macromolecules* **2011**, *44*, 7263.
42. Jung, J. H.; Furgal, J.; Goodson III, T.; Mizumo, T.; Schwartz, M.; Chou, K.; Vonet, J.-F.; Laine, R. M. *Chem. Mater.* **2012**, *24*, 1883.
43. Furgal, J. C.; Laine, R. M. *manuscript in preparation*.
44. Popova, V.; Laine, R. M. *manuscript in preparation*.
45. A) Kim, M.; Hinklin, T. R.; Laine, R. M. *Chem. Mater.* **2008**, *20*, 5154. B) Kim, M.; Laine, R. M. *J. Am. Chem. Soc.* **2009**, *131*, 9220.
46. Yi, E.; Laine, R. M. *manuscript in preparation*.
47. www.engin.umich.edu/college/about/news/stories/2013/september/distilling-silica-from-sand
48. Zhang, H.; Dunphy, D. R.; Jiang, X.; Meng, H.; Sun, B.; Tarn, D.; Xue, M.; Wang, X.; Lin, S.; Ji, Z.; Li, R.; Garcia, F. L.; Yang, J.; Kirk, M. L.; Xia, T.; Zink, J. I.; Nel, A.; Brinker, C. J. *J. Am. Chem. Soc.* **2012**, *134*, 15790.

Chapter 8

Overview: Summary, Importance, and Future Work of Dissertation

8.1 Explanation

As research scientists, it is important to connect the research with its impact and importance in regards to the field. In this chapter, the importance of the work as well as future work relative to this dissertation will be discussed. This chapter is significant as it summarizes the work to the general audience. Since my dissertation is diverse, each project will be discussed separately. The main focus of this chapter is to relate the research to the “big picture” of the problem. Although the work only addresses a small portion of the big picture, the research has contributed to each field in some aspects. Perhaps, the research can be applied to future work, which may lead to significant contributions in regards to the big picture. The work here paves the way for future research.

In addition to providing contributions to the big picture, there remains future work relative to each project. The future work is important as it extends our research. Research is a continuous process that never ends as researchers are trying to solve and understand complex issues. Research generally begins with solving the more simple challenges then moving onto the complex problems. Although the work here has aided in the understanding of these complex challenges, more research can be conducted to further

understand these issues and how they relate to the big picture. The objective of this chapter is to present future work at the end of each sub-chapter. The work will be carried out by future students and/or researchers. This chapter is important because it provides the foundation and background for others to continue future research.

8.2. The Drug Development Process

In order to commercialize a drug, there are various stages that must be endured. In this section, the drug development process will be briefly discussed to educate the reader. The successful drug development process begins with identifying a potential class of new drugs in a research setting. Once the news class of drugs has been synthesized and characterized, testing of these compounds is conducted in animals then humans. Ultimately, the drug will be approved by the FDA before being released to the public. The drug discovery phase is one of the most critical stages.

The first stage of drug development process is the discovery phase of the drug. This phase can last between two years to more than a decade.¹ The reason for this large time range is because there several factors that must be considered for a drug candidate to become eligible for testing in humans, which includes the chemical properties of the drug, complexity of the disease, and the amount of resources a company is willing to invest.^{2,3} Once a drug has been selected as a potential candidate, the drug will be screened through the final stages called the preclinical development stage, which involves testing in live animals.⁴ Pharmaceutical companies are required to test the drug in at least two different animal species as well as investigating the toxicology of drug. The preclinical development stage is governed by FDA approved good laboratory practices (GLP).⁵ After

promising preclinical results, the drug will be moved to Investigational New Drug (IND) status where further studies will be conducted.⁶

The next stage of the drug development process is clinical trials. During this stage, there are three main phases. Each phase is regulated by strict FDA guidelines that are governed by Good Clinical Practices (GCP). Phase I tests the safety of the drug in a small number of healthy individuals.⁶ The volunteers will receive increasing doses of the drug until side effects arise. This allows researchers to establish the maximum tolerate dose of the drug. This is critical because it becomes the benchmark for the remaining trials. During this phase, the number of applicants is relatively low ranging from 5 – 100 participants.⁷ After Phase I, Phase II begins with testing and measuring the efficacy of the drug. Researchers monitor the progression of the disease as the participants are administered with the drug. For example, tumor growth and blood pressure are monitored in the case of developing drugs aimed at cancer and diabetes, respectively. It important to note that a control group is require during Phase II where the applicants receive a placebo.⁵ Expected and unexpected effects of drug treatment are monitored throughout Phase II. Phase II trials generally contain 50 – 1000 participants.⁸ The final phase of the drug development process is Phase III where efficacy and safety are evaluated in a much larger group of applicants. Generally, a test group of 300 – 5000 participants are monitored.⁹ This large group allows for a better statistical analysis. In addition, double-blind studies are conducted to allow random assignment of the drug. This is important as it allows the study to be completely unbiased by both researcher and patient.¹⁰ If the drug appears to be effective, patients will be allowed to continue treatment after the conclusion

of the trial before if the drug is approved for market.¹¹ If the FDA approves the drug, it will be available to the public.

As noted, it is clear that the drug development process is complex and time-consuming. It should be emphasized that the most important phase is the drug discovery phase. Without this phase, the preclinical and clinical stages cannot be carried out. During the discovery phase, new drugs will be synthesized and characterized. In order to develop drugs that target specific processes or biological molecules, such as DNA or kinase activity, it is important to understand these processes with great depth. In addition, it is also critical that researchers have techniques and methodologies to examine such processes. This is where my research presented in the dissertation relates to the big picture as it contributes directly to the drug discovery phase. My research has focused on examining the DNA-binding interactions of small organic molecules. In addition, kinase activity was investigated, which plays a critical role in nearly all biological processes. In fact, both kinase and DNA-related processes have been targeted in the development of therapeutics. The impact and future work will be discussed in further detail in each chapter.

8.3 Investigating the DNA-Binding Interactions of Small Organic Molecules (Chapters 3 and 4)

8.3.1 TPA as a New Sensitive Methodology to Diagnose the DNA-Binding Interactions of Small Organic Molecules

The DNA-binding interactions of small organic molecules play a critical role in medicine as several therapeutics are aimed at DNA. Therefore, it is important to

understand such interactions since they can significantly influence the performance of DNA-targeted drugs. However, there remain limitations to investigate DNA-drug interactions at physiologically or biologically relevant conditions as several common techniques do not exhibit high sensitivity. It is important to study DNA-drug interactions at these conditions because their performance can be altered at non-biologically relevant conditions. In addition, common methods, such as circular dichroism, are very ambiguous when examining the DNA-binding mechanism of drugs. In other words, it is very difficult to understand how drugs interact with DNA based solely on these techniques. As a consequence, a combination of selected methodologies is required to gain a better understanding of such interactions. Many reliable techniques, such as X-ray diffraction, yield critical information, but they are often time consuming, expensive, and difficult to employ. Hence, new methodologies that provide valuable information while avoiding these undesirable conditions are of considerable interest.

Herein, we developed a new sensitive methodology to investigate the DNA-binding mechanism of small organics molecules targeted at DNA utilizing two-photon spectroscopy. Our methodology has contributed to the field of medicinal chemistry because it provides a means for pharmaceutical companies and researchers to probe DNA-drug interactions at biologically relevant conditions. This is critical especially in the research and development phase of new drugs. Our approach can be applied to examine the DNA-binding interactions with other macromolecules, such as proteins and peptides. This is significant as therapeutics can target these processes as well. Our methodology will be more applicable in the future as the size and cost of femtosecond

lasers are reduced significantly. Additionally, the process could be automated, which will allow for high-throughput screening.

We have demonstrated a new methodology to diagnose DNA-binding interactions by implementing two-photon spectroscopy. The proposed mechanism relative to the change in the TPA cross-section upon binding with DNA was presented. We hypothesized that the local DNA electric field from the DNA back-bone influences the transition dipole of the binding molecule upon DNA binding. For groove binding, the transition dipole of the binding molecule is parallel with the DNA electric field. As a result, the induced dipole is enhanced. Hence, we observed an increase in the TPA cross-section upon complexing with DNA. On the other hand, the transition dipole of an intercalator is perpendicular with the DNA electric field leading to a reduced induced dipole. As a consequence, a decrease in the TPA cross-section was noted upon binding with DNA.

We are interested in further examining the change in the TPA cross-section of the small molecule upon binding with DNA by either confirming or refuting our hypothesis. This can be achieved by carrying out molecular modeling and/or computational studies. A local DNA electric field can be generated in the computational software. The influence of the DNA electric field can be monitored by positioning the binding molecule at different angles relative to the DNA helical axis. The TPA cross-section would then be calculated as a function of the binding angle with respect to the DNA electric field. In addition, we can conduct experiments with other binding molecules with known binding angles relative to the helical axis. We expect a binding molecule to exhibit a larger TPA cross-section enhancement if the transition dipole moment of the molecule is aligned more parallel with the DNA electric field. Contrarily, we expect a larger TPA cross-

section decrease if the transition dipole moment of the molecule is more perpendicular with the DNA electric field. This will allow us to compare the experimental data with the computational studies to either confirm or disprove our proposed hypothesis.

The dipole of DNA is not necessarily known. This is something that we found interesting because we thought this property would be known. Another hypothesis is that the dipole of DNA can influence the transition dipole of the binding molecule upon DNA binding rather than the DNA electric field. Calculations can be carried out with various lengths of DNA to confirm or refute this hypothesis. One issue with this task is that the dipole of DNA is challenging to calculate because the value is uncertain. The TPA cross-section of the binding molecule can be measured experimentally with different lengths of DNA, which can be correlated with the calculations. Custom DNA with well-defined sequences can be purchased to avoid variations in the experimental data. This will allow us to compare the computational results with the experimental findings.

8.3.2 A New Design Strategy to Tailor the DNA-Binding Mechanism of Small Organic Molecules and Drugs

Design criteria for DNA-targeted therapies are important for drug discovery. The DNA-binding mechanism of small organic molecules is key to their performance. Because of this, it is important to control and modify the DNA-binding mechanism of small organic molecules, such as therapeutics, aimed at DNA. In order to develop drugs with specific properties that exhibit high selectivity and performance, selected moieties are of considerable interest. To be an effective drug, it must overcome many barriers, such as metabolic pathways.¹²² Once the drug enters the nucleus of the cell, the drug has

the capability of interacting with DNA, thus affecting physiological pathways. The design and development of DNA-targeted drugs is a complex task as their performance is dependent on several factors, such as the DNA-binding mechanism and biological conditions. The objective in drug design is to make the drug more selective and cytotoxic towards abnormal cells, such as cancer and/or tumor cells as compared to healthy cells. In order to accomplish this, design criteria of drugs with specific structural motifs and scaffolds are of considerable interest. Some common drugs that have been reported include acridines, alkaloids, and anthracyclines derivatives.¹ The field of designing and developing drugs is a continuous, ongoing field that has been explored. Thus, it is important to establish structure-property relationships of small organic molecules relative to its DNA-binding mechanism as it directly relates to its selectivity and performance.

Our work has led to the emergence of structure-property relationships of DNA-binding molecules that adopt a crescent or V-shaped scaffold. The findings reveal that the structure of these fluorophores can be designed to either intercalate or groove bind with calf thymus dsDNA by structurally modifying the electron accepting properties of the central heterocyclic core. This is the first example that has demonstrated an induced change in the DNA-binding mode of small organic molecules that adopt a crescent shape, which disagrees with the classical model for DNA groove binding molecules as it states that groove binding molecules should possess a crescent shape to closely match the helical groove of DNA. We present a new design strategy that does not obey this classical model. The results suggest that the electron accepting properties of the central heterocyclic core is the key factor in the DNA-binding mechanism. Our work represents a new strategy for the design and development of small molecules aimed at DNA. We hope

our contribution can be applied in drug discovery to target specific diseases and disorders. Perhaps our structure-property relationships will allow researchers to design new therapeutics that can target specific disorders based on the DNA-binding mechanism since this property is key to their performance and selectivity.

We have demonstrated that the optical properties of a series of novel fluorescent nuclear dyes can be finely tuned by varying the conjugation length and electron accepting properties of the heterocyclic core. Based on our work, new fluorophores and/or drugs can be developed and examined using modified heterocyclic cores and pendant arms. The motif of the fluorophore can also be altered to determine if the optical properties can be improved. For example, the motif can be varied to an acceptor-donor-acceptor motif. Other donor moieties may include carbazole-based structures. Carbazole-based fluorophores have been reported to exhibit excellent TPA properties, which have applications for two-photon excited fluorescence microscopy.¹³⁻¹⁵ Units that may be incorporated as the acceptor moiety include *N*-methylpyrimidine or benzoimidazole. The organic groups have also been shown to act both as an acceptor and recognition units to electrostatically with DNA, which have also been reported to exhibit promising TPA properties.¹⁶ Furthermore, new moieties may induce a change in the DNA-binding mode that can lead to enhanced and selective performance for small molecules aimed at DNA.

8.3.3 RNA as a Target for Therapeutics Aimed at Diseases and Disorders

Biological understanding of RNA has evolved as the intermediate between DNA and protein that regulates the genes and functions of cells in all living organisms.^{17,18} RNA catalyzes protein synthesis,¹⁹ controls gene expression,²⁰ and regulates transcription and

translation.^{21,22} RNA is a versatile molecule that has the capability of folding into a wide range of structures and conformations, which can be targeted by small organic molecules. RNA plays a critical role in the progressive of several diseases, such as HIV, hepatitis C, and cancer.²³ RNA has been recently targeted for therapeutics aimed at diseases and disorders. Interestingly, the US Food and Drug Administration (FDA) approved the first RNA-based drug for the treatment of cancer in 1998 called Fomivirsen as an antiviral drug by blocking the translation of mRNA.²⁴ Since the release of Fomivirsen, only one other RNA-based drug has been released to market over a 10 year period.²⁴ RNA has become a considerable target because of its potential to interfere with processes that allow gene and protein expression of diseases and disorders. RNA-based therapeutics can be classified into categories based on the mechanism of activity including mRNA translation, catalytically active RNA molecules (ribozymes), RNA interference (RNAi), and RNA that binds with proteins and other molecules.²⁵

One therapeutic approach that is highly promising is RNA interference (RNAi).²⁶ RNAi is a gene silencing technique that was discovered in the 1990's in petunia plants.²⁷ Messenger RNA (mRNA) is naturally single stranded and is required for protein synthesis and gene expression. Enzymes called Dicer and RISC recognize double stranded RNA (dsRNA) and terminate it because dsRNA generally signifies viral infection.²⁸ This can thought as an evolution consequence of cellular defense against viruses. Researchers have developed therapeutics that can take advantage of employing gene silencing towards disorders and diseases, which is referred to as target genes. This can be achieved by designing short strands of RNA that hybridize to the complementary strands of mRNA encoded by the target gene. Dicer and RISC enzymes then recognize

the dsRNA and degrade it.²⁹ As a result, mRNA is destroyed, which does not allow for protein synthesis or expression of the disease.

The structures of RNA and DNA differ significantly *in vivo*. Typically, DNA is a helical structure because of its double stranded structure. Contrarily, RNA folds into diverse conformations that adopt folds more similar to proteins and peptides. These differences can be directly attributed to RNA being single stranded, which allows the molecule fold onto itself to minimize its energy.³⁰ RNA exhibits unique binding pockets that can result in structural diversity. Because of this, these binding pockets can be exploited and targeted by small organic molecules. For example, small organic molecules that bind with RNA have been studied including antibiotics. These molecules have modest affinities and selectivity for RNA.³¹ Therapeutics that exhibit high selectivity and affinity for RNA are of considerable interest.

Because of the diverse functions of RNA, small organic molecules that selectively bind with RNA may provide points of interest that can be utilized as therapeutic intervention. Despite advances in drug discovery, there are only a few compounds that target RNA with high specificity and affinity,³⁰ which is in contrast to the large number of small organic drug molecules aimed at DNA.^{32,33} The groove of DNA has been a well-exploited target for drugs. On the other hand, only a small number of drugs have been targeted at the groove of RNA.³⁰ RNA-targeted drugs are a new emerging class of drugs that can be utilized as anti-cancer agents. In order to design such drugs, it is important to understand the RNA-binding interactions of small organic molecules.

One project that is currently ongoing by another graduate student is examining the binding interactions of small organic molecules with RNA utilizing TPA. The goal of this

project is to demonstrate that our methodology can be employed to differentiate between the RNA-binding modes. This is attractive since RNA has been recently explored as a new target for drug therapy. Thus, it is important to understand the interactions of therapeutics targeted at RNA. If our methodology can be employed towards RNA, this will be significant as it would allow researchers to probe RNA-drug interactions. If we can gain a deeper understanding on how small organic molecules interact with RNA, this could lead to an emergence of a new class of drugs targeted at RNA. Additionally, this will provide a new approach to probe RNA-drug interactions at biologically relevant conditions because TPA has been demonstrated to exhibit high sensitivity.^{34,35}

8.4 Examining Kinase Activity by Implementing a Chemosensor Peptide with Continuous Real-Time Analysis in Live Cells (Chapter 5)

Signaling in biological systems that are regulated by protein phosphorylation is critical for many cellular and biological processes. Such processes are complex and strategically orchestrated by diverse cellular species. More importantly, signaling cascades are important for cellular function, such as mediating cell proliferation and apoptosis.³⁶ Kinase enzymes are required for this phosphorylation processes. The objective of this work is to gain a better understanding of kinase activity in live cells with continuous real-time analysis, which has never been achieved thus far. Additionally, this will allow researchers to screen kinase inhibitors and drugs at biologically relevant conditions. It is important to note that the kinase catalytic activity is a very complex process that is required for cellular communication. Many disorders, such as cancer and diabetes, have been directly related to abnormal kinase activity.³⁷ Therefore,

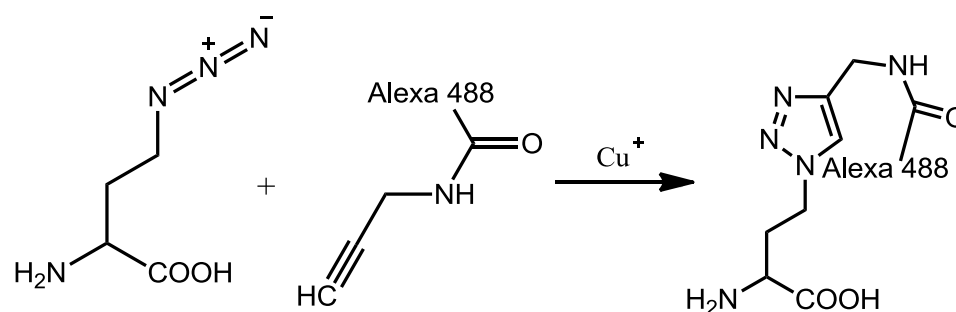
understanding kinase activity may lead to therapeutics aimed at abnormal kinase activity. Progress in molecular biochemistry has led to an emergence of mechanism-based processes and pathways, such as epidermal growth factor receptor and kinase inhibitors.³⁸ In fact, kinase inhibitors have been recently explored as chemotherapy medications.³⁹ These therapeutics work by blocking or inhibiting specific kinase activity. For example, ZD-1839 (Iressa) is a quinazoline derivative that selectively inhibits tyrosine kinase and is under clinical development in cancer patients.⁴⁰

The impact of our work is imbedded in the information gained, which could be applied towards therapeutics aimed at abnormal kinase activity. Additionally, this work has the potential to be implemented for high-throughput screening of kinase activity in live cells with continuous real-time analysis. Thus, this could have a profound impact on the drug research and development field as it will allow researchers to screen drugs at biologically relevant conditions. Likewise to the examination of the DNA-binding interactions of small organic molecules, the information gained about kinase-peptide interactions can contribute to the field of drug research and development. This work here will pave new a route to study clinical drugs with respect to kinase activity by continuous real-time analysis in live cells.

We have demonstrated the successful delivery of the Sox-peptide into live HeLa cells by FLIM. The next stage of the project is to monitor the phosphorylation process with continuous real-time analysis in live cells. This task will be accomplished by delivering the JNKS19 (unphosphorylated) peptide into the cell. The change in fluorescence and fluorescence lifetime will be monitored by confocal microscopy (multi-photon and fluorescence lifetime microscopy). As demonstrated, an excellent route to monitor the

phosphorylation process is by FLIM due to the autofluorescence. In particular, the autofluorescence has been a major issue in regards to the project. If a lower energy excitation wavelength could be used, this would solve many issues. One approach to resolve the autofluorescence issue is to integrate a fluorophore adjacent to the Sox-fluorophore via solid phase peptide synthesis (SPPS) where the fluorescence can be monitored at a lower energy emission wavelength through FRET as detailed in Scheme 8.1. Another issue with this project is that we need to confirm that the peptide is not interfering with other biological processes, which may cause an increase in the fluorescence lifetime. Hence, it is important to deliver the Sox-peptide omitted of the Sox-fluorophore as a control experiment. In addition, it is critical to stain both the cell wall and nucleus utilizing commercial stains as it will allow us to examine the localization of the Sox-peptide. Prof. Kuroda has provided excellent comments with regards to the future work of this project. I would like to thank him personally for these recommendations as it will significantly increase the quality and interpretation of our work.

Scheme 8.1. Synthesis of Alexa 488 amino acid derivative. This fluorophore can be integrated into the Sox-peptide substrate via SPPS, which can undergo FRET with the Sox-fluorophore. This will allow the fluorescence to be monitored at a lower energy wavelength to minimize autofluorescence from the cells.



Kinase inhibitors will be delivered into the cells to compare the kinase activity in the absence and presence of an inhibitor. These inhibitors will be delivered into the cell by incubating the cells with the inhibitors since they are cell permeable. One inhibitor that will be utilized is SP600125, which is a reversible inhibitor.⁴¹ SP600125 competes with the binding site of ATP during the phosphorylation process, thus inhibiting kinase activity. Another inhibitor that will be utilized is JNK-IN-8, which is an irreversible inhibitor discovered by Prof. Nathanael Gray at Harvard.⁴² The structures of the inhibitors are shown in Figure 8.1. JNK-IN-8 is a potent irreversible inhibitor that undergoes a nucleophilic attack on the cysteine residue proximal to the ATP-binding site leading to a blockage in the binding site. It has been shown that JNK-IN-8 demonstrates superior performance as compared to SP600125 by more than an order magnitude.⁴² This will allow us to compare the kinase activity by implementing the JNKS19 peptide with both a reversible and irreversible inhibitor. The goal is to correlate the fluorescence change (or fluorescence lifetime change) to the kinase activity as well as understanding peptide-kinase interactions at physiological conditions. We hope our work will provide a new route to examine kinase activity in live cells with continuous real-time analysis and high-throughput screening. Perhaps, the information gained will be employed in drug research and discovery. If this can be achieved, this will be a major contribution to the field. This work is currently being carried out by a new graduate student.

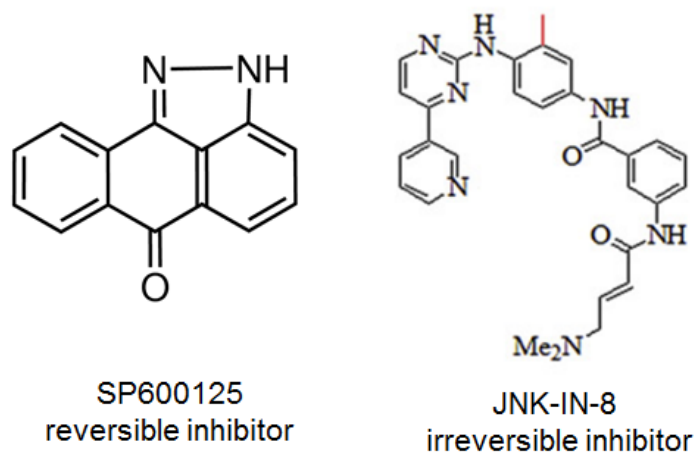


Figure 8.1. Chemical structures of kinase inhibitors.

8.5 Synthesis and Characterization of Silsesquioxane-Based Microporous Materials (Chapter 6)

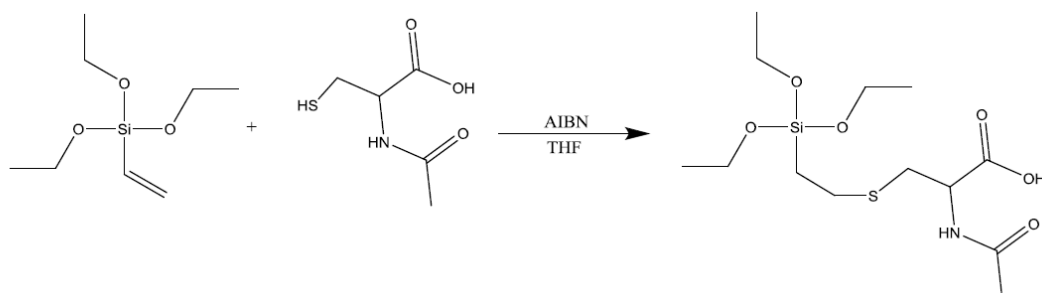
We developed a new route for the synthesis of silsesquioxane-based microporous materials by an oxysilylation reaction of cubic symmetry Q-type cages (OHS) with a series of ethoxysilane linkers. These materials offer several advantages over traditional porous materials, such as zeolites, metal organic frameworks (MOFs), and covalent organic frameworks (COFs) as these materials can be synthesized with fast reaction times, non-alkaline environments, and low temperatures. These materials are attractive because they have the potential to be tailored so that multiple functionalities can be introduced to the system. Moreover, these porous materials can be further functionalized and tailored for other applications including catalyst substrates, bio-adsorbents, drug storage and delivery, gas sieving, gas storage, and vacuum insulation materials.^{43–47} One example that will be discussed in greater detail is that these materials can be applied as chiral separation materials.

The separation of chiral molecules has been of considerable interest because a majority of bioorganic and drug molecules are chiral. Many compounds found in living organisms are chiral, such as nucleic acids, peptides, and proteins. Chiral separation is also critical for drug development.⁴⁸ Enantiomers of many drugs can have different pharmacological activities, mostly exhibiting negative effects. Receptors in humans react very specific to chiral molecules resulting in different responses to the drug. One isomer of a drug may be therapeutic while the other isomers may have negative consequences or may even be deadly. For example, Thalidomide was prescribed as a sedative or hypnotic in 1957.⁴⁹ Shortly after the drug was released, thousands of infants were born with phocomelia or malformation of the limbs. This was due to the different isomers of the drug having negative effects. This incident could have been avoided if the undesirable isomers were separated from the therapeutic isomer. Today, pharmaceutical companies pay close attention and detail to various isomers when developing new drugs. Thus, chiral separation materials are of great importance.

Several methods have been employed for chiral separation, such as HPLC, capillary electrophoresis, and electrochemistry.^{50,51} However, these methods are high cost and impractical for real-time analysis. In addition, they cannot be used for high-throughput assays. Therefore, new materials for chiral separation are of considerable interest. *N*-acetyl-*L*-cysteine is an excellent candidate to incorporate into such materials because of its ability to separate chiral compounds.⁵² One application of interest is the design and development of chiral separation materials based on our porous materials. This can be accomplished by functionalizing the Si(OEt)₃-vinyl with cysteine as shown in Scheme 8.2. Si(OEt)₃-cysteine can then be used a linker to form network polymers containing

cysteine functional groups. Because of its high surface area, these porous materials would be excellent candidates for chiral separation materials.

Scheme 8.2. Synthesis of Si(OEt)₃-cysteine.



Another potential avenue of these porous materials is for gas storage applications. Gas storage in porous materials has attracted a considerable amount of attention. The most well-known current area of research includes storing hydrogen for energy applications. However, other gases, such as CO₂, SO₂, and NO, are of interest as well.⁵³ There are specific criteria that must be required for any gas storage material. The advantage of our materials is that multiple functionalities can be introduced to the system, which allows the materials to be tailored to meet these specific criteria. Additionally, the properties of these materials can be modified, allowing for diverse applications. There are several advantages in storing gases in porous materials rather than enclosed volumes, such as a tank or a bottle.⁵⁴ Storing gas in tanks require liquefaction at very low temperatures and/or high pressures.⁵⁵ In general, there are safety advantages of storing gases in porous materials especially if high pressures can be avoided.⁵³ Furthermore, gases are easier to handle in small amounts when stored in porous materials. Because our materials are composed of silsesquioxane, the materials exhibit high thermal stability

unlike organic-based materials, indicating that they can be used for high temperature applications.⁵⁶ This is one prime example in which porous materials can be utilized for real-world applications. In particular, porous materials have contributed to the development in applications ranging from medical diagnosis to microelectronics.⁵⁷ Examples and future work were provided where the porous network materials can be used for industrial applications. These materials have the potential for the tailoring of the microstructure, chemical composition, surface properties, and porosity. The impact of this work is that these materials are low-cost and can be easily synthesized while introducing multiple functionalities. Because of its potential and diverse applications, this research has contributed to the big picture as it paves the road for the design and development of future materials.

8.6 Avoiding Carbothermal Reduction: Distillation of Alkoxysilanes from Biogenic, Green, and Sustainable Sources (Chapter 7)

Rice is considered one of the major food crops in the world. The protective coatings of rice grains are referred to as rice hulls, which are considered a byproduct of rice consumption. In order to cultivate rice grains for human consumption, the rice hulls must be removed since they are ingestible. Rice hulls have applications ranging from fertilizer to fuel.⁵⁸ Million of tons of rice hulls are burned each year for the generation of electricity resulting in a byproduct called rice hull ash (RHA). RHA is mainly composed of amorphous silica (90%) and does not contain heavy metals making it an attractive source of silica.^{59,60} RHA is high in silicon content because rice plants uptake silicon (water soluble silicates) from the roots directly from the dirt then transports it to the outer

surface of the plant to form a cellulose silica membrane.⁶¹ Upon combustion, silica and carbon are left behind. The production of RHA is a sustainable process and does not leave a large carbon footprint. A major disadvantage of generating RHA is the disposal processes. Because of its high silicon content, there has been considerable interest in using RHA as a precursor for many silicon containing materials.⁶²⁻⁶⁴ RHA has been mainly utilized for applications that are considered low-value applications. In order to use RHA for high-value applications, the silica source must be extracted to achieve relatively high purity (> 99%). Silica has been widely used in chromatograph columns, pharmaceutical applications, adhesives, detergents, and ceramics.^{65,66}

A common precursor used for many silicon containing materials include alkoxysilanes, which are produced in the following:⁶⁷



One major disadvantage of this process is that it requires the carbothermal reduction of SiO_2 to form Si_{met} . This process is energy intensive and requires elaborate equipment. Additionally, it produces toxic and corrosive chlorosilanes. Because of this, specialized equipment is required to contain the chlorosilane byproducts. If alkoxysilanes can be produced directly from SiO_2 while avoiding the carbothermal reduction step, this will be critical because it could significantly reduce the cost of many silicon containing contents.

We have demonstrated the first distillable alkyoxysilane synthesized directly from silica, which has been investigated for over 80 years without success.⁶⁸⁻⁷¹ Our process is an alternative to the carbothermal reduction of silica, which offers several advantages as it is not a high energy/temperature process, does not produce toxic byproducts, and does not leave a large carbon footprint. This is significant because this process has the potential to reduce the cost of many silicon containing products. Since these alkyoxysilanes can be distilled, they can be easily purified implying that this process can be employed for applications that require high purity silicon. This is very important in industries that require solar (6N) or electronic grade silicon (9N). As demonstrated, this work can have a profound impact in the real world by reducing the cost of silicon precursors as many consumer products contain silicon ranging from toothpaste to electronic applications (e.g. cell phones, computers).

The process and conditions have not been fully optimized to give higher yields. This would be considered a major parameter in order to move the technology to a larger scale (e.g. pilot lab). The process can be optimized by carrying out design of experiments (DOE). The yield would be monitored with respect to the reaction time, amount of catalytic base, volume of diol, and temperature. The data would be analyzed in statistical software to determine the best parameters to give optimal yields. We have shown that the dissolution rate is directly related to the surface area of the silica source. Therefore, the biogenic silica source (e.g. RHA) can be processed or modified to yield higher surface area silica sources. Such methods include ball milling the silica source before starting the dissolution process. Once the process has been fully optimized, it has the potential to be scaled up on a commercial level.

Other future work includes functionalizing the spiro-siloxane with various substituents, such as Grignard reagents, then converting the material to silsesquioxanes through fluoride catalyzed reactions, which will give T₈, T₁₀, and T₁₂ cage structures. This has the potential to lower the cost of commercially available silsesquioxanes. Furthermore, the spiro-siloxane can be used as a precursor to produce high purity fumed silica via liquid-feed flame spray pyrolysis (LF-FSP) and precipitated silica. One interesting avenue is that other metal alkyl- or alkoxy-based materials may be formed from biogenic metal sources, thus providing a low cost and more direct route to producing such materials. A summary of potential applications of the spiro-siloxane is presented in Figure 8.2.

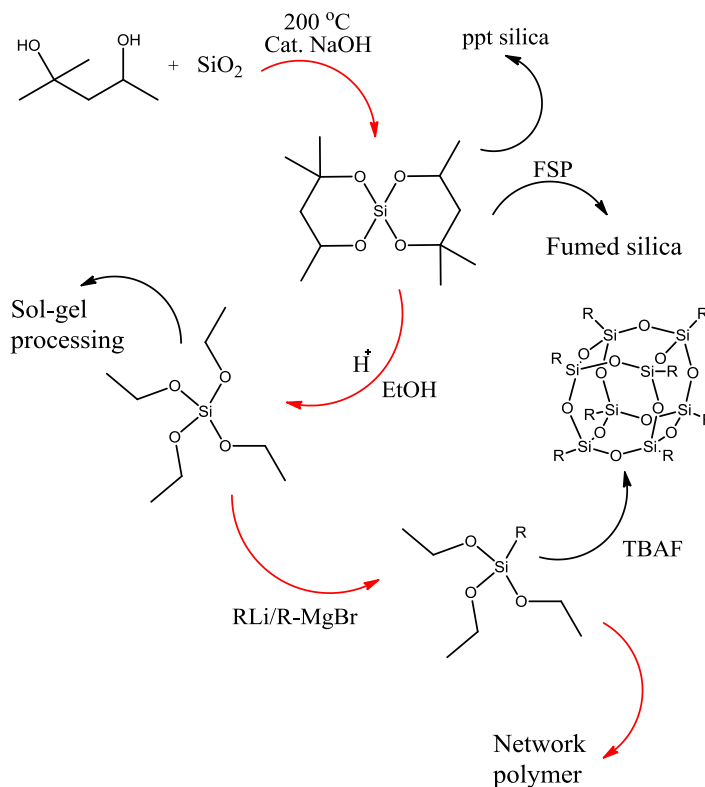


Figure 8.2. Potential applications of spiro-siloxane synthesized from RHA.

References

1. Drews, J. *Science* **2000**, 287, 1960.
2. *Clinical Trials in Neurology*; Guiloff, R. J., Ed.; Springer London: London, 2001.
3. DiMasi, J. A.; Hansen, R. W.; Grabowski, H. G. *J. Health Econ.* **2003**, 22, 151.
4. *Preclinical Drug Development, Second Edition*; CRC Press, 2009.
5. Begley, C. G.; Ellis, L. M. *Nature* **2012**, 483, 531.
6. www.fda.gov/ForPatients/Approvals/Drugs/ucm
7. Pocock, S. J. *Clinical Trials*; John Wiley & Sons Ltd,,: West Sussex, England, 2013.
8. Simon, R. *Control. Clin. Trials* **1989**, 10, 1.
9. Peto, R.; Pike, M. C.; Armitage, P.; Breslow, N. E.; Cox, D. R.; Howard, S. V.; Mantel, N.; McPherson, K.; Peto, J.; Smith, P. G. *Br. J. Cancer* **1977**, 35, 1.
10. Steinmetz, K. L.; Spack, E. G. *BMC Neurol.* **2009**, 9, S2.
11. Steiner, S.; Witzmann, F. A. *Electrophoresis* **2000**, 21, 2099.
12. Martinez, R.; Chacon-Garcia, L. *Curr. Med. Chem.* **2005**, 12, 127.
13. Zhang, Y.; Wang, J.; Jia, P.; Yu, X.; Liu, H.; Liu, X.; Zhao, N.; Huang, B. *Org. Biomol. Chem.* **2010**, 8, 4582.
14. Tan, L.-F.; Chao, H.; Zhen, K.-C.; Fei, J.-J.; Wang, F.; Zhou, Y.-F.; Ji, L.-N. *Polyhedron* **2007**, 26, 5458.
15. Feng, X. J.; Wu, P. L.; Bolze, F.; Leung, H. W. C.; Li, K. F.; Mak, N. K.; Kwong, D. W. J.; Nicoud, J.-F.; Cheah, K. W.; Wong, M. S. *Org. Lett.* **2010**, 12, 2194.
16. Dumat, B.; Bordeau, G.; Faurel-Paul, E.; Mahuteau-Betzer, F.; Saettel, N.; Metge, G.; Fiorini-Debuisschert, C.; Charra, F.; Teulade-Fichou, M.-P. *J. Am. Chem. Soc.* **2013**, 135, 12697.

17. Fire, A.; Xu, S.; Montgomery, M. K.; Kostas, S. A.; Driver, S. E.; Mello, C. C. *Nature* **1998**, *391*, 806.
18. Kruger, K.; Grabowski, P. J.; Zaug, A. J.; Sands, J.; Gottschling, D. E.; Cech, T. R. *Cell* **1982**, *31*, 147.
19. Fedor, M. J.; Williamson, J. R. *Nat. Rev. Mol. Cell Biol.* **2005**, *6*, 399.
20. Wu, L.; Belasco, J. G. *Mol. Cell* **2008**, *29*, 1.
21. Bayne, E. H.; Allshire, R. C. *Trends Genet.* **2005**, *21*, 370.
22. Johnstone, O.; Lasko, P. *Annu. Rev. Genet.* **2001**, *35*, 365.
23. Cooper, G. M. Sinauer Associates 2000.
24. Bonetta, L. *Cell* **2009**, *136*, 581.
25. Burnett, J. C.; Rossi, J. J. *Chem. Biol.* **2012**, *19*, 60.
26. Bumcrot, D.; Manoharan, M.; Koteliansky, V.; Sah, D. W. Y. *Nat. Chem. Biol.* **2006**, *2*, 711.
27. de Fougerolles, A.; Vornlocher, H.-P.; Maraganore, J.; Lieberman, J. *Nat. Rev. Drug Discov.* **2007**, *6*, 443.
28. Melnikova, I. *Nat. Rev. Drug Discov.* **2007**, *6*, 863.
29. Aagaard, L.; Rossi, J. J. *Adv. Drug Deliv. Rev.* **2007**, *59*, 75.
30. Guan, L.; Disney, M. D. *ACS Chem. Biol.* **2012**, *7*, 73.
31. Thomas, J. R.; Hergenrother, P. J. *Chem. Rev.* **2008**, *108*, 1171.
32. Palchaudhuri, R.; Hergenrother, P. J. *Curr. Opin. Biotechnol.* **2007**, *18*, 497.
33. Rask-Andersen, M.; Almén, M. S.; Schiöth, H. B. *Nat. Rev. Drug Discov.* **2011**, *10*, 579.
34. Clark, T. B.; Ziolkowski, M.; Schatz, G. C.; Goodson, T. *J. Phys. Chem. B* **2014**,

118, 2351.

35. Doan, P. H.; Pitter, D. R. G.; Kocher, A.; Wilson, J. N.; Goodson, T. *J. Am. Chem. Soc.* **2015**, *137*, 9198.
36. Vivanco, I.; Sawyers, C. L. *Nat. Rev. Cancer* **2002**, *2*, 489.
37. Karaman, M. W.; Herrgard, S.; Treiber, D. K.; Gallant, P.; Atteridge, C. E.; Campbell, B. T.; Chan, K. W.; Ciceri, P.; Davis, M. I.; Edeen, P. T.; Faraoni, R.; Floyd, M.; Hunt, J. P.; Lockhart, D. J.; Milanov, Z. V.; Morrison, M. J.; Pallares, G.; Patel, H. K.; Pritchard, S.; Wodicka, L. M.; Zarrinkar, P. P. *Nat. Biotechnol.* **2008**, *26*, 127.
38. Tan, D. S.-W.; Gerlinger, M.; Teh, B.-T.; Swanton, C. *Eur. J. Cancer* **2010**, *46*, 2166.
39. Zhang, J.; Yang, P. L.; Gray, N. S. *Nat. Rev. Cancer* **2009**, *9*, 28.
40. Ciardiello, F.; Caputo, R.; Bianco, R.; Damiano, V.; Pomatico, G.; De Placido, S.; Bianco, A. R.; Tortora, G. *Clin. Cancer Res.* **2000**, *6*, 2053.
41. Bennett, B. L.; Sasaki, D. T.; Murray, B. W.; O'Leary, E. C.; Sakata, S. T.; Xu, W.; Leisten, J. C.; Motiwala, A.; Pierce, S.; Satoh, Y.; Bhagwat, S. S.; Manning, A. M.; Anderson, D. W. *Proc. Natl. Acad. Sci.* **2001**, *98*, 13681.
42. Zhang, T.; Inesta-Vaquera, F.; Niepel, M.; Zhang, J.; Ficarro, S. B.; Machleidt, T.; Xie, T.; Marto, J. A.; Kim, N.; Sim, T.; Laughlin, J. D.; Park, H.; LoGrasso, P. V.; Patricelli, M.; Nomanbhoy, T. K.; Sorger, P. K.; Alessi, D. R.; Gray, N. S. *Chem. Biol.* **2012**, *19*, 140.
43. Flanigen, E. M.; Bennett, J. M.; Grose, R. W.; Cohen, J. P.; Patton, R. L.; Kirchner, R. M.; Smith, J. V. *Nature* **1978**, *271*, 512.

44. Kresge, C. T.; Leonowicz, M. E.; Roth, W. J.; Vartuli, J. C.; Beck, J. S. *Nature* **1992**, *359*, 710.
45. Beck, J. S.; Vartuli, J. C.; Roth, W. J.; Leonowicz, M. E.; Kresge, C. T.; Schmitt, K. D.; Chu, C. T. W.; Olson, D. H.; Sheppard, E. W. *J. Am. Chem. Soc.* **1992**, *114*, 10834.
46. Inagaki, S.; Guan, S.; Fukushima, Y.; Ohsuna, T.; Terasaki, O. *J. Am. Chem. Soc.* **1999**, *121*, 9611.
47. Yaghi, O.; Li, H.; Davis, C. *Accounts Chem.* **1998**.
48. *Chiral Separation Techniques: A Practical Approach*; John Wiley & Sons, 2008.
49. Miller, M. T. *Trans. Am. Ophthalmol. Soc.* **1991**, *89*, 623.
50. Su, H.; Zheng, Q.; Li, H. *J. Mater. Chem.* **2012**, *22*, 6546.
51. Wren, S. A. C. *J. Chromatogr. A* **1993**, *636*, 57.
52. Kühnle, A.; Linderoth, T. R.; Hammer, B.; Besenbacher, F. *Nature* **2002**, *415*, 891.
53. Morris, R. E.; Wheatley, P. S. *Angew. Chem. Int. Ed. Engl.* **2008**, *47*, 4966.
54. Schlapbach, L.; Züttel, A. *Nature* **2001**, *414*, 353.
55. Farha, O. K.; Yazaydin, A. Ö.; Eryazici, I.; Malliakas, C. D.; Hauser, B. G.; Kanatzidis, M. G.; Nguyen, S. T.; Snurr, R. Q.; Hupp, J. T. *Nat. Chem.* **2010**, *2*, 944.
56. Xu, H.; Kuo, S.-W.; Lee, J.-S.; Chang, F.-C. *Macromolecules* **2002**, *35*, 8788.
57. Davis, M. E. *Nature* **2002**, *417*, 813.
58. Proctor, A.; Clark, P. K.; Parker, C. A. *J. Am. Oil Chem. Soc.* **1995**, *72*, 459.
59. Kamath, S. R.; Proctor, A. **2007**.

60. Kalapathy, U. *Bioresour. Technol.* **2000**, *73*, 257.
61. Ma, J. F.; Yamaji, N. *Trends Plant Sci.* **2006**, *11*, 392.
62. Marchal, J. C.; Krug III, D. J.; McDonnell, P.; Sun, K.; Laine, R. M. *Green Chem.* **2015**, *17*, 3931.
63. Asuncion, M. Z.; Hasegawa, I.; Kampf, J. W.; Laine, R. M. *J. Mater. Chem.* **2005**, *15*, 2114.
64. www.ns.umich.edu/new/releases/23378-turning-rice-farming-waste-to-useful-silica-compounds
65. Prasad, R.; Pandey, M. *Bull. Chem. React. Eng. Catal.* **2012**, *7*, 1.
66. Sun, L.; Gong, K. *Ind. Eng. Chem. Res.* **2001**, *40*, 5861.
67. Laine, R. M.; Furgal, J. C.; Doan, P.; Pan, D.; Popova, V.; Zhang, X. *Angew. Chem. Int. Ed. Engl.* **2016**, *55*, 1065.
68. Frye, C. L. *J. Am. Chem. Soc.* **1964**, *86*, 3170.
69. Rosenheim, A.; Raibmann, B.; Schendel, G. *Zeitschrift für Anorg. und Allg. Chemie* **1931**, *196*, 160.
70. Flynn, J. J.; Boer, F. P. *J. Am. Chem. Soc.* **1969**, *91*, 5756.
71. Barnum, D. W. *Inorg. Chem.* **1972**, *11*, 1424.